





THÈSE de DOCTORAT

UNIVERSITÉ PIERRE ET MARIE CURIE (PARIS 6)

ED 391 : Sciences mécaniques, acoustique, électronique & robotique de Paris

Spécialité : **Mécanique**

présentée par

Bertrand LAGRÉE

pour obtenir le grade de

DOCTEUR de l'UNIVERSITÉ PIERRE ET MARIE CURIE

Sujet de thèse :

Modélisation de l'écoulement diphasique en milieu poreux par méthode Volume de Fluide

Modelling of two-phase flow in porous media with Volume-of-Fluid method

Soutenance effectuée le 17 septembre 2014 devant le jury composé de:

Pr. Ivan LUNATI	Rapporteur
M. Marc PRAT	Rapporteur
M. Igor BONDINO	Examinateur
M. Christophe JOSSERAND	Examinateur
Pr. Régis MARCHIANO	Examinateur
Pr. Mikhaïl PANFILOV	Examinateur
M. Stéphane POPINET	Examinateur
Pr. Stéphane ZALESKI	Directeur de Thèse

Ελωι ελωι λεμα σαβαχθανι
Mk 15, 34

dixitque Deus fiat lux et facta est lux
Gn 1, 3

Apprendre n'est pas savoir ; il y a les sachants et les savants :
c'est la mémoire qui fait les uns, c'est la philosophie qui fait les autres.
Alexandre Dumas, *Le Comte de Monte-Cristo*

Acknowledgments

I would like to express my deepest gratitude to my supervisor, Stéphane Zaleski, for his support, encouragement, good company and insightful directions throughout my PhD study. It has been a privilege to learn from him and be guided throughout the last three years.

I would like to extend my appreciation to Professor Ivan Lunati from *Université de Lausanne* and Mr Marc Prat from *Institut de Mécanique des Fluides de Toulouse* for agreeing to be my "thesis reporters" (*rapporteurs*). I am also very grateful to Christophe Josserand, Régis Marchiano, Mikhaïl Panfilov and Stéphane Popinet who agreed to judge my work as members of the thesis committee.

I would like to acknowledge the oil company TOTAL for having financially supported my PhD work. Special thanks are dedicated to both Fabrice Aubertin and Igor Bondino for their valuable advice and for having dedicated so much time to answer my many questions and solve my problems. I would also like to thank Xavier Britsch, Philippe Cordelier, Gérald Hamon, Javier Jimenez and Richard Rivenq who all helped me at some point.

My thanks also go to all members of *Institut Jean le Rond d'Alembert* at UPMC who worked alongside me for three years, and especially to Pierre-Yves Lagrée, the present director of the FCIH (*Fluides Complexes et Instabilités Hydrodynamiques*) research team in which I have completed my PhD work.

Last but by no means least, I would like to express my appreciation to my marvellous wife, my parents, my sister, my brothers and my numerous friends who endured this long process with me, always offering support, and without whom none of this would have been possible.

Contents

Acknowledgments **5**

Notations **13**

Introduction **17**

1 Elements of fluid and porous medium theory **31**

1.1 Elements of fluid dynamics theory 33

1.1.1 Gas, liquid or solid 33

1.1.2 Continuum approach to fluid materials 34

1.1.3 Fluid properties 36

1.1.3.1 Fluid viscosity 36

1.1.3.2 Conservation laws 38

1.1.3.3 Surface tension 40

1.1.3.4 Dimensionless parameters 42

1.1.4 Wettability 43

1.2 Porous medium 46

1.2.1 Definition of a porous medium 46

1.2.2 Continuum approach to porous media 48

1.2.3 Porosity and effective porosity 49
1.2.4 Darcy's law 51
1.2.4.1 Single-phase flows 51
1.2.4.2 Multiphase flows 51
1.2.4.3 Hele-Shaw cell and two-phase flow in porous media . . 54
1.2.4.4 Other approaches to describe flow in porous media . . 55
1.2.5 Tortuosity 58
1.2.5.1 Geometrical tortuosity 59
1.2.5.2 Hydraulic tortuosity 60
1.2.5.3 How is hydraulic tortuosity related to geometrical tortuosity? 64
1.2.6 What about surface tension? 64
1.3 Phenomenology of flows in porous media 69
1.3.1 Displacement of the meniscus at the pore scale 70
1.3.2 Phase diagram in the case of drainage 73
1.3.3 Phase diagram in the imbibition case 78
1.3.4 Deformable media 82
1.3.4.1 Labyrinthine structures 82
1.3.4.2 Stick-slip bubbles 84
1.3.4.3 Fracturing of deformable media 85
1.3.4.4 Phase diagramm 90
1.4 Conclusion 91

2 Gerris, a Direct Numerical Simulation code 95
2.1 Numerical scheme of the Gerris Flow Solver 98
2.1.1 Temporal discretisation 99
2.1.2 Spatial discretisation 101
2.1.3 Adaptive mesh refinement 103
2.1.4 Volume-of-Fluid advection scheme 105
2.1.5 Balanced-force surface-tension calculation 108
2.1.6 Gerris in parallel 111

2.1.7 Implementation of solid boundaries . . . 111
2.2 Gerris Flow Solver for porous geometry . . . 114
2.2.1 Scalability at low porosity . . . 114
2.2.1.1 Definitions . . . 114
2.2.1.2 Characteristics of the tests . . . 115
2.2.1.3 Results on cluster *babbage* . . . 116
2.2.1.4 Results on cluster *Rostand* . . . 119
2.2.2 CPU time and CFL number for two-phase flow invasion of porous geometries . . . 121
2.2.2.1 Wall-clock CPU time in a porous geometry . . . 122
2.2.2.2 CFL number in a porous geometry . . . 124
2.2.3 Single-phase and two-phase Poiseuille flows . . . 126
2.2.3.1 Single-phase Poiseuille flow . . . 127
2.2.3.2 Two-phase Poiseuille flow . . . 131
2.2.4 Permeability of a randomly-generated porous medium . . . 139
2.3 3D simulations of invasion in oil-filled real porous media . . . 144
2.3.1 X-ray microtomography . . . 144
2.3.2 Invasion of porous media in both water-wetting and oil-wetting cases . . . 146
2.3.2.1 Contact angle in Gerris . . . 146
2.3.2.2 Simulation of a single pore . . . 147
2.3.2.3 Invasion of a 3D porous medium with several pores . . . 150
2.4 Conclusion . . . 156

3 2D viscous fingering 159
3.1 Viscous fingering in a Hele-Shaw cell . . . 162
3.1.1 Growth in a Laplacian field . . . 163
3.1.2 Linear stability analysis of the front between two fluids of different viscosity . . . 163
3.1.2.1 The basic flow . . . 164
3.1.2.2 The disturbance of the interface . . . 165

3.1.2.3 Continuity of the normal velocities at the interfaces . . 166
3.1.2.4 The pressure jump at the interface due to surface tension 166
3.2 The existence of stable curved fronts 167
3.2.1 Isotropic case 167
3.2.1.1 Linear channel 167
3.2.1.2 Sector-shaped cells 170
3.2.1.3 Circular geometry 172
3.2.2 Non-isotropic case 172
3.2.2.1 The dendrite 172
3.2.2.2 The anomalous Saffman-Taylor finger 172
3.3 Stability of the curved fronts 175
3.3.1 Isotropic case 175
3.3.2 Anisotropic case 175
3.4 Implementing Darcy flows in the Gerris Flow Solver 177
3.5 Saffman-Taylor fingering in a Hele-Shaw cell with central injection . . . 178
3.5.1 Equations governing the flow 178
3.5.2 Effects of mesh-induced noise and viscosity ratio 179
3.5.2.1 Comparison with experimental results 182
3.5.3 Zero-pressure approximation in the less viscous fluid 182
3.5.4 Interface length and area of the resulting cluster 183
3.5.5 Accuracy of the asymptotic coefficient 185
3.5.6 Fractal dimension 186
3.5.7 Polar modelisation of viscous fingering 187
3.6 Conclusion 190

4 Lateral injection in a quasi-2D geometry 191
4.1 Experiments of lateral injection in square slabs 192
4.1.1 Description of the experiments 192
4.1.2 Measuring system 192
4.1.3 Water and polymer injection 193
4.1.3.1 Injection of brine 193

4.1.3.2 Injection of polymer . . . 194
4.1.4 Influence of waterflooding rate . . . 196
4.2 Simulation of Darcy flows in rectangular slabs with lateral injection . . 198
4.2.1 Waterflood simulation . . . 198
4.2.1.1 Square geometry . . . 198
4.2.1.2 Reduced geometry . . . 201
4.2.2 Injection of polymer after waterflooding . . . 205
4.3 Conclusion . . . 210

Conclusion and perspectives **213**

A Invasion percolation **217**
A.1 Basic process . . . 217
A.2 Algorithm . . . 218
A.3 Comparison with ordinary percolation . . . 219
A.4 Fractal dimension . . . 220

B Diffusion-Limited Aggregation **223**
B.1 The basic concept . . . 223
B.2 Laplacian growth and Dielectric Breakdown Model . . . 226
B.3 Conformal mapping . . . 229
B.3.1 Loewner evolution and the Hastings-Levitov scheme . . . 229

C Fractals and multifractals **233**
C.1 Definition . . . 233
C.2 Fractal dimension . . . 234
C.3 How to calculate the fractal dimension? . . . 237
C.4 Fatou and Julia sets . . . 237

D Simple Line Interface Calculation method **241**

E Two-phase Poiseuille flow **245**

List of Figures **249**

List of Tables **257**

Bibliography **259**

Extended summary in French **305**

Notations

Basic notations

b		Thickness of a Hele-Shaw cell
c		Color function
d, D		Embedding or topological dimension
D_F		Fractal dimension
$\mathbf{e} = (e_{ij})$		Strain rate tensor
$\mathbf{g}$		Body force per unit mass
h		Size of a cell
k		Absolute permeability
k_r		Relative permeability
l	*either*	Mean free path of the molecules
	or	Characteristic length scale of the flow
L		Macroscopic lengthscale
p		Thermodynamic pressure
Q		Flow rate
R		Mean radius of curvature
s		Specific surface
t		Time variable

T_c	Characteristic timescale of the flow
$\mathbf{u} = (u_i) = (u, v, w)$	Velocity
U	Characteristic velocity scale of the flow
V	Volume
W	Width of a Hele-Shaw cell
$\mathbf{x} = (x_i) = (x, y, z)$	Spatial position
Z	Number of cell updates per second
$Z_{/np}$	Number of cell updates per second and per core

Greek letters

$\boldsymbol{\delta} = (\delta_{ij})$	Kronecker delta
η	Solid fraction
ϕ	Porosity
ϕ_e	Effective porosity
κ	Curvature
λ_σ	Lengthscale of the influence of surface tension
μ	Viscosity
ν	Kinematic viscosity
Ω	Physical domain
Ω_s	Solid matrix
Ω_f	Fluid domain
ρ	Density/specific mass
σ	Surface tension
$\boldsymbol{\tau} = (\tau_{ij})$	Stress tensor
τ_r	Time of relaxation
τ_o	Time of observation
θ	Apparent contact angle
θ_a	Advancing contact angle
θ_r	Receding contact angle

Dimensionless numbers

Capillary number	$\mathrm{Ca} = \frac{\mu U}{\sigma}$
CFL number	$\mathrm{CFL} = \frac{U \Delta t}{h}$
Deborah number	$\mathrm{De} = \frac{\tau_r}{\tau_o}$
Knüdsen number	$\mathrm{Kn} = \frac{l}{L}$
Laplace number	$\mathrm{La} = \frac{\sigma \rho l}{\mu^2}$
Mobility ratio[1]	$M = \frac{k_{r,\mathrm{displaced}}}{k_{r,\mathrm{invading}}} \frac{\mu_{\mathrm{invading}}}{\mu_{\mathrm{displaced}}}$
Ohnesorge number	$\mathrm{Oh} = \frac{\mu}{(\sigma \rho l)^{1/2}}$
Reynolds number	$\mathrm{Re} = \frac{\rho l U}{\mu}$

Capital letters

$\mathbb{N}$ (resp. $\mathbb{N}^*$)	Set of non-negative (resp. positive) integers
$\mathbb{R}$	Set of the real numbers

Other notations

Δt	Timestep

[1] Viscosity ratio when neglecting the relative permeabilities

Acronyms

CFL	Courant-Friedrichs-Lewy
CPU	Central Processing Unit
CSF	Continuum Surface Force
CT	Computed Tomography (μCT: Computed MicroTomography)
DBM	Dielectric Breakdown Model
DLA	Diffusion-Limited Aggregation
DNS	Direct Numerical Simulation
EOR	Enhanced Oil Recovery
FCC	Face-Centred Cubic
FCHC	Face-Centred HyperCubic
HPC	High Performance Computer
LB	Lattice Boltzmann
LS	Level-Set
MYC	Mixed Youngs Centred
NGL	Natural Gas Liquid
PLIC	Piecewise Linear Interface Calculation
PNM	Pore-scale Network Modeling
REV	Representative Elementary Volume
SPH	Smoothed Particle Hydrodynamics
VOF	Volume of Fluid
WEC	World Energy Council

For the derivative, we will use both Leibniz's and Euler's notation, *i.e.* for a variable a and a function $f(a, \cdots)$

$$\frac{\partial f}{\partial a} = \partial_a f.$$

We use the following simplification: $\partial_{x_i} \equiv \partial_i$.

Introduction

Overall context

Throughout the world, the wealth of any country depends on energy, and consequently on the discovery and extraction of oil and other natural resources. As of today, more than 90% of the energy comes from fossil fuel (Figure 1). As no drastic change of this ratio is expected [1, 2, 3], the oil demand regularly increases with energy demand (Figure 2).

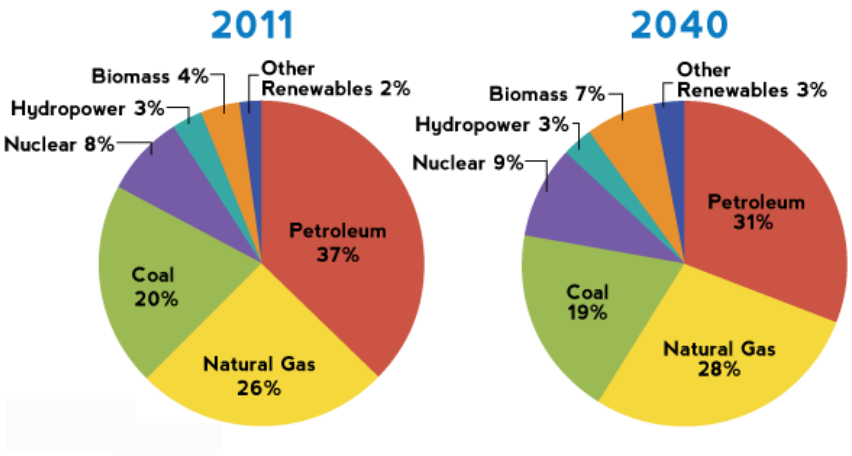

Figure 1: Energy Consumption Fuel Shares, 2011 and 2040. [1, 2, 3]

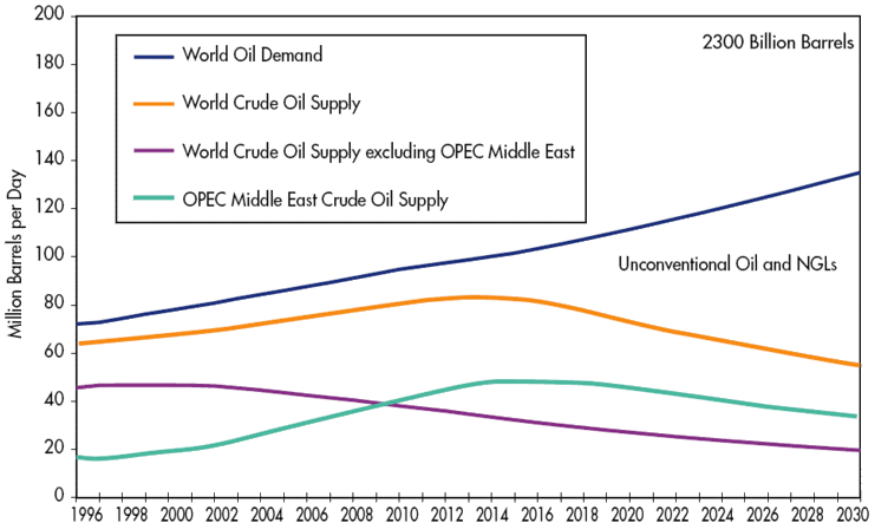

Figure 2: Oil supply profiles, 1996-2030 (NGLs: Natural Gas Liquids). [4]

In order to be able to supply this demand, research focuses in the oil industry on finding new deposits and organise their development strategies. This last point is of tremendous importance, as it affects directly the choice of surface installations and the global economy of the project [5]. Trying and understanding to the best the geological structure of the subsurface, alongside the different mechanisms governing the evolution of the reservoir, is thus a crucial step in a project of oil exploration and production. One can then obtain a better evaluation of the oil volume buried in the reservoir and of the expected production profiles. This extensive knowledge of the reservoir characteristics is required in order to optimise the exploitation of the oil field.

About fields and reservoirs

An oil field is a complex physical system whose observation is difficult at microscopic scale (porous medium). Understanding this system to the best is however essential, despite the lack of information. It is formed by one or more underground reservoirs resulting from sedimentation processes and containing liquid and/or gaseous hydrocarbons.

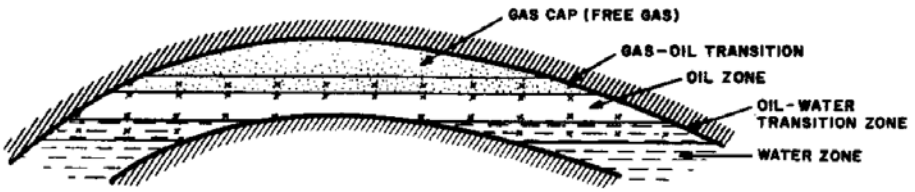

Figure 3: Associated oil-gas reservoir. [6]

A reservoir is a subsurface pool of hydrocarbons contained in porous or fractured rock formations. The naturally occurring hydrocarbons are generally trapped by overlying rock formations with lower permeability (*e.g.* clays). It is also common for the hydrocarbons to be trapped by an aquifer barrier. The vertical disposition of the fluids is a direct consequence of gravity. Indeed, when present the gas will appear in the higher parts of the reservoir, while the aquifer will generally be found at the base of the reservoir (Figure 3). The fluids fill the porous medium and will move even in pores of very small size ($\sim 1\,\mu$m).

Conventional and unconventional oil

The difference between conventional and unconventional oil is defined by the International Energy Agency (IEA) as follows:

"Conventional oil is a category that includes crude oil and natural gas liquids and condensate liquids, which are extracted from natural gas production. Crude oil production in 2011 stood at approximately 70 million barrels per day. Unconventional oil consists of a wider variety of liquid sources including oil sands, extra heavy oil, gas to liquids and other liquids. In general conventional oil is easier and cheaper to produce than unconventional oil. However, the categories *conventional* and *unconventional* do not remain fixed, and over time, as economic and technological conditions evolve, resources hitherto considered unconventional can migrate into the conventional category." [7]



Figure 4: Tar sandstone from the Monterey Formation of Miocene age (10 to 12 million years old), of southern California, USA. [8]

Conventional oil

Crude oil is a mineral oil consisting of a mixture of hydrocarbons of natural origin and associated impurities, such as sulphur. It exists in liquid form under normal surface temperatures and pressure. Its physical characteristics (for example, density) are highly variable. [7]

Unconventional oil

Oil sands, tar sands or, more technically, bituminous sands are loose sand or partially consolidated sandstone containing naturally occurring mixtures of sand, clay, and water, saturated with a dense and extremely viscous form of petroleum technically referred to as bitumen (or colloquially tar due to its similar appearance, odour and colour, see Figure 4). Natural bitumen deposits are reported in many countries, but in particular are found in extremely large quantities in Canada [9, 10]. Other large reserves are located in Kazakhstan and Russia. The estimated worldwide deposits of oil are more than 2 trillion barrels (320 billion cubic metres) [8]; the estimates include deposits that have not yet been discovered. Proven reserves of bitumen contain approximately 100 billion barrels [11], and total natural bitumen reserves are estimated

	Viscosity (in cp)	**API gravity**
Average heavy oils	From 10 to 100	From 18° to 25°
Extra-heavy oils	From 100 to 10000	From 7° to 20°
Bitumen and tar sands	More than 10000	From 7° to 12°
Oil shale	More than 10^6	

Table 1: Heavy oil classification. [5]

at 249.67 Gbbl[2] (39.694×10^9 m^3) globally, of which 176.8 Gbbl (28.11×10^9 m^3), or 70.8%, are in Canada [9].

Heavy crude oil or extra heavy crude oil is oil that is highly viscous, and cannot easily flow to production wells under normal reservoir conditions[12]. It is referred to as "heavy" because its density or specific gravity is higher than that of light crude oil. Heavy crude oil has been defined as any liquid petroleum with an API gravity[3] lower than 20° [13]. Physical properties that differ between heavy crude oils and lighter grades include higher viscosity and specific gravity, as well as heavier molecular composition. In 2010, the World Energy Council (WEC) defined extra heavy oil as crude oil having a gravity of less than 10° and a reservoir viscosity of no more than 10 000 centipoises[4]. When reservoir viscosity measurements are not available, extra-heavy oil is considered by the WEC to have a lower limit of 4° API [14].

A classification of heavy oils is presented above in Table 1.

[2] 1 Gbbl equals 10^9 barrels.

[3] The American Petroleum Institute gravity, or API gravity, is a measure of how heavy or light a petroleum liquid is compared to water. If its API gravity is greater than 10, it is lighter and floats on water; if less than 10, it is heavier and sinks. API gravity is thus an inverse measure of the relative density of a petroleum liquid and the density of water, but it is used to compare the relative densities of petroleum liquids. For example, if one petroleum liquid floats on another and is therefore less dense, it has a greater API gravity. Although mathematically, API gravity has no units (see the formula below), it is nevertheless referred to as being in "degrees". API gravity is gradated in degrees on a hydrometer instrument. The API scale was designed so that most values would fall between 10 and 70 API gravity degrees. The formula to obtain API gravity of petroleum liquids, from relative density (RD), is API gravity $= \frac{141.5}{\mathrm{RD}} - 131.5$ with $\mathrm{RD} = \rho_{\mathrm{oil}}/\rho_{\mathrm{water}}$.

[4] 1 cP $= 10^{-3}$ kg.m^{-1}.s^{-1}



Figure 5: Naturally burning oil shale. [17]

Oil shale is an organic-rich fine-grained sedimentary rock containing significant amounts of kerogen (a solid mixture of organic chemical compounds) from which technology can extract liquid hydrocarbons (shale oil) and combustible oil shale gas. The kerogen in oil shale can be converted to shale oil through the chemical processes of pyrolysis, hydrogenation, or thermal dissolution [15]. The temperature when perceptible decomposition of oil shale occurs depends on the time-scale of the pyrolysis; in the above ground retorting process the perceptible decomposition occurs at 300 °C, but proceeds more rapidly and completely at higher temperatures. The rate of decomposition is the highest at a temperature of 480 °C to 520 °C [15]. The ratio of shale gas to shale oil depends on the retorting temperature and as a rule increases with the rise of temperature. For the modern in-situ process, which might take several months of heating, decomposition may be conducted as low as 250 °C.

Depending on the exact properties of oil shale and the exact processing technology, the retorting process may be water and energy demanding. Oil shale has also been burnt directly as a low-grade fuel (Figure 5) [16].

Gas to liquids (GTL) is a refinery process to convert natural gas or other gaseous hydrocarbons into longer-chain hydrocarbons such as gasoline or diesel fuel. Methane-rich gases are converted into liquid synthetic fuels either via direct conversion—using non-catalytic processes that convert methane to methanol in one step—or via syngas

as an intermediate, such as in the Fischer Tropsch, Mobil and syngas to gasoline plus[5] processes.

Coal liquefaction also known as coal to liquids is a general term referring to a family of processes for producing liquid fuels from coal. Specific liquefaction technologies generally fall into two categories: direct (DCL) and indirect liquefaction (ICL) processes. Indirect liquefaction processes generally involve gasification of coal to a mixture of carbon monoxide and hydrogen (syngas[6]) and then using a process such as Fischer–Tropsch process to convert the syngas mixture into liquid hydrocarbons. By contrast, direct liquefaction processes convert coal into liquids directly, without the intermediate step of gasification, by breaking down its organic structure with application of solvents or catalysts in a high pressure and temperature environment. Since liquid hydrocarbons generally have a higher hydrogen-carbon molar ratio than coals, either hydrogenation or carbon-rejection processes must be employed in both ICL and DCL technologies.

As coal liquefaction generally is a high-temperature/high-pressure process, it requires a significant energy consumption and, at industrial scales (thousands of barrels a day), multi-billion dollar capital investments. Thus, coal liquefaction is only economically viable at historically high oil prices, and therefore presents a high investment risk.

Economics

Sources of unconventional oil will be increasingly relied upon when conventional oil becomes more expensive due to depletion. Nonetheless, conventional oil sources are currently still preferred because they are less expensive than unconventional sources (Figure 6).

[5]Syngas to gasoline plus (STG+) is a thermochemical process to convert natural gas, other gaseous hydrocarbons or gasified biomass into drop-in fuels, such as gasoline, diesel fuel or jet fuel, and organic solvents.

[6]Syngas, or synthesis gas, is a fuel gas mixture consisting primarily of hydrogen, carbon monoxide, and very often some carbon dioxide.

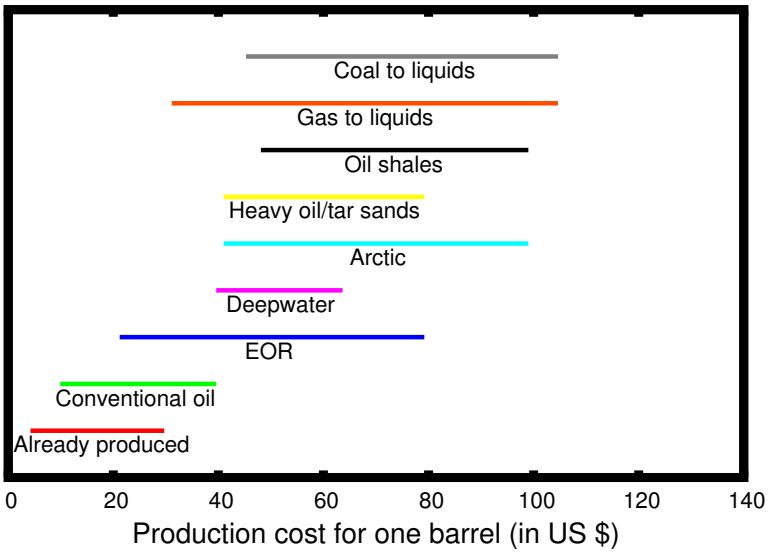

Figure 6: Costs of production by resource in 2008 (source: IEA).

Oil recovery

Extraction and recovery of crude oil from a reservoir is a two-to-three-step process. During primary recovery, some 5% to 15% of the original oil in place is produced by depletion of the overburden pressure through the oil wells drilled into the reservoir. Another 15% to 30% of oil can be produced by waterflooding, *i.e.* forced water injection, known as secondary recovery (one can note that many projects use waterflooding first, although it is still called secondary waterflooding)[18, 19]. A variety of additional techniques, generally referred to as Enhanced Oil Recovery (EOR) or tertiary recovery, can be employed to extract another 5% to 15%, yielding an overall recovery ratio of 30% to 60% depending on the properties of the oil initially in place (Figure 7) [19, 20, 21, 22, 23, 24]. Such techniques aim to recover the oil retained by capillary forces or immobilised due to high viscosity.

Enhanced Oil Recovery

Most EOR methods are presented extensively in reference [25].

Many EOR methods have been used in the past with varying degrees of success. Thermal methods are primarily intended for heavy oils and tar sands, although they

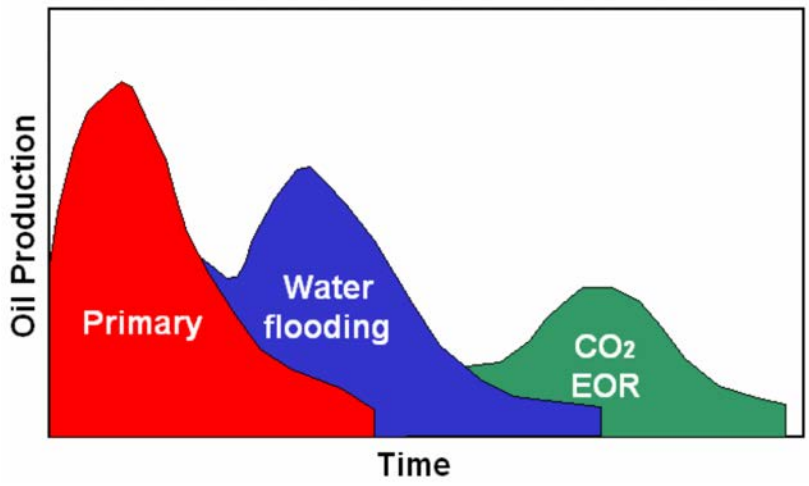

Figure 7: Expected sequence of oil recovery methods in a typical oil field in the case of immiscible CO_2 injection. [19]

are applicable to light oils in special cases. Non-thermal methods are normally used for light oils. Some of these methods have been tested for heavy oils. Above all, reservoir geology and fluid properties determine the suitability of a process for a given reservoir.

Thermal methods

Thermal methods have been tested since the 1950s and are for now the most advanced among EOR methods, as far as field experience and technology are concerned. They supply heat to the reservoir, and vaporize some of the oil. The major mechanisms include a large reduction in viscosity, and hence mobility ratio. The main thermal methods are Cyclic Steam Stimulation [26], Steamflooding [27, 28], Steam Assisted Gravity Drainage (Figure 8) [29, 30] and In Situ Combustion [31, 32].

Non-thermal methods

The two principal objectives in non-thermal methods are

- lowering the interfacial tension,
- improving the mobility ratio.

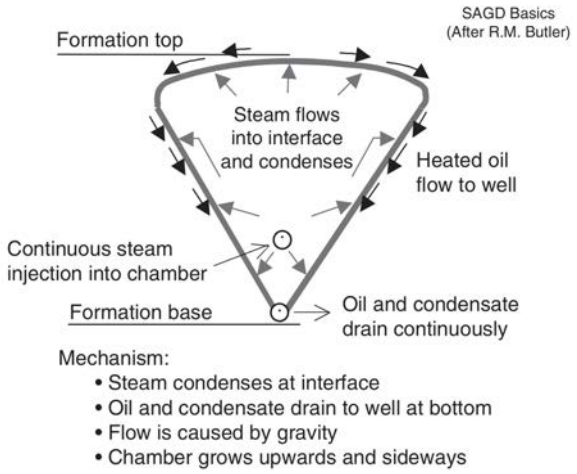

Figure 8: Steam Assisted Gravity Drainage. [25]

Most non-thermal methods require considerable laboratory studies for process selection and optimisation. The three main classes under non-thermal methods are: miscible, chemical and immiscible gas injection methods (Figure 9).

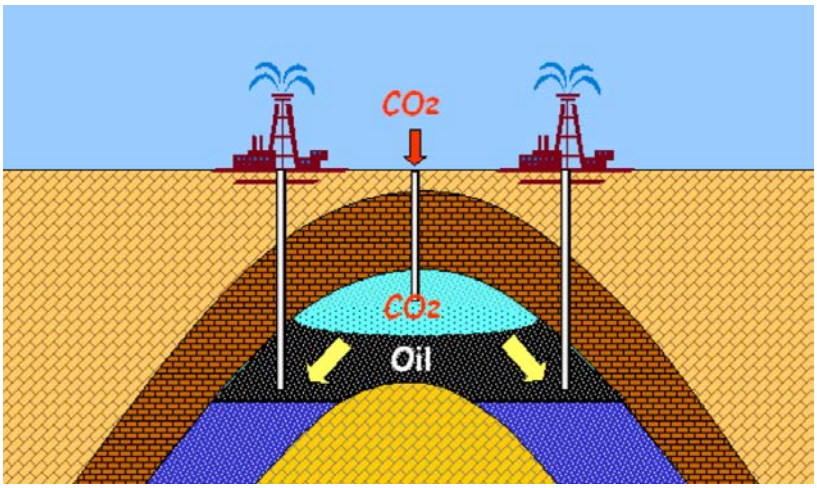

Figure 9: A schematic of the immiscible displacement technique in the case of immiscible CO_2 injection. [19]

Miscible flooding

Miscible flooding implies that the displacing fluid is miscible with the reservoir oil either at first contact or after multiple contacts. A narrow transition zone (mixing

zone) develops between the displacing fluid and the reservoir oil, inducing a piston-like displacement. The mixing zone and the solvent profile spread as the flood advances. Interfacial tension is reduced to zero in miscible flooding, therefore Ca $\rightarrow +\infty$. The various miscible flooding methods include miscible slug process, enriched gas drive, vaporizing gas drive and high pressure gas (CO_2 or N_2) injection [33, 34].

Chemical flooding

Chemical methods [35, 36] use a chemical formulation as the displacing fluid, which promotes either a decrease in mobility ratio or an increase in the capillary number, or both. Economics is the major deterrent in the commercialisation of chemical floods. It must also be noted that the technology does not exist currently for reservoirs of certain characteristics. The major chemical flood processes are polymer flooding [37, 38], surfactant flooding [39, 40], alkaline flooding [41, 42], micellar flooding [43, 44] and alkali-surfactant-polymer flooding [45, 46].

Wettability in the oil industry

Precise knowledge of reservoir wettability is essential in order to accurately determine several factors, such as residual oil saturation or relative permeability, which in turn are major factors for economic evaluations during both waterflooding and EOR [47, 48], especially when one considers that waterflooding has been a common practice in oil recovery for many years (see Figure 10) [49, 50].

In the case of a water-wet reservoir, the water advances through the porous medium in a fairly flat front during waterflooding [52]. Despite this seemingly uniform front on a macroscale, a considerable oil fraction remains inside the rock due to entrapment mechanisms on the microscale (Figure 11(a)) [53, 54]. For large aspect ratios[7] (wide pores connected through very small throats), water films in the throats frequently coalesce and cut off ganglia of oil from the continuous oil phase [55]. Due to capillary pressure, these ganglia are then trapped in the large pores [52, 56]. After the water

[7]Pore-to-throat effective diameter ratio

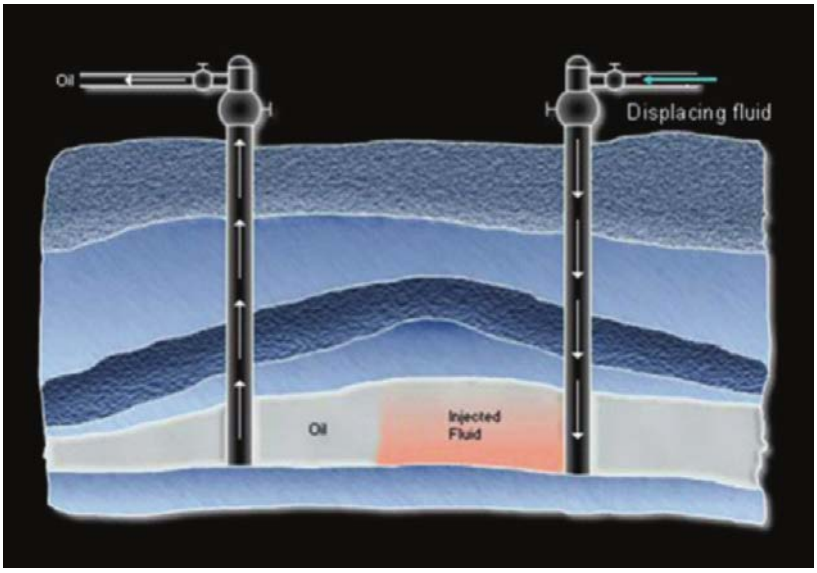

Figure 10: Secondary oil recovery by waterflooding: the displacing fluid (water) is injected into the reservoir through the injector well (right) and displaced oil is recovered at the production well (left). [51]

front passes, the remaining oil stays mostly immobile. Oil recovery rate thus decreases drastically shortly after water breakthrough (Figure 12).

In the case of an oil-wet reservoir, on the other hand, the rock preferentially remains in contact with the oil during the waterflooding process (Figure 11(b)). This process is therefore much less efficient [57].

Outline of the manuscript

Understanding multiphase flow in porous media is of great importance for many industrial and environmental applications at various spatial and temporal scales [58, 59, 60, 61, 62, 63, 64]. Indeed, this PhD work is part of an R&D project dedicated to the study of "Heavy Oils" at TOTAL SA. This project aims at understanding and modelling the invasion of heavy-oil-filled porous media (reservoirs) by brine and/or by polymer (EOR). At the scale of the reservoir, the ultimate goal is to increase the extracted oil ratio at reduced costs thanks to a better understanding of the overall physical laws governing the different flows inside the porous medium.

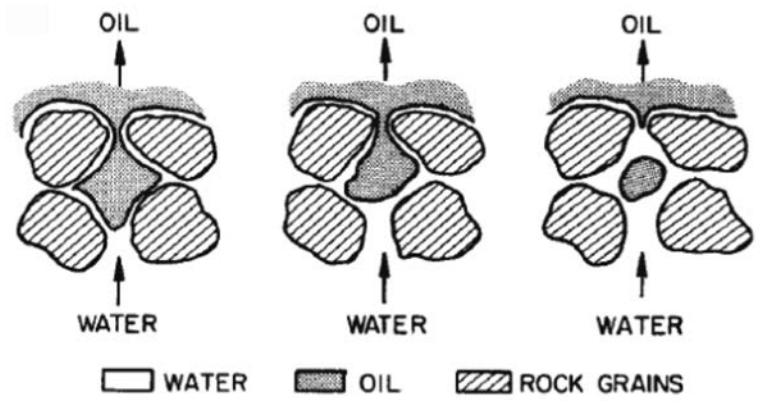

(a)

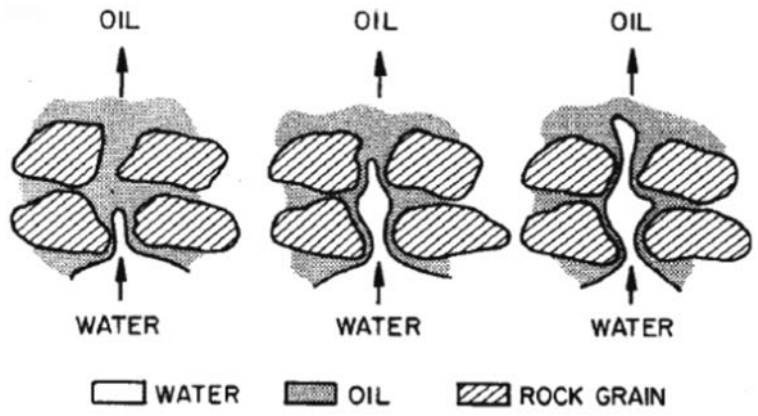

(b)

Figure 11: Water displacing oil from a pore in (a) a strongly water-wet rock, and (b) a strongly oil-wet rock. [53]

The present study focuses on modelling two-phase flows by Volume-of-Fluid method in porous media. Chapter 1 recalls some elements of both fluid and porous medium theories. After precisely defining what a fluid is (by opposition to a solid), the different equations governing a fluid flow are recalled. Wettability issues are also discussed. Porous media are then considered in order to define both porosity and tortuosity and to derive the macroscopic Darcy's law. This chapter finally considers the phenomenology of flows in porous media in the case of both drainage and imbibition, before presenting what occurs in deformable media.

Chapter 2 is dedicated to presenting Gerris Flow Solver, the open-source software that was used to study two-phase flows in porous media. As this software is based on

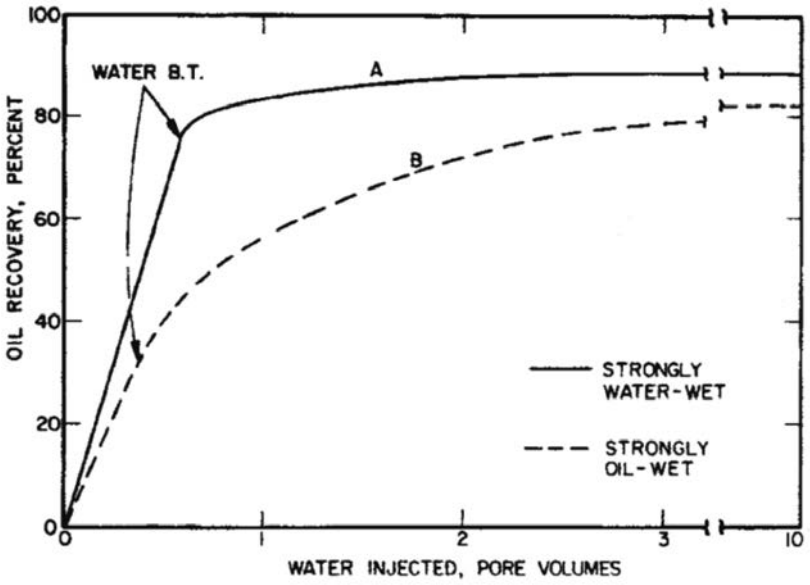

Figure 12: Typical waterflood performance in water-wet and oil-wet sandstone cores at moderate oil/water viscosity ratios. [53]

Volume-of-Fluid method, some aspects of this method are recalled, before realising some tests of pore-scale flow in porous medium, in order to validate the code for these uses. The results of 3D flow simulations in real rock are finally presented.

In Chapter 3, an extensive study of 2D viscous fingering in Hele-Shaw cells with central injection is presented. Some characteristics of both isotropic and non-isotropic viscous fingering in Hele-Shaw cells are first recalled, before presenting some results concerning fractal dimension of the resulting clusters. Special interest will be dedicated to exploring the relation between the perimeter of the resulting bubbles and their area.

Finally, Chapter 4 will focus on studying Saffman-Taylor instability in Hele-Shaw cells induced by lateral injection. This study aims at explaining some results that were obtained in experiments realised at Centre of Integrated Petroleum Research (CIPR, Bergen, Norway) and funded by TOTAL SA. These experiments of lateral injection of brine and/or polymer in quasi-2D square slab geometries of Bentheimer sandstone are reproduced numerically (to some extent).

CHAPTER 1

Elements of fluid and porous medium theory

Contents

1.1 Elements of fluid dynamics theory 33

1.1.1 Gas, liquid or solid 33

1.1.2 Continuum approach to fluid materials 34

1.1.3 Fluid properties 36

1.1.3.1 Fluid viscosity 36

1.1.3.2 Conservation laws 38

Conservation of mass 38

Conservation of momentum 39

1.1.3.3 Surface tension 40

Surface tension in the Navier-Stokes equation 41

1.1.3.4 Dimensionless parameters 42

Significance of the dimensionless parameters 43

1.1.4 Wettability 43

Hysteresis of the contact angle 45

1.2 Porous medium 46

1.2.1 Definition of a porous medium 46

1.2.2 Continuum approach to porous media 48

1.2.3 Porosity and effective porosity 49

1.2.4 Darcy's law 51

1.2.4.1 Single-phase flows 51

1.2.4.2 Multiphase flows 51

1.2.4.3 Hele-Shaw cell and two-phase flow in porous media 54

1.2.4.4 Other approaches to describe flow in porous media 55

1.2.5 Tortuosity 58

1.2.5.1 Geometrical tortuosity 59

1.2.5.2 Hydraulic tortuosity 60

Capillary models of pore structure for hydraulic transport 60

Kozeny's equation 61

Dupuit's relation 62

The Kozeny-Carman equation 63

1.2.5.3 How is hydraulic tortuosity related to geometrical tortuosity? 64

1.2.6 What about surface tension? 64

Case of Hele-Shaw cells 64

Proof of equation 1.48 65

Case of porous media 68

1.3 Phenomenology of flows in porous media 69

1.3.1 Displacement of the meniscus at the pore scale 70

1.3.2 Phase diagram in the case of drainage 73

1.3.3 Phase diagram in the imbibition case 78
1.3.4 Deformable media 82
1.3.4.1 Labyrinthine structures 82
1.3.4.2 Stick-slip bubbles 84
1.3.4.3 Fracturing of deformable media 85
1.3.4.4 Phase diagramm 90
1.4 Conclusion 91

1.1 Elements of fluid dynamics theory

1.1.1 Gas, liquid or solid

A fluid is a continuous medium that cannot be kept at rest under shear stress. In most cases, this property is enough to establish a clear distinction between fluids and solids. It should however be noted that some materials (*e.g.* polymers) react as solids under several stresses and as fluids for different stress intensity.

Another way to distinguish fluids from solids is to consider the so-called Deborah number [65]

$$\mathrm{De} = \frac{\tau_r}{\tau_o} \tag{1.1}$$

where τ_r is the time of relaxation of the material and τ_o the time of observation. The magnitude of this Deborah number then defines the difference between solids and fluids. For very large times of observation, or, conversely, if the time of relaxation of the material under observation is very small, one can see the material flowing, *i.e.* it acts as a fluid. On the other hand, if the time of relaxation of the material is larger than the time of observation, the material, for all practical purposes, is a solid. Heraclitus's famous terse catchphrase "$\tau\alpha\ \pi\alpha\nu\tau\alpha\ \rho\varepsilon\iota$" ("everything flows") [66] is thus valid either for infinite time of observation, or for infinitely small time of relaxation. One should also consider Prophetess Deborah's song after the victory over the Philistines: "The mountains flowed before the Lord" [67]. Indeed, in her statement, God can see that mountains flow; the same cannot however be stated

for any living man, for only the time of observation of the Lord is infinite. For any member of mankind and *a fortiori* in this study, the greater the Deborah number, the more solid the material; the lower the Deborah number, the more fluid it is.

A fluid can be either a liquid or a gas. From a mechanical point of view, a gas is mostly distinguished from a liquid by its higher compressibility: the variations of its specific mass due to a given variation of pressure are greater. However, in some classes of liquid or gaseous flows, the fluid can be considered as incompressible. Finally, liquids and gases obey the same laws of fluid mechanics.

1.1.2 Continuum approach to fluid materials

The concept of the fluid requires some further elaboration. Actually, fluids are composed of a large number of molecules (overlooking the existing submolecular structure [68]) that move about, colliding with each other and with the solid walls of the container in which they are placed. With the help of various theories of classical mechanics, it would be possible to obtain a complete description of a given system of molecules. However, despite the apparent simplicity of this approach, it is exceedingly difficult to solve even the three-body problem[1]. With the help of powerful computers, the many-body problem can be confronted, in the principle, numerically. It is still impossible, however, to determine the motion of 10^{23} molecules in one mole of gas or liquid. In addition, due to the (very) large number of molecules, their initial positions and momenta cannot actually be determined, for example, by observation.

This embarassingly large number of equations ultimately provides a way out, at least under certain conditions. Instead of treating the problems, say of fluid motion, at the molecular level, a statistical approach is adopted to derive information regarding the motion of a system composed of many molecules. In such an approach the results of an analysis or an experiment are obtained only in statistical form. Indeed it is possible to determine the average value of successive measurements, but one cannot predict with certainty the outcome of a single measurement in the future [69]. In this context, an "experiment" means, for example, the position of a certain molecule at a

[1] assuming that we know all the forces, which is quite doubtful

certain time, or its moment, etc. Statistical mechanics is an analytical science that allows to infer statistical properties of the motion of a very large number of molecules (or of particles in general) from laws governing the motion of individual molecules [70].

When abandoning the molecular level of treatment aims at describing phenomena as a fluid continuum, the statistical approach is usually referred to as the macroscopic approach.

In order to be able to treat fluids as continua, one has to define the essential concept of a fluid particle. It is a set of many molecules contained in a small volume. Its size has to be much larger than the mean free path of a single molecule. It should however be sufficiently small as compared to the overall fluid domain so that by averaging fluid and flow properties over the molecules included in it, meaningful values will be obtained. These values are then related to some centroid of the particle. Then, at every point in the domain occupied by a fluid, we have a particle with definite dynamic and kinematic properties.

Let us consider the flow of a fluid around an obstacle of characteristic size L. We focus on an elementary volume $\delta\Omega(x,\varepsilon)$ of size ε, centered on an arbitrary point M at position x and containing a set of molecules. Provided $\delta m(x,t,\varepsilon)$ is the mass of the fluid in $\delta\Omega(x,\varepsilon)$, the fluid's average density (or specific mass) at M is

$$\rho_m(x,t,\varepsilon) = \frac{\delta m(x,t,\varepsilon)}{\delta\Omega(x,\varepsilon)} \tag{1.2}$$

If one supposes the presence of a spatial resolution (ε) sensor at point M to determine the fluid density at this point, the measured value is the average density $\rho_m(x,t,\varepsilon)$ and varies with the resolution ε (see Figure 1.1). When ε is of order L, the measured value is not constant: it obviously depends on the variations of density on the macroscopic lengthscale L.

On the contrary, for ε of order l (microscopic lengthscale defined by the mean free path of the molecules), $\delta\Omega(x,\varepsilon)$ only contains a few molecules: the measuring device registers random fluctuations and one cannot define any average value. The fluid can be considered as a continuous material if one finds an amplitude of spatial resolution

$$l \ll \varepsilon \ll L \tag{1.3}$$

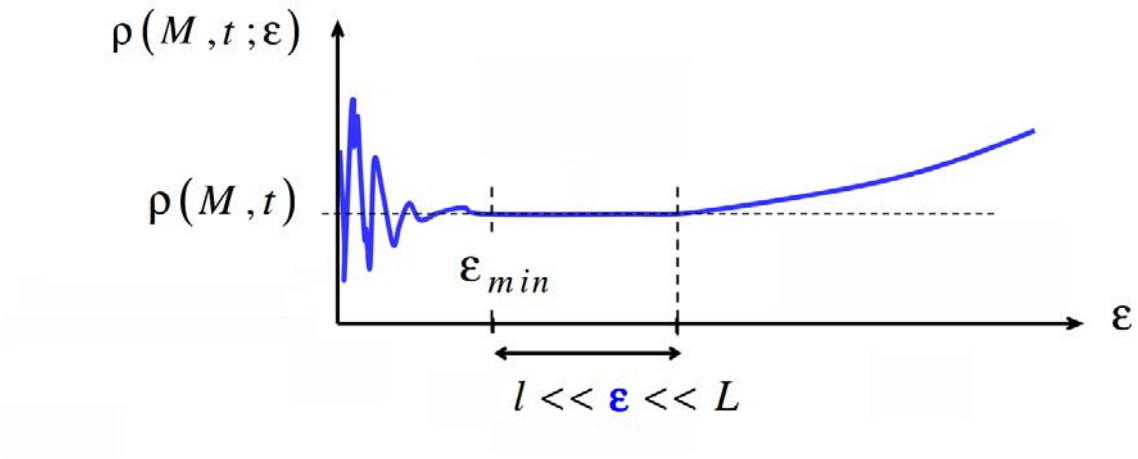

Figure 1.1: Measured value as a function of resolution. [71]

where $\rho_m(x,t,\varepsilon)$ is a constant with no dependence on ε. Such value defines the specific mass $\rho(x,t)$ at point M [72].

The continuum approach to fluid dynamics is justified only when l and L are of distinct lengthscale. This scale separation is characterised by the (dimensionless) Knüdsen number

$$\boxed{\mathrm{Kn} = \frac{l}{L}} \tag{1.4}$$

A fluid behaves as a continuous material if $\mathrm{Kn} \ll 1$.

As in some cases one may require a still higher, or coarser, level of treatment, reached by averaging phenomena in the fluid continuum filling the void space, the fluid continuum level will be referred to as the microscopic approach from now on.

1.1.3 Fluid properties

1.1.3.1 Fluid viscosity

Unlike solids, fluids continue to deform as long as a shear stress is applied [73]. This continuous deformation constitutes the flow and the property by virtue of which a fluid resists any such deformation is known as the viscosity. Viscosity is thus a measure of the reluctance of the fluid to yield to shear whenever the fluid is in motion.

Let τ_{yx} denote the shear stress exerted in the direction $+x$ on a fluid surface whose outer normal is in the direction $+y$ (*i.e.* when the material of greater y exerts a shear

in the $+x$ direction on the material at lesser y). Then for a point M

$$\tau_{yx} = \mu \frac{\partial \mathbf{u}}{\partial y} \tag{1.5}$$

where $\mathbf{u}$ is the velocity. The constant of proportionality μ is called the dynamic viscosity of the fluid. The kinematic viscosity is also defined as $\nu = \mu/\rho$ with ρ the fluid density.

Equation (1.5) states that the shear force per unit area is proportional to the local velocity gradient. When τ_{yx} is defined as the shear stress exerted in the $+x$ direction on a fluid surface of constant y by the fluid in the region of lesser y, equation (1.5) becomes

$$\tau_{yx} = -\mu \frac{\partial \mathbf{u}}{\partial y} \tag{1.6}$$

Fluids whose behaviours obey equation (1.6) are called Newtonian fluids (*e.g.* all gases and most simple liquids).

Among the non-Newtonian fluids one may mention:

- Bingham plastic fluids, which exhibit a yield stress at zero shear rate, followed by a straight-line relationship between shear stress and shear rate. A certain shear stress has thus to be exceeded for flow to begin;
- pseudoplastic fluids are characterised by a progressively decreasing slope of shear stress versus shear rate (*i.e.* μ decreases with increasing rate of shear);
- in dilatants fluid the apparent viscosity increases with increasing shear rate.

These three examples (Figure 1.2) address only time-independent non-Newtonian fluids. Some fluids are more complex in that their apparent viscosity depends not only on the shear rate but also on the time the shear rate has been applied. There are two general classes of such fluids (Figure 1.3):

- thixotropic fluids, whose apparent viscosity depends both on time of shearing and on the shear rate; as the fluid is sheared from a state of rest, it breaks down on a molecular scale, but then the structural reformation will increase with time. If allowed to rest, the fluid builds up slowly, and eventually regains its original consistency.

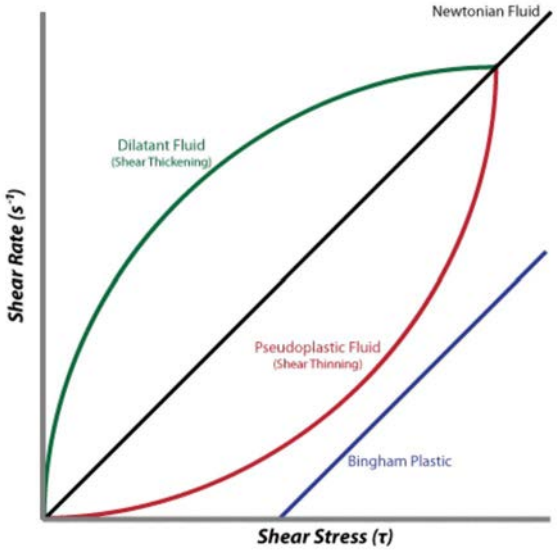

Figure 1.2: Behaviour of time-independent non-Newtonian fluids. [74]

- in rheopectic fluids the molecular structure is formed by shear and the behaviour is opposite to that of thixotropy.

From now on, we will only consider Newtonian fluids.

1.1.3.2 Conservation laws

Conservation of mass The differential form of the principle of conservation of mass is written for a fluid as

$$\frac{\partial \rho}{\partial t} + \nabla \cdot (\rho \mathbf{u}) = 0 \tag{1.7}$$

which is called the continuity equation. Rewriting the divergence term in equation (1.7) as

$$\frac{\partial}{\partial x_i}(\rho u_i) = \rho \frac{\partial u_i}{\partial x_i} + u_i \frac{\partial \rho}{\partial x_i},$$

the equation of continuity becomes

$$\frac{1}{\rho}\frac{\mathrm{D}\rho}{\mathrm{D}t} + \nabla \cdot \mathbf{u} = 0. \tag{1.8}$$

The derivative $D\rho/Dt$ is the rate of change of density following a fluid particle. A fluid is usually called incompressible when its density is independent of pressure. Liquids are almost incompressible. Although gases are compressible, for speeds inferior to

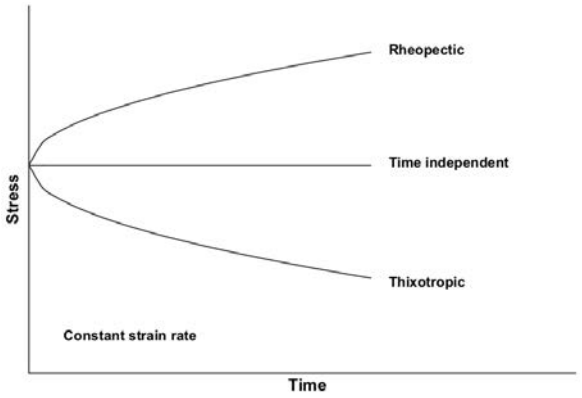

Figure 1.3: The two classes of time-dependent fluids compared to the time-independent presented in a generic graph of stress against time. [75]

100 m.s^{-1} the fractional change of absolute pressure in the flow is small [73]. In this and several other cases the density changes in the flow are also small. The neglect of $\rho^{-1}D\rho/Dt$ in the continuity equation is part of the simplifications resulting in the Boussinesq approximation [76, 77]. In such a case the continuity equation (1.8) reduces to the incompressible form

$$\boxed{\nabla \cdot \mathbf{u} = 0,} \tag{1.9}$$

whether or not the flow is steady.

Conservation of momentum Considering the motion of an infinitesimal fluid element, Newton's law gives Cauchy's equation of motion

$$\rho \frac{\mathrm{D}u_i}{\mathrm{D}t} = \rho g_i + \frac{\partial \tau_{ij}}{\partial x_j}, \tag{1.10}$$

where $\mathbf{g}$ is the body force per unit mass and $\boldsymbol{\tau} = (\tau_{ij})$ the symmetric stress tensor $(\tau_{ij} = \tau_{ji})$.

The constitutive equation for a Newtonian fluid is [73]

$$\tau_{ij} = -\left(p + \frac{2}{3}\mu \nabla \cdot \mathbf{u}\right)\delta_{ij} + 2\mu e_{ij} \tag{1.11}$$

where $\boldsymbol{\delta} = (\delta_{ij})$ is the Kronecker delta, p is the thermodynamic pressure and $\mathbf{e} = (e_{ij})$ is the strain rate tensor

$$e_{ij} \equiv \frac{1}{2}\left(\frac{\partial u_i}{\partial x_j} + \frac{\partial u_j}{\partial x_i}\right).$$

The equation of motion for a Newtonian fluid is obtained by sustituting the constitutive equation (1.11) into Cauchy's equation (1.10). It leads to a general form of the Navier-Stokes equation

$$\rho\frac{\mathrm{D}u_i}{\mathrm{D}t} = -\frac{\partial p}{\partial x_i} + \rho g_i + \frac{\partial}{\partial x_j}\left[2\mu e_{ij} - \frac{2}{3}\mu(\nabla\cdot\mathbf{u})\delta_{ij}\right]. \tag{1.12}$$

For incompressible fluids with constant viscosity, the Navier-Stokes equation reduces to

$$\boxed{\rho\frac{\mathrm{D}\mathbf{u}}{\mathrm{D}t} = -\nabla p + \rho\mathbf{g} + \mu\nabla^2\mathbf{u}.} \tag{1.13}$$

If viscous effects are negligible, which is generally found to be true far from boundaries of the flow field, one obtains the Euler equation

$$\rho\frac{\mathrm{D}\mathbf{u}}{\mathrm{D}t} = -\nabla p + \rho\mathbf{g}. \tag{1.14}$$

In the case of incompressible and viscosity-dominated flows in a permanent regime, the fluid obeys the so-called Stokes equation:

$$\mu\nabla^2\mathbf{u} = \nabla p - \rho\mathbf{g} \tag{1.15}$$

1.1.3.3 Surface tension

Whenever two immiscible fluids are in contact, the interface behaves as if it were under tension. The presence of such a tension at an interface results from the intermolecular attractive forces [78, 79]. Let us imagine a liquid drop surrounded by a gas. Near the interface, all the liquid molecules are trying to pull the molecules on the interface inwards (see Figure 1.4). The net effect of these attractive forces is for the interface to contract. The magnitude of the tensile force per unit length of a line on the interface is called surface tension σ. The value of σ depends on the pair of fluids in contact, the temperature and the pressure [80].

As a result of surface tension one can observe the existence of a pressure jump across the interface whenever it is curved. If p_i (concave side) and p_o are the pressures on the two sides of the interface, the pressure jump across the interface is given by

$$p_i - p_o = \sigma\left(\frac{1}{R_1} + \frac{1}{R_2}\right) = \frac{2\sigma}{R} = \sigma\kappa, \tag{1.16}$$

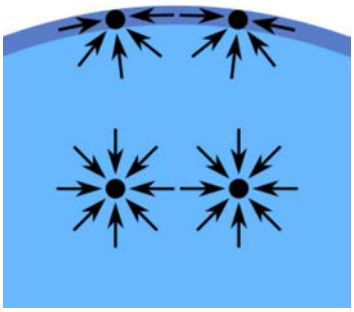

Figure 1.4: Diagram of the forces on molecules of a fluid. [81]

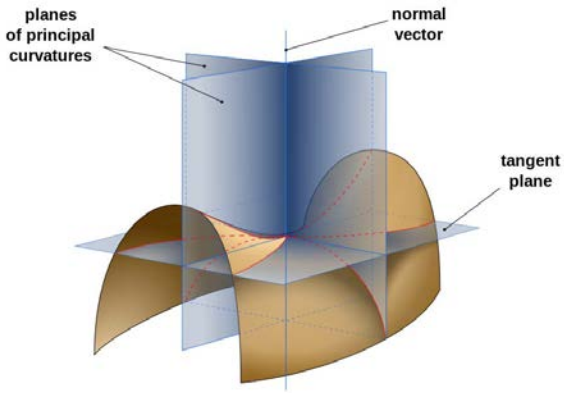

Figure 1.5: Saddle surface with normal planes in directions of principal curvatures. [82]

where R_1 and R_2 are the radii of curvature of the interface along two orthogonal directions (see Figure 1.5), R is the mean radius of curvature of the interface and κ is the mean curvature of the interface.

Surface tension in the Navier-Stokes equation Let us consider a two-phase flow (concerning fluids 1 and 2) with an interface S of surface tension σ. In order to be able to compute the effect of surface tension in the Navier-Stokes equation (1.12), one can consider a marker function $c(\mathbf{x}, t)$ such as

$$c(\mathbf{x}, t) = \begin{cases} 0 \text{ in fluid 1} \\ 1 \text{ in fluid 2} \end{cases} \tag{1.17}$$

The surface tension is given by [83]

$$\mathbf{f}_\sigma = \sigma\kappa\delta_S\mathbf{n} \tag{1.18}$$

where κ is the curvature and $\delta_S(\mathbf{x},t) = |\nabla c(\mathbf{x},t)|$ at the interface S in the distribution sense. By considering that $\mathbf{n}$ points towards the fluid with an excess of pressure (concave side of the interface, supposed to be fluid 2), one can write $\mathbf{n} = \nabla c/|\nabla c|$ and $\kappa = -\nabla\cdot\mathbf{n} = 2/R(\mathbf{x},t)$ with R the mean radius of curvature of the interface.

The Navier-Stokes equation with surface tension is thus written for incompressible fluids as

$$\rho\frac{\mathrm{D}\mathbf{u}}{\mathrm{D}t} = -\nabla p + \rho\mathbf{g} + \mu\nabla^2\mathbf{u} + \frac{2\sigma}{R(\mathbf{x},t)}\nabla c. \tag{1.19}$$

This method can easily be extended to more-than-two-phase flows by using as many marker functions as the number of different kind of interfaces.

1.1.3.4 Dimensionless parameters

The Navier-Stokes equation (1.19) can easily be nondimensionalized by defining a characteristic length scale l and a characteristic velocity scale U. Accordingly, we introduce the following dimensionless variables, denoted by primes[2]

$$\begin{aligned} x_i' &= \tfrac{x_i}{l} & \qquad t' &= \tfrac{tU}{l} \\ u_i' &= \tfrac{u_i}{U} & \qquad p' &= \tfrac{pl}{\mu U} \end{aligned} \tag{1.20}$$

A two-phase flow where there is no volume force ($\mathbf{g} = 0$) is considered. A dimensionless radius of curvature is defined as $R' = R/l$. Substituting the dimensionless variables defined in equation (1.20) into equation (1.19) gives

$$\frac{\rho lU}{\mu}\frac{\mathrm{D}\mathbf{u}'}{\mathrm{D}t'} = -\nabla p' + \frac{\sigma}{\mu U}\frac{2\nabla c}{R'} + \nabla^2\mathbf{u}'. \tag{1.21}$$

It is apparent that two flows having different values of U, l, μ or σ will obey the same nondimensional differential equation if the values of both dimensionless groups $\rho lU/\mu$ and $\sigma/\mu U$ are identical in te two different flows.

These dimensionless parameters are known as:

[2]Here the pressure is nondimensionalized by the viscous stress $\mu U/l$, but depending on the nature of the flow, this could also be realised with a dynamic pressure ρU^2 or a hydrostatic pressure ρgl.

- the Reynolds number $\mathrm{Re} \equiv \frac{\rho l U}{\mu}$,
- the capillary number $\mathrm{Ca} \equiv \frac{\mu U}{\sigma}$.

The dimensionless Navier-Stokes equation (1.21) can thus be written as

$$(\mathrm{Re})\frac{\mathrm{D}\mathbf{u}'}{\mathrm{D}t'} = -\nabla p' + (\mathrm{Ca})^{-1}\frac{2\nabla c}{R'} + \nabla^2 \mathbf{u}'.$$

Significance of the dimensionless parameters

- The Reynolds number is the ratio of inertia force to viscous force

$$\mathrm{Re} \equiv \frac{\text{Inertia force}}{\text{Viscous force}} \propto \frac{\rho u \partial u/\partial x}{\mu \partial^2 u/\partial x^2} \propto \frac{\rho U^2/l}{\mu U/l^2} = \frac{\rho U l}{\mu}.$$

  Equality of Re is a requirement for the dynamic similarity of flows in which viscous forces are important.

- The capillary number is the ratio of viscous force to surface tension

$$\mathrm{Ca} = \frac{\text{Viscous force}}{\text{Surface tension}} \propto \frac{\mu \partial^2 u/\partial x^2}{\sigma \nabla c/R} \propto \frac{\mu U/l^2}{\sigma/l^2} = \frac{\mu U}{\sigma}$$

  Equality of Ca is a requirement for the dynamic similarity of flows in which surface tension is important.

1.1.4 Wettability

Wettability describes the ability of a fluid to remain in contact with a solid surface with respect to a second immiscible fluid [51]. Wettability is a result of the competition between adhesive forces between a liquid and a solid, which cause a liquid to spread across the solid surface, and cohesive forces within the liquid, which tend to minimise its surface area and maintain it in a compact form (*e.g.* a sphere) [84, 85]. Wettability is quantified by the contact angle θ, which represents the angle at which the fluid/fluid interface meets the solid surface. For a drop of liquid deposited on a surface (Figure 1.6), the contact angle obeys the Young equation [86]

$$\sigma_{SG} - \sigma_{SL} - \sigma_{LG}\cos\theta = 0 \tag{1.22}$$

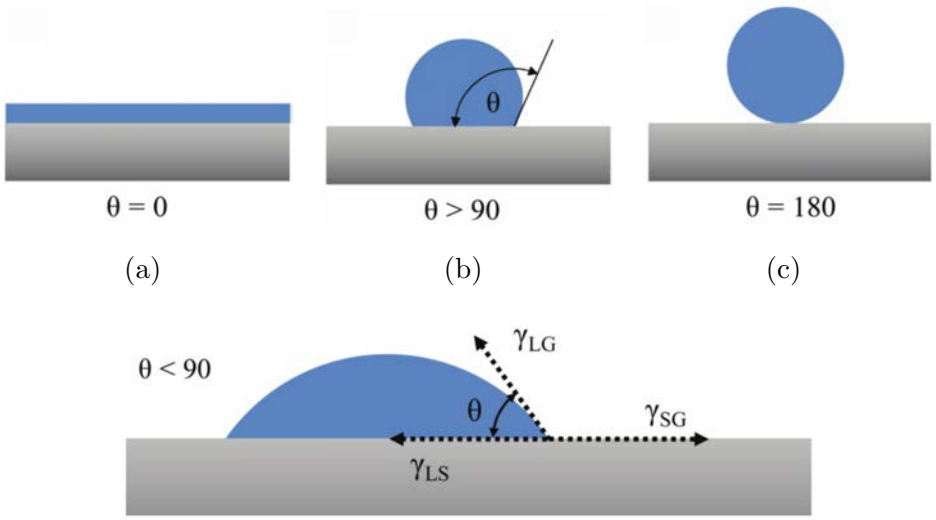

Figure 1.6: Idealised examples of contact angle and spreading of a liquid (blue) on a flat, smooth solid (grey). Different wetting states are shown: (a) complete wetting or spreading, (b) low wettability, (c) complete non-wetting (repulsion) and (d) high wettability. The contact angle θ is precised in degrees (°). [51]

where σ_{SG}, σ_{SL} and σ_{LG} are the interfacial tensions between solid/gas, solid/liquid and liquid/gas respectively. Equation (1.22) describes the force balance of tangential forces [87] which requires to be satisfied in order to obtain static conditions at the triple line (between gas, liquid and solid, see Figure 1.6(d)). For very strong liquid-solid affinity, complete wetting or spreading occurs, which represents the limit of the contact angle $\theta = 0$ (Figure 1.6(a)). For contact angles smaller than 90°, the liquid has a high wettability (Figure 1.6(d)), while for contact angles larger than 90° the liquid has a low wettability (Figure 1.6(b)). For very weak solid/liquid affinity, complete non-wetting or repulsion occurs, which is represented by a contact angle of 180° (Figure 1.6(c)).

Capillary pressure p_c, or Laplace pressure, describes a surface-tension-induced pressure difference across a fluid/fluid interface [88]

$$\Delta p = p_c = p_{nw} - p_w$$

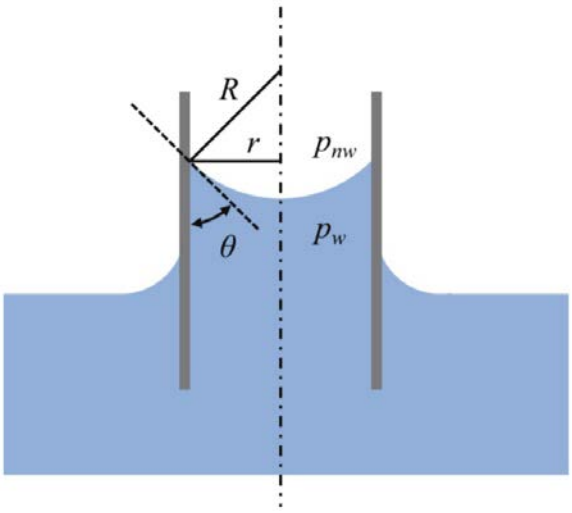

Figure 1.7: Capillary rise in a cylindrical tube of radius r. The tube (grey) shown in cross-section is dipped in water (blue). Water is wetting the tube material and a spherical meniscus of radius R is formed. [51]

where p_{nw} and p_w are the pressures in the non-wetting and wetting phase[3], respectively (Figure 1.7).

For a spherial meniscus in a cylindrical tube as shown in Figure (1.7) the capillary pressure is given as

$$p_c = \frac{2\sigma \cos\theta}{r}$$

with r the radius of the cylindrical tube.

Hysteresis of the contact angle An outside sollicitation (*e.g.* gravity) on a drop will tend to move the contact line. In an ideal case, this movement occurs at constant contact angle. Sometimes, however, such a sollicitation happens and no visible movement of the contact line appears at the macroscopic scale: the contact line is then anchored (see Figure 1.8).

For inhomogeneous solid surfaces, the anchoring effect can occur everywhere. The contact angle can thus vary everywhere on the surface. Its highest possible value is

[3]In the case of porous media, the Brooks-Corey correlation for capillary pressure states that $p_c = cS_w^{-a}$ where c is the entry capillary pressure, $1/a$ is called the pore-size distribution index and S_w is the normalized water saturation [89].

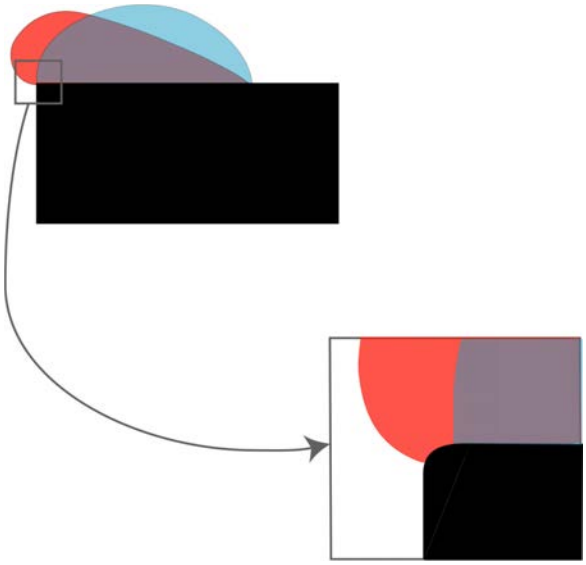

Figure 1.8: Anchoring of a drop on a strong edge. The zoom on the contact point shows the contact angle does not change. Indeed, the drop shape adapts its curvature to take the edge into account. [90]

called the advancing contact angle θ_a and the lowest one is referred to as the receding contact angle θ_r.

The contact line begins to move on whenever the contact angle exceeds θ_a. Similarly, it begins to recede only when becoming inferior to θ_r [88].

One should note that both the advancing contact angle θ_a and the receding one θ_r can depend on the position of the contact line on the solid surface (due to asperities).

It can also be noted that for liquid moving quickly over a surface, the contact angle can be altered from its value at rest. The advancing contact angle will increase with speed and the receding contact angle will decrease [91].

1.2 Porous medium

1.2.1 Definition of a porous medium

A porous medium (see Figure 1.9) is defined by three different properties [92, 93].

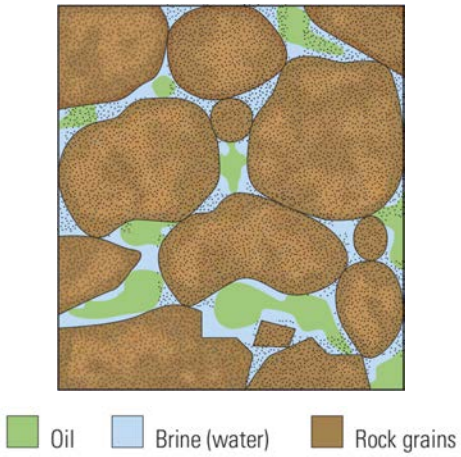

Figure 1.9: Structure of a porous material: the matrix (rock grains) determines cavities also known as pores (brine and oil) more or less connected one with the other by canals. [94]

1. It is a portion of space occupied by heterogeneous or multiphase matter comprising at least both one solid and one fluid phase. The fluid phase(s) may be gaseous and/or liquid. The solid phase is referred to as the solid matrix. The space within the porous medium domain that is not part of the solid matrix is called the void space (or pore space).

2. The solid phase should be distributed throughout the porous medium within the domain occupied by the porous medium. An essential characteristic of a porous medium is that the specific surface[4] of the solid matrix is relatively high. Another basic feature of a porous medium is that the various openings comprising the void phaseare relatively narrow.

3. At least some of the pores comprising the void space should be interconnected. The interconnected pore space is sometimes termed the effective pore space. As far as flow through porous media is concerned, unconnected pores may be considered as part of the solid matrix. Several portions of the interconnected pore space may, in fact, also be ineffective as far as flow through the medium

[4]The specific surface (s) of a porous material is defined as the total insterstitial area or the pores (A_s) per unit bulk volume (U_b) of the porous medium: $s = A_s/U_b$.

is concerned. For example, pores may be dead-end pores (or blind pores), *i.e.* pores or channels with only a narrow single connection to the interconnected pore space, so that almost no flow can occur through them. Another way to define this porous medium characteristic is by requiring that any two points within the effective pore space may be connected by a curve that lies completely within it. Furthermore, except for special cases, any two such points may be connected by many curves with an arbitrary maximal distance between any two of them. For a finite porous medium domain, this maximal distance is obviously dictated by the domain's dimension.

1.2.2 Continuum approach to porous media

In section 1.1.2 it was precised that the concept of a continuum requires to define a (fluid) particle, or physical point, or representative volume over which an average is performed. This is also true when going from the microscopic to the macroscopic level. One should therefore try and determine the size of the representative porous medium volume around a point M within it. From the discussion in the referred section one can state that this volume should be much smaller than the size of the entire flow domain. On the other hand, it has to be larger than the size of a single pore in order to include a sufficient number of pores to permit the meaningful statistical average required in the continuum concept.

When the medium is inhomogeneous, the upper limit of the length dimension of the representative volume should be a characteristic length that indicates the rate at which changes occur. The lower limit is related to the size of pores or grains.

It is now possible to define the volumetric porosity and the representative elementary volume (REV) associated with it. Porosity is, in a sense, the equivalent of density discussed in section 1.1.2. This might be more easily visualised if we defined the REV through the concept of the solid's bulk density (unit weight of solids).

Let M be a mathematical point inside the domain occupied by the porous medium. Consider the volume $\delta\Omega(x, \epsilon)$ of characteristic length scale ϵ much larger than a single pore or grain, for which M is the centroid. For this volume one can determine the

ratio

$$\phi_{\mathbf{x},\epsilon} \equiv \phi_{\mathbf{x},\epsilon}(\delta\Omega(x,\epsilon)) = \frac{\delta\Omega_v(x,\epsilon)}{\delta\Omega(x,\epsilon)} \tag{1.23}$$

where $\delta\Omega_v(x,\epsilon)$ is the volume of the void space within $\delta\Omega(x,\epsilon)$.

For large values of ϵ, the ratio $\phi_{\mathbf{x},\epsilon}$ may undergo gradual changes as ϵ is reduced, especially for inhomogeneous porous media. Below a certain value of ϵ depending on the distance of M from boundaries of inhomogeneity, these changes or fluctuations tend to decay, leaving only negligible amplitude fluctuations that are due to the random distribution of pore sizes in the neighbourhood of M. However, below a certain value ε one suddenly observes large fluctuations in the ratio $\phi_{\mathbf{x},\epsilon}$. This happens as ϵ approaches the size of a single pore. Finally, as $\epsilon \to 0$, converging on the mathematical point M, $\phi_{\mathbf{x},\epsilon}$ will become either one or zero, depending on whether M is inside a pore or inside the solid matrix of the medium (see Figure 1.1 for an equivalent curve for density).

The medium's volumetric porosity $\phi(\mathbf{x})$ at point M is defined as the limit of the ratio $\phi_{\mathbf{x},\epsilon}$ as $\epsilon \to \varepsilon^+$

$$\phi(\mathbf{x}) = \lim_{\epsilon\to\varepsilon^+} \phi_{\mathbf{x},\epsilon}(\delta\Omega(x,\epsilon)) = \lim_{\epsilon\to\varepsilon^+} \frac{\delta\Omega_v(x,\epsilon)}{\delta\Omega(x,\epsilon)} \tag{1.24}$$

The volume $\delta\Omega(x,\varepsilon)$ is then the representative elementary volume (REV) or the physical point of the porous medium at the mathematical point M.

By introducing both the concept of porosity and the definition of REV, the actual medium has been replaced by a fictitious continuum in which it is possible to assign values of any property (whether of the overall medium or of the fluids filling the pore space) to any mathematical point in it.

1.2.3 Porosity and effective porosity

Similar to section 1.2.2, the porosity of a macroscopic porous medium sample is defined as the ratio of volume of the void space (V_{pores}) to the bulk volume (V_{bulk})

$$\phi \equiv \frac{V_{\text{pores}}}{V_{\text{bulk}}} = \frac{V_{\text{pores}}}{V_{\text{pores}} + V_{\text{matrix}}} \tag{1.25}$$

where V_{matrix} is the volume of the solid matrix within V_{bulk}. Usually, the porosity is expressed in percentage.

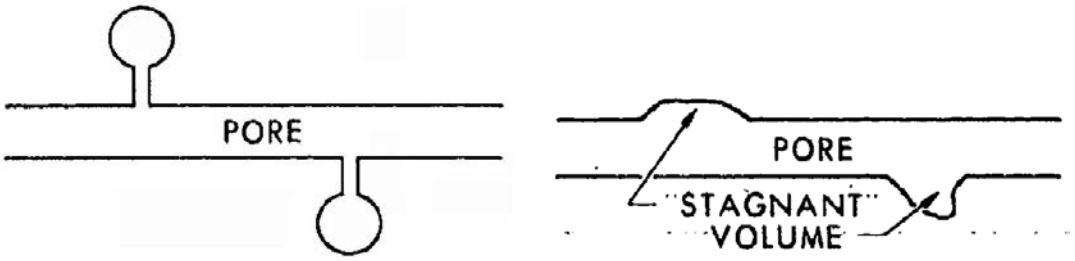

(a) Dead-end pores (b) Practically stagnant pockets

Figure 1.10: Idealised types of dead-end pore volume. [95]

When V_{bulk} in equation (1.25) is the total void space, regardless of whether pores are interconnected or not, the porosity is referred to as absolute or total porosity. However only interconnected pores are of interest from the standpoint of flow through the porous medium. Hence the concept of effective porosity ϕ_e (defined as the ratio of the interconnected pore volume $V_{\text{pores},e}$ to the total volume of the medium) is introduced

$$\phi_e \equiv V_{\text{pores},e}/V_{\text{bulk}}. \tag{1.26}$$

Another type of pores, which seem to belong to the class of interconnected pores but contribute very little to the flow, are the dead-end pores (Figure 1.10(a)) or stagnant pockets (Figure 1.10(b)) [95]. Owing to their geometry, the fluid in such pores is practically stagnant.

Various investigators report that in fine-textured porous media (*e.g.* clays) there are indications of an immobile or highly viscous water layer (resulting from electrostatic forces [96]) on the particle surfaces that makes the effective porosity (with respect to the flow through the porous medium) much smaller than the measured one. On the basis of experimental evidence, they also conclude that the viscosity of the water increases as the particle surface approaches [97]. This phenomenon may lead to yet another definition of effective porosity.

1.2.4 Darcy's law

1.2.4.1 Single-phase flows

During a seminal experiment concerning flow in porous media, Henry Darcy highlighted in 1856 the linear law existing between the flow rate Q of a fluid in a porous material and the pressure gradient imposed between the entrance and exit faces of this material [98]

$$Q = \frac{kA}{\mu}\frac{\Delta p}{L} \tag{1.27}$$

where A and L are the specific area and the length of the porous medium respectively and μ the viscosity of the fluid. k is the permeability of the porous material. This parameter describes the capacity for a porous material to let a fluid pass, without modifying its internal structure. This intrinsic property of the material does not depend on the nature of the flowing fluid but only on the geometry of the porous medium. k is usually called the absolute permeability of the material. There is no obvious link between porosity and permeability: most models highlight the importance of the pore size [99, 100].

This macroscopic law (equation 1.27), valid for low-Reynolds-number flows, is commonly referred to as Darcy's law and concerns homogeneous and isotropic porous media, saturated in fluid.

When the medium deformation can be neglected and the flow in the pores obeys Stokes equation (1.15), Darcy's law can be written for single-phase flow of an incompressible Newtonian fluid with viscosity μ

$$\mathbf{u} = -\frac{k}{\mu}\nabla p \tag{1.28}$$

where $\mathbf{u}$ is the Darcy velocity of the flow in the porous medium[5]. A mathematical derivation from the Navier-Stokes equation can be found in [101, 102].

1.2.4.2 Multiphase flows

In this section only two-phase flows are considered. The different equations may however easily be extended to more-than-two-phase flows.

[5] $\mathbf{u} = \phi\overline{\mathbf{v}}$ with $\overline{\mathbf{v}}$ the average velocity of the flow.

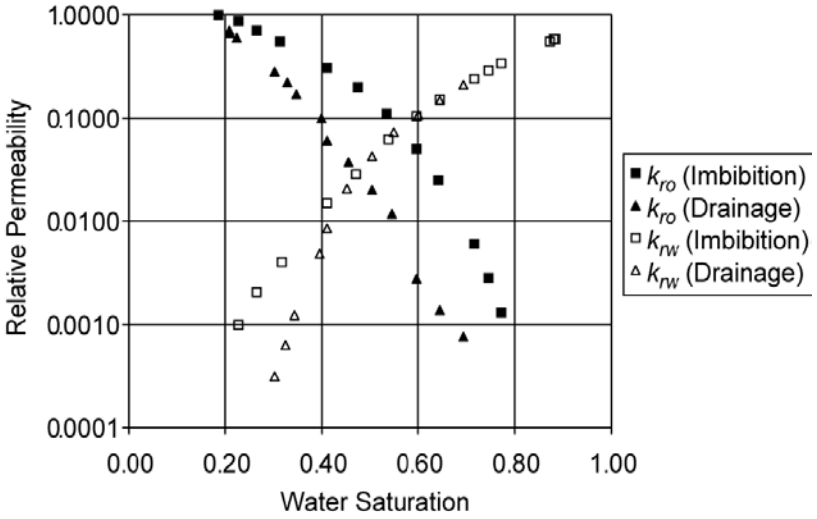

Figure 1.11: Relative permeability hysteresis for a mixed-wet sample from the Kingfish field. [104]

When considering a two-phase flow in a porous medium where a fluid (called fluid 1) is displaced by another non-miscible injected fluid (fluid 2), one has to take into account the behaviour of the interface at the pore scale. Then, the viscous forces in both injected and displaced fluids must be considered, in addition to the capillary forces at the interface between the two fluids.

Thus, it requires to take into account the important local fluctuations of pressure generated by the interactions occuring at the interface between the fluids. Moreover, the injected-fluid capacity to flow through the porous medium is affected by the previous presence of the displaced fluid. One can then write a Darcy equation for each phase by introducing relative permeabilities $k_{r,i}$ and different pressure fields for the two fluids [103]

$$\mathbf{u}_i = \frac{k k_{r,i}}{\mu_i} \nabla p_i, i \in \{1, 2\}. \tag{1.29}$$

The relative permeabilities insert in Darcy's law the fact that the flow of a fluid depends on the local configuration of the other fluid. The entire porous medium is thus not accessible to both fluids. With this description, the {previously-saturating fluid + solid matrix} set is seen as a unique porous medium inside which the injected fluid

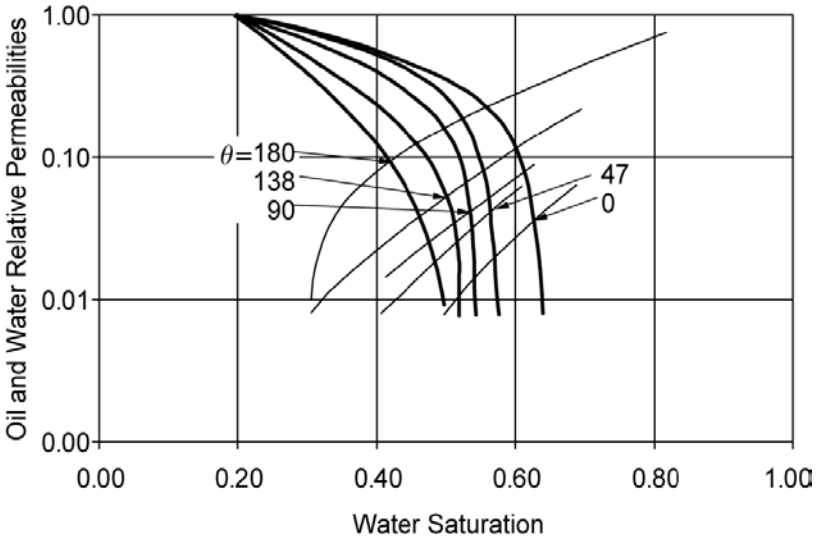

Figure 1.12: Oil/water relative permeabilities for Torpedo sandstone with varying wettability. Contact angles measured through the water phase are shown in degrees. For all measurements, the water saturation was increasing, as it does in waterflooding. [107]

penetrates with a lower permeability than the absolute one. The relative permeabilities are functions of the volume fractions (also called saturations) occupied by each of the fluids in the porous material. Usually, they are determined from experimental data, with different values in the case of drainage when compared to those in the case of imbibition (see Figure 1.11). There exist several models which describe the evolution of the relative permeabilities with the saturation: Corey model in which the permeability varies as a power law of the saturation [105], Buckley-Leverett model which tries to determine the relative permeabilities from experimental data [106]. The relative permeabilities are also strongly dependent on wettability (see Figure 1.12). A derivation of Darcy's law in two-phase flow can be found in [108].

The capacity of a fluid to move inside the porous medium is described by the mobility parameter

$$\text{Mob} \equiv \frac{kk_r}{\mu}.$$

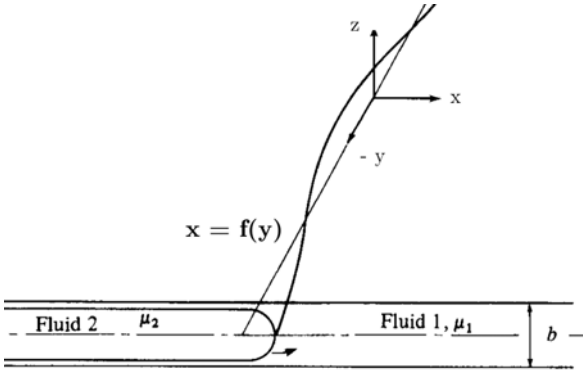

Figure 1.13: Two-phase flow in a Hele-Shaw cell. [110]

The mobility ratio is the ratio of the mobility of the displaced fluid divided by that of the invading fluid

$$M \equiv \frac{\text{Mob}_{\text{displaced}}}{\text{Mob}_{\text{invading}}} = \frac{k_{r,\text{displaced}}}{k_{r,\text{invading}}} \frac{\mu_{\text{invading}}}{\mu_{\text{displaced}}}. \tag{1.30}$$

This parameter is of usual use in the oil industry to evaluate the capacity of the invading solution to move the oil from the reservoir: the larger this ratio, the more favourable the injection. If one neglects the effect of relative permeabilities in equation (1.30), the mobility ratio reduces to

$$M = \frac{\mu_{\text{invading}}}{\mu_{\text{displaced}}} \tag{1.31}$$

i.e. the viscosity ratio. From now on, the mobility ratio and viscosity ratio will be considered as equal.

1.2.4.3 Hele-Shaw cell and two-phase flow in porous media

By analogy with Darcy's law, it is possible to study the flows in porous media in a Hele-Shaw cell [109]. This cell is constituted with a linear canal between two glass plates separated by a short distance b when compared with the width w (Figure 1.13). Although the 2D Hele-Shaw equations are well known [73], the reader may find the key ideas in the context of a two-fluid flow in Section 1.2.6 (paragraph Proof of equation 1.48). In such a system, the average velocity $\mathbf{u}$ of the flow of some fluid of viscosity μ is

$$\mathbf{u} = -\frac{b^2}{12\mu} \nabla p. \tag{1.32}$$

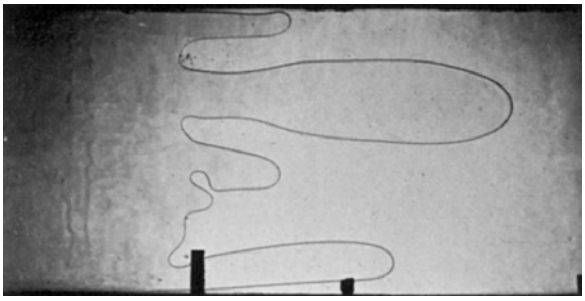

Figure 1.14: Interface between air and glycerine in a Hele-Shaw cell with inhibiting effect of a finger which gets ahead of its neighbour. [114]

This equation is similar to Darcy's law for a permeability $b^2/12$. This system is thus adequate to model a 2D flow in a porous medium. As the stability analysis of two-phase saturated flow in porous media is of much interest in petroleum engineering [111, 112, 113], Saffman and Taylor studied the displacement in a Hele-Shaw cell of a more viscous fluid by a less viscous fluid [114]. Indeed, in this case, the interface between both fluids becomes unstable and starts to generate the so-called Saffman-Taylor fingering (Figure 1.14). For two specific fluids and a specific geometry, the width of these fingerings depends on the velocity. This width is the result of the competition between the viscous forces (which tend to thin down the fingering) and the capillary forces (the reverse): for increasing velocities, *i.e.* when the effect of the viscous forces is the most important one, the width of the fingering diminishes. At high velocity, the resulting fingers will tend to fill half of the cell's width [115].

1.2.4.4 Other approaches to describe flow in porous media

So far, there exists no analytical solution, based on fluid mechanics equations, that can describe flows in porous media thoroughly at the pore scale [75]. Four different kinds of approach are used to study these flows [116]:

- a continuous approach in which the porous medium is caracterised by macroscopic parameters (*e.g.* the permeability) [117, 118, 119, 120, 121, 122, 123]. These parameters are strongly dependent on the microscopic structure of the medium and reflect its average properties. Darcy's law is an example [124, 125].

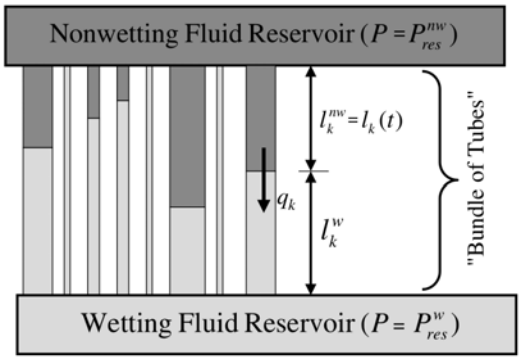

Figure 1.15: Bundle of tubes model. [126]

- the capillary bundle model where the volume that can be reached by the flow is assimilated to a set of capillaries (Figure 1.15) [126, 127]. It is then possible to determine the permeability of the medium by both applying Darcy's law and considering that the flow in the capillaries is of the Poiseuille type.

- an approach based on numerical methods (*e.g.* finite elements) to describe the porous medium at the pore scale and consider the physical phenomena at this scale, in order to solve the flow equations [128, 129, 130]. Lattice-Boltzmann (LB, see Figure 1.16(a)) [131, 132, 133, 134], Smoothed Particle Hydrodynamics (SPH, see Figure 1.16(b)) [135], Modified Moving Particle Semi-implicit [136, 137, 138] and Level-Set (LS, see Figure 1.16(c)) [139] methods are several examples.

- an approach by Pore-scale Network Modelling (PNM) [140, 141, 142, 143, 144, 145, 146, 147, 148, 149]. The pore volume is described with a network of pores and throats with ideal geometry and specific chosen laws for the flow (Figure 1.17). The next step to describe the flow is to solve the system of coupled equations for the set of all the throats. This approach is a compromise between the continuous and numerical approaches: as it combines the appropriate pore-scale physical phenomena and a simple description of the pore volume, this approach enables the development of models that can predict the average flow at the macroscopic scale [153, 154]. The first step is to model the flow in a single capillary, then by considering a network of nodes connected by one or more

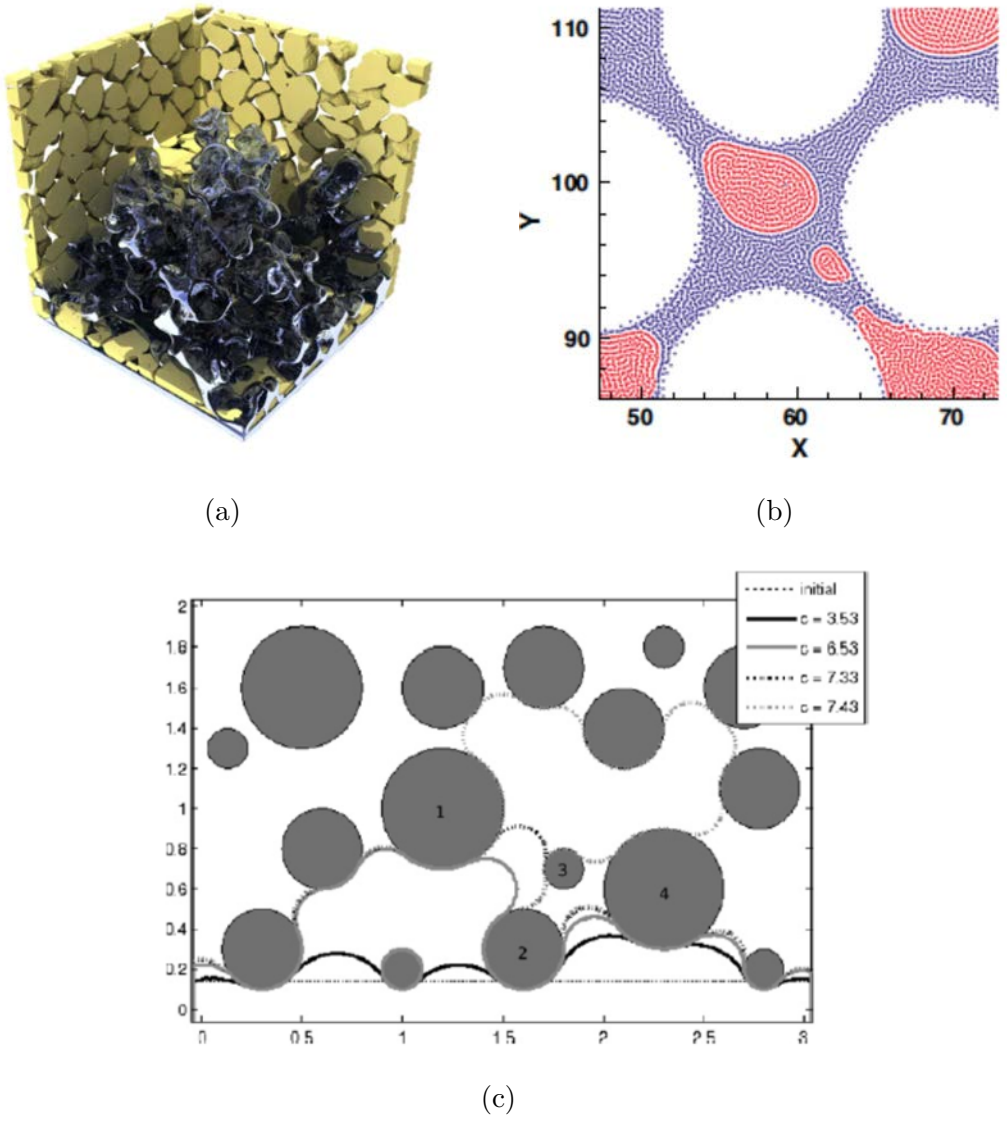

(a) (b)

(c)

Figure 1.16: (a) Snapshot of a fully resolved transient Lattice Boltzmann simulation of drainage in a porous medium where the wetting phase (invisible) is replaced by a gaseous phase [134]. (b) A single pore solved by Smoothed Particle Hydrodynamics simulation [135]. (c) Simulation by Level-Set method of a cycle of drainage followed by imbibition in a 2D model granular porous medium [139].

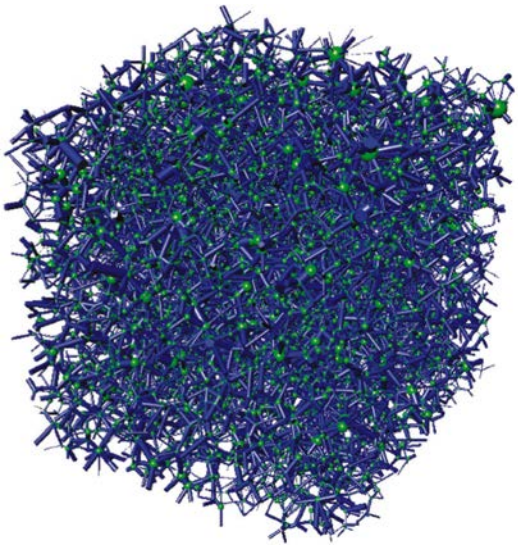

Figure 1.17: A network of pores connected by throats. This network is topologically equivalent to the void space of a Berea sandstone [150, 151]. The pores and throats are assigned volumes, conductances, inscribed radii and shapes that mimic essential features of the reconstructed pore space. [152]

> throats, one can establish a system of equations that model the flow in the set of throats. Finally, after having added an equation of mass conservation, this set of coupled equations is solved to determine the pressure field of the network [155].

1.2.5 Tortuosity

In porous materials, tortuosity characterises the sinuosity and interconnectedness of pore space. This concept common to many models aims at relating macroscopic transport properties of porous materials to their microstructure [156]. It is used for phenomena as diverse as molecular diffusion, fluid permeation, electrical or thermal conduction, and sound propagation [157]. In practice, tortuosity is often an empirical factor that is used to match *a posteriori* experimental data to a specific model. When used for making predictions, crude approximations are generally used. For instance, in the context of molecular diffusion the tortuosity is often equated to the inverse of the porosity [158]. Therefore, although the qualitative meaning of tortuosity is clear,

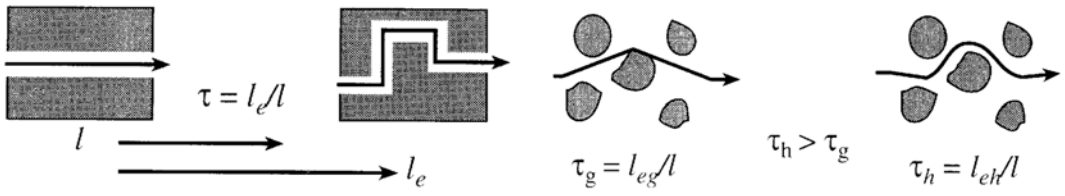

Figure 1.18: (a) The most basic definition of tortuosity is the path length tortuosity τ. This is the ratio of the length of the tortuous flow path l_e to the straight line length l in the direction of flow. This is most easily visualised in a pore space consisting of single capillaries of constant width with no branching. (b) Geometrical tortuosity is defined as the shortest length between inflow and outflow points that avoids the solid obstacles, and this is realised as a zigzag path passing grains with close tangents. Carman's definition of hydraulic tortuosity differs from geometrical tortuosity in that it is the effective path length taken by the fluid (l_{eh}), rather than the shortest possible path (l_{eg})which is considered. Fluid passes along a smoothed route through porous media so that τ_h is always greater than τ_g. [157]

it is a loosely defined quantity. The exact geometrical meaning of tortuosity in the context of various transport phenomena may be differently dependent, say, on pore size or the presence of bottlenecks [159].

1.2.5.1 Geometrical tortuosity

Geometrical tortuosity can be defined as the ratio of the shortest path of connected points entirely embedded in the fluid medium (*i.e.*, continuously through the pores, see Figure 1.18(a)) that joins any two points defined by the vectors $\mathbf{r}_1$ and $\mathbf{r}_2$ ($l_{\min}$), with the straight line distance between them. Geometrical tortuosity, τ_g, can thus be expressed mathematically as [156]

$$\tau_g(\mathbf{r}_1, \mathbf{r}_2) = \frac{l_{min}(\mathbf{r}_1, \mathbf{r}_2)}{|\mathbf{r}_1 - \mathbf{r}_2|}, \mathbf{r}_2 \in f(\mathbf{r}_1), \tag{1.33}$$

where the pore region, occupied by the fluid, is denoted by f.

A more general definition of geometrical tortuosity can be found in the work of Russian engineers [160]. The tortuosity coefficient is defined as the "averaged ratio

of pore length to the projection of the pores in the direction of flow". This at once accepts that geometrical tortuosity is an averaged parameter, and that it is a structural characteristic of the medium, independent of any particular transport process.

The concept of a purely geometrical tortuosity factor has not found broad favour in the consideration of permeability, conductivity or diffusivity. However, some workers [161] have used a random-walk model to estimate tortuosity, and this can be considered to be a purely geometrical measure (Figure 1.19).

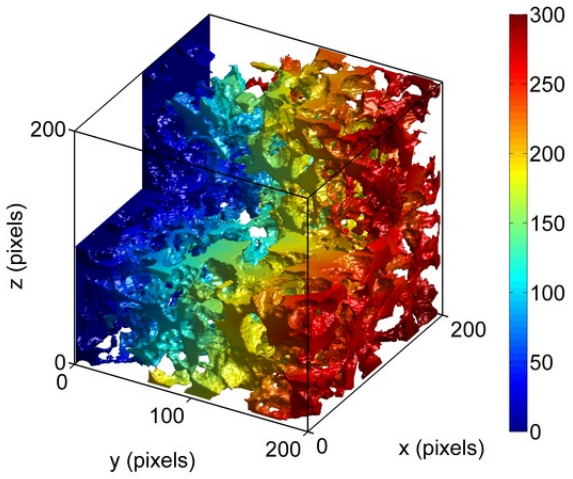

Figure 1.19: Tortuosity calculation from an X-ray tomography reconstruction of a porous sandstone (the pores are shown): the color represents the shortest distance within the pore space from the left limit of the image to any point in the pores. Comparing this distance to the straight-line distance shows that the tortusosity is about 1.5 for this sample. [159]

1.2.5.2 Hydraulic tortuosity

Capillary models of pore structure for hydraulic transport Fluid flow in a straight cylindrical tube or capillary of radius r_0 can be described by the Hagen-Poiseuille equation

$$Q = -\frac{\pi r_0^4}{8\mu}\frac{\Delta p}{l} \tag{1.34}$$

where Q is the volumetric flow rate and Δp is the macroscopic pressure difference between the two ends of the tube of length l. As the tube dimension decreases, the cross-sectional area decreases as the square of the radius, and the relative effect of viscous drag at the channel walls also increases in the same proportion. Thus overall fluid flow rate scales as the channel radius raised to the fourth power. In a porous medium consisting of an aggregate of equal sized grains, one could reason that the flow channels would be represented by a cluster of identical capillaries with a particular effective radius r_{eff}. The effect of reducing the grain size by a factor of two would be to reduce the flow velocity through each channel by a factor of 16. However, the number of flow channels would be increased by a factor of four, so the overall rate of flow, and so permeability, would scale with the square of the effective radius:

$$Q \propto r_{\text{eff}}^2 \qquad \text{and} \qquad k \propto r_{\text{eff}}^2 \tag{1.35}$$

Though this reasoning led to many empirical models of permeability prediction for granular materials based on identification of the characteristic pore dimension, it was soon realised that knowledge of the grain size alone is not sufficient to predict the characteristic radius, and so permeability of the material. Indeed the nature of the packing, which dictates the size and shape of the pores, also exerts a strong control.

Kozeny's equation In granular materials (such as sands), the pore surface area can be calculated from the size and shape of the constituent grains. On this basis, Kozeny introduced a semi-empirical equation to estimate the permeability of granular aggregates [162]

$$k = \frac{\phi r_h^2}{C_k}. \tag{1.36}$$

C_k is the so-called "Kozeny constant" and r_h is the hydraulic radius, defined as

$$r_h = \frac{\text{cross-sectional area normal to flow}}{\text{"wet perimeter" of the flow channels}}. \tag{1.37}$$

It corresponds to the radius of the ideal circular capillary that would have the same hydraulic conductance as the granular material [163].

Kozeny assumed the pore space was equivalent to a bundle of parallel capillaries with a common hydraulic radius and cross-sectional shape described by r_h/C_k, then

introduced the concept that the real flow path could be tortuous, with an effective hydraulic path length l_{eh} (see Figure 1.18(b)). The permeability is then reduced by a factor of the sinuous length l_{eh} divided by the straight-line length in the direction of flow l_{min}. The hydraulic tortuosity of Kozeny is thus [162]

$$\tau_{\mathrm{hK}} = \frac{l_{\mathrm{eh}}}{l_{\mathrm{min}}}. \tag{1.38}$$

His equation for permeability then becomes

$$k = \frac{\phi r_h^2}{\beta \tau_{\mathrm{hK}}}. \tag{1.39}$$

In this way, the Kozeny constant is subdivided into a shape factor β with a conservative value for a particular type of granular material, and a tortuosity factor τ_{hK} which represents the sinuous nature of the pore space. The shape factors for spheres and other regular particles can be calculated from estimates of their coefficients of hydrodynamic drag in Stokes flow [164].

Dupuit's relation When considering the movement of fluid through a porous rock, it is common to consider the flux in terms of Darcy velocity $\mathbf{u}$ which is equal to the product of the intrinsic phase average velocity $\bar{\mathbf{v}}$, and the porosity ϕ [165]

$$\mathbf{u} = \phi \bar{\mathbf{v}}. \tag{1.40}$$

This intrinsic phase average velocity is the average velocity at which a fluid particle is transported through the medium by steady laminar Newtonian viscous flow and, like $\mathbf{u}$, is a vector defined with reference to the macroscopic flow direction. Equation (1.40) is called Dupuit's relation [166].

Carman pointed out that when introducing the tortuosity factor, Dupuit's relation had to be modified [167]. At constant porosity, the interstitial velocity must indeed increase in order to ensure the external Darcy velocity remains unchanged while the fluid traverses a longer path through the medium (see Figure 1.18(a)). Thus, the time taken for a fluid element to complete the path l_{eh} along the bent or twisted capillary at the faster interstitial velocity $(\mathbf{u}/\phi)(l_{\mathrm{eh}}/l)$ equals the measured time for the fluid to traverse the bulk sample length l at Darcy velocity $\mathbf{u}$. Equation (1.40) then becomes

$$\mathbf{u} = \phi \bar{\mathbf{v}} \frac{l}{l_{\mathrm{eh}}}. \tag{1.41}$$

If Darcy's law is applied for one dimensional flow Darcy velocity is

$$\mathbf{u} = \left(\frac{l}{l_{\text{eh}}}\right)^2 \frac{\phi r_h^2}{\beta\mu}\frac{\Delta p}{l} \tag{1.42}$$

through each tortuous capillary. Therefore, the flow rate is retarded in a bent capillary by an overall factor which is proportional to the tortuosity squared [168].

The Kozeny-Carman equation Carman modified Kozeny's equation to include a tortuosity factor that is the square of the ratio of the effective hydraulic path length l_{eh} for fluid flow through the "equivalent hydraulic channels" in a medium, to the straight-line distance through the medium in the direction of macroscopic flow [167]. This measure has become known as the "channel equivalent" hydraulic tortuosity factor [169], here denoted T_{hC}

$$T_{\text{hC}} = \left(\frac{l}{l_{\text{eh}}}\right)^2 = \tau_{\text{hK}}^2. \tag{1.43}$$

A more mundane explanation of the length squared relationship is given by Dullien [169], who explains that if a bundle of capillaries are increased in length while the volume they occupy remains constant (porosity is conserved) obviously the number of flow channels must be reduced. This reduces to an argument of whether or not the flow paths fill space. Carman himself admitted that this exponent of two was not rigorously derived but that experimental results suggested a value close to two for granular media and well sorted porous rocks.

Providing that a granular aggregate is not crushed or cemented, and that the grains do not interpenetrate or deform, the surface area is independent of the porosity, or tightness of packing of the material. However, the surface area per unit volume (known as the "specific surface", see above) increases as the packing density increases. Thus, with knowledge of specific surface area S_0 and porosity, the size of the "equivalent hydraulic channels" can be estimated

$$r_h = \frac{\phi}{S_0}. \tag{1.44}$$

Kozeny's equation for permeability becomes

$$k = \frac{\phi^3}{\beta\tau_{\text{hK}}^2(1-\phi)^2 S_0^2} \tag{1.45}$$

which is known as the Kozeny-Carman equation. Though this equation is only semi-empirical, it has been found to be nearly exact for random packs of monodisperse spheres when comparing results of experiments with numerical simulations [170]. The Kozeny constant is about 4.8 in this case, while for reasonably well sorted and rounded sands, a value of about 5 is generally accepted. Estimated shape factors range in value from about 2 to 3 for typical granular materials [163, 166]. The value of Kozeny hydraulic tortuosity τ_{hK} therefore ranges from about $\sqrt{2}$ to 2 in unconsolidated granular aggregates. In consolidated rocks and soils the value of τ_{hK} ranges up to about five [169]. An upper limit on tortuosity in uncemented granular media of about 10 was suggested by Witt and Brauns [171], even when the grains are platy rather than rounded.

1.2.5.3 How is hydraulic tortuosity related to geometrical tortuosity?

In general, hydraulic tortuosity and geometrical tortuosity are different. This is due to the fact that the paths taken by fluid as it flows through the porous medium are not straight lines, or close tangents to the rock grains, but rather are smooth curves tending to follow the axes of the flow channels (Figure 1.18). Also, as a result of viscous drag, fluid flow is more retarded at the channel walls than along channel axes, so all paths are not equally favoured. This matter is discussed in a mathematical context by Coussy [172].

Despite these obvious differences, some workers have attempted to estimate permeability using geometrical tortuosities [173, 174]. Both of these studies employed a "ray-tracing" technique which tracks the shortest path, skirting obstacles, from one face of the material to the other. The advantage of such methods is their simplicity, but the results obtained cannot be used interchangeably in a formulation such as the Kozeny-Carman equation.

1.2.6 What about surface tension?

Case of Hele-Shaw cells In the case of simultaneous flow of two phases in Hele-Shaw cells, boundary conditions must be given at the interface which hold for the

depth-averaged fields. It is common to write these as

$$[\![\mathbf{n}\cdot\mathbf{u}]\!] = 0 \tag{1.46a}$$

$$[\![p]\!] = \frac{2\sigma}{b}\cos\theta + \frac{\sigma}{R} \tag{1.46b}$$

Here $[\![\ ]\!]$ denotes a jump, σ is the surface tension, θ the apparent contact angle and R the principal radius of curvature of the projection onto the plane, of the tip of the meniscus separating the two phases. Park and Homsy [175] recall that though equation (1.46a) is obvious, the same cannot be stated for equation (1.46b) except at equilibrium under conditions of no flow. It seems that equation (1.46b) was at first adopted with reservation [114, 176], as a "simplest assumption". Later works have cast serious doubt on the validity of this boundary condition [177, 178] and other formulations have been suggested [175]

$$\frac{b\Delta p}{2\sigma} = 1 + 3.80\ \mathrm{Ca}^{2/3} - \frac{1}{16}\pi f''\epsilon^2 + O(\mathrm{Ca}, \epsilon^2\mathrm{Ca}^{2/3}) \tag{1.47}$$

where f describes the interface ($x = f(y)$ see Figure 1.13), ϵ is the ratio of gap width to transverse characteristic length ($\epsilon = b/\lambda_f$ with λ_f fingering wavelength) and Ca the capillary number associated with the receding fluid.

From now on, the following approximations are considered: $\mathrm{Ca} \sim 0$ and $\epsilon \sim 0$. Therefore the surface tension term is added (whenever needed) in equation (1.32) as thus

$$\mathbf{u} = \frac{b^2}{12\mu}(-\nabla p + \sigma\kappa\nabla c). \tag{1.48}$$

Proof of equation 1.48

This paragraph is extracted from [83] with slight modifications.

Let us consider a Hele-Shaw cell Ω of size $l \times h \times b$ ($\Omega = \{(x, y, z) \in \mathbb{R}^3 : 0 \leqslant x \leqslant l, |y| \leqslant \frac{w}{2}, 0 \leqslant z \leqslant b\}$). The governing equations prior to a Hele-Shaw approximation are the 3D Stokes equations and incompressibility

$$-\nabla p(x, y, z, t) + \mu\nabla^2\mathbf{u}(x, y, z, t) + \mathbf{f}_\sigma = 0, \tag{1.49}$$

$$\nabla\cdot\mathbf{u}(x, y, z, t) = 0, \tag{1.50}$$

where $\mathbf{f}_\sigma$ denotes the body force with the continuum surface tension formulation [179]. The fluid viscosity of fluid i is $\mu = \mu_i, i = 1, 2$. Fluid 1 occupies $\Omega_1 = \{(x, y, z) \in \mathbb{R}^3 : 0 < h(y,t) \leqslant x \leqslant l, |y| \leqslant \frac{w}{2}, 0 \leqslant z \leqslant b\}$. Fluid 2 occupies $\Omega_2 = \{(x, y, z) \in \mathbb{R}^3 : 0 \leqslant x \leqslant h(y,t) < l, |y| \leqslant \frac{w}{2}, 0 \leqslant z \leqslant b\}$.

1. Similar to section 1.1.3.3, we introduce a marker function[6] $\tilde{c}(x, y, z, t)$ equal to 0 in fluid 1 and 1 in fluid 2. We suppose that the pressure in fluid 2 is higher than in fluid 1. Thus both ∇p and $\mathbf{n} = \nabla\tilde{c}/|\nabla\tilde{c}|$ point into fluid 2. Therefore

$$\mathbf{f}_\sigma = \sigma\kappa\delta_S\mathbf{n} \tag{1.51}$$

   where $\delta_S(x, y, z) = |\nabla\tilde{c}(x, y, z, t)|$ at the interface S in the distribution sense and $\kappa = -\nabla \cdot \mathbf{n}$. The fluids are advected by the velocity field

$$\frac{\partial\tilde{c}(x, y, z, t)}{\partial t} + \mathbf{u} \cdot \nabla\tilde{c}(x, y, z, t) = 0. \tag{1.52}$$

2. In the momentum equation for the x-y plane, $\rho\frac{D\mathbf{u}}{Dt}$ is assumed to be negligible compared with ∇p and $\nabla^2\mathbf{u}$. The assumption is that b is small, so that $\nabla^2 \sim \frac{\partial^2}{\partial z^2} = O(\frac{1}{b^2})$. This means $p = O(\frac{1}{b^2})$. Thus $\rho\frac{D\mathbf{u}}{Dt}$ in the x-y plane is assumed to be smaller order than $O(\frac{1}{b^2})$.

3. The vertical depth between the walls, b, is assumed small compared with the length l of the walls in the x-direction and the width w in the y-direction: $\frac{b}{w} \ll 1, \frac{b}{l} \ll 1$. The components of the velocity have magnitudes $u = O(1), v = O(1), w = O(b)$. We define an in-place depth-averaged velocity field $\mathbf{U} = (U(x, y, t), V(x, y, t))$

$$\mathbf{U}(x, y, t) = \frac{1}{b}\int_0^b (u(x, y, z, t), v(x, y, z, t))\,\mathrm{d}z. \tag{1.53}$$

4. The out-of-plane interface shape is assumed to be semi-circular, with contact angle 180° at the walls, and radius $b/2$. Thus, the out-of-plane curvature is $2/b$ and contributes $-\sigma\frac{2}{b}\nabla\tilde{c}$ to the surface tension force. From here, we replace κ in equation (1.51) by $\frac{2}{b} + \kappa(x, y, t)$

$$\mathbf{f}_\sigma = \sigma\left(\frac{2}{b} + \kappa(x, y, t)\right)\nabla\tilde{c}. \tag{1.54}$$

[6] Note the use of the ˜ sign to distinguish the 3D marker function from the 2D one.

5. We integrate equation (1.52) with respect to z. We have $\mathbf{u}\cdot\nabla\tilde{c}(x,y,z,t) = \nabla\cdot(\mathbf{u}\tilde{c}(x,y,z,t))$ since $\nabla\cdot\mathbf{u}=0$. Thus,

$$\int_0^b \left[\frac{\partial\tilde{c}(x,y,z,t)}{\partial t} + \nabla\cdot(\mathbf{u}\tilde{c}(x,y,z,t))\right] \mathrm{d}z = 0. \tag{1.55}$$

The first term is $\frac{\partial}{\partial t}\int_0^b \tilde{c}(x,y,z,t)\,\mathrm{d}z$. The second term is $\frac{\partial}{\partial x}\left[\int_0^b u\tilde{c}(x,y,z,t)\,\mathrm{d}z\right] + \frac{\partial}{\partial y}\left[\int_0^b v\tilde{c}(x,y,z,t)\,\mathrm{d}z\right] + \int_0^b \frac{\partial}{\partial z}\left[w\tilde{c}(x,y,z,t)\right]\mathrm{d}z$. We define a depth-averaged marker function $c(x,y,t)$

$$c(x,y,t) = \frac{1}{b}\int_0^b \tilde{c}(x,y,z,t)\,\mathrm{d}z. \tag{1.56}$$

The first integral becomes $b\frac{\partial}{\partial t}c(x,y,t)$. The last integral vanishes because $\tilde{c}$ is bounded and $w(x,y,0,t) = w(x,y,b,t) = 0$ due to zero penetration at the walls. The interface occupies approximately a volume $O(b^2)$. The projection in the x-y plane has area $O(b)$, which shrinks to 0 as $b\to 0$. We replace $\int_0^b \left[u\tilde{c}(x,y,z,t)\right]\mathrm{d}z$ with $c(x,y,t)\left[\int_0^b u\,\mathrm{d}z\right]$, and we define an error $E(x,y,t)$ in L_∞ by

$$E(x,y,t) = \frac{1}{b}\left|\int_0^b u\left(\tilde{c}(x,y,z,t) - c(x,y,t)\right)\mathrm{d}z\right|. \tag{1.57}$$

We see in equation (1.56) that $\tilde{c}-c$ is bounded in the interfacial region, and vanishes away from it. The L_1 norm of this error is $\int_\Omega E(x,y,t)\,\mathrm{d}x\,\mathrm{d}y \sim b$, which goes to 0 as $b\to 0$. Therefore, we can approximate equation (1.55) by $\frac{\partial}{\partial t}c(x,y,t) + \frac{1}{b}\frac{\partial}{\partial x}\left[c(x,y,t)\int_0^b u\,\mathrm{d}z\right] + \frac{1}{b}\frac{\partial}{\partial y}\left[c(x,y,t)\int_0^b v\,\mathrm{d}z\right] = 0$ in the L_1 norm. In terms of the depth-averaged velocity,

$$\frac{\partial}{\partial t}c(x,y,t) + \frac{\partial}{\partial x}[c(x,y,t)U(x,y,t)] + \frac{\partial}{\partial y}[c(x,y,t)V(x,y,t)] = 0. \tag{1.58}$$

Integration of the incompressibility condition $\int_0^b(\nabla\cdot\mathbf{u})\,\mathrm{d}z = 0$ yields $\nabla_{plane}\cdot\mathbf{U} = 0$, where $\nabla_{plane} \equiv (\frac{\mathrm{d}}{\mathrm{d}x}, \frac{\mathrm{d}}{\mathrm{d}y})$. Therefore, $\nabla_{plane}(c\mathbf{U}) = \mathbf{U}\cdot\nabla_{plane}c$, which means the advection equation (1.58) becomes

$$\frac{\partial}{\partial t}c(x,y,t) + \mathbf{U}\cdot\nabla_{plane}c(x,y,t) = 0. \tag{1.59}$$

6. We return to equation (1.49) and define, for convenience, a modified pressure $p^*(x,y,z,t) = p(x,y,z,t) + \frac{2\sigma}{b}\tilde{c}(x,y,z,t)$. The classical Hele-Shaw approximation is $w = O(b)$, $\frac{\partial}{\partial z} = O(\frac{1}{b})$ and $\nabla^2 \sim \frac{\partial^2}{\partial z^2} = O(\frac{1}{b^2})$ as $b\to 0$. The z-component of equation (1.49) is $\frac{\partial p^*}{\partial z} = \mu\frac{\partial^2 w}{\partial z^2} - \sigma\kappa(x,y,t)\frac{\partial\tilde{c}}{\partial z}$. We assume that the coefficients μ, σ and κ are of

order $O(1)$. We see that $\frac{\partial p^*}{\partial z}$ dominates over the other terms if $p^* = O(\frac{1}{b})$. With $\frac{\partial p^*}{\partial z} \sim 0$, we conclude that p^* is independent of z. Upon consideration of the rest of equation (1.49), $\frac{\partial p^*(x,y,t)}{\partial x} \sim \mu \frac{\partial^2 u}{\partial z^2} - \sigma\kappa(x,y,t)\frac{\partial \tilde{c}}{\partial x}$ and $\frac{\partial p^*(x,y,t)}{\partial y} \sim \mu \frac{\partial^2 u}{\partial z^2} - \sigma\kappa(x,y,t)\frac{\partial \tilde{c}}{\partial y}$, we obtain $\frac{\partial p^*(x,y,t)}{\partial x} + \sigma\kappa(x,y,t)\frac{\partial \tilde{c}}{\partial x} = O(\frac{1}{b^2})$. Hence, the z-dependence disappears and we have

$$p^*(x,y,t) = p(x,y,t) + \frac{2\sigma}{b} c(x,y,t). \tag{1.60}$$

Away from the interface, $\tilde{c}$ is a constant, and equation (1.49) reduces to the classical Hele-Shaw equation. The $\nabla_{plane} p^*$ terms and $\nabla \tilde{c}$ drive the Poiseuille flow [180]. Also, we find that $p^* = O(\frac{1}{b})$. Together with $u = v = w = 0$ at $z = 0, b$, we find $u = \frac{1}{2\mu}\left(\frac{\partial p^*(x,y,t)}{\partial x} + \sigma\kappa(x,y,t)\frac{\partial c}{\partial x}\right)(z^2 - bz)$, $v = \frac{1}{2\mu}\left(\frac{\partial p^*(x,y,t)}{\partial y} + \sigma\kappa(x,y,t)\frac{\partial c}{\partial y}\right)(z^2 - bz)$ and $w = 0$. The depth-averaged velocities are

$$U(x,y,t) = -\frac{b^2}{12\mu}\left(\frac{\partial p^*(x,y,t)}{\partial x} + \sigma\kappa(x,y,t)\frac{\partial c}{\partial x}\right), \tag{1.61a}$$

$$V(x,y,t) = -\frac{b^2}{12\mu}\left(\frac{\partial p^*(x,y,t)}{\partial y} + \sigma\kappa(x,y,t)\frac{\partial c}{\partial y}\right). \tag{1.61b}$$

In vector form, the Hele-Shaw equations are

$$\boxed{\mathbf{U} = \frac{b^2}{12\mu}(-\nabla p^* + \mathbf{f}_\sigma).} \tag{1.62}$$

7. In the interface region, the flow does not satisfy the assumption that $\nabla_{plane} p^* + \sigma\kappa\nabla_{plane}\tilde{c}$ is constant with respect to z. However, even though equation (1.62) does not hold pointwise near the interface, the Hele-Shaw limit is correctly obtained in the sense of distributions. This implicitly enforces the normal stress balance at the interface, which is the continuity of

$$p^* + \sigma\kappa c.$$

If this is violated, then the velocity normal to the interface contains a Delta function, which contradicts incompressibility.

Case of porous media In the case of Darcy modelling of simultaneous flow of two phases in a porous medium, boundary conditions at the interface cannot be written as for flow in a Hele-Shaw cell. Indeed, though equation (1.46a) is obviously still true, the same cannot be said of equation (1.47) and *a fortiori* for equation (1.46b). The

interface between two fluids flowing in a porous space is defined by the geometry of the porous medium. Consequently, the excess of pressure of one fluid over the other is imposed by the geometry at the pore size and not by the overall macroscopic radius of curvature

$$[\![p]\!] = \frac{2\sigma}{R_p} \neq \frac{2\sigma}{R_c} \tag{1.63}$$

where R_p is the pore radius and R_c the macroscopic radius of curvature ($R_p \ll R_c$).

To consider surface tension, equation (1.32) should be written as

$$\mathbf{u} = -\frac{k}{\mu}(\nabla p + 2\sigma/R_p \nabla c(x, y, z, t)) \tag{1.64}$$

Defining $p^* = p + 2\sigma/R_p c(x, y, z, t)$ in equation (1.64) allows to use only equation (1.32) with no reference to surface tension [83].

1.3 Phenomenology of flows in porous media

Using basic theory of flows in porous media, Roland Lenormand studied Newtonian two-phase flows in networks with both an organic and an aqueous phase [181]. Considering a system previously filled with one of the phases, he injected the second (non-miscible) phase in the system either at constant flow rate or at constant pressure gradient between the entry and the exit faces. He then observed the displacement of both phases during the experiment and precisely described the behaviour of the oil/water interface at pore scale in order to link it to the aspect of the interface at the network scale [182]. Besides, he hightlighted the influence of several parameters such as the injection velocity of the fluids, or their viscosities, upon the behaviour of both phases [183]. Finally, two different cases of displacement were analysed:

1. drainage, *i.e.* the injection of a non-wetting fluid to displace a wetting fluid previously filling the system [183].

2. imbibition, *i.e.* the injection of a wetting fluid to displace a non-wetting fluid previously filling the system [184].

In order to realise this study, he used a 2D network of pores of width L connected by throats with 6 possible different widths, randomly distributed. The distance between

two pores was constant while the size of the pores was randomly varying. The system had a uniform depth of $z = 1$ mm and a tranverse area $\Sigma = Lz$. Two parameters are identified to establish the phase diagrams: the capillary number of the injected fluid $\mathrm{Ca} = \frac{\mu_{injected} Q}{\sigma \Sigma}$ (Q is the flow rate of the injected fluid) and the viscosity ratio $M = \frac{\mu_{injected}}{\mu_{displaced}}$.

1.3.1 Displacement of the meniscus at the pore scale

Lenormand *et al.*'s work [182] highlighted that during the displacement of one fluid by the other in a network of capillaries, both fluids were present simultaneously in the throats. The non-wetting fluid is present in the bulk of the throat while the wetting one stays stuck in the corners of the throat (Figure 1.20(a)). The accessible displacement types for the meniscus depend on the injection configuration: drainage or imbibition.

In the case of drainage, in a simple straight throat of width x and height y, the meniscus can only move in a piston-like mode (left part of Figure 1.20(a)): to penetrate a wetting-fluid-filled throat, the pressure inside the non-wetting fluid has to be higher than a threshold pressure P_t defined as

$$P_t = 2\sigma \left(\frac{1}{x} + \frac{1}{y} \right). \tag{1.65}$$

Then, when the non-wetting fluid reaches a pore, *i.e.* the intersection of at least three different throats, it fills it right away and invades the adjacent throats if the pressure is high enough.

In the case of imbibition, the meniscus can also move piston-like in straight throats (see Figure 1.20(b)). When the wetting fluid reaches an intersection, two other displacement modes are observed, depending on the fluid present in the adjacent throats. One can distinguish modes I_1 and I_2 illustrated by Figures 1.20(d) and 1.20(e) respectively.

In mode I_1, the wetting fluid arrives at the intersection by three adjacent throats and tends to fill the last throat: successive positions and shapes adopted by the meniscus are displayed in the figures alongside Figure 1.20(d). When position 2 is reached, the meniscus no longer touches the walls and an instability occurs. Then

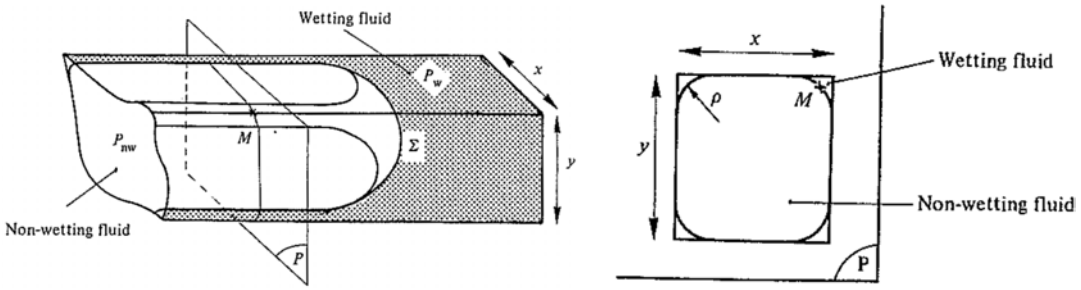

(a) Simultaneous presence of both fluids in a throat

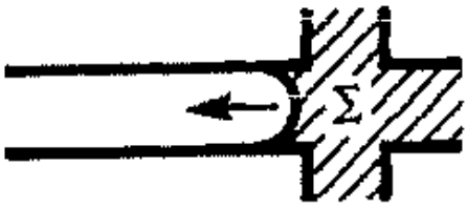

(b) Piston-like

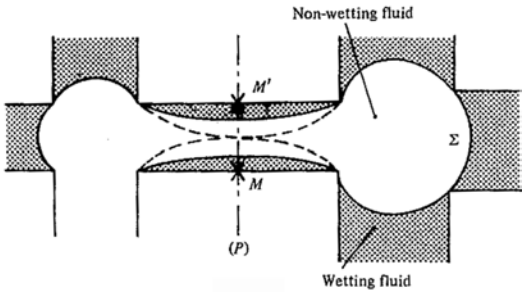

(c) Snap-off

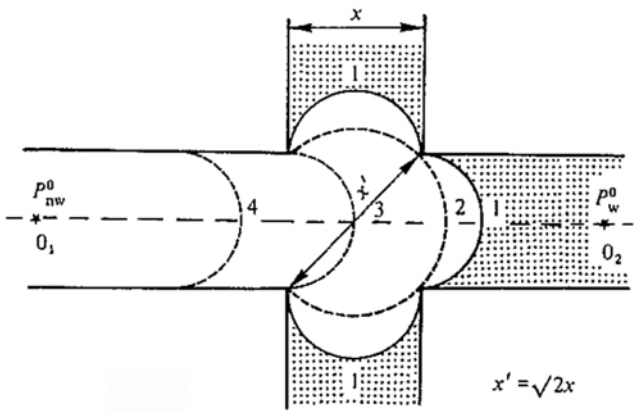

(d) Imbibition I_1

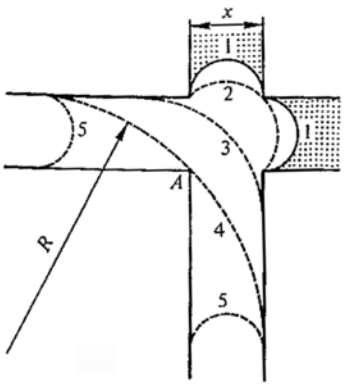

(e) Imbibition I_2

Figure 1.20: Circulation of the fluids in the system and displacement of the meniscus at pore scale [182]. (a) Disposition of the fluids in a throat, prespective view (left) and sectional view (right): the non-wetting fluid flows in the center of the throat while the wetting one stays stuck in the corners. (b)-(e) Displacement mechanisms at the pore scale. (b) A common mode to both drainage and imbibition: piston-like mode. The other modes only happen in the case of imbibition: (c) snap-off, (d) I_1, (e) I_2. Each mechanism has an associated threshold pressure depending only on pore and throat geometries. [116]

the radius of curvature of the meniscus decreases and the pressure difference asociated with the interface increases, resulting in the flow of the wetting fluid and the movement of the meniscus inside the intersection. Position 2 is reached when the pressure in the non-wetting fluid exceeds the threshold pressure P_{I_1} (case of four throats with the same width x)

$$P_{I_1} = \sigma \left(\frac{\sqrt{2}}{x} + \frac{2}{y} \right). \tag{1.66}$$

In mode I_2, the wetting fluid arrives at the intersection by two adjacent throats and tends to fill the last two throats. It occurs when the meniscus reaches point A (see Figure 1.20(e)), when the pressure in the non-wetting fluid exceeds the threshold pressure P_{I_2} (case of four throats with the same width x)

$$P_{I_2} = 2\sigma \left(\frac{0.15}{x} + \frac{1}{y} \right). \tag{1.67}$$

Finally, the meniscus can also move in a snap-off mode[7]. In Figure 1.20(c), the meniscus has not yet moved into the throat, but the presence of wetting fluid in the corners implies that the interface moves alongside the walls of the throat. The pressure difference between the two fluids is then a function of the radius of curvature in the corners. This configuration is stable as long as the pressure in the wetting fluid induces a radius of curvature in the corners lower than $L/2$ with $L = \min(x, y)$. Then the non-wetting fluid no longer touches the walls: the configuration becomes unstable and the wetting fluid fills the throat when the pressure is higher than a threshold pressure

$$P_S = 2\frac{\sigma}{L}. \tag{1.68}$$

The expressions of the different threshold pressures are presented assuming a spreading condition *i.e.* a zero contact angle.

[7]Experiments under quasistatic conditions show that the aspect ratio (pore-to-throat effective diameter ratio) necessary for snap-off is $r_p/r_t \geqslant 1.5$ when advancing contact angles (θ_A) are equal to zero and increases only slightly, to $r_p/r_t \geqslant 1.75$, when θ_A is equal to 55°. Above 70° (approximately), snap-off in throats does not occur in systems with pressure equilibrium between pores and throats [185].

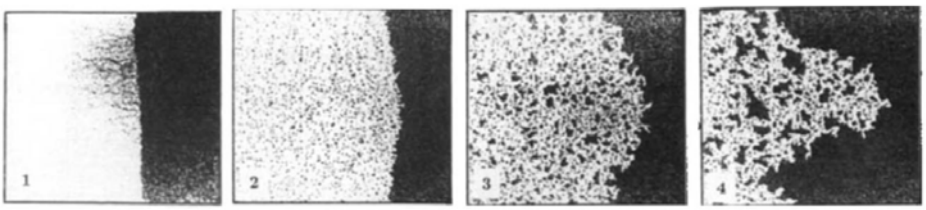

(a) From stable viscous flow to capillary fingering

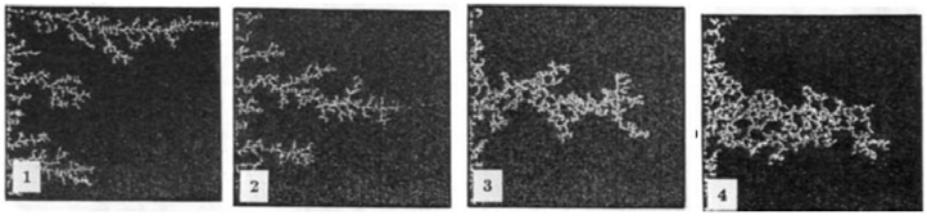

(b) From unstable viscous flow to capillary fingering

Figure 1.21: Shape of the front in the case of drainage [183]. (a) Solution of glucose displacing oil ($\log_{10} M = 2$) at decreasing capillary numbers from left to right ($\log_{10}$ Ca varies from -1.0 to -5.2). (b) Air displacing a highly viscous oil ($\log_{10} M = -4.7$) at decreasing capillary numbers from left to right ($\log_{10}$ Ca varies from -6.3 to -9.1).

1.3.2 Phase diagram in the case of drainage

In the case of drainage, as the injected fluid is non-wetting, it can move only in the bulk of the throats. The meniscus only moves piston-like. Capillary forces prevent the spontaneous entry of the injected fluid in the network: the only way to force its way inside a throat is to impose a pressure difference between the injected and the displaced fluids higher than the threshold pressure P_P of this throat.

By varying both the injection flow rate of the non-wetting fluid and the viscosity ratio, it was possible to identify three different regimes, based on the shape of the front at the network scale [183], and to establish the phase diagram presented in Figure 1.22:

- stable viscous displacement: the boundary between the fluids is flat and the quantity of trapped fluid behind the boundary is low (Figure 1.21(a)). This regime is identified for high capillary numbers and viscosity ratios ($M > 1$): the

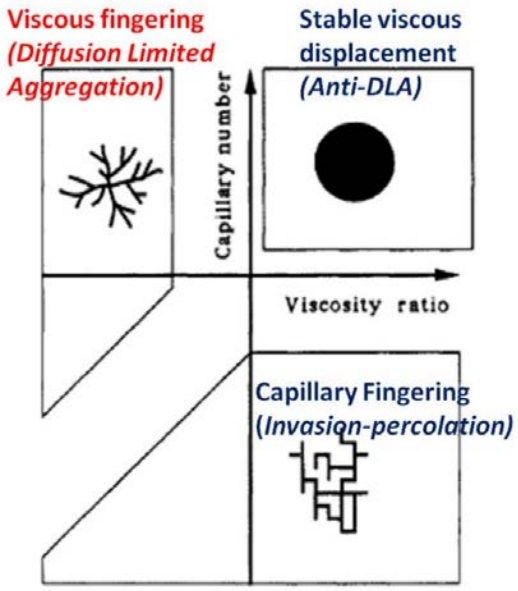

Figure 1.22: Phase diagram in the case of drainage [181]. Three domains are identified in the (Ca, M) plane corresponding to the different shapes of the front at network scale. These shapes are associated to statistical models that can represent them. At high capillary number, viscous forces are dominant and govern the flow: the front is unstable for $M < 1$ and can be represented by a Diffusion-Limited Aggregation (DLA) model, but is stable for $M > 1$ (anti-DLA model). When the capillary number is decreased, viscous forces become negligible and it becomes possible to identify a capillary-fingering regime, corresponding well to the Invasion-Percolation model.

flow is governed by the viscous forces and the pressure gradient in the displaced fluid is negligible, leading to a stable displacement.

According to Peters & Flock [186], when considering a porous medium where the endpoint permeabilities[8] are approximately equal to the absolute permeability, the dimensionless numbers

$$I_{sc} = \frac{(\mu_{\mathrm{oil}} - \mu_{\mathrm{water}})UD^2}{C^\star \sigma k}$$

[8]permeability to oil at connate water saturation, and permeability to water at residual oil saturation

for cylindrical geometry (D is the core diameter, U the velocity of the interface and $C^\star$ is a wettability constant such that $C = 2\pi\sqrt{3C^\star}$ is Chuoke's constant [176]) and

$$I_{sr} = \frac{(\mu_{\text{oil}} - \mu_{\text{water}})UL_x^2L_y^2}{C^\star\sigma k(L_x^2 + L_y^2)}$$

for rectangular geometry (L_x and L_y are the thickness and width of the domain respectively) characterise the onset of instability. For $I_{sc} < 13.56$ (or $I_{sr} < \pi^2$) the displacement is stable, whereas it is unstable for higher values of the dimensionless numbers.

A critical velocity of the interface has also been derived in references [187, 188, 189].

- viscous fingering [190]: the boundary is characterised by the presence of several fingers that gain ground in the network. Then one specific finger grows faster than the others and inhibit their development. These fingers are all oriented towards the exit of the network without the formation of any loop (Figure 1.21(b)). This regime occurs for high capillary numbers and low viscosity ratios ($M < 1$): the flow is therefore still governed by the viscous forces, but the pressure gradient is negligible in the injected fluid, generating an instable displacement (Saffman-Taylor instability).

- capillary fingering: the boundary is characterised by the development of one or more fingerings, that can form loops and be oriented in the tranverse direction of the flow (right part of Figures 1.21(a) and 1.21(b)). This situation occurs at low capillary number: the viscous forces are negligible in both fluids. The shape of the front is a result of the random distribution of throat sizes, as the fluid flows from pore to pore through the least resisting pathway.

As the non-wetting fluid can move only in the bulk of the throats, it can flow only if there exists a connected path of pores from one end to the other of the network. After percolation, at the exit of the network, the injected fluid thus defines a preferential pathway and cannot explore other parts of the network. It also traps clusters of wetting fluid.

Besides, it is possible to represent those three regimes by the statistical models indicated in the phase diagrams, which allow to obtain by numerical simulation similar fronts to those obtained by experiments [183, 191].

The capillary fingering regime corresponds to the invasion-percolation model [192, 193]. For a given pressure in the non-wetting fluid, the fluid can only penetrate the so-called active throats, whose size is higher than a critical value r_0. Given the pore size distribution, it is then possible to determine the proportion of active throats: the fluid invades all active throats connected to the entry face. It is realised in simulations by attributing a fixed probability to each throat depending on its size: at each step, the fluid will enter the throat with maximum probability and so on till it reaches the exit of the network. For more on invasion-percolation model, see Appendix A.

In the case of displacements dominated by viscosity (stable or unstable), the pressure gradient between the entry and the exit of the network governs the flow. Thus, a local model based on the displacement of the meniscus at the microscopic scale (*i.e.* similar to the invasion-percolation model, to some extent) cannot be realistic. It is usual to use a continuous model to calculate the pressure field, and to couple it to a discrete displacement of the meniscus allowing to take into account the granular structure of the porous medium. Two specific models are of special interest: the Diffusion-Limited Aggregation model (DLA) [194, 195] for the case $M \to 0$ to describe the unstable viscous regime, and the anti-DLA model [196, 197] for the case $M \to +\infty$ to describe the stable viscous regime.

- The DLA model can be illustrated by the following principle: one begins with a particle or a line in a network and launches another particle from a distant point of the network. This particle can move randomly and stops when it meets the first particle/line. Several particles are launched as presented above: the diffusion processes that govern the path followed by the particles produce a ramified cluster. For more on DLA model, see Appendix B. Viscous fingering in Hele-Shaw flow is also very similar to both DLA and viscosity-dominated displacements in porous media (section 1.2.4.3 and Figure 1.23): the "bubble" of



Figure 1.23: Fingering pattern realised in a Hele-Shaw cell (cluster diameter 200 mm). [198]

inviscid fluid plays the role of the DLA cluster in section B.2, ϕ is the pressure[9], and the Laplace equation is the direct result of incompressibility and Darcy's law [196].

This resemblance is more than a mere coincidence. Indeed, the measured fractal dimension (see Appendix C) of patterns like the one in Figure 1.23 is close to 1.71, as for DLA. On this basis there are several claims in the literature that the large-scale structure of the patterns is identical [196, 199, 200]. Many authors have disagreed and given ingenious arguments about how to verify this. For example, some have claimed that viscous patterns become two-dimensional at large scales [201] or that viscous fingering patterns are most like Dielectric Breakdown Model (DBM, see Appendix B) patterns with $\eta \approx 1.2$ [202]. Most recently a measurement of the growth probability of a large viscous fingering pattern was found to agree with that of DLA [203]. On this basis, the authors claim that DLA and viscous fingering are in the same universality class.

- The anti-DLA model can be thus illustrated: a particle (representing the injected fluid) is launched in the vicinity of a compact aggregate (displaced fluid). This particle moves randomly and eventually reaches a site occupied by the aggregate. One then removes both the particle and the site and launches the next particle, and so on.

[9] Obviously, simulating DLA does not require the calculation of the pressure field.

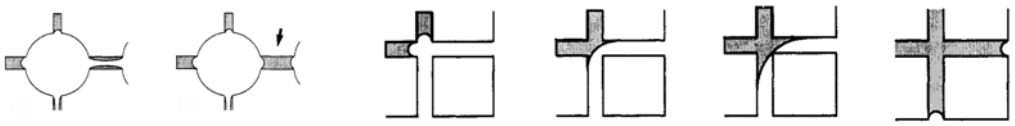

(a) (b)

Figure 1.24: Identification of two types of pores: (a) large pores which promote the filling of the throats and the trapping of non-wetting fluid in the pores, (b) small pores which promote the filling of the pores and consequently of the adjacent throats. [181]

1.3.3 Phase diagram in the imbibition case

In the case of imbibition, the injected fluid is a wetting one and can move in three different modes: in the bulk of the throats, at the walls of the throats through corner films, or in the case of really low capillary numbers (*i.e.* $\log_{10} \mathrm{Ca} \leqslant -7$) along the roughness of the walls of the system. Furthermore, the meniscus can move in four different ways (see section 1.3.1): the selection of a specific mode depends on the geometry of the network (in particular the aspect ratio of pore size versus throat size) and the possibility of creating films alongside the walls [184, 204].

The porous medium is modelised as a network of throats with several different and randomly distributed sizes. For each size, it is possible to determine the threshold pressure associated to the four different displacement modes of the meniscus: P_P, P_{I_1}, P_{I_2} and P_S [182, 184]. During imbibition, as the pressure difference between wetting and non-wetting fluids decreases, the dominating process in a throat is the one with the highest threshold pressure. However, due to the diverse throat sizes, the four development modes can co-exist in the network. The front shape at network scale will depend on the order followed by these modes.

Two extreme cases can receive further attention:

- $P_S > P_{I_1}, P_{I_2}$ for each throat size: this is the large-pore configuration presented in Figure 1.24(a). The invasion of the network is realised by filling the throats and trapping non-wetting fluid in the pores.

- $P_S < P_{I_1}, P_{I_2}$ for each throat size: this is the small-pore configuration presented in Figure 1.24(b). The network is invaded by filling the pores.

For these two cases, two phase diagrams are realised with similar structure but different regimes (Figure 1.25) [181, 184]. In both cases, the diagram is divided in

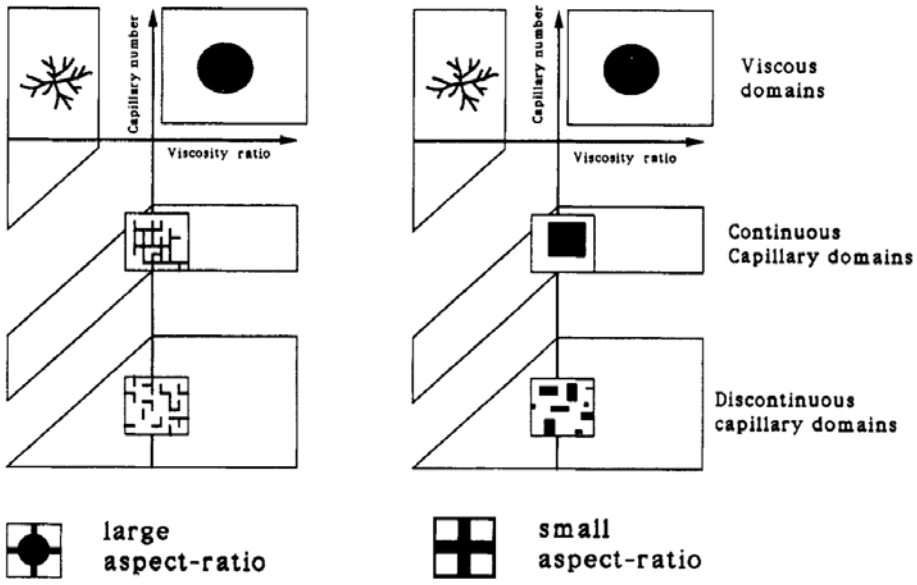

Figure 1.25: Phase diagrams in the case of imbibition [181]. The different regimes depend on the pore geometry, but the diagram structure is similar in both cases. The diagrams are divided in three domains corresponding to three different ranges of capillary number associated to the circulation areas of the wetting fluid in the system: bulk of the throats (viscous domains identical to the case of drainage, see Figure 1.22), corner films (continuous capillary domains), surface roughness (discontinuous capillary domains).

three different domains associated with the type of flow of the wetting fluid in the throats:

- a high-capillary-number domain ($\log_{10} \mathrm{Ca} > -4$) *i.e.* with viscous-force-dominated flow: the fluid flows in the bulk of the throats and one can distinguish the same stable and unstable domains as in the case of drainage.

- a continuous capillary domain, with moderate capillary numbers ($-6 \leqslant \log_{10} \mathrm{Ca} \leqslant -4$) associated with a flow of the wetting fluid via corner films.
- a discontinuous capillary domain, with really low capillary numbers ($\log_{10} \mathrm{Ca} \leqslant -7$), associated with a flow of the wetting fluid alongside the wall roughness.

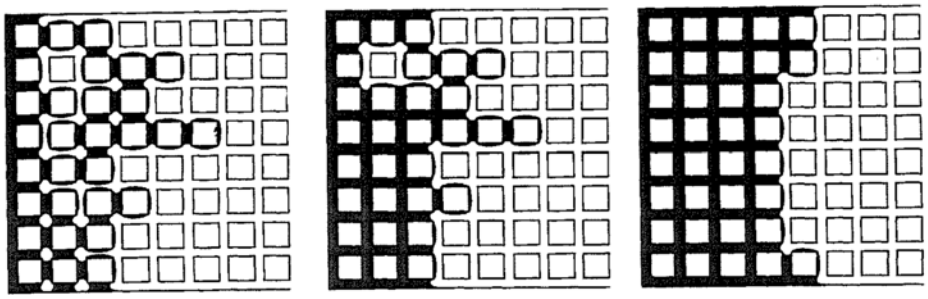

(a) Flow along the corners (from left to right: large, medium-sized and small pores)

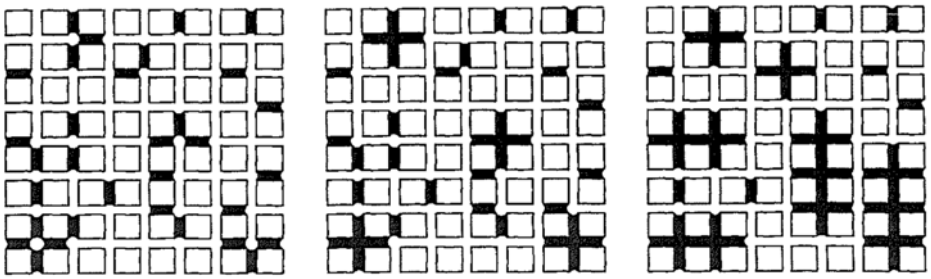

(b) Flow along the surface roughness (from left to right: large, medium-sized and small pores)

Figure 1.26: Description of the patterns obtained by statistical models [184], for different pore geometries: small, medium-sized and large. (a) Result of simulations of a wetting fluid flowing along the corners. (b) Result of simulations of a wetting fluid flowing along the surface roughness.

When the wetting fluid flows in corner films in the large-pore configuration, the pressure decreases in the pores and the throats while the corners are being filled. When the threshold pressure P_S is reached, the smallest throat connected to the entry face of the network will be filled resulting in a sudden pressure increase. The fluid will thus progress in the network by jumps, filling the smallest throats first and trapping

	Large pores	*Medium size pores*	*Small pores*
Roughness	Bond percolation	Bond percolation + correlations	Nucleation cluster growth
Corners	Invasion percolation dual network	Invasion percolation + correlations	Frontal drive
Bulk of the ducts	Frontal drive	Frontal drive	Frontal drive

Table 1.1: Table summarising the different shapes at network scale, for the three types of pore geometries and the three types of flow circulation. [184]

non-wetting fluid in the pores (left of Figure 1.26(a)). In the small-pore configuration, the meniscus mainly moves with modes I_1 and I_2, filling at first the pores, and then the adjacent throats. The network is filled line by line as a uniform front (right of Figure 1.26(a)).

When the wetting fluid flows alongside the surface roughness, the filling mode is identical to above, but can be initiated in throats that are not connected to the entry face of the network. In the case of large pores, the first filled throat can be any throat of the network, and the number of filled throats increases with time. Links of the network that was previously entirely filled with non-wetting fluid are thus erased, until the network seems discontinuous (left of Figure 1.26(b)). In the case of small pores, the filling of the network begins in snap-off mode, but when two adjacent throats are filled, displacement I_2 occurs to fill the two remaining adjacent throats, and thus cluster grows in the network. As the initial filling can occur in several places of the network, on can identify the formation of several disconnected clusters (right of Figure 1.26(b)).

The different shapes at network scale, for the three types of pore geometries and the three types of flow circulation are summarised in Table 1.1.

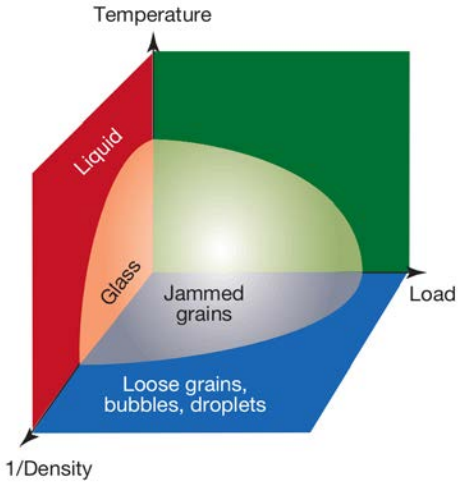

Figure 1.27: The jamming phase diagram proposed by Liu and Nagel. [205]

1.3.4 Deformable media

In a deformable medium such as a granular bed, fluid flow can displace the particles and thus affect the pore geometry, which in turn can affect the flow.

Indeed, in Liu and Nagel's generalised description of jamming (Figure 1.27), an arrested assembly of grains can be fluidised either through dilation or by increasing the applied stress [205, 206, 207]. The origin of jamming is closely linked to the presence of force chains within the packing [208, 209], and the unjamming, or yielding, occurs when grain–grain contacts become mobilised, leading to destabilisation and buckling of the load carrying force chains [210].

Due to the interplay between the displacements of the fluids and the particles, a wide variety of patterns may be observed in deformable media, including desiccation cracks [211], granular fingers [212], labyrinth structures [213], stick-slip bubbles [214], open channels [215, 216] and fractures [214, 217, 218, 219, 220, 221].

1.3.4.1 Labyrinthine structures

A pattern formation process was demonstrated and characterised by Sandnes *et al.* [213], where labyrinthine structures emerge during slow drainage of a fluid-grain mixture confined in a Hele-Shaw cell (Figure 1.28). The final cluster of compacted granular material is simply-connected, random, with a characteristic wavelength. Both

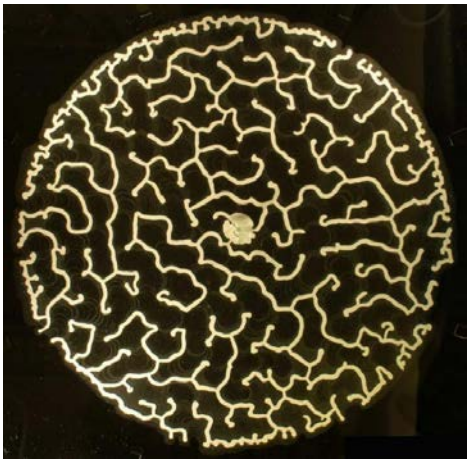

Figure 1.28: Branching structure of close-packed grains obtained by injecting air in an initially circular granular-fluid system. The Hele-Shaw cell plate spacing was 0.4 mm and the volume fraction of grains 20%. [213]

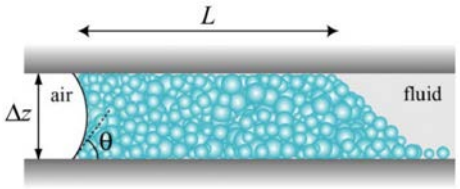

Figure 1.29: Layer of compacted grains of width L ahead of the interface. [213]

experiments and simulations revealed that the interface instability results from a compromise between capillary forces and granular friction. These labyrinthine structures were highlighted by draining an initially grain-and-fluid-filled circular Hele-Shaw cell from the centre.

When one gradually removes the fluid from the cell, the fluid-air interface at the perimeter of the circular disc eventually begins to recede. Due to the capillary forces between the wetting fluid and the grains, a growing layer of close-packed grains is gradually compiled ahead of the interface as it moves (see Figure 1.29). After a transient period where a layer of grains is formed all along the circular perimeter, the interface starts to destabilise and fingers of air slowly invade the fluid-grain disc. One may then observe both the gradual advance and splitting of fingers resulting in the final labyrinthine pattern. Unlike pinning-dominated drying processes [222, 223], the

finger-splitting results from a jamming of the interface on a length scale larger than the individual grains. The invading fingers move and reorganise the initially uniformly distributed grains into a branching structure of close-packed particles. Each branch is obtained from the compact layer of grains pushed ahead by two adjoining fingers.

The final labyrinth pattern is characterised by a uniform wavelength throughout the area occupied by the structure. The pattern forming process results from local mass transport in a direction normal to the advancing interface. The shape of the initially circular interface is continuously modified, but as the interface is both stabilised and kept separate from other fingers thanks to frictional jamming, no pinch-off of the interface can occur during the experiment, and the interface remains a deformed circle. Consequently both the fingers and grain cluster are topologically simply connected.

The apparent randomness seen in the final pattern comes from the symmetry-breaking associated with fingers going either left or right. Disorder is always present in the experiments in form of, *e.g.*, small inhomogeneities in mass distribution, governing the dynamics of the pattern formation, in addition to the history of the moving interface.

Changing the initial volume fraction of grains[10] φ in the experiment influences the process, with notable effects. Indeed the characteristic wavelength λ in the pattern decreases significantly as the volume fraction of grains increases. Sandnes *et al.* demonstrated that

$$\lambda = \frac{2L}{\varphi} \tag{1.69}$$

where L is the width of the compact layer of grains along the straight interface segments [213].

1.3.4.2 Stick-slip bubbles

Similar experiments were later realised by Sandnes *et al.* [214] in linear Hele-Shaw cells rather than circular ones. Though labyrinthine patterns were indeed observed for low volume fraction of grains, they obtained significantly different results for increasing volume fractions.

[10] normalised such that $\varphi = 1$ for the close-packed grains



Figure 1.30: Stick-slip bubbles. [214]

When increasing φ above a threshold value, a drastic dynamics change occurs, with the emergence of a different morphology (Figure 1.30). The advancement of the interface is no longer slow and creeping, instead its motion becomes highly intermittent. The front stays stationary for an extended period, followed by a sudden displacement of the granular-fluid mixture generated by a burst of air in the shape of a bubble. The displacement thus progresses bubble by bubble in a stick-slip manner.

During the static periods, the gas pressure increases linearly due to the compression of the air by the constant, slow driving of the piston. The gas pressure is balanced by the frictional stress from the jammed granular front. As the pressure increases, the weakest point along the front eventually yields, and the pressurised air invades rapidly through a narrow neck before expanding radially. The air decompresses, thus stopping the expansion. The granular material accumulated by the interface settles and gradually compacts into a jammed front where once again the weakest point determines the location and yield pressure for the next bubble (and therefore its size).

1.3.4.3 Fracturing of deformable media

A model was developed by Holtzman and Juanes [224], that predicts the transitions among capillary fingering, viscous fingering and fracturing in gas invasion of liquid-filled deformable granular media. The authors used pore-scale simulations and scaling analysis to demonstrate that fracturing caused by elastic deformation of particles is the dominant mode of invasion for fine, soft particles under low confining stress. In the

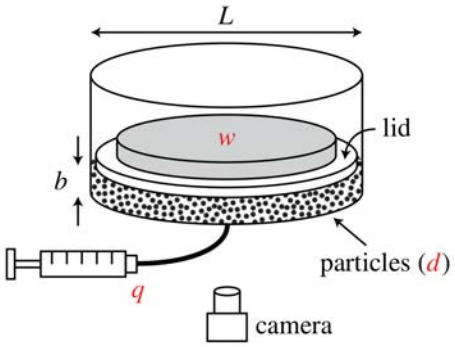

Figure 1.31: Experimental setup: a thin bed (thickness b) of water-saturated glass beads (mean diameter d) is confined in a cylindrical acrylic cell (internal diameter L). Vertical confinement is supplied by a weight, w, placed on a disk ("lid") that rests on top of the beads. The disk is slightly smaller than the cell to allow fluids (but not particles) to leave the cell. Air is injected into the center of the cell at a fixed flow rate q. [225]

case of rigid particles, Holtzman, Szulczewski and Juanes [225] showed that the key mechanism controlling fracturing is frictional sliding, rather than elastic deformation. They provided experimental evidence (quasi-2D experiments with several layers of beads, see Figure 1.31)) for three displacement regimes — capillary fingering, viscous fingering, and capillary fracturing (see Figure 1.32) — and derived two dimensionless groups that govern the transitions among these regimes.

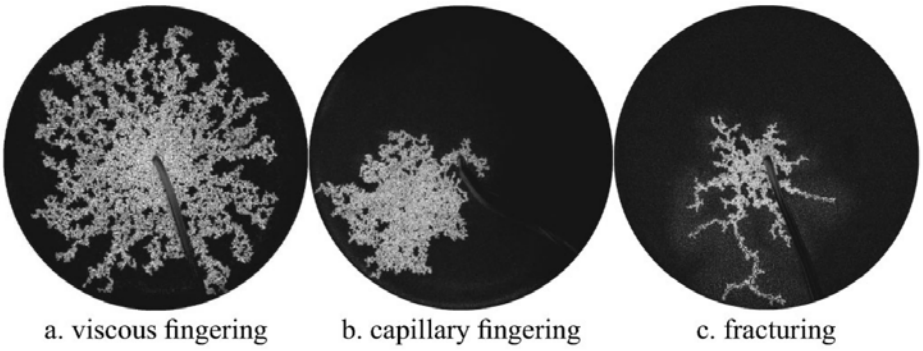

Figure 1.32: Experimental patterns of viscous fingering, capillary fingering and fracturing. [225]

They identified the regimes based on the qualitative characteristics of the invasion pattern [183, 196, 217, 224, 226]:

- in viscous fingering, the interface growth is continuous and occurs simultaneously at several locations (see section 1.3.2). The resulting pattern is radial and exhibits thin fingers and few trapped higher-viscosity clusters.
- in capillary fingering, the interface propagates intermittently (see section 1.3.2). Since the air invasion is controlled by the spatial distribution of capillary entry pressures, which in turn is controlled by the distribution of pore throat sizes, the patterns are typically not radially symmetric [191, 227].
- in capillary fracturing, the interface advances continuously in thin fingers with long, straight segments. The resulting pattern is asymmetric and occupies a much smaller portion of the domain compared with capillary fingering and viscous fingering.

The three regimes display transition zones, in which the invasion patterns exhibit mixed characteristics of the end-member patterns.

Their classification of the displacement pattern is based on visual appearance as well as the fractal dimension D_F (using box-counting [228]). As the estimation of the fractal dimension from the mass *vs* distance curves is subject to large fluctuations for finite-size systems [195, 229, 230, 231], visual appearance is an essential consideration in the classification.

The mode of displacement depends on the competition between forces. The transition between capillary fingering and viscous fingering depends on the competition between viscous forces and capillary forces (section 1.3.2 and Figure 1.33) [232, 233], whereas the transition between fingering and fracturing depends on the competition between hydrodynamic forces that promote pore opening, and mechanical forces that resist it. As these forces depend on a combination of the control parameters, the same transition between the regimes can be achieved by changing different parameters: the displacement can transition from capillary fingering to viscous fingering either by increasing the injection rate q or reducing the bead size d; and from fingering to fracturing either by reducing the confining weight w, or the bead size d (see Figure 1.34).

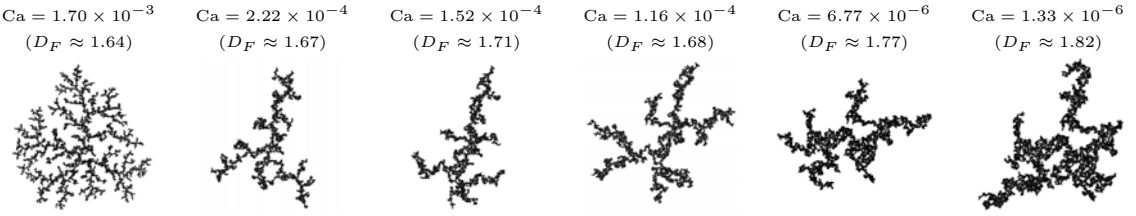

Figure 1.33: Fractal dimension and displacement pattern for rigid medium (pore-scale disorder $\lambda = 0.1$) showing a transition from viscous fingering to capillary fingering as the capillary number is reduced. [224]

The wide transition zone between capillary and viscous fingering has been observed by Lenormand *et al.* (see above) [183], and results from gradual changes in the governing forces with the experimental conditions. The capillary fracturing patterns transition from few, small fractures to many, large fractures as the confinement is reduced [225].

From the analysis of their results, Holtzman, Szulczewski and Juanes defined two different parameters:

- a modified capillary number

$$\mathrm{Ca}^* \equiv \mathrm{Ca}\frac{L}{d}\chi^{-1}(\lambda) = \frac{\mu q L}{\sigma b d^2}\chi^{-1}(\lambda), \tag{1.70}$$

  where $\chi(\lambda)$ describes the distribution of capillary entry pressures[11], a function of the degree of pore-scale disorder $\lambda \in [0, 1]$ [226]. According to this scaling and assuming similar disorder across experiments, the phase boundary between viscous fingering and capillary fingering is $q/b \sim d^2$, in agreement with their experimental data.

- a fracturing number

$$N_f \equiv \frac{\sigma L^2}{\mu w d}(1 + \mathrm{Ca}). \tag{1.71}$$

  For this scaling one can suppose that, for a given fluid pair, particle material, and system size, the transition from fingering to fracturing occurs at $w \sim d^{-1}$.

[11] For instance, for a uniform aperture distribution, $r \in [(1-\lambda)\bar{r}, (1+\lambda)\bar{r}]$, one gets $\chi(\lambda) = \lambda/(1-\lambda^2)$ [224].

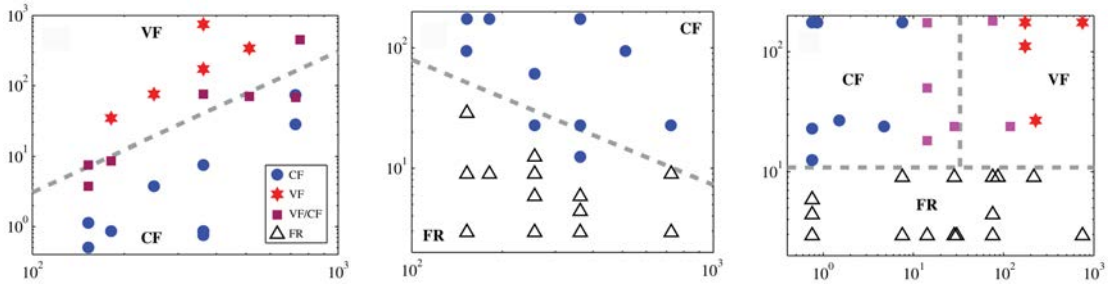

(a) (b) (c)

Figure 1.34: Phase diagrams of fluid-fluid displacement patterns in the experiments. The diagrams demonstrate how changing the control parameters affects the patterns. Diagram (a) (abscissa: d (μm); ordinate: q/b (cm^2/min)) shows that the transition from viscous fingering (VF) to capillary fingering (CF) occurs at $q/b \sim d^2$ (fixing $w = 181$ N). Intermediate patterns are marked as VF/CF. Diagram (b) (abscissa: d (μm); ordinate: w (N)) shows that the transition from capillary fingering to fracturing (FR) occurs at $w \sim d^{-1}$ ($q = 0.1$ mL/min). Diagram (c) (abscissa: q/b (cm^2/min); ordinate: w (N)) shows that the transition from fingering to fracturing is independent of q/b ($d = 360$ μm). [225]

The scaling analyses allowed them to collapse their data from a three-parameter dimensional phase space (q, w, d) into a two-parameter dimensionless space (Ca^*, N_f). For $N_f \gg 1$, the dominant mode of invasion is fracturing. For $N_f \ll 1$, the medium is essentially rigid (negligible particle rearrangements), and the transition from capillary to viscous fingering occurs at $\mathrm{Ca}^* \approx 1$ (see Figure 1.35) [225].

It should be noted that another fracturing number was defined by Holtzman and Juanes in a previous paper, with similar results [224],

$$N_f' \equiv \frac{2\sigma}{\lambda d E \epsilon_0^{1/2}}, \tag{1.72}$$

where ϵ_0 is the strain generated by the compression, and E the Young modulus of the particle material. The fracturing pattern is distinguished from viscous fingering by fingers with straight segments and a lower fractal dimension (see Figure 1.36).

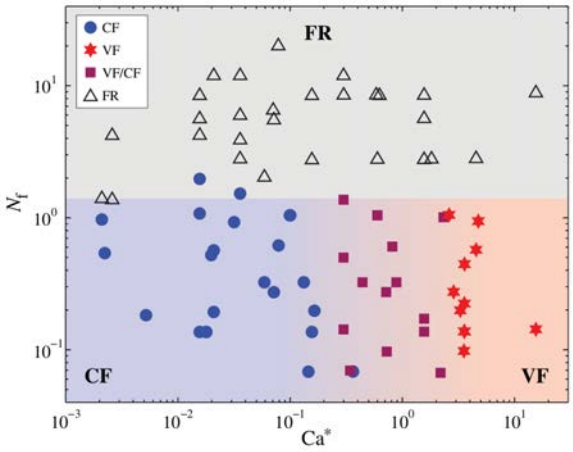

Figure 1.35: Phase diagram of drainage in granular media, showing three invasion regimes: viscous fingering (VF), capillary fingering (CF), and fracturing (FR). The tendency to fracture is characterized by the "fracturing number" N_f : drainage is dominated by fracturing in systems with $N_f \gg 1$. At lower N_f values, the type of fingering depends on the modified capillary number, Ca*. [225]

1.3.4.4 Phase diagramm

To elucidate the relationship between the frictional fluid morphologies and displacement patterns observed in porous media, Sandnes *et al.* [214] combined their findings with recent results from other authors [217, 224, 230] and drew a tentative $\varphi^{-1} - q$ phase diagram (q is the injection rate), including fracturing, and capillary and viscous fingering in porous media where $\varphi \approx 1$ (Figure 1.37). The demarcation lines are for illustration purposes, and the location of the phase boundaries may depend

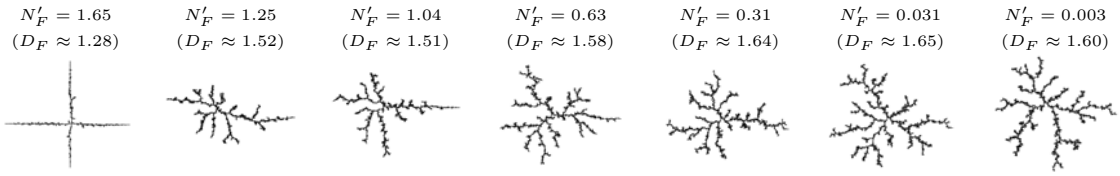

Figure 1.36: Fractal dimension and displacement pattern for deformable medium, with a value of Ca* ≈ 10, showing a transition from fracturing to fingering as the fracturing number is reduced. [224]

on numerous system specific factors. The rate-dependent transition between capillary and viscous fingering is well documented [191, 230, 234], and following Holtzman and Juanes [224] they depicted the fracturing phase as rate independent. Their results suggested that the transition between frictional dynamics and fluidized front [214] is largely φ independent, whereas the boundary between fluidized front and viscous fingers is drawn slanted as the re-suspension process depends on the shear rate of the flow across the layer of settled material, and this shear rate increases with increasing φ as the free gap narrows.

1.4 Conclusion

A porous medium can be considered in two different ways. Either each phase is considered separately (pore-scale modelling), or one considers the fluid displacements by averaging them on volumes whose size is bigger than the pore one, but small compared to that of the overall domain (Darcy-scale modelling).

Four main approaches are then used to study flows in porous media: a continuous approach in which the porous medium is caracterised by macroscopic parameters (*e.g.* Darcy's law), the capillary bundle model, an approach based on numerical methods to describe the porous medium at the pore scale and solve the flow equations at this scale, and an approach by Pore-scale Network Modelling.

It is also possible to consider these flows in a simpler geometry, the Hele-Shaw cell, where the equation govering the flow is analogous to Darcy's law. One can then easily consider the surface tension either by slightly modifying the Darcy equation (Hele-Shaw cells) or by considering a modified pressure field (porous media).

Roland Lenormand studied Newtonian two-phase flows in networks with both an organic and an aqueous phase, and established phase diagrams in the case of both drainage and imbibition.

In both cases, three different domains were identified in the (M, Ca) plan: a domain where the flow is dominated by viscous fingering ($M < 1$ and high Ca), a domain of stable viscous displacement ($M > 1$ and high Ca) and a domain dominated by capillary fingering (low Ca).

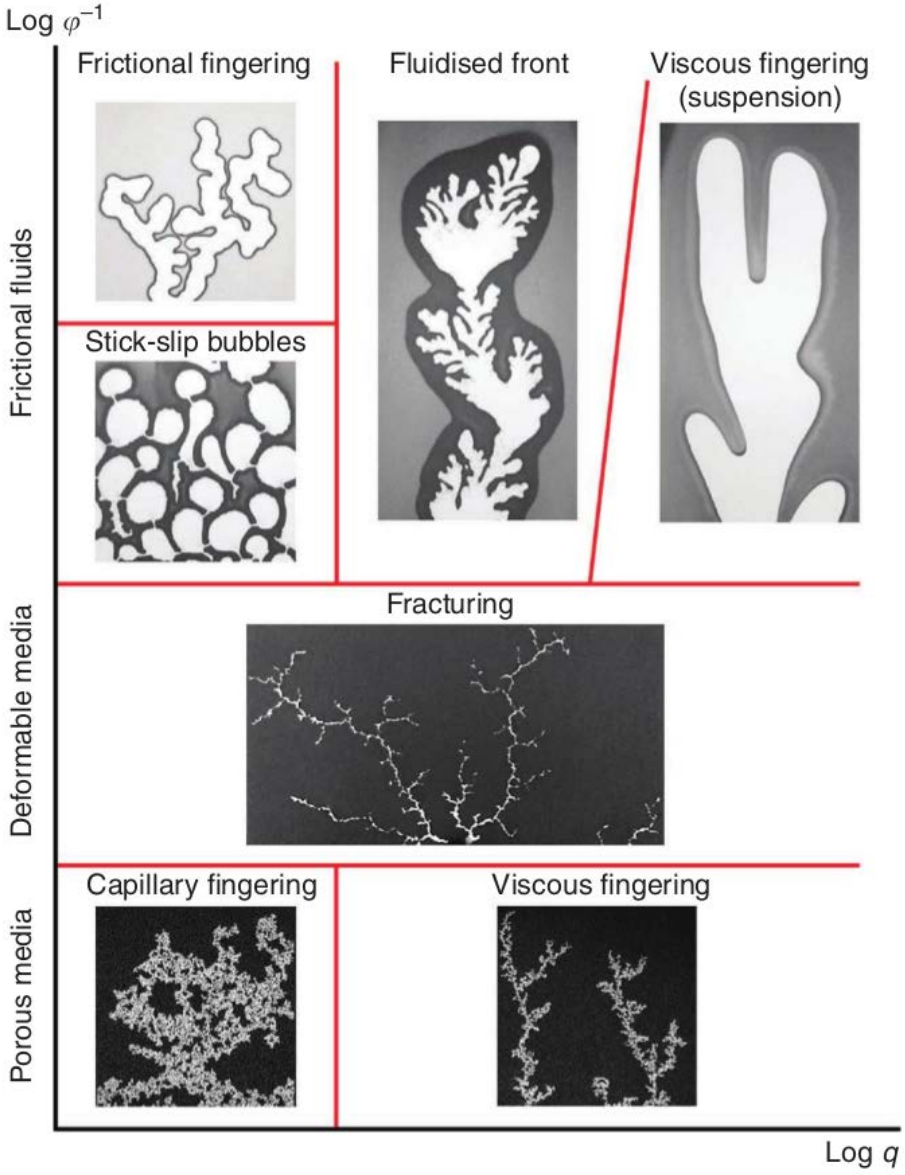

Figure 1.37: Tentative phase diagram of morphologies in the $\varphi^{-1} - q$ plane extended to the $\varphi = 1$ limit corresponding to a close-packed porous medium. Various displacement morphologies in the frictional fluid give way to fracturing at $\varphi > 0.9$, followed by a transition to capillary/viscous fingering in porous media ($\varphi \approx 1$). [214]

In the case of imbibition, the domain dominated by capillary fingering can be subdivided in two subdomains: a continuous one with corner-film flows, and a discontinuous one where the wetting fluid flows alongside the wall roughness.

Finally, in deformable media, such as granular media, the flow of a fluid can move the solid particles and thus modify the pore geometry, which in turn can affect the flow. Due to this interaction between fluid and particles, a great variety of patterns can be observed, including desiccation cracks, granular fingers, labyrinth structures, stick-slip bubbles, open channels and fractures. All these patterns were summarised by Sandnes *et al.* in a tentative phase diagram.

As flows in porous media often result in fingering patterns, due either to viscous or to capillary effects, the use of a software allowing mesh adaptive refinement is in order to efficiently study such flows from a numerical point of view, hence the use the multiphase flow solver Gerris in the following chapters.

CHAPTER 2

Gerris, a Direct Numerical Simulation code

Numerical fluid mechanics consists of studying the motion of a fluid, or its effects, by solving numerically the equations governing the flow (Chapter 1). It has become an essential tool in many branches of fluid dynamics and allows the access to all the instantaneous characteristics of the fluid (velocity, pressure, concentration) for each computational point, for a usually reasonable cost compared to the corresponding experiments.

More particularly the multiphase (respectively two-phase) flow simulation allows to numerically study what happens when several (respectively two) fluids flow together: it can be a single fluid in two different phases, several different fluids in the same phase or several different fluids in different phases.

The numerical schemes that allow two-phase flow simulation are still challenging due to the necessity to track in space the interface between the two fluids. Several efficient methods have been proposed recently, but it is still an open field of research. Several schemes can be highlighted:

- the Front-Tracking method (Figure 2.1) uses a set of so-called marker particles situated along the interface. The reconstruction of the interface is realised by

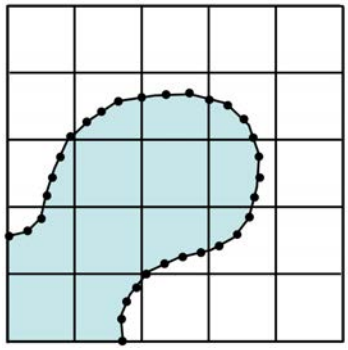

Figure 2.1: When using a Front-Tracking method, the fluid interface is represented by connected marker particles that are advected by the fluid velocity, interpolated from the fixed grid. [235]

connecting the different marker particles by a curve (2D) or a surface (3D) [236, 237, 238, 239].

- the Level-Set method uses a regular level function with value zero on the interface (Figure 1.16(c)) [139, 235, 240, 241, 242]. A generalisation of the method can be found in [243].

- the Boundary-Integral method calculates a Stokes flow solely by reference to what happens at the flow boundaries [244, 245, 246]. Since reference is only made to boundary values, the dimension of the problem is effectively reduced by one.

- the Volume-of-Fluid (VOF) method tracks the interface using the volume fraction of one of the fluids in each cell of the mesh, and builds the interface as a piecewise affine function [247, 248, 249, 250, 251, 252].

In this chapter, the different methods implemented in the multiphase flow solver Gerris will be presented: they will be used in the following chapters. This is an open-source software (The Gerris Flow Solver: http://gfs.sf.net) using both finite-volume numerical methods for solving the Navier-Stokes equation for single- or multiphase incompressible flows (see equation 1.13 in section 1.1.3.2) on an adaptive mesh and the VOF method for interface tracking. This code was developed by Stéphane Popinet

[253, 254] and financed by both the National Institute of Water and Atmospheric research[1] (NIWA) and the Royal Society of New Zealand[2]. Though written in C, Gerris is object-oriented. It allows the simulation of non-stationary incompressible flows of varying density with surface tension.

Contents

2.1 Numerical scheme of the Gerris Flow Solver 98

2.1.1 Temporal discretisation 99

2.1.2 Spatial discretisation 101

2.1.3 Adaptive mesh refinement 103

2.1.4 Volume-of-Fluid advection scheme 105

2.1.5 Balanced-force surface-tension calculation 108

2.1.6 Gerris in parallel 111

2.1.7 Implementation of solid boundaries 111

Another way to deal with solid boundaries. 112

2.2 Gerris Flow Solver for porous geometry 114

2.2.1 Scalability at low porosity 114

2.2.1.1 Definitions 114

2.2.1.2 Characteristics of the tests 115

2.2.1.3 Results on cluster *babbage* 116

2.2.1.4 Results on cluster *Rostand* 119

2.2.2 CPU time and CFL number for two-phase flow invasion of porous geometries 121

2.2.2.1 Wall-clock CPU time in a porous geometry 122

2.2.2.2 CFL number in a porous geometry 124

2.2.3 Single-phase and two-phase Poiseuille flows 126

2.2.3.1 Single-phase Poiseuille flow 127

[1] http://www.niwa.co.nz/

[2] http://www.royalsociety.org.nz/

Horizontal geometry 127
Slanted geometry 128
2.2.3.2 Two-phase Poiseuille flow 131
Horizontal geometry 131
Slanted geometry 134
2.2.4 Permeability of a randomly-generated porous medium . . . 139
2.3 3D simulations of invasion in oil-filled real porous media 144
2.3.1 X-ray microtomography 144
2.3.2 Invasion of porous media in both water-wetting and oil-wetting cases 146
2.3.2.1 Contact angle in Gerris 146
2.3.2.2 Simulation of a single pore 147
2.3.2.3 Invasion of a 3D porous medium with several pores 150
Case with 256^3 voxels 151
Case with 400^3 voxels 153
2.4 Conclusion 156

2.1 Numerical scheme of the Gerris Flow Solver

The numerical scheme of the Gerris Flow Solver was presented in [253, 254]. We recall the main aspects of this scheme in the case of two-phase flows with no claim of comprehensiveness.

2.1.1 Temporal discretisation

Two-phase Navier-Stokes equations for an incompressible flow with surface tension are (equation (1.19))

$$\rho(\partial_t \mathbf{u} + \mathbf{u}\cdot\nabla\mathbf{u}) = -\nabla p + \nabla\cdot(2\mu\mathbf{e}) + \sigma\kappa\delta_s\mathbf{n} + \mathbf{f}_{\text{ext}}, \tag{2.1}$$

$$\partial_t\rho + \nabla\cdot(\rho\mathbf{u}) = 0, \tag{2.2}$$

$$\nabla\cdot\mathbf{u} = 0. \tag{2.3}$$

As a reminder (chapter 1), $\mathbf{e}$ is the strain rate tensor, $\rho \equiv \rho(\mathbf{x},t)$ the density and $\mu \equiv \mu(\mathbf{x},t)$ the viscosity. For the surface tension term, see section 1.1.3.3. The force term $\mathbf{f}_{\text{ext}}$ represents all exterior forces acting on the system.

For two-phase flow, we introduce the volume fraction $c(\mathbf{x},t)$ (equation (1.17)) of the second fluid, and define the density and the viscosity of the system by

$$\begin{aligned}\rho(c) &= (1-c)\rho_1 + c\rho_2,\\ \mu(c) &= (1-c)\mu_1 + c\mu_2,\end{aligned}$$

with ρ_1, ρ_2, μ_1 and μ_2 the densities and viscosities of the first and second fluid respectively.

A time-delayed discretisation of the volume fraction, the density and the pressure, using a timestep Δt, gives a second-order time discretisation of equations (2.1-2.3) for the timestep n

$$\begin{aligned}\rho_{n+\frac{1}{2}}\left[\frac{\mathbf{u}_{n+1}-\mathbf{u}_n}{\Delta t} + \mathbf{u}_{n+\frac{1}{2}}\cdot\nabla\mathbf{u}_{n+\frac{1}{2}}\right] &= -\nabla p_{n+\frac{1}{2}} + \nabla\cdot\left[\mu_{n+\frac{1}{2}}(\mathbf{e}_n + \mathbf{e}_{n+1})\right]\\ &\quad + (\sigma\kappa\delta_s\mathbf{n})_{n+\frac{1}{2}} + \mathbf{f}_{\text{ext}}, \qquad (2.4)\\ \nabla\cdot\mathbf{u}_n &= 0. \qquad (2.5)\end{aligned}$$

This system can be simplified by using Helmholtz-Hodge decomposition [255] for the velocity

$$\mathbf{u}_\star = \mathbf{u}_{n+1} + \frac{\Delta t}{\rho_{n+\frac{1}{2}}}\nabla p_{n+\frac{1}{2}}, \tag{2.6}$$

with

$$\nabla\cdot\mathbf{u}_{n+1} = 0. \tag{2.7}$$

Thus the equation system (2.4-2.5) becomes [256, 257]

$$\rho_{n+\frac{1}{2}}\left[\frac{\mathbf{u}_\star-\mathbf{u}_n}{\Delta t}+\mathbf{u}_{n+\frac{1}{2}}\cdot\nabla\mathbf{u}_{n+\frac{1}{2}}\right] = \nabla\cdot\left[\mu_{n+\frac{1}{2}}(\mathbf{e}_n+\mathbf{e}_\star)\right] + (\sigma\kappa\delta_s\mathbf{n})_{n+\frac{1}{2}}+\mathbf{f}_{\text{ext}}, \tag{2.8}$$

$$\mathbf{u}_{n+1} = \mathbf{u}_\star-\frac{\Delta t}{\rho_{n+\frac{1}{2}}}\nabla p_{n+\frac{1}{2}}, \tag{2.9}$$

$$\nabla\cdot\mathbf{u}_{n+1} = 0, \tag{2.10}$$

inducing the Poisson equation

$$\nabla\cdot\left(\frac{\Delta t}{\rho_{n+\frac{1}{2}}}\nabla p_{n+\frac{1}{2}}\right)=\nabla\cdot\mathbf{u}_\star. \tag{2.11}$$

The discretised equation of motion (2.8) can be reorganised as

$$\frac{\rho_{n+\frac{1}{2}}}{\Delta t}\mathbf{u}_\star-\nabla\cdot\left[\mu_{n+\frac{1}{2}}\mathbf{e}_\star\right] = \nabla\cdot\left[\mu_{n+\frac{1}{2}}\mathbf{e}_n\right]+\rho_{n+\frac{1}{2}}\left[\frac{\mathbf{u}_n}{\Delta t}-\mathbf{u}_{n+\frac{1}{2}}\cdot\nabla\mathbf{u}_{n+\frac{1}{2}}\right] + (\sigma\kappa\delta_s\mathbf{n})_{n+\frac{1}{2}}+\mathbf{f}_{\text{ext}} \tag{2.12}$$

where the right-hand side member only depends on values at time n and $n+\frac{1}{2}$. The advection term $\mathbf{u}_{n+\frac{1}{2}}\cdot\nabla\mathbf{u}_{n+\frac{1}{2}}$ is estimated using the Bell–Colella–Glaz second-order unsplit upwind scheme [258]. This scheme is stable for CFL numbers[3] [259] smaller than one. This Helmholtz-type equation can be solved efficiently by using a multiscale Poisson solver with a quad-/octree meshing. The Crank-Nicholson resulting discretisation of the viscous term [260] is formally second-order and unconditionnally stable. However, it is only applicable to scalar fields and cannot be used directly to solve equation (2.12) to obtain the vector field $\mathbf{u}_\star$. A work-around is to decouple the equations for each of the components of $\mathbf{u}_\star$ and then use the scalar multilevel algorithm to solve for each component independently. The equations for each component are coupled through the cross-terms $(\nabla\mathbf{u}_\star)^T$ appearing in $\nabla\cdot\left[\mu_{n+\frac{1}{2}}\mathbf{e}_\star\right]$ in equation (2.12). To obtain scalar Helmholtz-like problems for each component we discretize the cross-terms explicitly such that the Laplacian operator in equation (2.12) is approximated as [257]

$$2\nabla\cdot(\mu_{n+\frac{1}{2}}\mathbf{e}_\star)\approx\nabla\cdot(\mu_{n+\frac{1}{2}}\nabla\mathbf{u}_\star)+\nabla\cdot(\mu_{n+\frac{1}{2}}(\nabla\mathbf{u}_n)^T) \tag{2.13}$$

[3]As a reminder the Courant-Friedrichs-Lewy (CFL) number is CFL $=\frac{U\Delta t}{h}$ with h the length interval.

The explicit cross-terms can be further rearranged as we have the tensorial general identity

$$\nabla \cdot (\mu(\nabla \mathbf{u})^T) = (\nabla \mathbf{u})^T \nabla \mu + \mu \nabla \cdot (\nabla \mathbf{u})^T = (\nabla \mathbf{u})^T \nabla \mu + \mu \nabla (\nabla \cdot \mathbf{u}) = (\nabla \mathbf{u})^T \nabla \mu,$$

where we have used the incompressibility condition $\nabla \cdot \mathbf{u} = 0$. The final decoupled scalar equations for each velocity component can then be written in vector form

$$\begin{aligned} \frac{\rho_{n+\frac{1}{2}}}{\Delta t}\mathbf{u}_\star - \frac{1}{2}\nabla \cdot \left(\mu_{n+\frac{1}{2}} \nabla \mathbf{u}_\star\right) &= \nabla \cdot \left(\mu_{n+\frac{1}{2}} \mathbf{e}_n\right) + \rho_{n+\frac{1}{2}} \left(\frac{\mathbf{u}_n}{\Delta t} - \mathbf{u}_{n+\frac{1}{2}} \cdot \nabla \mathbf{u}_{n+\frac{1}{2}}\right) + \mathbf{f}_{\text{ext}} \\ &\quad + (\sigma \kappa \delta_s \mathbf{n})_{n+\frac{1}{2}} + \frac{1}{2}(\nabla \mathbf{u}_n)^T \nabla \mu_{n+\frac{1}{2}}. \end{aligned} \tag{2.14}$$

Note that the explicit viscous term on the right-hand-side vanishes for a constant viscosity. For variable viscosities, it is only dependent on the viscosity gradient. The robustness of the implicit scheme is preserved for large values of viscosities provided the spatial viscosity variations are small enough. This scheme has been validated for numerous problems with variable viscosity such as two-phase flows of Newtonian fluids with different properties [254, 261, 262], as well as generalised Newtonian fluids [263] including yield-stress rheologies [264].

2.1.2 Spatial discretisation

The domain is spatially discretised using square (cubic in 3D) finite volumes organised hierarchically as a quadtree (octree in 3D), a tree-like structure [265]. In the following each finite volume will be referred to as a cell. Each cell can be parent of up to four children (eight in 3D).The level of a cell is defined by starting from zero for the root cell and by adding one every time a group of four descendant children is added. An example of spatial discretisation and the corresponding tree representation is given in Figure 2.2. Each cell has a direct neighbour at the same level in each direction (four in 2D, six in 3D). Each of these neighbours is accessed through a face of the cell. In two-phase flow, we also define mixed cells which are cut by the interface between the two fluids.

In order to simplify the computation, several rules are edicted concerning neighbouring cells:

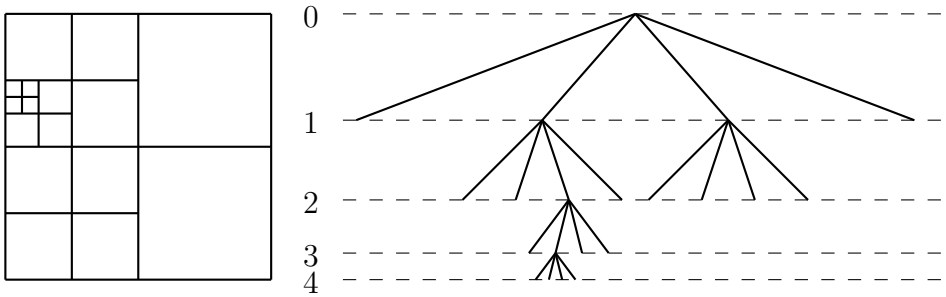

Figure 2.2: Example of quadtree discretisation and corresponding tree representation. [253]

1. the levels of direct neighbouring cells cannot differ by more than one,

2. the levels of diagonally neighbouring cells cannot differ by more than one,

3. all the cells directly neighbouring a mixed cell must be at the same level.

These constraints greatly simplify the gradient and flux calculations.

All variables (components of the momentum, pressure and passive tracers) are located at the centre of each cell. Thus the conservation of the momentum is easier to describe when using an adaptive mesh. What is more, this choice of localisation of all the variables is required to use the Godunov scheme for the momentum advection developed by Bell, Colella & Glaz [258] and simplifies the implementation of the Crank-Nicholson discretisation of the viscous term [260].

A projection method [266, 267, 268, 269] is used for the spatial discretisation of both the modified pressure equation (2.9) and its associated divergence in the Poisson equation (2.11). First, the auxiliary velocity field at the centre of the cells $\mathbf{u}_\star^c$ is computed using equation (2.14). Then a face-centred auxiliary velocity field $\mathbf{u}_\star^f$ is computed on all the faces of the cartesian-discretisation cells by using the average of the cell-centred values. When the face concerns the boundary between two different refinement levels of the octree/quadtree meshing, weights are added in order to ensure the consistence of the corresponding flux volumes.

The divergence of the auxiliary velocity field, appearing in the right-hand side of equation (2.11), is computed in each cell as a finite-volume approximation

$$\nabla \cdot \mathbf{u}_\star = \frac{1}{h} \sum_f \mathbf{u}_\star^f \cdot \mathbf{n}^f, \tag{2.15}$$

where $\mathbf{n}^f$ is the face normal unit vector and h the lengthscale of the control volume (*i.e.* the cell).

After having solved equation (2.11) with the finite-volume approximation (2.15), the pressure correction is added at the face-centred auxiliary field

$$\mathbf{u}_{n+1}^f = \mathbf{u}_\star^f - \frac{\Delta t}{\rho_{n+\frac{1}{2}}^f} \nabla^f p_{n+\frac{1}{2}}, \tag{2.16}$$

where $\rho_{n+\frac{1}{2}}^f$ is obtained as the average of the cell-centred values $\rho_{n+\frac{1}{2}}^c$, and ∇^f is the gradient with respect to the centre of a cell face. The resulting face-centred velocity field is divergence-free by construction.

The cell-centred velocity field at time $n+1$ is obtained by adding the pressure correction at the centre of the cell

$$\mathbf{u}_{n+1}^c = \mathbf{u}_\star^c - \left| \frac{\Delta t}{\rho_{n+\frac{1}{2}}^f} \nabla^f p_{n+\frac{1}{2}} \right|^c, \tag{2.17}$$

where the $|\cdot|^c$ operator denotes averaging over all the faces delimiting the control volume. The resulting cell-centred velocity field $\mathbf{u}_{n+1}^c$ is approximately divergence-free.

2.1.3 Adaptive mesh refinement

A particular aspect of the Gerris Flow Solver is its hierarchical adaptive mesh refinement. This adaptation occurs in two steps. In a first step, all the leaf cells which satisfy a given criterion are refined (as well as their neighbours when necessary, in order to respect the constraints described in section 2.1.2), generating smaller cells (see Figure 2.3). Several refinement criteria can be used simultaneously. For example, it is possible to refine the mesh depending on the gradient of some variable. The

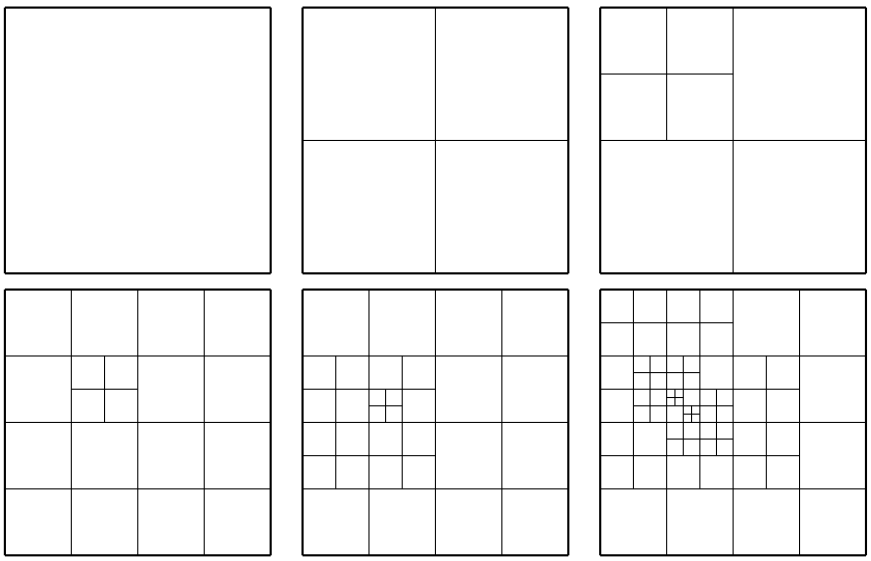

Figure 2.3: Optimised hierarchical adaptation used by Gerris. The adaptation ensures that no neighbouring cells differ by more than one refinement level. [253]

criterion then states that when this gradient exceeds some value in a second-order discretisation the refinement has to be finer.

In a second step, we consider the parent cells of all the leaf cells (*i.e.*, the immediately coarser discretisation). All of these cells which do not satisfy the refinement criterion are coarsened (*i.e.*, become leaf cells). The values of the cell-centred variables for newly created or coarsened cells must be initialised. For newly coarsened cells, it is consistent to compute these values as the volume-weighted average of the values of their (defunct) children, so that quantities such as momentum and vorticity are preserved exactly. For newly created cells, those values are computed by a linear interpolation procedure using the parent cell value and its gradients, which ensures a local conservation of momentum but tends to introduce numerical noise in the vorticity field.

On the new discretisation, there is no guarantee that the velocity field is divergence-free anymore. A projection step is then needed. To avoid the cost of an extra projection step when adapting the grid, the grid refinement is performed at the fractional timestep, using the provisional velocity field $\mathbf{u}_\star$, just before the approximate projection is applied.

2.1.4 Volume-of-Fluid advection scheme

For two-phase flows, the approximation of infinitely-thin interface is used and the position of some point $\mathbf{x}$ of the first fluid with respect to the second one is realised with the Heaviside function $c(\mathbf{x}, t)$ defined as

$$c(\mathbf{x}, t) = \begin{cases} 1 \text{ if } \mathbf{x} \text{ is in fluid 1,} \\ 0 \text{ if } \mathbf{x} \text{ is in fluid 2.} \end{cases} \tag{2.18}$$

Note that the definition differs from that of section 1.1.3.3.

The volume fraction c_γ of a square cell γ of volume V is defined as the average value of the Heaviside function in this cell [270]

$$c_\gamma = \frac{1}{V} \int_V c(\mathbf{x}, t)\, d\mathbf{x}. \tag{2.19}$$

The advection equation (2.2) of density can be replaced by an equivalent advection equation for the volume fraction

$$\partial_t c_\gamma + \nabla \cdot (c_\gamma \mathbf{u}) = 0. \tag{2.20}$$

To solve the advection equation (2.20) of the volume fraction, a piecewise-linear geometrical Volume-Of-Fluid (VOF) scheme [235, 271, 272, 273] generalised for the quad/octree spatial discretisation is used. Geometrical VOF schemes classically proceed in two steps:

1. interface reconstruction,

2. geometrical flux computation and interface advection.

In a piecewise-linear VOF scheme the interface is represented in each cell (Figure 2.4) by a line (resp. plane in three dimensions) described by equation

$$\mathbf{n} \cdot \mathbf{x} = \alpha \tag{2.21}$$

where $\mathbf{n}$ is the local normal to the interface[4] and $\mathbf{x}$ is the position vector. Given $\mathbf{n}$ and the local volume fraction c_γ; α is uniquely determined by ensuring that the Volume-Of-Fluid contained in the cell and lying below the plane is equal to c_γ. This volume

[4]obtained from the gradients of the local volume fraction

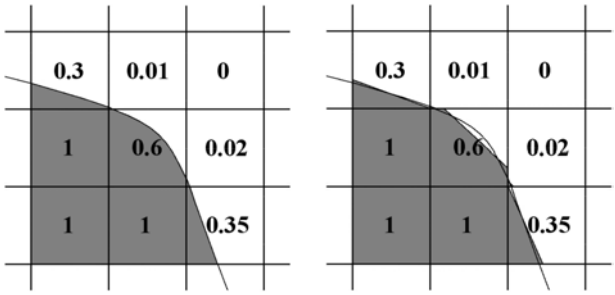

Figure 2.4: Interface cut by a mesh and its associated volume fraction field (left), with its piecewise linear reconstruction (right). [274]

can be computed relatively easily by taking into account the different ways a square (resp. cubic) cell can be cut by a line (resp. plane) which leads to matched linear and quadratic (resp. cubic) functions of α [275, 276]. Then an approximate of the interface normal $\mathbf{n}$ is computed by considering the volume fractions in the neighbouring cells of the considered finite volume. Mixed-Youngs-Centred (MYC) implementation [277] is used on a 3×3 (resp. $3 \times 3 \times 3$) regular Cartesian stencil.

Once the interface reconstruction is done, the direction-split geometrical fluxes have to be computed on Cartesian grids [278, 279] (Figure 2.5). This advection is realised in Gerris with the so-called Piecewise Linear Interface Calculation (PLIC) scheme[5] [271] (see Appendix D), also called the Explicit Lagrangian advection scheme [280]. It is possible to generalise this advection scheme to a quadtree/octree discretisation by slightly modifying the scheme where fluxes occur between cells with different refinement levels (Figure 2.6).

This advection scheme ensures the validity of condition $0 \leqslant c_\gamma \leqslant 1$ at each timestep. It has been proved to give results close to the solution when an analytical one exists [277]. Though this scheme is, strictly-speaking, not conservative [281], the total error for computationally-demanding problems usually is inferior to 0.01%.

[5]or, in French, *Construction d'Interface Affine par Morceaux* (*CIAM*).

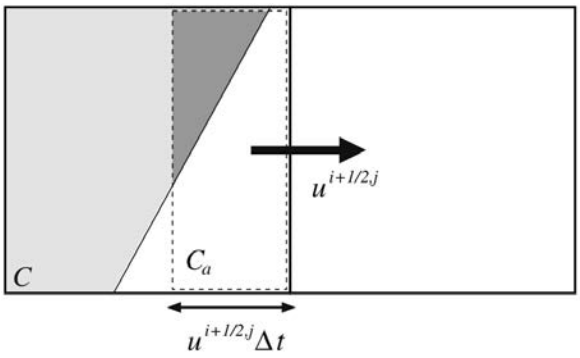

Figure 2.5: Geometrical flux estimation. The total volume of cell C which needs to move to the right at velocity $\mathbf{u}^{i+1/2,j}$ (at face situated between cell i and $i+1$ of row j) is delimited by the dashed line. In the dark grey triangle: the volume fraction of the first phase which will accordingly move to the right. [254]

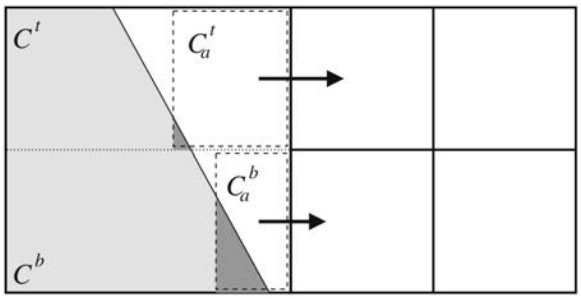

Figure 2.6: Geometrical flux estimation for quadtree discretisation. The coarser cell C is divided in two cells, C^t on top and C^b at the bottom. Thus the displaced volume C_a^t of the top sub-cell is computed independently from that of the bottom sub-cell C_a^b. [254]

2.1.5 Balanced-force surface-tension calculation

The accurate estimation of the surface-tension term $(\sigma\kappa\delta_s\mathbf{n})_{n+\frac{1}{2}}$ in the discretised momentum equation (2.8) has proven to be one of the most difficult aspects of the application of VOF methods to surface-tension-driven flows. The continuum-surface-force (CSF) approach [179] proposes the following approximations

$$\sigma\kappa\delta_S\mathbf{n} \approx \sigma\kappa\nabla^h\tilde{c}, \tag{2.22}$$

$$\kappa \approx \nabla^h \cdot \tilde{n} \tag{2.23}$$

where $\tilde{n} \equiv \frac{\nabla^h\tilde{c}}{|\nabla^h\tilde{c}|}$, ∇^h is a finite-difference operator and $\tilde{c}$ a spatially-filtered volume fraction field. This approach is known to suffer from problematic parasitic currents[6] (known as spurious currents) when applied to the case of a stationary droplet in theoretical equilibrium [282, 283, 284]. More recently it was noted [285, 286] that in this case, since the discretised momentum equation reduces to

$$-\nabla^h p_{n+\frac{1}{2}} + \sigma\kappa(\delta_s\mathbf{n})_{n+\frac{1}{2}} = 0, \tag{2.24}$$

or equivalently using the CSF approximation

$$-\nabla^h p_{n+\frac{1}{2}} + \sigma\kappa(\nabla^h c)_{n+\frac{1}{2}} = 0, \tag{2.25}$$

it is possible to recover exact discrete equilibrium between surface tension and pressure gradient provided:

1. the discrete approximations of both gradient operators in equation (2.25) are compatible,

2. the estimated curvature κ is constant.

In the present collocated scheme, the cell-centred pressure gradient is computed by averaging the face-centred pressure gradients as indicated in equation (2.17). Thus, in order to verify condition 1, the surface tension is determined by first applying the

[6] *i.e.* non-physical velocity fields

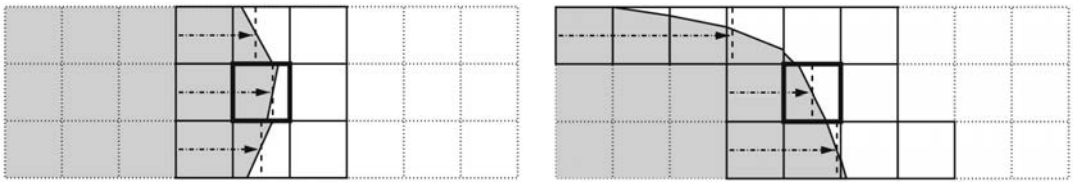

(a) (b)

Figure 2.7: Examples of the grids used to calculate the curvature, indicated by solid lines: (a) a 3×3 symmetric stencil is sufficient to obtain a consistent estimate of the interface height for weakly-curved interfaces aligned with the grid, but (b) bigger stencils can be needed for highly-curved and/or less aligned interfaces. [254]

surface-tension force to the auxiliary face-centred velocity field $\tilde{\mathbf{u}}^f_\star$ and generating a new velocity field

$$\mathbf{u}^f_\star = \tilde{\mathbf{u}}^f_\star + \frac{\Delta t \sigma \kappa^f_{n+\frac{1}{2}}}{\rho\left(c^f_{n+\frac{1}{2}}\right)} \nabla^f c_{n+\frac{1}{2}}. \tag{2.26}$$

Then the surface-tension force is applied at the centre of the cell corresponding to $\mathbf{u}^c_\star$

$$\mathbf{u}^c_\star = \tilde{\mathbf{u}}^c_\star + \left| \frac{\Delta t \sigma \kappa^f_{n+\frac{1}{2}}}{\rho\left(c^f_{n+\frac{1}{2}}\right)} \nabla^f c_{n+\frac{1}{2}} \right|^c. \tag{2.27}$$

This implementation is applied immediately before the projection steps.

To achieve a robust and easy-to-implement estimation of the curvature, the calculation uses a height function. Indeed, such a calculation can be summarised in three steps for 2D Cartesian grids [287]. First, one has to determine a 3×7 (resp. 7×3) stencil centred on the cell where the curvature is to be evaluated (Figure 2.7); an estimate of the interface orientation is used to choose the stencil best aligned with the normal direction to the interface. Then the second step builds a discrete approximation of the interface height $y = f(x)$ (resp. $x = f(y)$) by summing the volume fractions in each column (resp. line). Finally, it is possible to use finite-difference approximations of the derivatives of the discretised height-function to compute the curvature

$$\kappa = \left. \frac{h''}{(1 + (h')^2)^{3/2}} \right|_{x=0 \text{ (or } y=0)}. \tag{2.28}$$

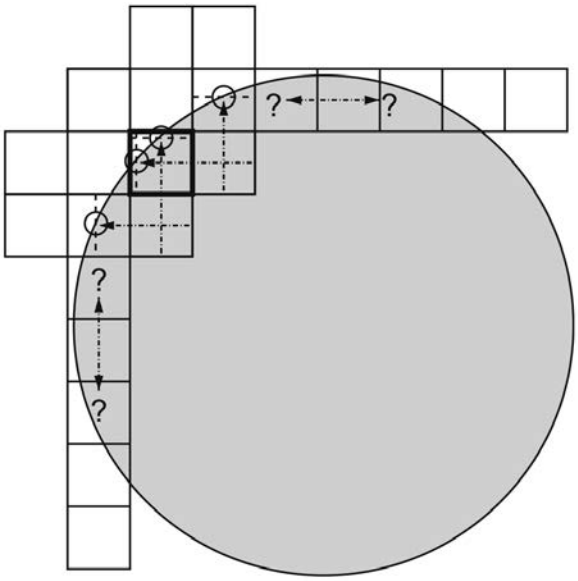

Figure 2.8: In this case only two of the three interface heights are consistent for either the vertical or the horizontal stencils. Neither the horizontal nor the vertical stencils on their own can be used to construct a twice-differentiable discrete approximation of the interface height. [254]

An important drawback of the standard height-function method is that even moderately curved interfaces can lead to configurations where consistent interface heights cannot be formed (Figure 2.8).

While neither the horizontal nor the vertical stencils on their own can be used to construct a twice-differentiable discrete approximation of the interface height in this case, it is clear that a combination of all the stencils can allow such an approximation. Fitting a curve (*e.g.* a parabola in 2D, paraboloid in 3D) through the points that can be estimated and differentiating the resulting analytical function will give an estimate of the curvature *via*

$$h(\mathbf{x}) \equiv \begin{cases} a_0x^2 + a_1x + a_2 & \text{in 2D} \\ a_0x^2 + a_1y^2 + a_2xy + a_3x + a_4y + a_5 & \text{in 3D} \end{cases} . \tag{2.29}$$

0	**1**	**2**	**3**
4	**5**	**6**	**7**
8	**9**	**10**	**11**
12	**13**	**14**	**15**

Figure 2.9: Example of sixteen square cells (2D) with their attributed number N_p.

Thus the mean curvature is obtained through equation (2.28)

$$\kappa = \begin{cases} \dfrac{2a_0}{(1+a_1^2)^{3/2}} & \text{in 2D} \\ 2\dfrac{a_0(1+a_4^2)+a_1(1+a_3^2)-a_2a_3a_4}{(1+a_1^2+a_4^2)^{3/2}} & \text{in 3D} \end{cases} . \tag{2.30}$$

2.1.6 Gerris in parallel

In order to reduce the computational time, the Gerris Flow Solver can also be used in parallel. As the code uses squares in 2D (or cubes in 3D), parallelization can be realised with root cells at non-zero level. Thus each cell or cell set is awarded a processor, and is distinguished by a number $N_p \in \mathbb{N}^*$ (Figure 2.9).

2.1.7 Implementation of solid boundaries

In order to handle embedded solid boundaries during spatial discretisation, the cells which are cut by a solid boundary are also considered as mixed cells. What is more, all cells that happen to be totally embedded in the solid phase are removed from the computation.

In mixed cells, the solid boundary is defined through a volume-of-fluid type approach. Specifically, the code uses:

- the volume fraction a as the ratio of the volume occupied by the fluid to the total volume of the cell;

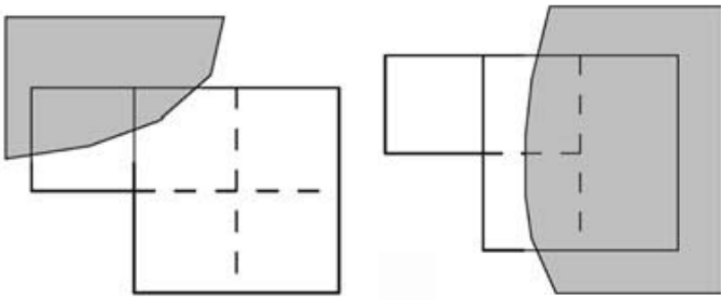

Figure 2.10: Additional constraints on the quadtree discretisation due to solid boundaries. The refinement necessary to conform to the given constraint is indicated by the dotted lines. [253]

- the surface fraction in direction d, s_d as the ratio of the area of face C_d occupied by the fluid to the total area of the face.

This solid boundary description assumes that the represented geometries do not possess features with spatial scales smaller than the mesh size. In particular, sharp angles or thin bodies cannot be represented correctly. This can be an issue for some applications, but more importantly it will restrict the efficiency of the multigrid solver [288].

The boundary condition for the velocity at solid wall boundaries is the no-flow condition

$$\mathbf{u} \cdot \mathbf{n} = 0, \tag{2.31}$$

where $\mathbf{n}$ is the outward unit vector at the solid boundary $\partial\Omega_s$.

In presence of solid boundaries, the method used to solve the Poisson equation is first-order accurate near the solid boundaries and second-order accurate elsewhere [253].

Another way to deal with solid boundaries. As the purpose of this study is to address multiphase flows in porous media, *i.e.* solve really complex flows in really complex geometries over large physical times, the efficiency of the multigrid solver can rapidly become an issue of the utmost importance. Consequently, the efficiency restriction presented above for sharp angles or thin bodies had to be dealt with.

It is possible to get round the problem by using another way to consider solid boundaries and entirely-solid cells. In this new method usually referred to as the "virtual solids" method, the solid domain $\Omega_s = \overline{\Omega}_s$ is not removed from the computation. Consequently, one considers that the entire domain $\Omega = \overline{\Omega}$ is filled with fluid, and not only the domain $\Omega_f = \Omega \backslash \mathring{\Omega}_s$ situated outside of the solid phase. Incidently, as a reminder, this method is formally true for extremely large observation times (or low Deborah number, see section 1.1.1), but is only an approximation for lower observation times (the so-called "physical" time of a simulation). Then, in order to simulate the behaviour of a solid matrix, the solid domain is imposed a no-velocity condition

$$\forall \mathbf{x} \in \Omega_s, \mathbf{u}(\mathbf{x}) = 0. \tag{2.32}$$

This condition is imposed at each timestep. The fluid properties (viscosity, density) also have to remain constant inside any arcwise connected subset of the solid matrix:

$$\forall \mathbf{x}, \mathbf{y} \in \Omega_s, \left(\exists \zeta \in C^0([0,1], \Omega_s) : \left\{ \begin{array}{l} \zeta(0) = \mathbf{x} \\ \zeta(1) = \mathbf{y} \end{array} \right. \right) \Rightarrow \left\{ \begin{array}{l} \mu(\mathbf{x}) = \mu(\mathbf{y}) \\ \rho(\mathbf{x}) = \rho(\mathbf{y}) \end{array} \right. . \tag{2.33}$$

As the calculation is realised inside the solid phase, a non-physical velocity could be generated between two timesteps, due to the computed pressure gradient. In order to reduce this unwanted velocity, a drag force is added to the Navier-Stokes equation inside the solid matrix[7]

$$\mathbf{f}_{\text{drag}} = -M\mathbf{u} \tag{2.34}$$

with $M \gg 1$. This drag force uses a robust implicit discretisation. Thus, according to equation (2.14), at each grid point of the solid phase and each timestep the Gerris Flow Solver solves the following equation

$$\rho_{n+\frac{1}{2}} \frac{\mathbf{u}_{n+1}}{\Delta t} = -\nabla p_{n+\frac{1}{2}} + \nabla \cdot \left[\mu_{n+\frac{1}{2}} \mathbf{e}_\star \right] - \rho_{n+\frac{1}{2}} \left[\mathbf{u}_{n+\frac{1}{2}} \cdot \nabla \mathbf{u}_{n+\frac{1}{2}} \right] - M\mathbf{u}_{n+1}. \tag{2.35}$$

The computed velocity inside the solid matrix is written as (first order in $\mathbf{u}$)

$$\mathbf{u}_{n+1} \approx -\left(M + \frac{\rho_{n+\frac{1}{2}}}{\Delta t} \right)^{-1} \left(\nabla p_{n+\frac{1}{2}} + \nabla \cdot \left[\mu_{n+\frac{1}{2}} \mathbf{e}_\star \right] \right). \tag{2.36}$$

[7]This method is basically a Brinkman penalisation [289, 290].

Thus, at each timestep, the unwanted velocity generated inside the solid phase between two timestep verifies $\mathbf{u}_{n+1} \approx 0$ for $M \gg 1$.

In order to ensure an even smaller velocity inside the solid matrix, it was tried to increase the density inside the solid matrix (equation (2.36)), independently from the one inside the "real" fluids. Though the result was indeed more accurate, the consequent increase of CPU[8] time incites not to use this approach.

2.2 Gerris Flow Solver for porous geometry

In order to compare both modelisations of the solid phase, several test cases were realised focusing on both computational speed and accuracy.

2.2.1 Scalability at low porosity

2.2.1.1 Definitions

In computer science, the scalability is defined as the ability of a system to accommodate an increasing number of elements or objects, to process growing volumes of work gracefully, and/or to be susceptible to enlargement [291]. A system whose performance improves after adding hardware, proportionally to the capacity added, is said to be a scalable system.

In the context of high performance computing there are two common notions of scalability:

- The first is strong scaling, which is defined as how the solution time varies with the number of processors for a fixed total problem size.
- The second is weak scaling, which is defined as how the solution time varies with the number of processors for a fixed problem size per processor.

In order to study the scalability of the Gerris Flow Solver, we introduce the number of cell updates per second

$$Z \equiv \frac{N_x \times N_y \times N_z \times N_{dt}}{T_{CPU}},$$

[8]Central Processing Unit

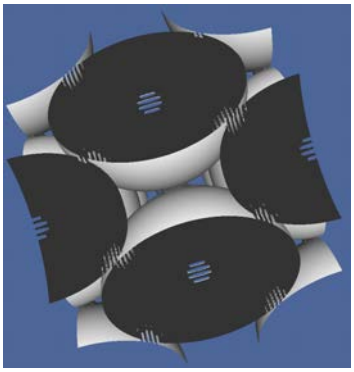

Figure 2.11: Cubic cell of a Face-Centred Cubic lattice.

where N_x (resp. N_y, N_z) is the number of cells in the x (resp. y, z) direction, N_{dt} the number of considered timesteps, and $T_{CPU/np}$ the required wall-clock CPU time to compute these timesteps. In order to calculate an intensive parameter, we focus on the number of cell updates per second and per core

$$Z_{/np} \equiv \frac{Z}{N_p} = \frac{N_x \times N_y \times N_z \times N_{dt}}{T_{CPU/np} \times N_p}, \tag{2.37}$$

with N_p the number of cores. It can be noted that some Lattice-Boltzmann and Volume-of-Fluid codes apparently reach $Z_{/np} \sim 10^7$ [292].

In order to neglect the increased time of timestep 0 (due to the initialisation of the code), we consider the five timesteps from the fifth to the tenth timestep. Thus $N_{dt} = 5$ and $T_{CPU/np} = T_{CPU/np}(10 \text{ timesteps}) - T_{CPU/np}(5 \text{ timesteps})$.

2.2.1.2 Characteristics of the tests

We realise single-phase scalability tests in an ideal porous structure. The solid matrix is a face-centred cubic (FCC) lattice of spheres. The nodes (*i.e.* sphere centres) of such a lattice are the eight vertices of a cube, and the centre of each face of this cube. The cubic cell of the network is presented in Figure 2.11. We remind that this cubic cell is not the primitive unit cell of the network[9]. The atomic packing factor is 0.74 or, equivalently, the porosity of such a structure is $\phi = 26\%$.

Due to the octree structure of the meshing in the Gerris Flow Solver, we consider several lattices at different levels. We define a level-1 lattice as the basic FCC cell

[9]The primitive unit cell of the FCC lattice is a rhombohedron.

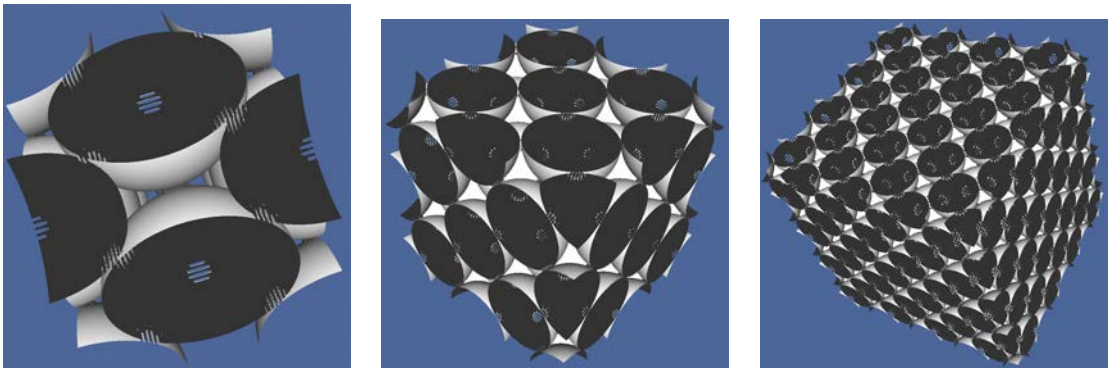

(a) (b) (c)

Figure 2.12: Face-Centred Cubic lattices at different levels: (a) a level-1 lattice, (b) a level-2 lattice, (c) a level-3 lattice.

in a domain of size 1^3. Level $(n+1)$ is defined recursively from level n as dividing the domain of size 1^3 in eight subdomains of size $\left(\frac{1}{2}\right)^3$. Each subdomain is then filled with a level-n lattice shrinked to the eighth (Figure 2.12).

At the beginning, a fluid of kinematic viscosity $\nu = 10^4$ is at rest inside the domain and is imposed a volume force in the x direction such that the Reynolds number never exceeds $\mathrm{Re}_{\max} = 5.10^{-5}$.

The scalability tests are realised in two different clusters:

- cluster *babbage2* at *Institut Jean le Rond d'Alembert* (UPMC-Paris VI): tests on 1 to 64 cores,
- cluster *Rostand* at *Centre Scientifique et Technique Jean-Féger* (TOTAL SA): tests on 1 to 4096 cores.

2.2.1.3 Results on cluster *babbage*

Three kinds of domain modelling are used:

1. case 1: the default modelling of the solids by the Gerris Flow Solver (*i.e.* removing all the cells full of solid phase from the computation, see Figure 2.13(a)),
2. case 2: the method described in the second part of section 2.1.7 (Figure 2.13(b)),

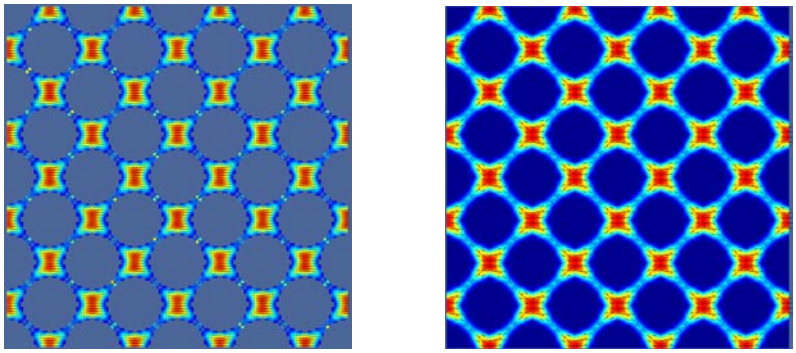

(a) (b)

Figure 2.13: Velocity field after ten timesteps: (a) in the case of the default modelling of the solids, (b) with a fluid spanning the entire domain. Closer to red: higher velocity; closer to blue: lower velocity.

3. case 3: as the Reynolds number of the flow is extremely low, one can neglect the advection term $\mathbf{u} \cdot \nabla \mathbf{u}$ in the Navier-Stokes equation. This simplification is combined with the method described in the second part of section 2.1.7.

Lattices from level 1 to level 3 are considered for weak scalability tests, and level-3 lattices for strong scalability tests. Each cubic cell of the FCC lattice is meshed with 16^3 cells (*i.e.* a total number of cells going from 16^3 up to 64^3). The tests are realised with two different solvers:

- the default one of Gerris Flow Solver,
- the parallel High Performance Preconditioners[10] (*Hypre*).

The results of weak scalability are presented in Figure 2.14 and those of strong scalability in Figure 2.15. The missing data for *Hypre* solver in both figures highlight the fact that in some cases, the computation crashes before reaching the end of timestep 10.

It seems obvious that both weak and strong scalability results are worse when using *Hypre* solver. These bad results are apparently due, either to a bug inside *Hypre*, or more probably to a problem in the initialisation of *Hypre* by the Gerris Flow Solver.

[10] http://computation.llnl.gov/casc/hypre/software.html

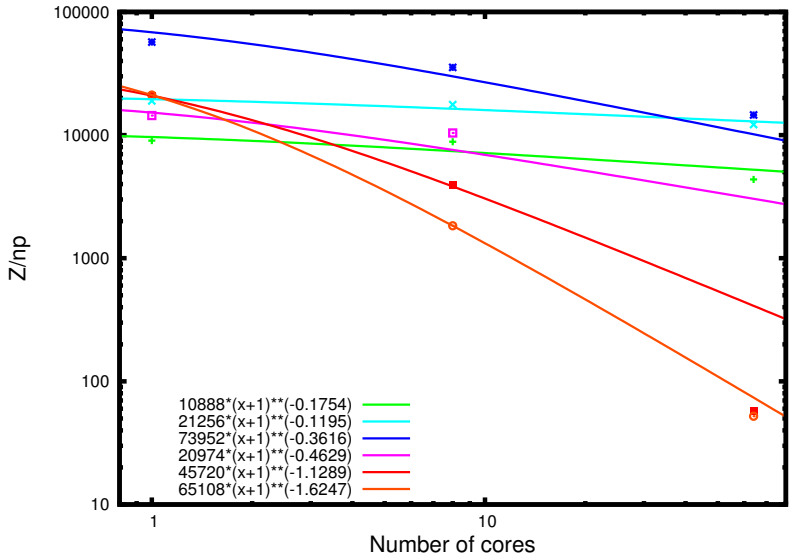

Figure 2.14: Weak scalability on cluster *babbage2*. In green (+): results obtained for case 1 with the default solver, in light blue (×): case 2 with default solver, in dark blue (✱): case 3 with default solver, in magenta (⊡): case 1 with *Hypre*, in red (■): case 2 with *Hypre*, in orange (⊙): case 3 with *Hypre*.

Indeed, we realised that the required memory to compute a simulation was a linear function of the number of cores when using *Hypre*. Apparently, each core stores the entire computation in its own allocated memory (instead of storing only part of it).

Nonetheless, the results obtained with the default solver of Gerris are much more promising. Indeed, it seems that $Z_{/np}$ is in the worst cases only divided by a factor 3 when increasing the number of cores from 1 to 64. In some cases, the overall scalability is close to perfection (nearly constant value for $Z_{/np}$ with increasing number of cores). Furthermore, it appears that the simulations realised with the default modelling of the solids are slower than those realised with a fluid spanning the entire domain: indeed the number of cell updates per second and per core is multiplied by a factor 2 to 5 when moving from case 1 to case 2.

Moreover, this factor is underestimated due to the blatant overestimation of $Z_{/np}$ when using the default modelling of solids. Indeed, as the cells totally embedded in the solid are removed from the computation, the actual number of cells in the domain

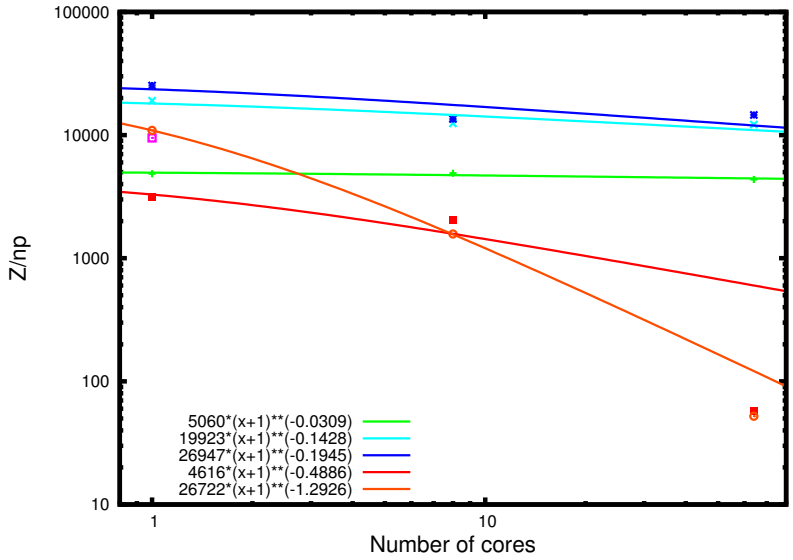

Figure 2.15: Strong scalability on cluster *babbage2*. In green (+): results obtained for case 1 with the default solver, in light blue (×): case 2 with default solver, in dark blue (✱): case 3 with default solver, in magenta (⊡): case 1 with *Hypre*, in red (■): case 2 with *Hypre*, in orange (⊙): case 3 with *Hypre*.

is much lower[11] than $N_x \times N_y \times N_z$. This difference is the cause of the overestimation of the computational speed in this case.

The CPU time for the first ten timesteps (including initialisation) is presented for case 2 with both Poisson solvers in Table 2.1.

2.2.1.4 Results on cluster *Rostand*

As a consequence of the results obtained previously on cluster *babbage2*, only two kinds of domain modelling are used: cases 2 and 3 presented above. The standard modelling of solids in the Gerris Flow Solver is neglected due to its poorer computational speed.

Lattices from level 2 to level 6 are considered for weak scalability tests, and level-5 lattices for strong scalability tests. Each cubic cell of the FCC lattice is meshed with 16^3 cells (*i.e.* a total number of cells going from 32^3 up to 512^3). The tests are realised

[11] As a matter of fact, it is of order $\phi \times N_x \times N_y \times N_z$.

Lattice level	Number of cores	Standard solver	*Hypre* solver
1	1	1.14	2.03
2	8	2.37	9.50
3	1	142.24	813.04
3	8	27.72	161.75
3	64	4.06	718.82

Table 2.1: CPU time (in s) required to compute ten timesteps for case 2 for both the standard solver of the Gerris Flow Solver and *Hypre* solver.

with the default solver of Gerris. *Hypre* solver is not considered, due to the problem presented above.

The results of weak scalability are presented in Figure 2.16 and those of strong scalability in Figure 2.17.

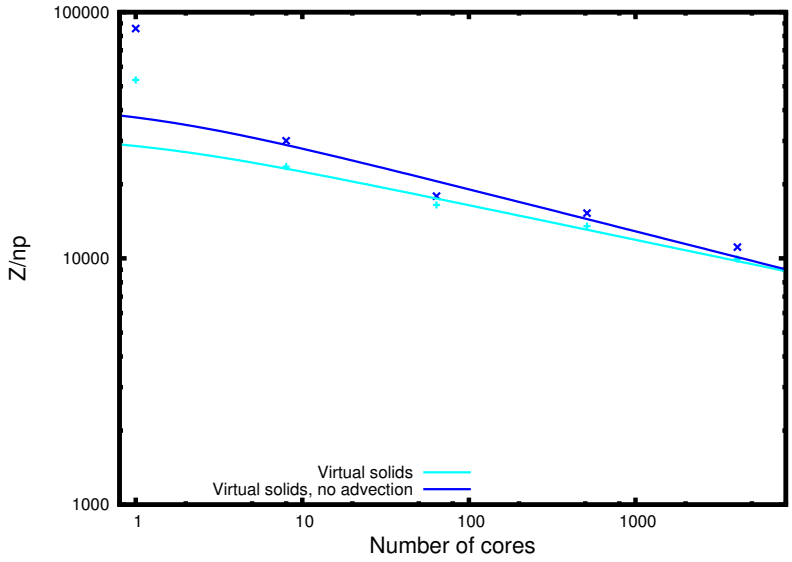

Figure 2.16: Weak scalability on cluster *Rostand*. In light blue (+): results obtained for case 2 with the default solver ($y \propto x^{-0.1}$), in dark blue (×): case 3 with default solver ($y \propto x^{-0.2}$).

These results look very promising. Indeed, it seems that $Z_{/np}$ is in the worst cases only divided by a factor 10 when increasing the number of cores from 1 to 4096. A

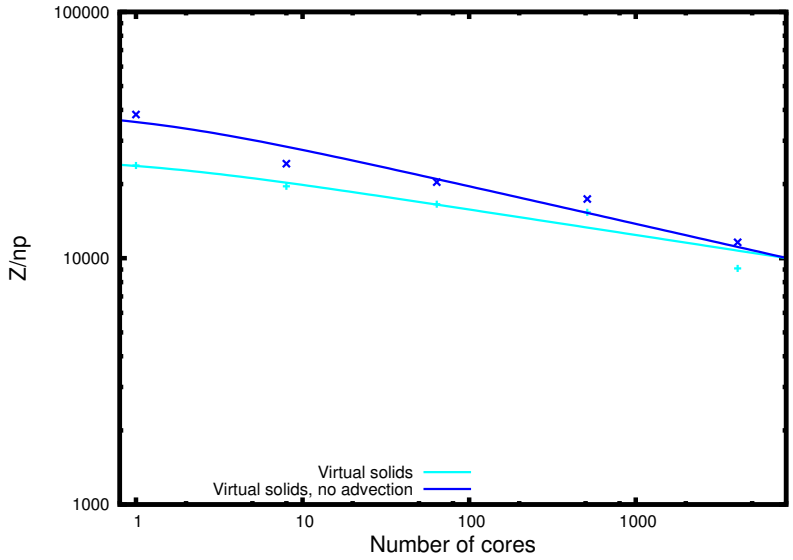

Figure 2.17: Strong scalability on cluster *Rostand*. In light blue (+): results obtained for case 2 with the default solver ($y \propto x^{-0.1}$), in dark blue (×): case 3 with default solver ($y \propto x^{-0.2}$).

drastic decrease of computing performance is also to be noted when going from one to multiple cores in the case of weak scalability (Figure 2.16). However, this decrease is curiously not present in the case of strong scalability (at least the amplitude is not as important, see Figure 2.17). Sadly, no satisfactory explanation has been found.

The CPU time for the first ten timesteps (including initialisation) is presented for case 2 with the standard Poisson solver in Table 2.2.

2.2.2 CPU time and CFL number for two-phase flow invasion of porous geometries

In this section, the CFL number will be referred to as χ.

Using the same notations as in section 1.1.3.4, we define the Ohnesorge number Oh [293, 294] as the ratio between viscous forces for one part and surface tension and

Number of cores	Lattice level	CPU time (s)	Lattice level	CPU time (s)
1	2	6.34	5	7048.43
8	3	14.34	5	1710.78
64	4	21.45	5	248.68
512	5	43.20	5	43.20
4096	6	108.50	5	22.97

Table 2.2: CPU time required to compute ten timesteps for case 2 for the standard solver of Gerris Flow Solver.

inertia for the other part

$$\begin{aligned} \mathrm{Oh} &\equiv \frac{\text{Viscous force}}{(\text{Inertia force} \times \text{Surface tension})^{1/2}} \propto \frac{\mu \partial^2 u/\partial x^2}{(\sigma \nabla c/R \times \rho u \partial u/\partial x)^{1/2}} \\ &\propto \frac{\mu U/l^2}{(\sigma/l^2 \times \rho U^2/l)^{1/2}} = \frac{\mu}{(\sigma \rho l)^{1/2}}. \end{aligned} \tag{2.38}$$

We also define the Laplace number La as

$$\mathrm{La} \equiv \mathrm{Oh}^{-2} = \frac{\sigma \rho l}{\mu^2} = \frac{\mathrm{Re}}{\mathrm{Ca}}. \tag{2.39}$$

It should be noted that the Laplace number is not necessarily negligible in porous media, contrary to what one could expect. Indeed for the invasion of water in an oil-filled porous medium with a characteristic pore size equal to 10 μm, La ~ 100, *i.e.* Oh ~ 0.1.

2.2.2.1 Wall-clock CPU time in a porous geometry

We consider a simulation of two-phase flow in porous media till breakthrough. By definition of Z (see section 2.2.1.1)), the wall-clock CPU time varies for a Gerris simulation as

$$T_{CPU/np} = \frac{N^3 N_{dt}}{Z}, \tag{2.40}$$

where $N = N_x = N_y = N_z$ is the number of cells in each direction and N_{dt} the number of timesteps. For a simulation in a domain of size L with mesh size h, it is possible to write $N = \frac{L}{R_p}\frac{R_p}{h}$ with R_p the characteristic size of a pore. One also has

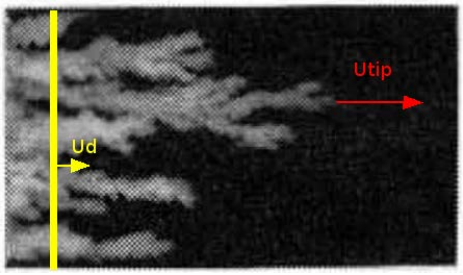

Figure 2.18: Velocity of the tip of the fingering (Utip) *vs* Darcy velocity (Ud). [295]

$N_{dt} = \frac{\Delta T}{\delta t}$ where ΔT is the physical time of the simulation, and δt the average length of a timestep. It is thus possible to write

$$T_{CPU/np} = \left(\frac{L}{R_p}\right)^3 \left(\frac{R_p}{h}\right)^3 \frac{\Delta T}{\delta t} (Z_{/np} \times n_p)^{-1} \tag{2.41}$$

with n_p the number of cores.

As the simulation ends at breakthrough, $\Delta T = L/U_{tip}$ where U_{tip} is the velocity of the tip of the resulting fingering (Figure 2.18). By definition of the CFL number, one can write $V_{tip} = \chi \times h/\delta t$. Thus $\frac{\Delta T}{\delta t} = \frac{L}{\chi h}$, and it follows

$$T_{CPU/np} = \left(\frac{L}{R_p}\right)^3 \left(\frac{R_p}{h}\right)^3 \frac{L}{h} (\chi Z_{/np} \times n_p)^{-1}. \tag{2.42}$$

Finally, the wall-clock CPU time to breakthrough is given, in the case of the invasion of a 3D porous medium, by

$$\boxed{T_{CPU/np} = N_{P/L}^4 \, n_{ce/p}^4 \, (\chi Z_{/np} \times n_p)^{-1}} \tag{2.43}$$

with

$$\begin{cases} N_{P/L} &= \text{number of “pores” in each direction} \\ n_{ce/p} &= \text{number of cells per pore} \\ \chi &= \text{CFL number} \\ Z_{/np} &= \text{Computational speed per core} \\ n_p &= \text{number of cores} \end{cases}$$

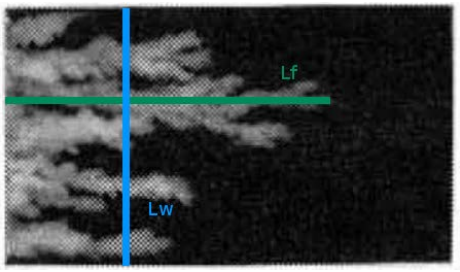

Figure 2.19: Length of the longest finger (Lf) *vs* characteristic lengthscale of the injection surface (Lw). [295]

2.2.2.2 CFL number in a porous geometry

We call L_f the length of the longest finger and L_w a characteristic lengthscale of the injection surface (Figure 2.19). In the simulation of an invasion of the porous medium, the number of pores n_{pores} filled by the invading fluid varies as $n_{pores} \sim \left(\frac{L_f}{R_p}\right)^{D_F} \sim \frac{\text{Injected volume}}{R_p^3} \propto L_w^2 \frac{U_D t}{\phi} \frac{1}{R_p^3}$ with U_D the Darcy velocity of the flow, ϕ the porosity of the domain and D_F the fractal dimension of the fingering.

If we suppose $L_f = L_w$ (cubic domain at breakthrough) we obtain

$$t \propto L_f^{D_F-2} R_p^{3-D_F} \frac{\phi}{U_D}. \tag{2.44}$$

Using the definition of U_{tip}, one gets $U_{tip} = \frac{L_f}{t} \propto \left(\frac{L_f}{R_p}\right)^{3-D_F} \frac{U_D}{\phi} = \beta \frac{U_D}{\phi}$ with $\beta = \left(\frac{L_f}{R_p}\right)^{3-D_F}$.

As the fluid cannot go further than one cell size at each timestep, we have $\chi < 1$. Furthermore, δt has to be lower than the characteristic time of capillary wave propagation[12] $\delta t_{cap} = \left(\frac{\rho h^3}{\sigma}\right)^{1/2}$. As a consequence $\chi = \min\left(1, \frac{U_{tip}\delta t_{cap}}{h}\right) = \min(1, \chi_{cap})$.

[12]For a derivation of δt, see [73].

From δt_{cap}, one gets

$$\begin{aligned}
\chi_{cap} &= \frac{U_{tip}}{h}\left(\frac{\rho h^3}{\sigma}\right)^{1/2} \\
\chi_{cap} &= \frac{\sigma^{1/2}h^{1/2}}{\sigma^{1/2}}\frac{U_D}{\phi}\beta \\
\chi_{cap} &= \frac{\mu U_D}{\sigma}\left(\frac{\sigma\rho R_p}{\mu^2}\right)^{1/2}\left(\frac{h}{R_p}\right)^{1/2}\frac{\beta}{\phi} \\
\chi_{cap} &= \mathrm{Ca}_D \mathrm{La}^{1/2} n_{ce/p}^{-1/2}\frac{\beta}{\phi}
\end{aligned}$$

By considering that $\chi = \chi_{cap}$, one gets

$$\chi = \mathrm{Ca}_D \mathrm{La}^{1/2} n_{ce/p}^{-1/2}\frac{\beta}{\phi} \tag{2.45}$$

with

$$\begin{cases}
n_{ce/p} &= \text{number of cells per pore} \\
\mathrm{Ca}_D &= \text{capillary number associated with the Darcy velocity} \\
\mathrm{La} &= \text{Laplace number based on the pore size} \\
\phi &= \text{porosity}
\end{cases}$$

One should not forget that $\mathrm{Ca}_D \neq \mathrm{Ca}_{tip}$ (usually $\mathrm{Ca}_D \ll \mathrm{Ca}_{tip}$, see Figure 2.18).

We finally consider the following term $\Lambda = \frac{|\nabla p|}{\sigma}k$. Using Darcy's law, $\Lambda = \frac{\mu U_D}{\sigma} = \mathrm{Ca}_D$.

Moreover, according to [296, 297, 298, 299], the correlation length L_w in invasion percolation with a gradient varies as $L_w \propto R_p \Lambda^{-\frac{\nu}{\nu+1}}$. Thus, as $L_f = L_w$

$$\beta = \left(\frac{L_w}{R_p}\right)^{3-D_F} \propto \Lambda^{-\frac{\nu}{\nu+1}(3-D_F)}$$

To conclude, the CFL number for the simulation of the invasion of a 3D porous medium varies as

$$\boxed{\chi \propto \mathrm{Ca}^{\gamma}\,\mathrm{La}^{1/2}\,n_{ce/p}^{-1/2}/\phi} \tag{2.46}$$

with

$$\left\{\begin{array}{rcccl} \mathrm{Ca} & = & \mu V_D/\sigma & = & \text{capillary number associated with Darcy velocity} \\ & & \mathrm{La} & = & \text{Laplace number} \\ & & \phi & = & \text{porosity} \\ & & n_{ce/p} & = & \text{number of cells per pore} \\ \gamma & = & 1-\frac{\nu}{\nu+1}(3-D_F) & = & \text{exponent due to the fractal structure of the fingering} \\ & & D_F & = & \text{fractal dimension} \\ & & \nu & = & \text{exponent of the correlation length} \end{array}\right.$$

In 3D, $\nu/(\nu+1) \approx 0.5$ [299]. Thus for $D_F \approx 2.5$ one gets $\gamma \approx 3/4$.

From equation (2.46), one can state that

- the CFL number decreases with decreasing capillary number. This is bad news for reservoir engineering applications if one considers that flows in porous media occur at really low capillary number (of order $10^{-8} - 10^{-6}$).
- the CFL number depends on the Laplace number, which could be bad news due to the great variety of possible fluid viscosities (especially for low-viscosity fluids).

The influence of these drawbacks could be reduced by implementing an improved computation of surface tension (implicit in time).

2.2.3 Single-phase and two-phase Poiseuille flows

For any $\mathbf{a} = (a_i)_{i\in[\![1,n]\!]} \in \mathbb{R}^n$ with $n \in \mathbb{N}^*$, we define the three following norms:

- L_∞ norm: $L_\infty(\mathbf{a}) = \max_i(|a_i|)$,
- L_1 norm: $L_1(\mathbf{a}) = \frac{1}{n}\sum_{i=1}^{n}|a_i|$,
- L_2 norm: $L_2(\mathbf{a}) = \left(\frac{1}{n}\sum_{i=1}^{n}|a_i|^2\right)^{1/2}$.

As $\mathbb{R}^n$ is of finite dimension, all three norms are equivalent, *i.e.*

$$\forall (N,n) \in \{L_\infty, L_1, L_2\}^2, \exists 0 < a \leqslant b : \forall u, a \cdot n(u) \leqslant N(u) \leqslant b \cdot n(u).$$

These three norms are extended to the set of all solutions returned by the Gerris Flow Solver as follows. For a solution field ξ on a domain of size N^3 we define

- $L_\infty(\xi) = \max\limits_{c \in Cells} L_\infty(\xi(c))$,
- $L_1(\xi) = \frac{1}{N^3} \sum\limits_{c \in Cells} L_1(\xi(c))$,
- $L_2(\xi) = \left(\frac{1}{N^3} \sum\limits_{c \in Cells} (L_2(\xi(c)))^2 \right)^{1/2}$.

For all of these norms, the error e_j is measured as

$$e_j = L_j(\mathbf{a}_{Gerris} - \mathbf{a}_{theory}), j \in \{\infty, 1, 2\}. \tag{2.47}$$

To check the accuracy of the Gerris Flow Solver, we realise tests of Poiseuille flow [180] in both single- and two-phase cases.

2.2.3.1 Single-phase Poiseuille flow

Horizontal geometry Let us consider a Poiseuille flow in a horizontal geometry (*i.e.* the direction of the flow is aligned with the principal directions of the mesh). The geometry of the test is presented in Figure 2.20.

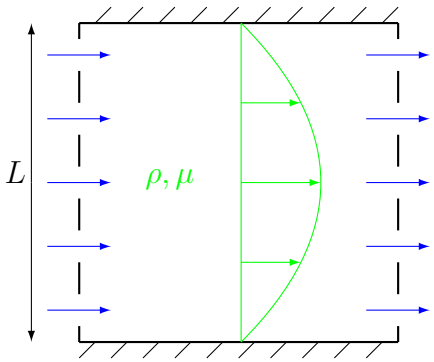

Figure 2.20: Single-phase Poiseuille flow in a horizontal geometry.

One can easily define a characteristic velocity

$$U = \frac{\rho g L^2}{8\mu}. \tag{2.48}$$

The corresponding Reynolds number is

$$\mathrm{Re} = \frac{\rho U L}{\mu} = \frac{\rho^2 g L^3}{8\mu^2}. \tag{2.49}$$

In the following tests, $\mathrm{Re} = 1$.

The analytical solution centred on $y = 0$ is (Appendix E)

$$\boxed{u(y) = \frac{\rho g L^2}{8\mu}\left(1 - \left(\frac{2y}{L}\right)^2\right) = U\left(1 - \left(\frac{2y}{L}\right)^2\right)} \tag{2.50}$$

The simulation begins with $\mathbf{u} = 0$ everywhere. The simulation is ended when the permanent regime is reached. It is considered that this permanent regime is reached when the variation of the velocity is inferior to 10^{-7} in each cell of the domain between two timesteps. The convergence of the error norms as functions of the resolution is presented in Figure 2.21.

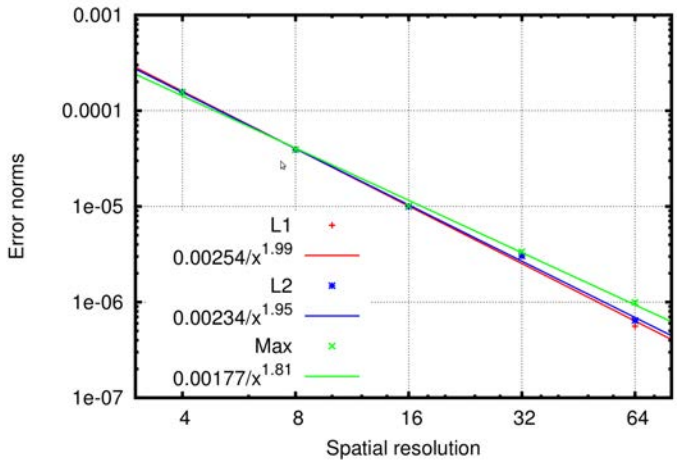

Figure 2.21: Convergence of the error norms as functions of the resolution in the case of single-phase horizontal Poiseuille flow.

For all three norms, a quasi-quadratic convergence with the resolution is obtained, which is in agreement with the theory.

Slanted geometry The same test is then realised for a slanted geometry, *i.e.* the direction of the Poiseuille flow is not aligned with the principal direction of the meshing.

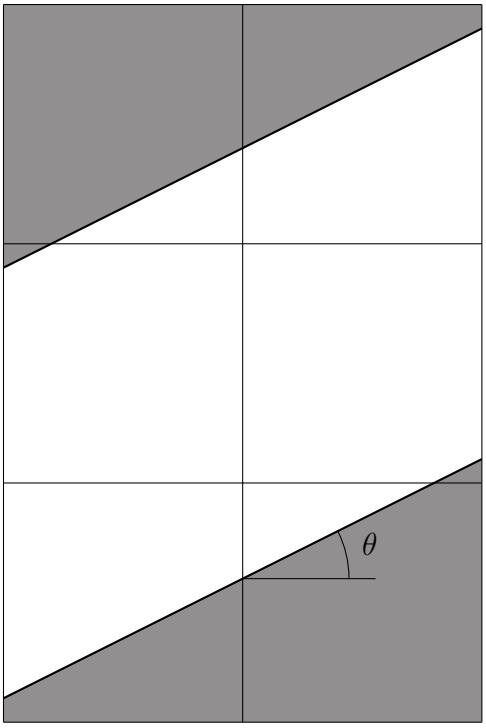

Figure 2.22: Single-phase Poiseuille flow in a slanted geometry ($\theta = \arctan 1/2 \pmod{2\pi}$). In white: the fluid phase, in grey: the solid phase

The angle between the flow direction and the x axis is chosen equal to $\theta = \arctan 1/2 \pmod{2\pi}$. The geometry of the test is presented in Figure 2.22.

The simulation begins with $\mathbf{u} = 0$ everywhere. The simulation is ended when the permanent regime is reached. The convergence of the error norms as functions of the resolution is presented in Figure 2.23.

The convergence is limited to an error of order 10^{-4}, whatever the norm and whatever the way the solids are generated. The convergence is however slightly better for the standard modelling of the solids.

The floor value is nonetheless sufficiently small to consider that the convergence of the result returned by Gerris is good.

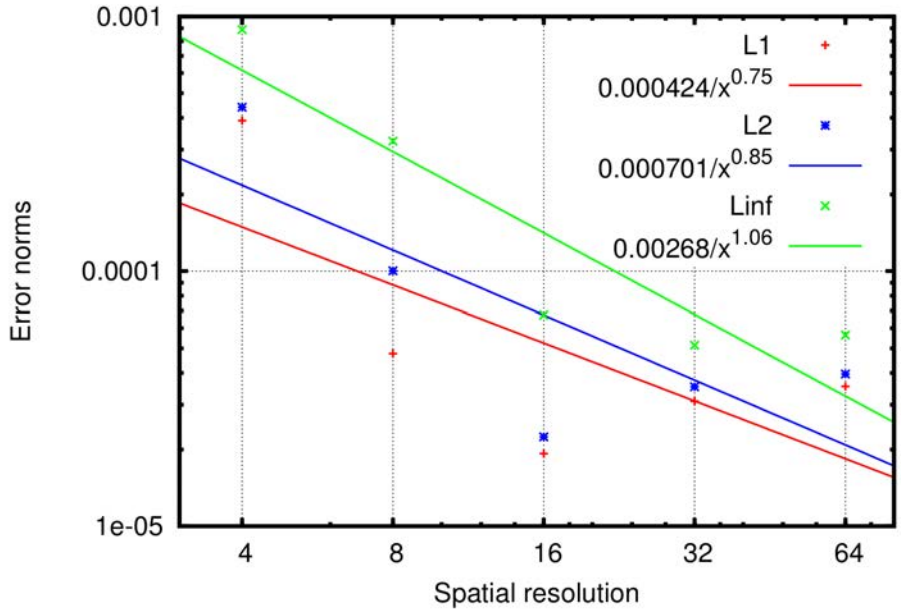

(a)

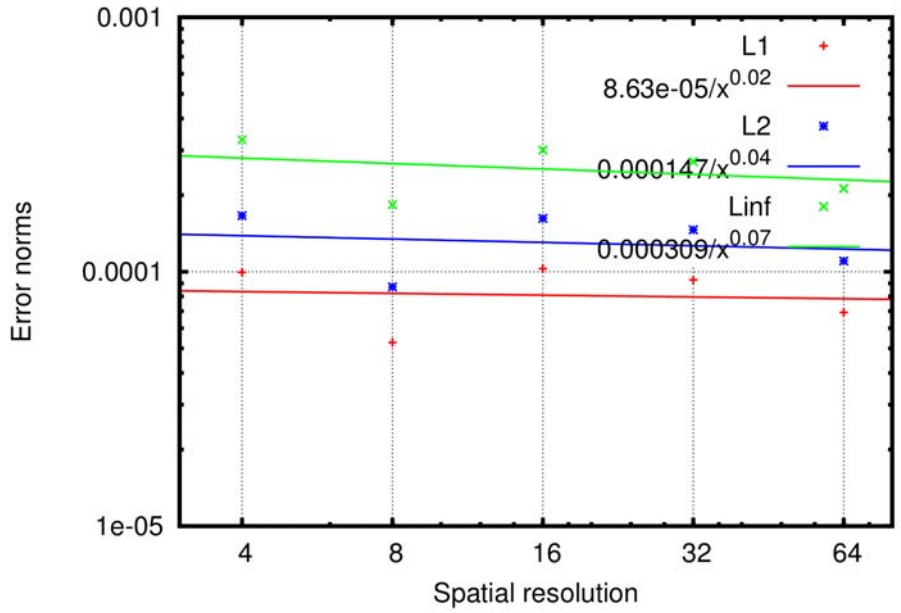

(b)

Figure 2.23: Convergence of the error norms as functions of the resolution in the case of single-phase slanted Poiseuille flow (a) with the default solids of the Gerris Flow Solver, (b) with fluid everywhere.

2.2.3.2 Two-phase Poiseuille flow

As the convergence results obtained for single-phase flow are satisfactory, two-phase flows are considered in order to check the convergence of the Gerris Flow Solver in the case of multiphase flow.

Horizontal geometry A Poiseuille flow is considered in a horizontal geometry. The geometry of the test is presented in Figure 2.24. The more viscous fluid is supposed to be at the centre. At the interface between both fluids, the viscosity is derived as an arithmetic average of both values.

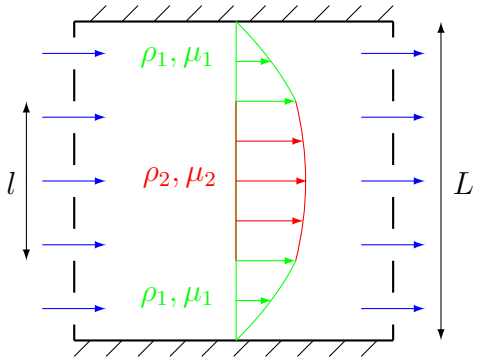

Figure 2.24: Two-phase Poiseuille flow in a horizontal geometry.

One can easily define three characteristic velocities

$$U_1 = \frac{\rho_1 g L^2}{8\mu_1}, \qquad \Delta U = \frac{(\rho_2 - \rho_1) g l L}{8\mu_1}, \qquad U_2 = \frac{\rho_2 g l^2}{8\mu_2}. \tag{2.51}$$

The analytical solution centred on $y = 0$ is

$$\begin{aligned} \forall y \in [-L, -l] \cup [l, L], u(y) &= U_1 \left(1 - \left(\frac{2y}{L}\right)^2\right) + 2\Delta U \left(1 - \left|\frac{2y}{L}\right|\right) \\ \forall y \in [-l, l], u(y) &= \begin{cases} U_2 \left(1 - \left(\frac{2y}{l}\right)^2\right) + \\ U_1 \left(1 - \left(\frac{l}{L}\right)^2\right) + 2\Delta U \left(1 - \frac{l}{L}\right) \end{cases} \end{aligned} \tag{2.52}$$

A derivation of equation (2.52) can be found in Appendix E.

The simulation begins with $\mathbf{u} = 0$ everywhere. The simulation is ended when the permanent regime is reached. The convergence of the error norms as functions of the resolution is presented in Figure 2.25. For all three norms, the convergence is worse

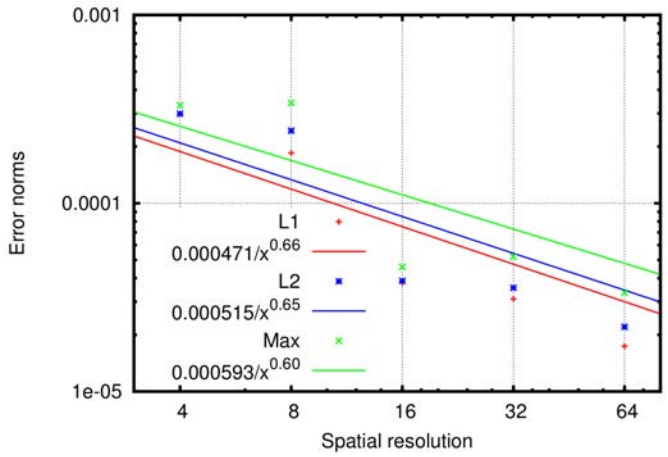

Figure 2.25: Convergence of the error norms as functions of the resolution in the case of two-phase horizontal Poiseuille flow.

than in the case of single-phase flow. Instead of being quadratic the convergence is worse than linear. A comparison between the results returned by the Gerris Flow Solver and the theoretical curve is presented in Figure 2.26 in the case $\mu_2/\mu_1 = 2$. The corresponding error is presented in Figure 2.27.

As could be expected, the results obtained by Gerris underestimate the theoretical velocity, and the maximum error is obtained at the centre of the domain. Indeed as the initial velocity field is equal to zero everywhere, the maximum change has to occur for y close to 0 and the simulation will stop when $\forall(i,j), |u^n(x_i,y_j) - u^{n-1}(x_i,y_j)| \leqslant 10^{-7}$ *i.e.*

$$\forall(i,j), \frac{|u^n(x_i,y_j) - u^{n-1}(x_i,y_j)|}{\max\limits_y u_{\text{theory}}(y)} \leqslant 2.5 \times 10^{-5},$$

where (x_i, y_j) are the computational points, the exponents $n-1$ and n are the numbers of the timesteps and $|u^n(x_i,y_j) - u^{n-1}(x_i,y_j)|$ is maximal for y_j close to 0.

As the error is always lower than 2% the Gerris-obtained result is more than satisfactory for two-phase Poiseuille flow in horizontal geometry.

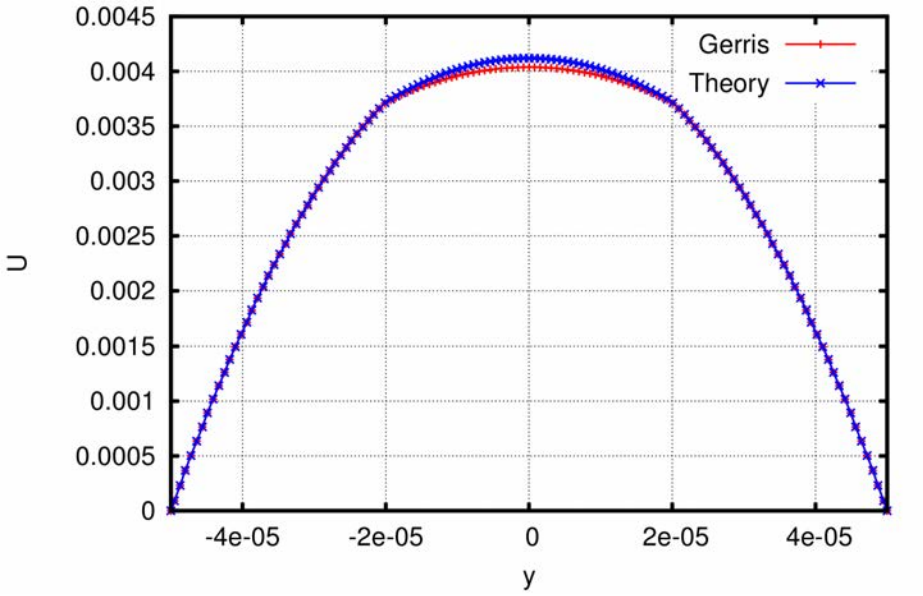

Figure 2.26: Comparison of Gerris Flow Solver results with analytical curve in horizontal geometry in the case of two-phase Poiseuille flow with $\mu_2/\mu_1 = 2$.

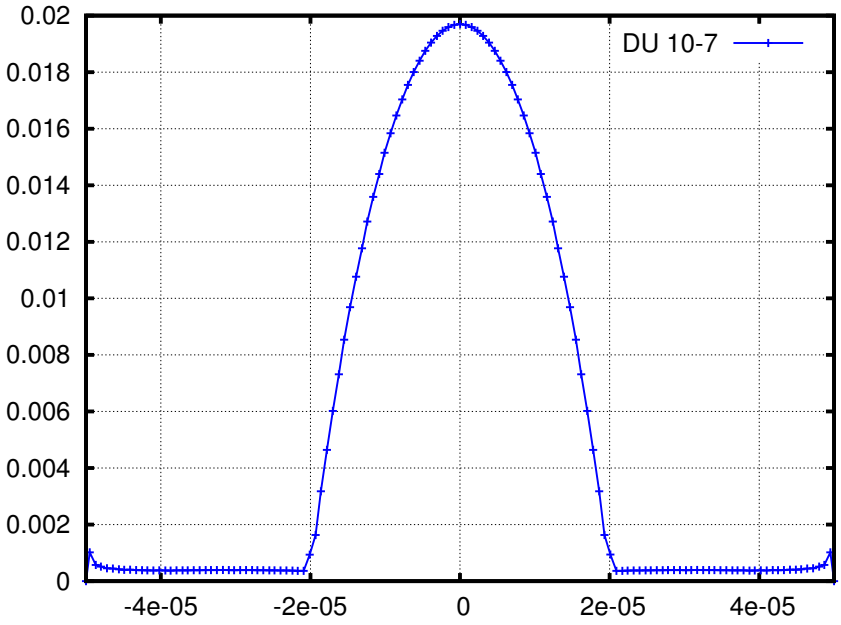

Figure 2.27: Error between Gerris Flow Solver results and theoretical value for a two-phase Poiseuille flow with $\mu_2/\mu_1 = 2$ in horizontal geometry. In abscissa y; in ordinate $\dfrac{|u_{\text{Gerris}} - u_{\text{theory}}|}{u_{\text{theory}}}$.

Slanted geometry The same test is then realised in a slanted geometry. Once again the angle between the flow direction and the x axis is chosen equal to $\theta = \arctan 1/2 \pmod{2\pi}$. The geometry of the test is presented in Figure 2.28.

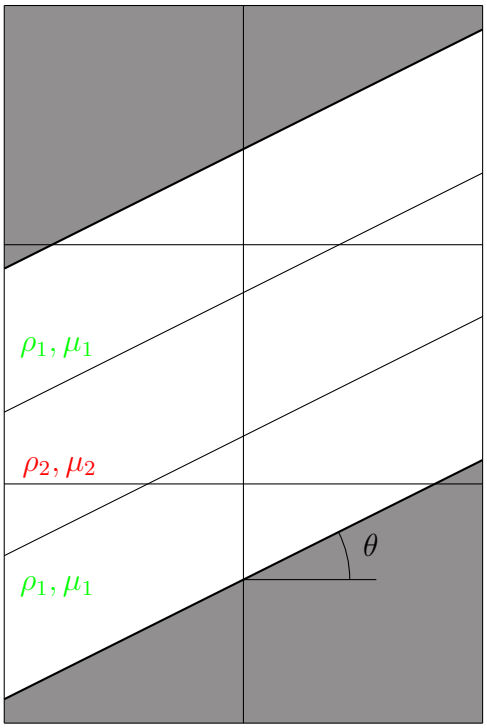

Figure 2.28: Two-phase Poiseuille flow in a slanted geometry ($\theta = \arctan 1/2 \pmod{2\pi}$). In white: the fluid phases, in grey: the solid phase

The simulation begins with $\mathbf{u} = 0$ everywhere. The simulation is ended when the permanent regime is reached. The convergence of the error norms as functions of the resolution is presented in Figure 2.29.

The convergence is limited to an error of order 10^{-4}, whatever the norm and whatever the way the solids are generated. The convergence is however slightly better for the standard modelling of the solids. One can also note that the convergence is slightly worse than in the single-phase case.

The floor value is nonetheless sufficiently small to consider that the convergence of the result returned by Gerris is good.

A comparison between the results returned by the Gerris Flow Solver and the theoretical curve is presented in Figure 2.30 in the case $\mu_2/\mu_1 = 2$. The corresponding

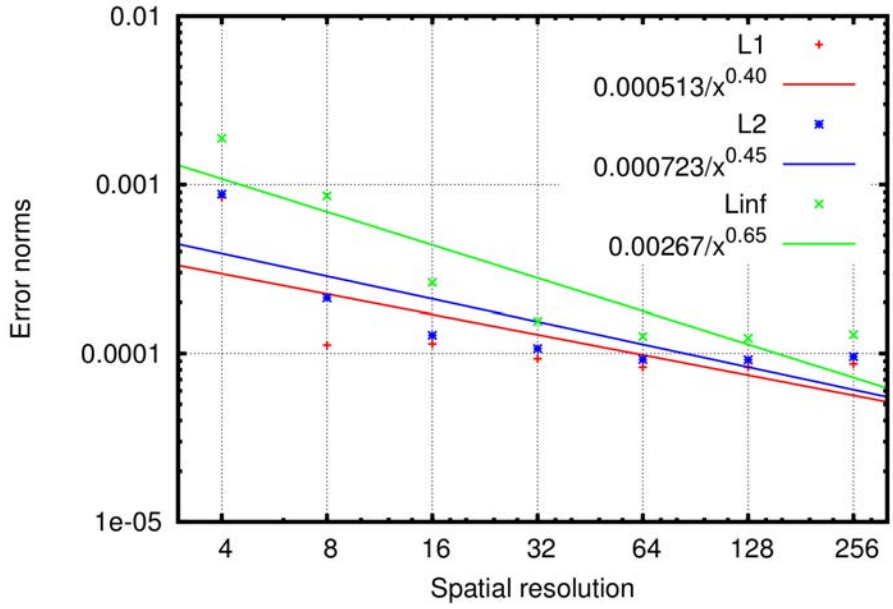

(a)

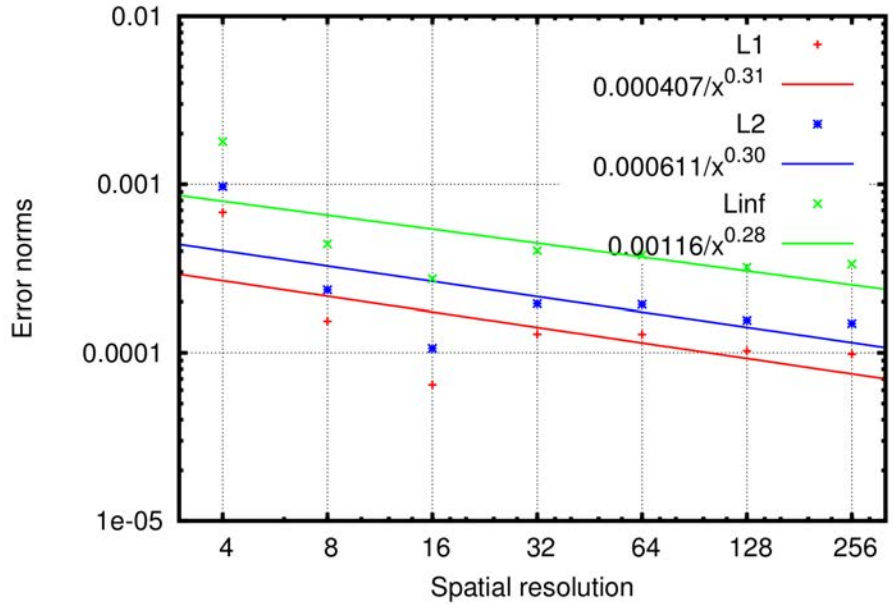

(b)

Figure 2.29: Convergence of the error norms as functions of the resolution in the case of two-phase slanted Poiseuille flow (a) with the default solids of Gerris Flow Solver, (b) with fluid everywhere.

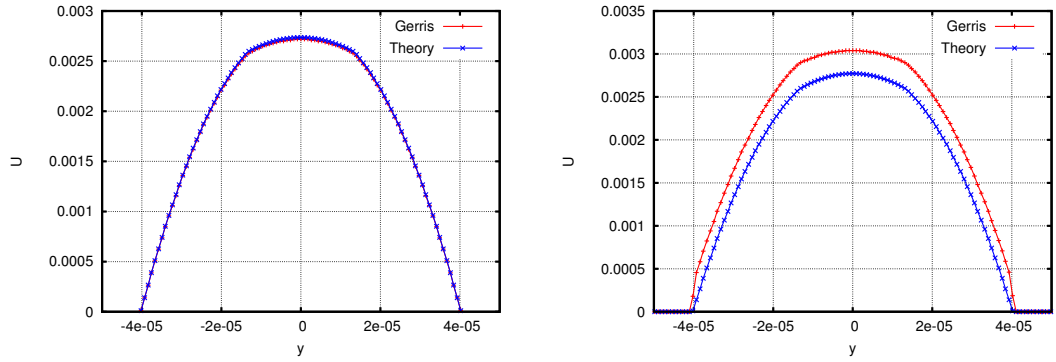

(a) (b)

Figure 2.30: Comparison of Gerris Flow Solver results with analytical curve in slanted geometry in the case of two-phase Poiseuille flow with $\mu_2/\mu_1 = 2$. (a) Standard modelling of solids, (b) fluid in the whole domain.

error is presented in Figure 2.31 divided by the theoretical value at each point and in Figure 2.32 divided by the maximum theoretical value.

For the same reason as above, when using the standard modelling of solids by the Gerris Flow Solver, the results underestimate the theoretical velocity, and the maximum error is obtained at the centre of the domain.

On the contrary, when using the modelling of the solid phase presented in the second part of Section 2.1.7, the results overestimate the theoretical velocity and this overestimation can be of order 10% of the maximum theoretical velocity. This higher difference between the theoretical and computed results is mainly due to the fact that the zero velocity condition is not imposed at the boundary between fluid and solid phases, but at the nearest computational point. This problem is illustrated in Figure 2.33.

Indeed in this Figure the zero-velocity condition should be imposed at the interface between fluid and solid phase, *i.e.* close to computational point (x_i, y_j). Due to the modelling of the solid phase, this condition is imposed at the computational point (x_i, y_{j-1}), resulting in the overestimation of the velocity Δu.

As a consequence of the solid modelling, though the highest error (in absolute) is found close to the centre of the flow when using the standard modelling of solids,

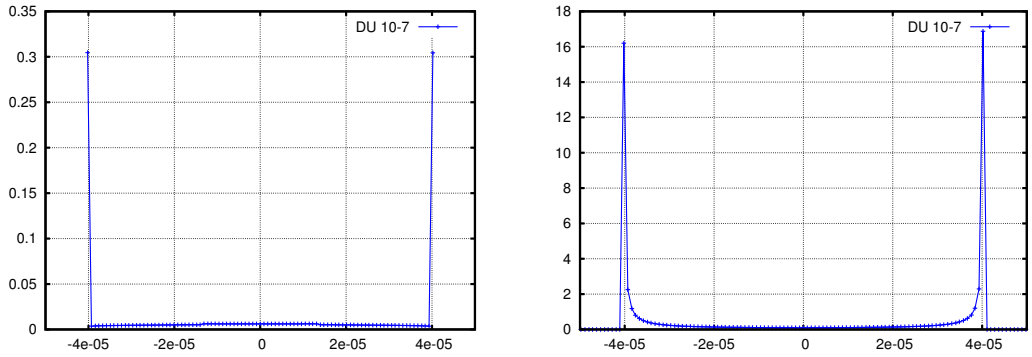

(a) (b)

Figure 2.31: Error between Gerris Flow Solver results and theoretical value for a two-phase Poiseuille flow with $\mu_2/\mu_1 = 2$ in slanted geometry. In abscissa y; in ordinate $\dfrac{|u_{\text{Gerris}} - u_{\text{theory}}|}{u_{\text{theory}}}$. (a) Standard modelling of solids, (b) fluid in the whole domain.

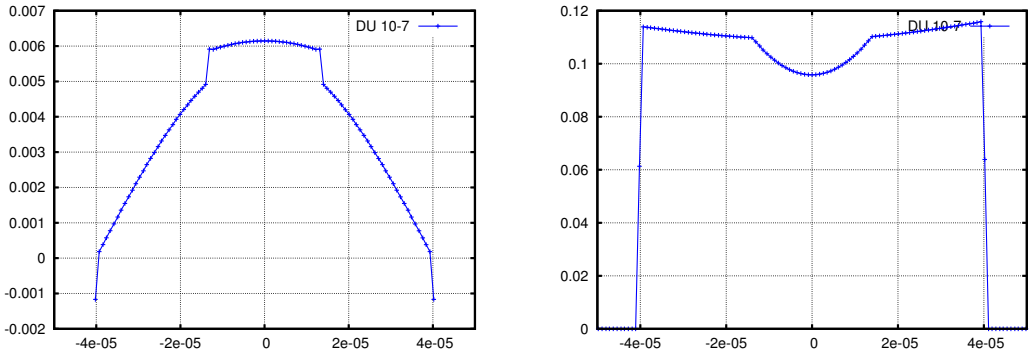

(a) (b)

Figure 2.32: Error between Gerris Flow Solver results and theoretical value for a two-phase Poiseuille flow with $\mu_2/\mu_1 = 2$ in slanted geometry. In abscissa y; in ordinate $\dfrac{|u_{\text{Gerris}} - u_{\text{theory}}|}{\max\limits_{y} u_{\text{theory}}(y)}$. (a) Standard modelling of solids, (b) fluid in the whole domain.

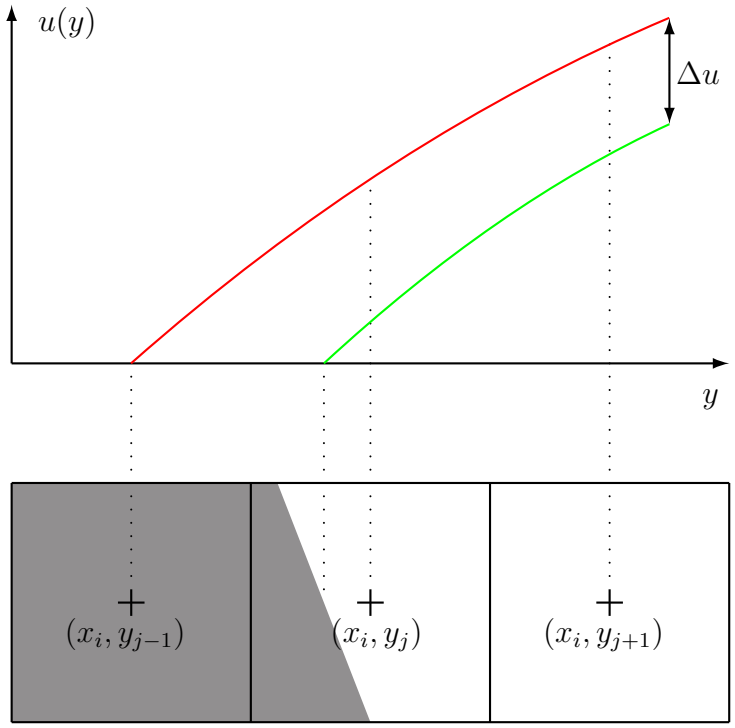

Figure 2.33: Difference between theoretical and computed velocities when modelling the solid phase with a no-velocity fluid. In the lower part three different cells are represented with in grey the solid phase and in white the fluid one, while the corresponding velocity field is shown in the upper part (green: the theoretical velocity field; red: the computed one).

when using a fluid modelling of solid phase the highest error occurs at the interface between fluid and solid phases (see Figure 2.32).

It can also be noted in Figure 2.31 that proportionally to the theoretical value, the error is higher close to the boundary in both modellings of the solid phase. The origin of such a high error is a result of the really low expected value, *i.e.* $(u_{\text{theory}})^{-1} \gg 1$. When removing the values close from the boundaries, one gets curves looking very much like those of Figure 2.27, but with higher error values for abscissae far from the centre of the flow.

2.2.4 Permeability of a randomly-generated porous medium

In order to address accuracy issues in 3D simulations of invasion in a porous medium, we measured the numerical permeability of a 3D random porous medium at different porosities.

Cancelliere *et al.* [170] compared numerical calculations of the permeability obtained from lattice-Boltzmann equation in three-dimensional porous geometries constructed by the random positioning of penetrable spheres of equal radii with previously established rigorous variational upper bounds (see Figure 2.34). Their results are however to be criticised [300] for while they present permeability results for porosities going down to 0.022, it has been shown that for the overlapping sphere models percolation cannot occur when $\phi \leqslant 0.03$. We will nonetheless compare our results to theirs.

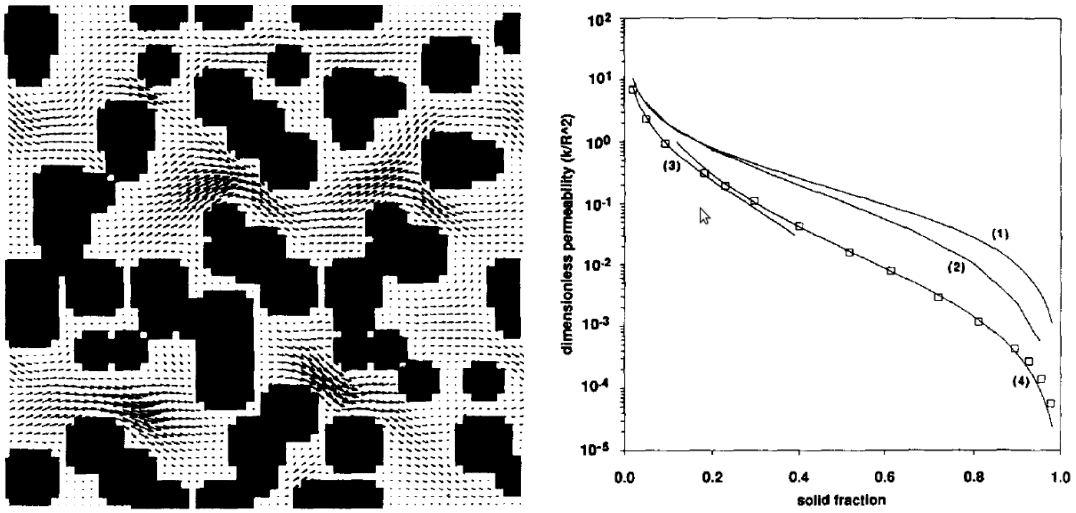

(a) (b)

Figure 2.34: Results from Cancelliere *et al.*, 1990. (a) 2D projection of 3D flow in a porous medium composed of penetrable spheres on a 64^3 lattice, (b) Dimensionless permeability k/R^2 as a function of solid fraction [170]; curve 1: Weissberg-Prager bound [301]; curve 2: Berryman-Milton bound[14][302]; curve 3: Brinkman estimate [303]; curve 4: Kozeny-Carman estimate [93].

[14] a refinement of the Weissberg-Prager bound

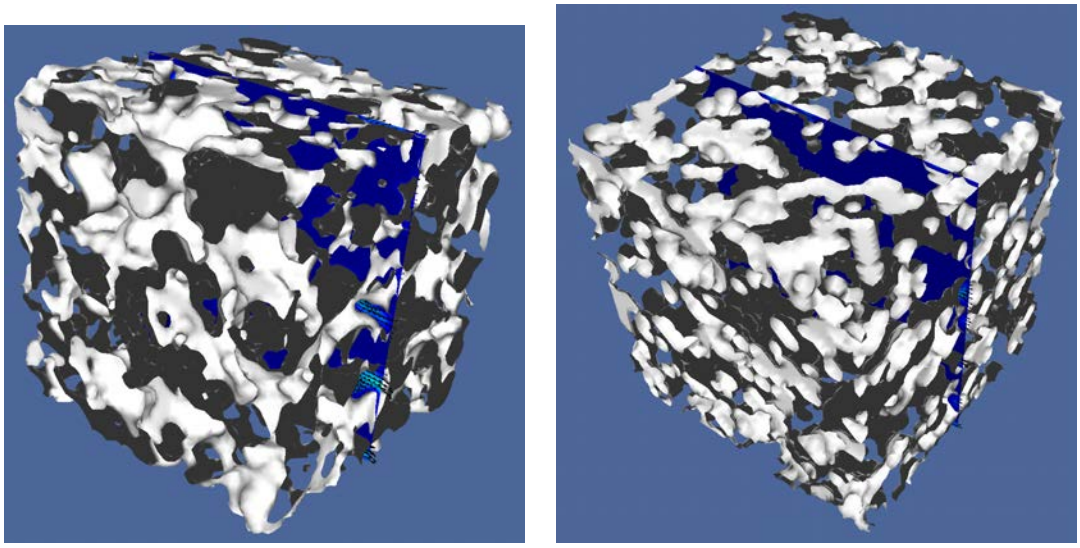

(a) (b)

Figure 2.35: Examples of randomly generated porous media. (a) $\phi = 0.1627$, (b) $\phi = 0.05333$.

Porous media are generated with spheres of radius 1/16 randomly spread on a macroscopic lattice of size 16^3. One should note that the chosen lattice is not the exact same one as that of Cancelliere *et al.*: while they consider the 3D projection of a face-centred-hypercubic (FCHC) lattice, only a FCC lattice is used here. The results will also be compared to another Volume-of-Fluid code (results obtained by S. Zaleski): ParisSimulator, a code jointly developed by Sadegh Dabiri[15], Gretar Tryggvason[16] and Stéphane Zaleski. Two examples of the resulting porous media are presented in Figure 2.35.

A volume force $\mathbf{g} = g\mathbf{e}_x$ is imposed in the resulting pores. The domain is considered periodic. The simulation is stopped when the permanent regime is reached (defined similarly to the Poiseuille-flow test, see above). The permeability is obtained from Darcy's law as

$$k = \frac{\mu U_{\text{Darcy}}}{\rho g}. \tag{2.53}$$

[15] http://www3.nd.edu/~sdabiri/

[16] http://www3.nd.edu/~gtryggva/

Similarly to [170], the results are confronted to an established rigorous variational upper bound and several estimates of the permeability.

Weissberg and Prager [301] were indeed able to calculate an upper limit of the permeability for a specific solid fraction (when considering every possible geometry) in the penetrable-sphere model

$$k^* \equiv \frac{-2\phi R^2}{9\ ln\phi} = \frac{\phi}{6\pi R n}, \tag{2.54}$$

where ϕ is the porosity, R the radius of the spheres and n the number of sphere centres per volume unit.

Brinkman presented an estimate of the permeability [303], which is applicable to a dilute collection of nonoverlapping spheres, *i.e.* at high porosity. This approximation can be written as

$$k = \frac{1}{6\pi R n}\left[1 + \frac{3}{4}\eta(1 - \sqrt{8/\eta - 3})\right] \tag{2.55}$$

with $\eta = 1 - \phi$ the solid fraction.

The second theoretical curve is the semiempirical Kozeny-Carman equation (medium- and low-porosity model) [162, 166, 167]

$$k = \frac{\phi^3}{6s^2}, \tag{2.56}$$

where the specific surface area s is given analytically for the penetrable-sphere model by $s = 4\pi R^2 n\phi$ [301]. This particular form of the Kozeny-Carman equation results from a model of a porous medium constructed from a collection of capillary tubes placed with equal probability in each of the three orthogonal directions.

One should note that, unlike the small η agreement with the Brinkman estimate, agreement with the Kozeny-Carman equation is not expected, in general: some porous media conform to it while others do not [170].

The solid phase is modelled by fluid with zero-velocity condition in both Gerris Flow Solver and ParisSimulator simulations. In the case of Gerris, two cases are considered: with and without the addition of the drag force introduced in section 2.1.7. As there was no notable difference between the results obtained with or without drag force for high porosity, those obtained with the addition of a drag force in the solid

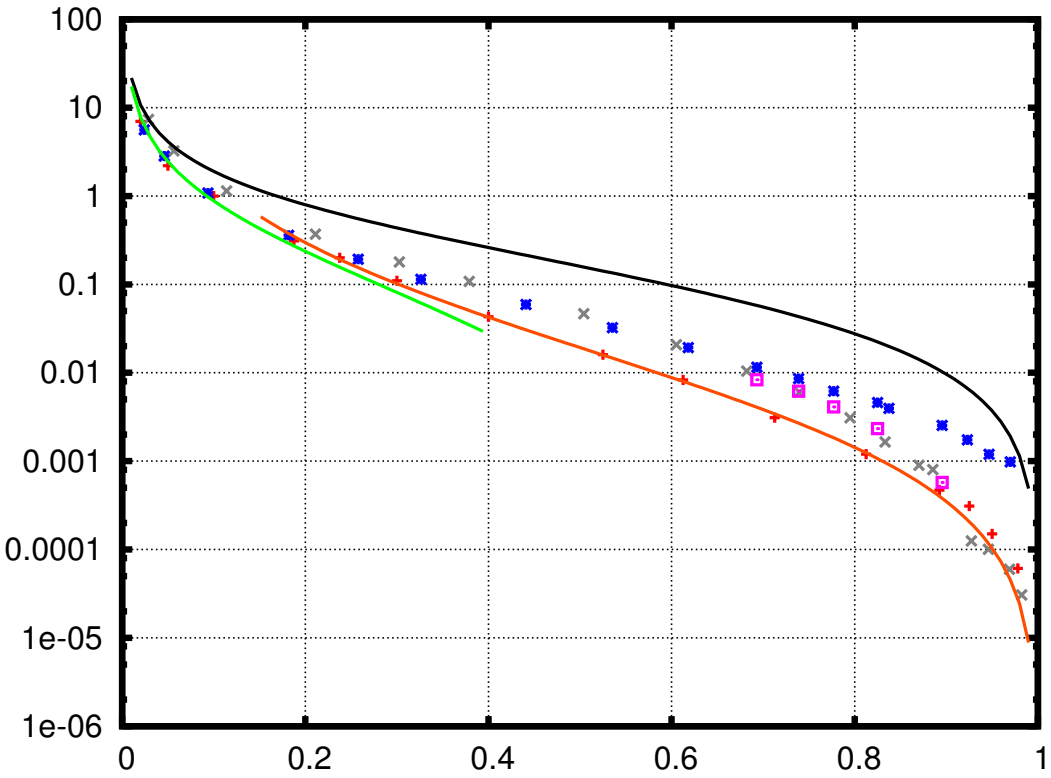

Figure 2.36: Dimensionless permeability k/R^2 as a function of solid fraction. Black curve: Weissberg-Prager bound; green curve: Brinkman estimate; orange curve: Kozeny-Carman estimate; blue data (✱): Gerris without drag force; magenta data (⊡): Gerris with additional drag force; grey data (×): ParisSimulator; red data (+): Cancelliere *et al.*, 1990 [170].

phase are presented only for low porosity ($\phi \leqslant 30\%$). The permeability results are presented in Figure 2.36.

It should be noted that these permeability results are consistent with the Weissberg-Prager bound whatever the case one chooses to consider. Indeed the numerical permeability is always lower than the one calculated with equation (2.54).

At high porosity, the results obtained with Gerris are in perfect agreement with the Brinkman estimate (equation (2.55)), as expected from the theory and similarly to Cancelliere *et al.*'s results. The results obtained with ParisSimulator are however slightly less in agreement.

At moderate porosity ($20\% \leqslant \phi \leqslant 70\%$), the calculated permeabilities are slightly higher than the Kozeny-Carman curve (equation (2.56)). The permeability obtained both with the Gerris Flow Solver and ParisSimulator is more or less twice to thrice both the Kozeny-Carman value and Cancelliere *et al.*'s results. One can wonder whether this higher permeability is a result of the problem presented in Figure 2.33, *i.e.* whether it is due to an overestimation of the velocity as a result of the imposition of the zero-velocity at the computational nodes rather than at the interface between fluid and solid phases. As this effect is corrected in ParisSimulator, it was easy to conclude that its influence in the higher permeability was negligible (at least for these porosities). Finally, it seems that this higher permeability is a result of the geometry and maybe of the way it was obtained (based on different lattices, see above).

At low porosity, the effect of the presence or the absence of a drag force to oppose the development of a velocity between two timesteps becomes noticeable. While in absence of such a drag force the permeability of the system decreases as $\ln k \sim -m\eta + p, (m,p) \in (\mathbb{R}^+)^2$ (as a reminder, $\eta = 1-\phi$), resulting in much too high permeabilities at low porosity and *a fortiori* when percolation cannot occur ($\phi \leqslant 3\%$, see above) due to numerical error, the calculated permeabilities follow the same curve whether obtained with Gerris or with ParisSimulator when adding this force. With decreasing porosities these permeabilities tend to come closer to the Kozeny-Carman estimate. For really low porosities ($\phi \leqslant 10\%$), the results obtained with ParisSimulator are even closer to the Kozeny-Carman curve than those of Cancelliere *et al.* Due to a lack of precision there is no data with the Gerris Flow Solver at such porosities.

A convergence study was realised by considering the variation of the measured permeability for different timesteps at a specific porosity, with unconcluding results. It was indeed impossible to observe any convergence of the measured permeability with decreasing timesteps (see Figure 2.37).

One can however conclude that for a huge range of porosities the permeability obtained with the Gerris Flow Solver seems satisfactory, from a qualitative point of view. One should nonetheless not forget to add the drag force in the solid phase for low porosity *i.e.* those of interest when considering flow in porous media. Provided one adds it, the model is validated by these results.

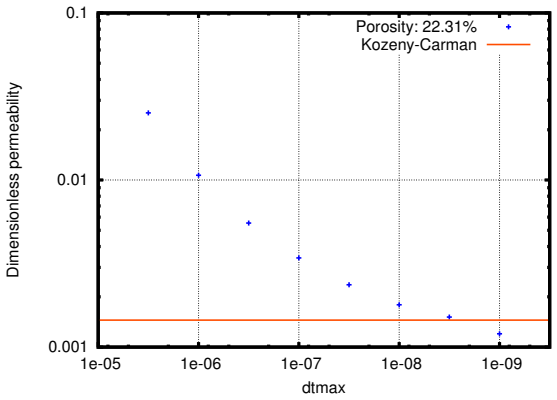

Figure 2.37: Dimensionless permeability k/R^2 as a function of maximum timestep.

2.3 3D simulations of invasion in oil-filled real porous media

Simulations of invasion of brine in 3D real porous media are realised. The considered rock is a sandstone whose geometry was obtained by X-ray microtomography.

2.3.1 X-ray microtomography

X-ray (micro)tomography ((μ)CT) is a means to view porous medium interior without destroying it. It was first developed for radiological imaging purposes in 1972 [304]. CT scanners measure the attenuation of a beam of X-rays as it is rotated around the object at angular increments within a single plane and then generate cross-sectional images of the objet [305]. Fourier transforms are then used to reconstruct a cross-sectional image. Three-dimensional images can finally be generated by interpolating among cross-sectional images. Considering three X-ray-based techniques for measuring fluid saturations (*i.e.* single-beam attenuation, xeroradiography[17] and CT), all these methods give similar results. However CT has a finer resolution at the millimeter scale (micrometer scale for μCT) [307].

[17]Xeroradiography is a type of X-ray in which a picture of the body is recorded on paper rather than on film. In this technique, a plate of selenium, which rests on a thin layer of aluminium oxide, is charged uniformly by passing it in front of a scorotron. [306]

During a CT scanner, X-rays penetrate a small volume of porous medium at different angles as the X-ray source rotates around the medium. The transmitted X-ray intensity is then recorded by a series of detectors. The measure focuses in each volume element (or voxel) on the linear attenuation coefficient defined in Beer-Lambert law [308, 309, 310]

$$\frac{I}{I_0} = \exp(-\xi h) \tag{2.57}$$

with I_0 the incident X-ray intensity, I the remaining intensity after the X-ray penetrates a slice of homogeneous sample of thickness h, and ξ the linear attenuation coefficient. This equation is easily modified for a heterogeneous medium and gives the energy transmitted along a particular ray path

$$\ln\left(\frac{I}{I_0}\right) = \int_0^L \xi(h(x,y))\,\mathrm{d}h \tag{2.58}$$

with $h(x,y)$ the 2D variation attenuation coefficient and L the path length from source to detector.

Though Beer-Lambert law considers only a narrow monochromatic X-ray beam, usual beams are polychromatic, resulting in possible imaging artefacts. Moreover the efficiency of the detectors is energy-dependent. Thus

$$I = \int_{e_l}^{e_h} \frac{\mathrm{d}I_0}{\mathrm{d}E}\varepsilon(E)\exp\left(-\int_0^h \xi(h(x,y))\,\mathrm{d}L\right)\mathrm{d}E \tag{2.59}$$

where $\mathrm{d}I_0/\mathrm{d}E$ is the spectral distribution of the incident radiation, $\varepsilon(E)$ the detector efficiency at energy E and e_l and e_h the boundaries of the relevant spectrum of energy. The attenuation coefficient now depends on the position and the energy.

In practice, one assumes that attenuation is uniform for all energies and equation (2.58) is used. As the images are consequently blurred, it is usual to add a convolution or filtering process in order to enhance the precision.

One should also note that the attenuation coefficient depends on both the electron density ρ and an effective atomic number Z [311]

$$\xi = \rho(a + bZ^{3.8}/E^{3.2}) \tag{2.60}$$

where a is called the Klein-Nishina coefficient [312] and b is a constant.

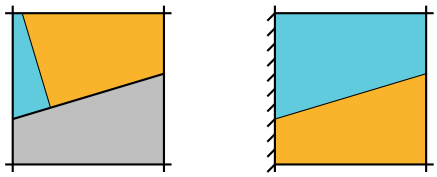

(a) (b)

Figure 2.38: (a) A 90° contact angle in a computational cell. In grey the solid phase, in blue the aqueous phase and in yellow the organic phase. (b) Contact angle with water-wetting condition imposed at the left boundary of a computational cell (boundary of the overall computational domain).

2.3.2 Invasion of porous media in both water-wetting and oil-wetting cases

The invasion of an oil-filled porous medium by water is simulated both in water-wetting and in oil-wetting case.

2.3.2.1 Contact angle in Gerris

In default mode (*i.e.* with the default modelling of the solid phases) and with the present implementation, Gerris only considers 90° contact angles (Figure 2.38(a)) at the interface between solid and fluid phases. It is however possible to consider different contact angles as boundary conditions (Figure 2.38(b)).

It could be possible to adapt this possibility of the boundary conditions to any solid/fluid interface, but it would require some modification in the source code. One should only take care to reconstruct first the solid/fluid interface inside the cell and second the fluid/fluid interface.

When modelling the solid phase as a fluid phase with no velocity (section 2.1.7), it is no longer possible to obtain 90° contact angle. Due to the modelling of the solid phase as a fluid, the software considers the solid phase to be either a part of the aqueous phase or a part of the organic one (Figure 2.39). Due to surface tension, the only possible cases are either totally wetting (the solid phase is then aqueous phase with no velocity) or totally non-wetting (the solid phase is then organic phase with

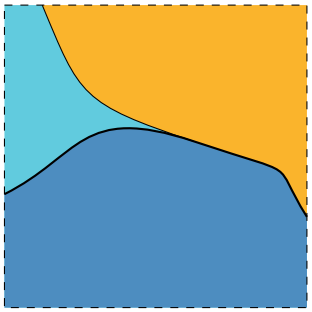

Figure 2.39: Totally wetting contact angle due to surface tension when modelling the solid phase with a zero-velocity fluid phase. In light blue the aqueous phase, in darker blue the solid phase and in yellow the organic phase.

no velocity). Note also that any connected subregion of the solid phase only has one wettability by construction[18]. Disconnected subregions can however present diverse wettabilities.

2.3.2.2 Simulation of a single pore

The geometry was obtained through the successive steps of X-ray microtomography, image analysis and segmentation all operated by TOTAL researchers. The 3D rock is Bentheimer sandstone with a permeability $k \sim 2$ Darcy. Only part of the overall geometry file is considered, *i.e.* 32^3 voxels corresponding to a single pore (see Figure 2.40). As the typical size of a voxel is $2.88\,\mu$m, the simulation size is $92.16^3\,\mu\text{m}^3$. The simulation is realised with 64^3 computational cells.

The injection is realised at constant massflow from one side of the cubic domain. The opposite face is imposed an outflow boundary condition

$$p = 0, \tag{2.61a}$$

$$\partial_x u = 0. \tag{2.61b}$$

Periodic boundary conditions are imposed to the other faces of the domain. The viscosity ratio is $M = \frac{\mu_{\text{water}}}{\mu_{\text{oil}}} = 1/2500$, the capillary numbers are $\text{Ca}_{\text{oil}} \sim 10$ and $\text{Ca}_{\text{water}} \sim 4 \times 10^{-3}$, and the Reynolds numbers $\text{Re}_{\text{oil}} \sim 8 \times 10^{-5}$ and $\text{Re}_{\text{water}} \sim 2.5$.

[18]The fluid properties (viscosity, density, marker function) are constant inside any arcwise connected subset of the solid phase (see section 2.1.7).

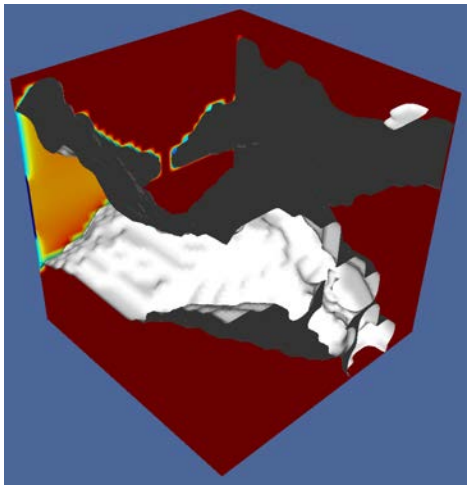

Figure 2.40: A single pore of size $92.16^3\,\mu m^3$ obtained through X-ray μCT as considered by the Gerris flow solver. The white face of the interface is directed towards the void space of the porous medium. Note that periodic boundary conditions are used.

The computational time to breakthrough is 19 hours on 64 cores corresponding to 25900 timesteps in the case of oil-wetting porous medium (contact angle $\theta = 180°$), and 22 hours corresponding to 26900 timesteps in the case of water-wet porous medium ($\theta = 0°$).

Logically, the time to breakthrough is shorter in the oil-wetting case than in the water-wetting case (Figure 2.41). As the fluid fills a bigger part of the pore in the water-wetting case (Figure 2.42), both the average position of the interface and the position of the tip of the finger will move less rapidly in the pore and be closer to the entry face at a given time than in the oil-wetting case.

Moreover, due to wettability effects, the shape of the injected finger will be closer to that of the pore in the water-wetting case (Figure 2.43). Indeed, in the oil-wetting case, surface tension will tend to smooth the shape of the finger.

In a second time, the viscosity ratio was varied (from $M = 1/2.5$ to $M = 1/2500$) in order to study its effect on the modification of the breakthrough time. The results showed that the physical time to breakthrough in a single pore does not change much when changing the viscosity ratio, especially in the oil-wetting case (Figure 2.44).

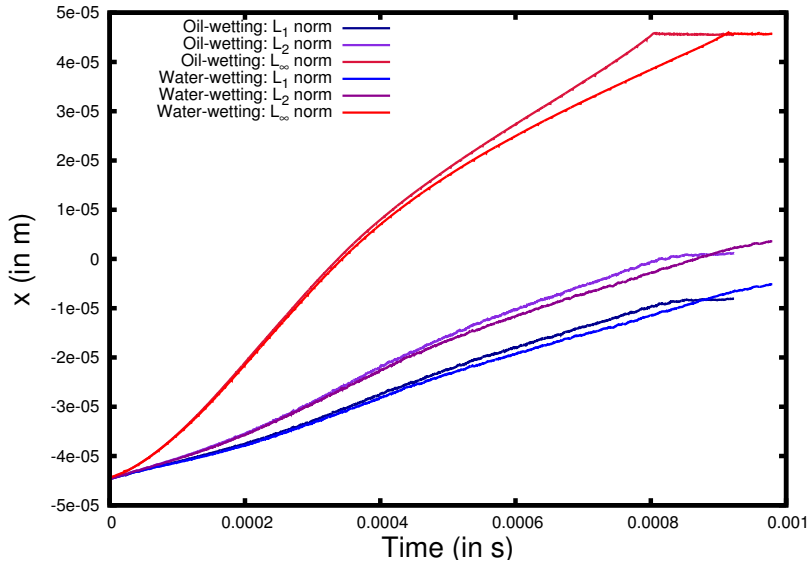

Figure 2.41: Position of the interface during injection in a single pore in both oil-wetting and water-wetting cases for $M = 1/2500$. In red: position of the tip; in purple: average position calculated with L_2 norm; in blue: average position calculated with L_1 norm.

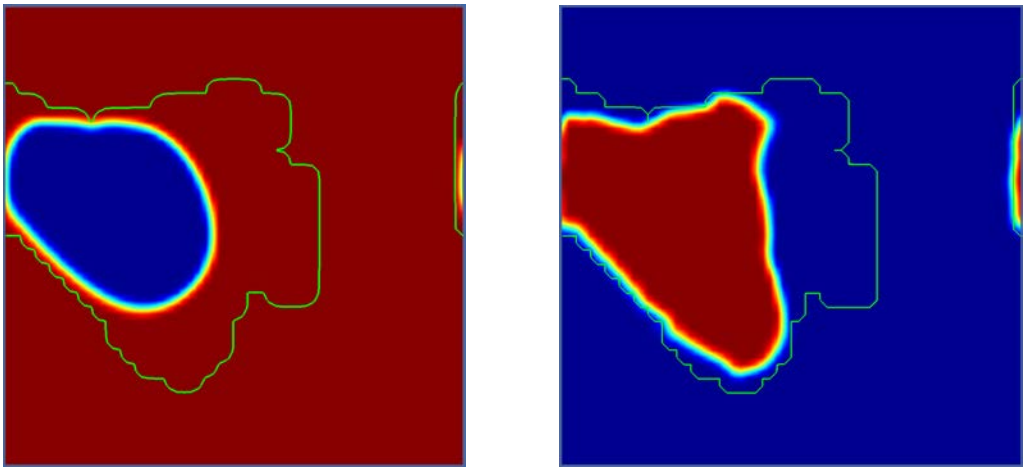

(a) (b)

Figure 2.42: The pore space is more filled at breakthrough in the water-wetting case. Sections at abscissa $x = 23.04 \times 10^{-6}$ m. The interface between the solid matrix and the void space is represented by the green curve. The color of the solid matrix should be ignored (based on a computational trick...). (a) In blue the aqueous phase and in red the organic one (oil-wetting case). (b) The reverse (water-wetting case).

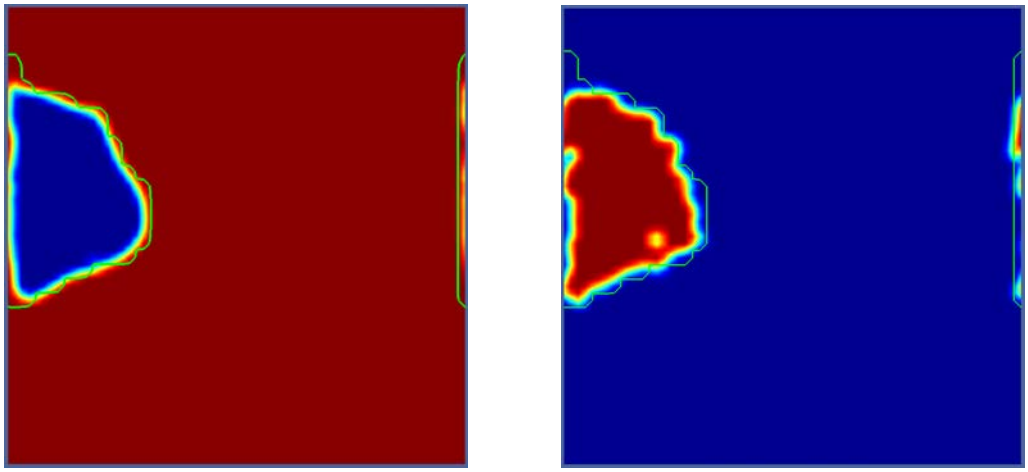

(a) (b)

Figure 2.43: The shape of the injected finger will be closer to that of the pore in the water-wetting case. Sections at abscissa $x = -23.04 \times 10^{-6}$ m. Same colors and wettabilities as those in Figure 2.42.

M	CPU time	Number of timesteps
1/2.5	27790 s	12510
1/25	30540 s	10040
1/250	34316 s	12030
1/2500	68744 s	25870

Table 2.3: CPU time to breakthrough in oil-wetting case.

Finally, it should be noted that the CPU time required to reach breakthrough is increasing for decreasing viscosity ratios (Table 2.3). It should also be noted that though this increase is small for high viscosity ratios ($M > 1/250$), it takes twice as much time to reach breakthrough when $M = 1/2500$ as for $M = 1/250$ (more iterations required to converge, which is bad for the overall scalability).

2.3.2.3 Invasion of a 3D porous medium with several pores

A 3D porous medium with several pores is then considered.

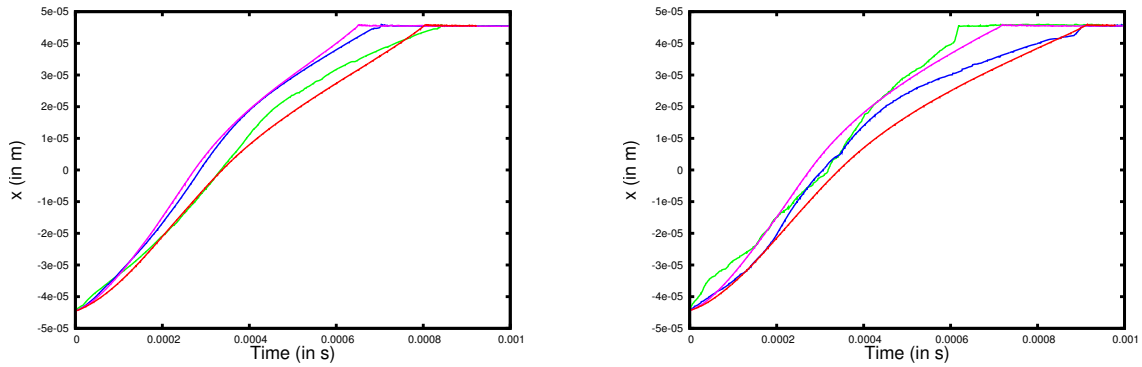

(a) (b)

Figure 2.44: Position of the tip of the interface during injection in a single pore for different viscosity ratios. In green $M = 1/2.5$, blue $M = 1/25$, magenta $M = 1/250$, red $M = 1/2500$. (a) Oil-wetting case, (b) water-wetting case.

Case with 256^3 voxels A geometry file with 256^3 voxels is considered. The physical size of the simulation is thus $737.28^3\,\mu\text{m}^3$, meshed with 256^3 computational cells.

The injection is realised at constant massflow from one side of the cubic domain. The opposite face is imposed an outflow boundary condition. Periodic boundary conditions are imposed to the other faces of the domain. The viscosity ratio is $M = \frac{\mu_{\text{water}}}{\mu_{\text{oil}}} = 1/10$, the capillary number of the invading fluid is $\text{Ca} \sim 3 \cdot 10^{-2}$, and the Reynolds number[19] $\text{Re} \sim 100$. The simulation is realised with both 8 cores and 64 cores on the cluster *babbage2*, to compare CFL numbers and Z/np.

One can observe that the number of cell updates per second and per core Z/np is multiplied by a factor 2 when using 64 cores compared to simulations realised with 8 cores (Figure 2.45). This increase is quite astounding if we also consider that moving from 8 to 64 cores implies using several nodes instead of only one, with all the subsequent increase of connection times. An explanation would be that the low value of Z/np for 8 cores results from a saturation of the cache memory, due to a geometry overload.

[19]As the CFL number varies as $\text{CFL} \propto \text{Ca}^{\gamma-1/2}\text{Re}^{1/2}$ (equation 2.46), it was chosen to consider arbitrarily high Reynolds number in order not to reduce the CFL number too much and to allow to reduce the capillary number in a second step with reasonable additional CPU time.

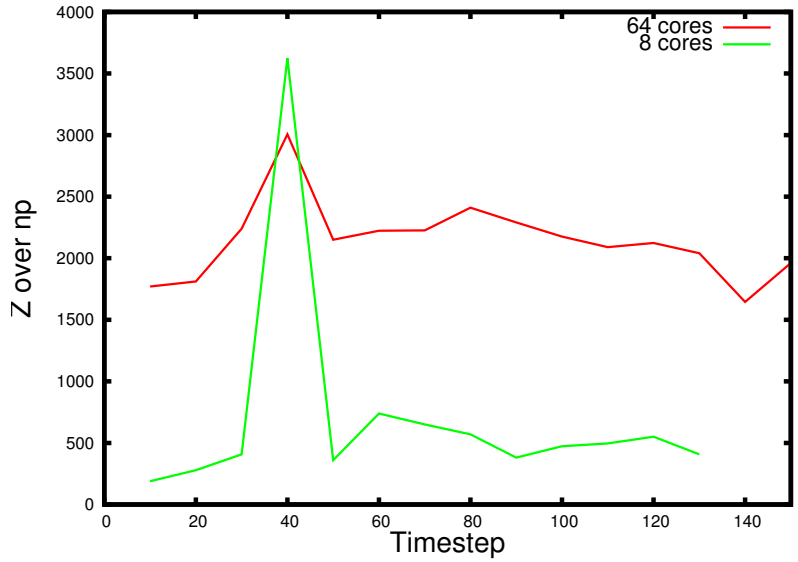

Figure 2.45: Comparison of Z/np when using 8 or 64 cores on cluster *babbage2*. The data are the average over the last ten timesteps. In green 8 cores, in red 64 cores.

It can also be noted that when using 64 cores the number of cell updates per second and per core is suddenly reduced by a factor 2 to 4 after 500 timesteps (Figure 2.46). This collapse of the overall computing performance does not seem to be a result of a drastic change in the flow, and is consequently for now unexplained. For high number of timesteps, a sudden increase (of shape close to a Dirac function) is observed at regular interval. It is thought that the simulation has to synchronise itself with the clock interval at which an output is generated. As a consequence it uses a low timestep (compared to the usual ones), and the Poisson solver converges much faster.

The same simulation was realised on clusters *Jade* at *Centre Informatique National de l'Enseignement Supérieur* (CINES, Montpellier) and *Rostand* at *Centre Scientifique et Technique Jean-Féger* (Pau) with better results (Figure 2.47): amongst other considerations, the sudden decrease of the velocity after 500 timesteps does not occur on any of those clusters.

Concerning the CFL number, obviously it does not depend on the number of cores (Gerris is a deterministic code, Figure 2.48(a)). Note that the curve for 64 cores is hidden at lower times by the curve for 8 cores. It should also be noted that the value

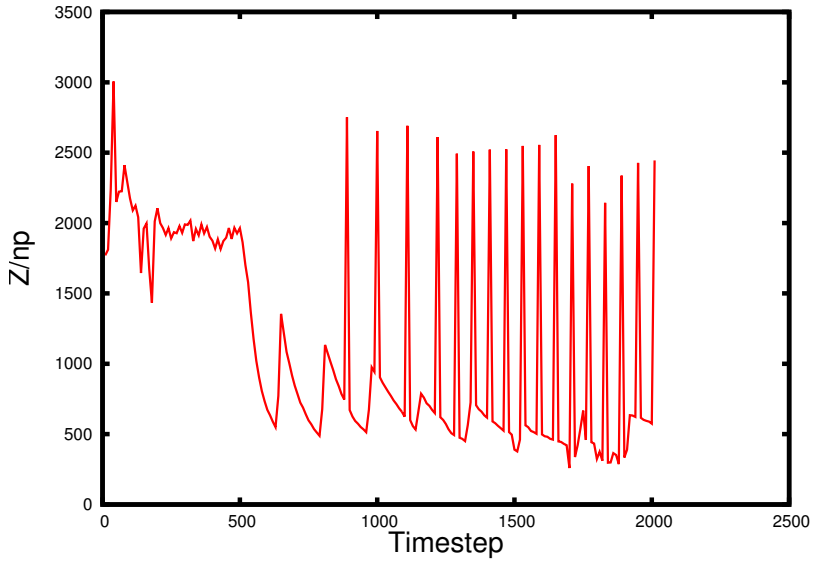

Figure 2.46: Number of cell updates per second and per core when using 64 cores on cluster *babbage2*. The data are the average over the last ten timesteps.

of the CFL number is quite good, as it stays quite close to the best possible value for VOF methods (*i.e.* 0.5, see Figure 2.48(b)).

Finally, obvisously the CFL number depends on the characteristics of the simulations, even for slight modifications. For example, the simulations whose CFL numbers are represented in Figure 2.49 differ only by how the meshing is adapted (everything else is unchanged). The change of cluster can be overlooked when considering that the simulation leading to the results obtained on cluster *Rostand* was also realised on cluster *Jade* with minor modifications.

Case with 400^3 voxels We consider a geometry file with 400^3 voxels, *i.e.* a simulation of physical size $1.152^3\,\mathrm{mm}^3$, meshed with 1024^3 computational cells. A cross section of the geometry is presented in Figure 2.50 for both ParisSimulator modelling (picture 2.50(a)) and Gerris modelling (picture 2.50(b)).

The injection is realised at constant massflow from one side of the cubic domain. The opposite face is imposed an outflow boundary condition. Periodic boundary conditions are imposed to the other faces of the domain. The viscosity ratio is $M = \frac{\mu_{\mathrm{water}}}{\mu_{\mathrm{oil}}} = 1/10$, the capillary number of the invading fluid is $\mathrm{Ca} \sim 3 \cdot 10^{-3}$, and the

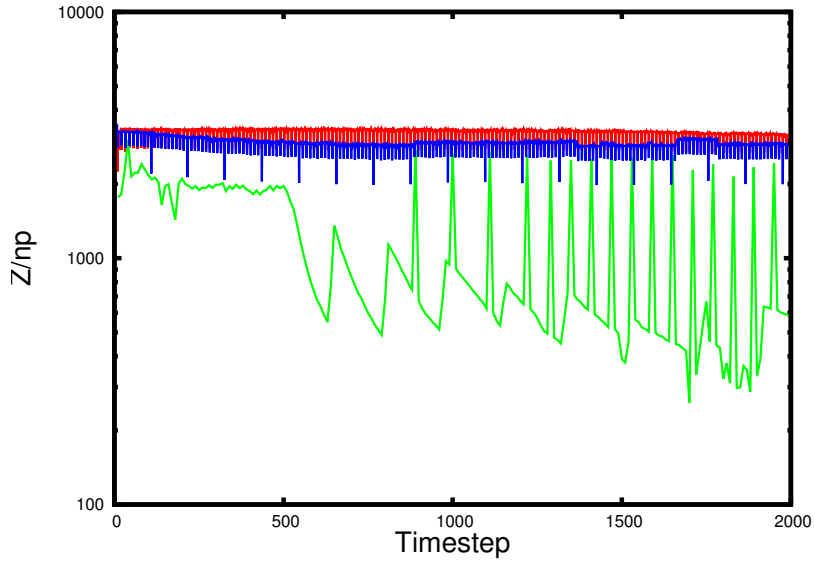

Figure 2.47: Number of cell updates per second and per core when using 64 cores. In green results with cluster *babbage2*, in red *Rostand* and in blue *Jade*.

Reynolds number Re ~ 250 (based on a lengthscale equal to a quarter of the domain size, as the exact typical pore size is unknown.). The simulation is realised on cluster *Rostand* on 400 cores. Breakthrough is reached after one day of wall-clock CPU time. The development of the fingering process is presented in Figure 2.51.

On these pictures, the interface between injected and receding fluids is represented. The color of the interface depends on the velocity of the fluid (closer to blue is slower while closer to red is faster). The geometry-induced fingering process is obvious, as one could expect.

The same simulation is finally realised for varying capillary numbers at constant Reynolds number. The different capillary numbers range from $3 \cdot 10^{-2}$ down to $3 \cdot 10^{-5}$. The position of the tip of the most-advanced finger (can vary during the simulation) is presented in Figure 2.52.

For decreasing capillary number, the velocity of the tip of the most-advanced finger decreases substantially. Due to this drastic decrease of the invasion velocity, one can wonder whether, though the unwanted numerical velocity that is created between two timesteps inside the solid matrix is small (see section 2.1.7), its amplitude is high enough to allow the invading fluid to penetrate the fluid-modelled solid matrix.

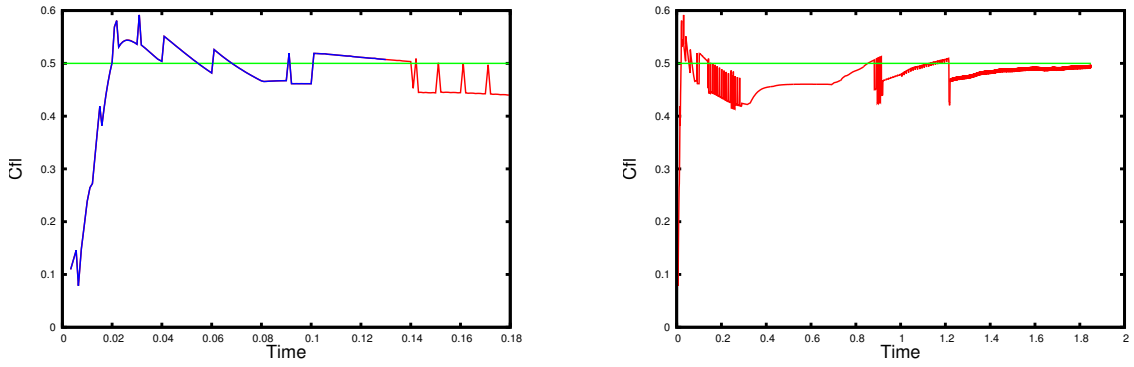

(a) (b)

Figure 2.48: (a) CFL number for different number of cores. In blue 8 cores, in red 64 cores. (b) CFL number when using 64 cores on cluster *babbage2*.

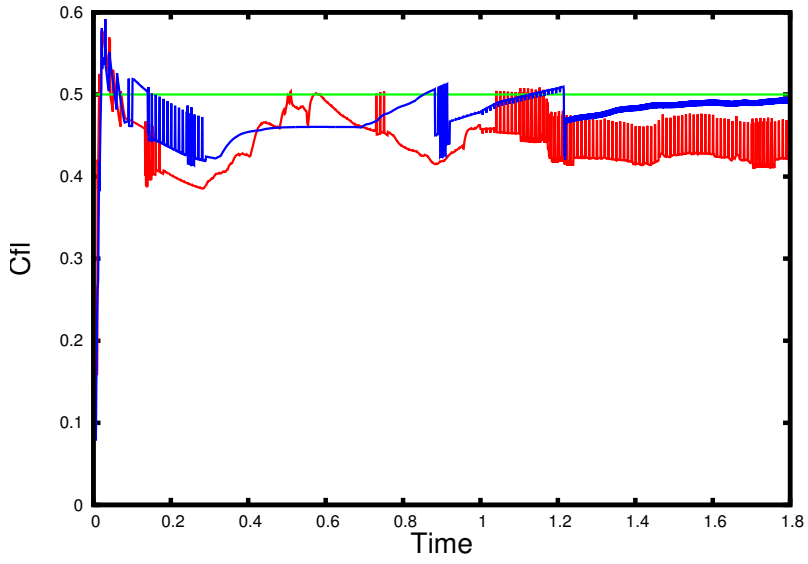

Figure 2.49: CFL number when only changing the adaptivity. In blue results when adapting on the marker function and all the components of the velocity (*babbage2*), in red when adapting on the marker function and the geometry (*Rostand*).

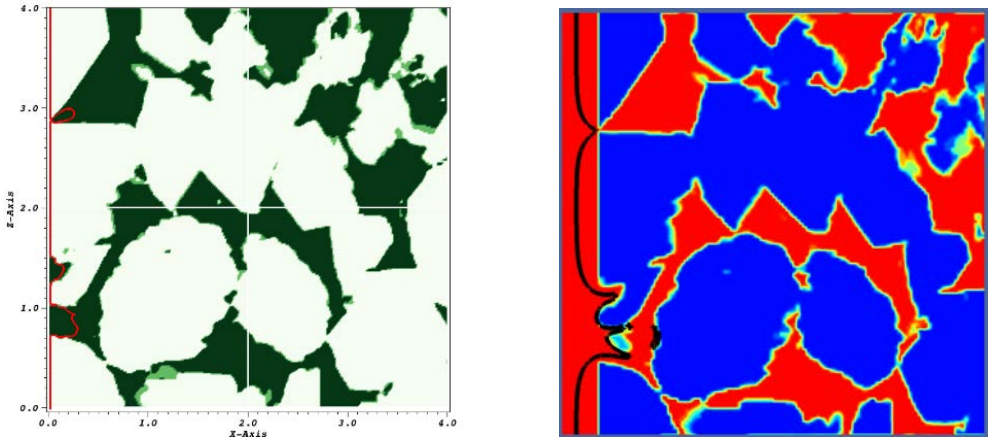

(a) (b)

Figure 2.50: Cross section of the overall geometry obtained by X-ray μCT. (a) Modelled by ParisSimulator, (b) modelled by Gerris.

The pictures presented in Figure 2.53 contradict this hypothesis. It can however be observed in those pictures that the invading fluid creates thicker fingers for lower capillary number. This seems logical because as the effect of surface tension is more important in those cases it will tend to reduce the curvature of the fingers. Thus the invading fluid fills the pores more extensively, *i.e.* expels a higher part of the receding fluid from the pores it invades. This effect will create the well-known Bretherton films whose thickness t varies as[20] $\mathrm{Ca}^{2/3}$ [313, 314].

2.4 Conclusion

The Gerris Flow Solver, written in C, was used to solve two-phase Navier-Stokes equations for an incompressible flow in a quad/octree adaptive mesh. In this code, the time-delayed discretisation uses Helmholtz-Hodge decomposition for the velocity and the pressure field is obtained by averaging the multigrid Poisson solver on all faces of a each mesh cell. Advection of the interface is realised with the Volume-of-Fluid

[20]To be precise, in Hele-Shaw cells, $t = 1.337\,\mathrm{Ca}^{2/3}[1 + \epsilon^2(\frac{\pi}{4}f'' + (f')^2)] + O(\epsilon^2\mathrm{Ca}, \mathrm{Ca}^{4/3})$ [110], where f describes the interface ($x = f(y)$ on Figure 1.13), ϵ is the ratio of gap width to transverse characteristic length ($\epsilon = b/\lambda_f$ with λ_f fingering wavelength).

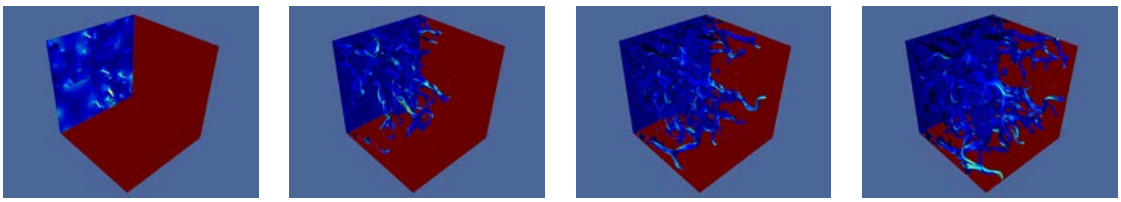

t = 0.107 t = 0.534 t = 0.961 t = 1.388

(a)

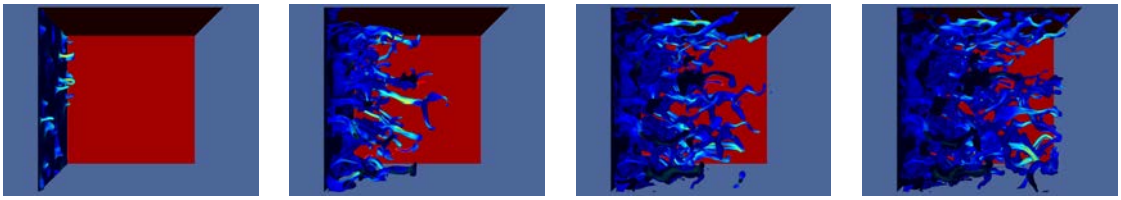

t = 0.107 t = 0.534 t = 0.961 t = 1.388

(b)

Figure 2.51: Time series of invasion of a real rock for $M = 1/10$, Ca $\sim 3 \cdot 10^{-3}$ and Re ~ 250: (a) observed from afar, (b) observed from the top. The dimensionless time (t = 1 at breakthrough) is precised below the pictures.

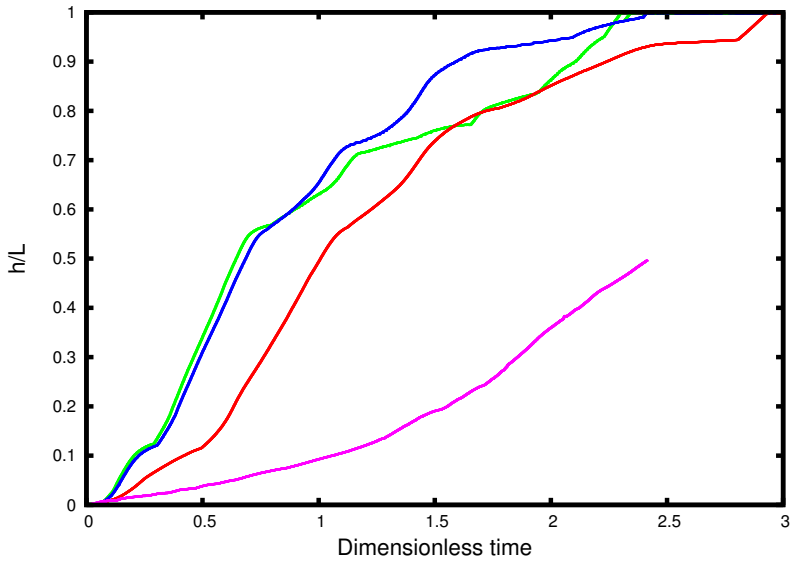

Figure 2.52: Dimensionless abscissa (0 corresponds to the left-hand side of the box, 1 to the right-hand side) of the tip of the most-advanced finger as a function of dimensionless time. Green curve: Ca $\sim 3 \cdot 10^{-2}$; blue curve: Ca $\sim 3 \cdot 10^{-3}$; red curve: Ca $\sim 3 \cdot 10^{-4}$; magenta curve: Ca $\sim 3 \cdot 10^{-5}$.

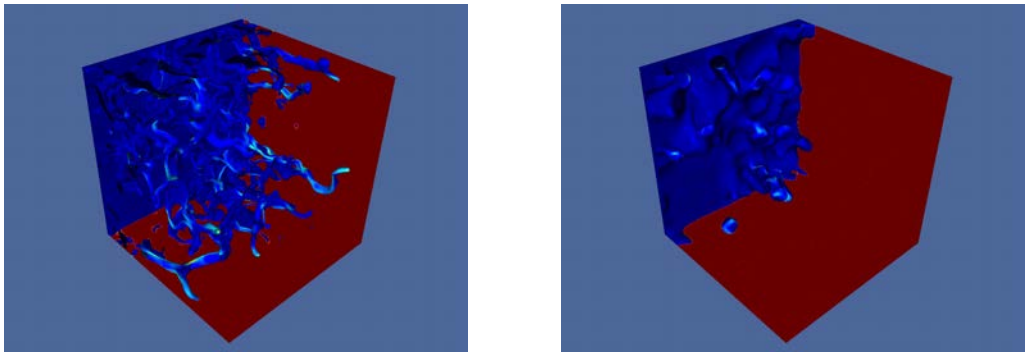

(a) (b)

Figure 2.53: Invasion of a real rock at dimensionless time $t = 2.25$ for $M = 1/10$ and $\mathrm{Re} \sim 250$ observed from afar: (a) $\mathrm{Ca} \sim 3 \cdot 10^{-3}$, (b) $\mathrm{Ca} \sim 3 \cdot 10^{-5}$.

method and surface tension is obtained with a CSF approach. Gerris can be used in parallel and allows adaptive mesh refinement.

Two different modellings of the solid phase are considered: the default one and the "virtual solids" method. As the use of the second approach results in a better computational speed, with reasonable accuracy, the default modelling of solids is not used in the remainder of the study.

In 3D invasion of porous media, the wall-clock CPU time to breakthrough (obviously) varies as the inverse of the CFL number. However, it was shown that the CFL number varies as $\mathrm{CFL} \propto \mathrm{Ca}^{\gamma}\mathrm{La}^{1/2} = \mathrm{Ca}^{\gamma-1/2}\mathrm{Re}^{1/2}$ with $\gamma > 1/2$ depending on the fractal aspect of the fingering process. This is bad news, when one considers that flows in porous media occur at low Reynolds and capillary numbers.

Simulations of real rocks were realised in three dimensions with very promising results. It was however not possible to attain realistic Reynolds and capillary numbers, due to the dependency of the CFL number to both dimensionless numbers. It was nonetheless possible to simulate flows in domains of physical size up to 1 mm3 in reasonable CPU time.

From such simulations, it would be possible to obtain absolute and/or relative permeabilities of rocks, to be used in Darcy-scale studies of viscous fingering.

CHAPTER 3

2D viscous fingering

A variety of pattern forming phenomena, ranging from the growth of bacterial colonies to snowflake formation, share similar underlying physical mechanisms and mathematical structure. Viscous fingering, considered here, is a paradigm for such phenomena. Dense-branching or dendritic morphologies are amongst the most common forms of microstructural patterning in systems driven out of equilibrium [315, 316, 317]. By understanding the formation kinetics and the interplay of system parameters one could provide understanding of growth and form in nature as well as to achieve improved control and efficiency in a variety of physical, biological, and engineering systems. Prediction and control of the shape of emergent patterns are both difficult due to the nonlocality and nonlinearity of the system.

In a Hele-Shaw cell [109], Saffman and Taylor [114] demonstrated, using linear stability theory, that when a fluid of lower viscosity is injected into a fluid of higher one at a constant pressure or injection rate, the interface becomes unstable and develops a fingered pattern. Though surface tension suppresses the growth of perturbations, linear theory predicts that successively higher wave number perturbations become unstable as the air bubble grows (Figure 3.1). Nonlinear interactions amongst different

modes then become important and the nonlinear evolution leads to the usual dense-branching morphologies [114, 176, 177, 318, 319, 320, 321, 231, 322].

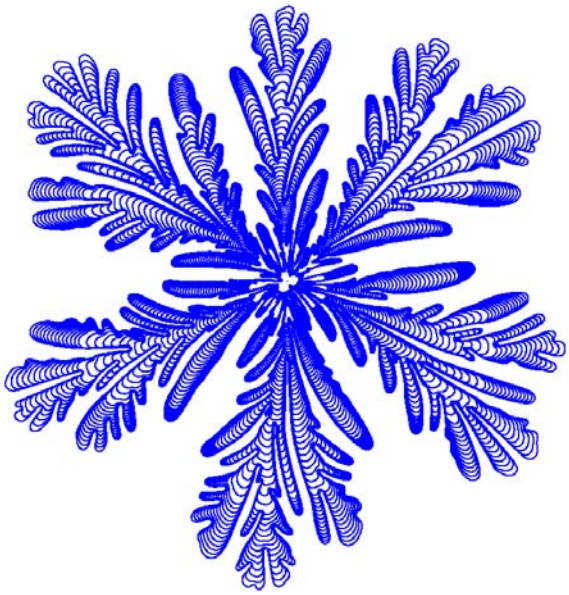

Figure 3.1: Numerical simulation of a highly ramified bubble in the nonlinear regime expanding under a constant flux. A time sequence of bubble shapes is shown that tends towards a dense-branching morphology. For all we know this is the largest and most ramified viscous fingering simulation to date and uses the algorithm developed by Li *et al.* [322]

In a theoretical study of viscous fingers in 90° sector geometry, Brener *et al.* [323] suggested that if the injection rate instead scales with time like $t^{1/3}$ it may be possible to obtain self-similar growing single fingers for finite surface tension, thus avoiding the dense-branching morphology regime. Indeed, this is the unique scaling for which non-linear self-similar evolution can be obtained [323, 324, 325].

When one considers the limit in which the viscosity of one fluid and the surface tension tend to zero, the equations governing the flow are quite simple. Whilst the pressure field p satisfies the Laplace equation [326], the interface will move according to Darcy's law (a precise derivation can be found in Section 1.2.6, paragraph Proof of equation 1.48). With adequate boundary conditions, these equations precisely describe the interface between the two fluids.

This problem is formally close both to Diffusion-Limited Aggregation (DLA) and viscous flows in porous media. Indeed, Witten and Sander got the same set of equations when they tried to derive a mean-field equation for their DLA [327]. It is also possible to derive Darcy's law from the Navier-Stokes equations in a porous medium in both single- and two-phase cases [101, 102, 108] (a Hele-Shaw cell is then partially[1] equivalent to a porous medium of permeability $b^2/12$ where b is the thickness of the cell).

While the cell initially used by Saffman and Taylor was a long narrow Hele-Shaw channel with parallel walls, more recent works have considered radial [328, 329, 330, 331] and wedge [324, 332, 333] geometries, alongside the historical linear one [175, 177, 334, 335, 336], in both experimental and numerical ways. Because of the typical fingering that can be observed in DLA simulations [194, 200], flow in porous media experiments [195, 226, 295, 337, 338] and flow in a Hele-Shaw cell [110], interest was historically focused on the fractal aspect of these fingers [339, 340].

Sharon *et al.* [198] showed, while studying the coarsening of viscous fingering, that in the case of central injection of a less viscous fluid in a Hele-Shaw cell filled with a more viscous fluid, the fractal dimension of the resulting fingering was close to the one of circular DLA (both measured [341] and theoretical [342]).

Contents

3.1 Viscous fingering in a Hele-Shaw cell 162

3.1.1 Growth in a Laplacian field 163

3.1.2 Linear stability analysis of the front between two fluids of different viscosity 163

3.1.2.1 The basic flow 164

3.1.2.2 The disturbance of the interface 165

3.1.2.3 Continuity of the normal velocities at the interfaces 166

3.1.2.4 The pressure jump at the interface due to surface tension 166

3.2 The existence of stable curved fronts 167

[1] As the capillary forces act on different length scales, the role played by the interface is different.

3.2.1 Isotropic case 167
3.2.1.1 Linear channel 167
3.2.1.2 Sector-shaped cells 170
3.2.1.3 Circular geometry 172
3.2.2 Non-isotropic case 172
3.2.2.1 The dendrite 172
3.2.2.2 The anomalous Saffman-Taylor finger 172
3.3 Stability of the curved fronts 175
3.3.1 Isotropic case 175
3.3.2 Anisotropic case 175
3.4 Implementing Darcy flows in the Gerris Flow Solver . . 177
3.5 Saffman-Taylor fingering in a Hele-Shaw cell with central injection 178
3.5.1 Equations governing the flow 178
3.5.2 Effects of mesh-induced noise and viscosity ratio 179
3.5.2.1 Comparison with experimental results 182
3.5.3 Zero-pressure approximation in the less viscous fluid 182
3.5.4 Interface length and area of the resulting cluster 183
Third scaling coefficient? 185
3.5.5 Accuracy of the asymptotic coefficient 185
3.5.6 Fractal dimension 186
3.5.7 Polar modelisation of viscous fingering 187
3.6 Conclusion 190

3.1 Viscous fingering in a Hele-Shaw cell

This section is mainly extracted from reference [115] with minor modifications.

3.1.1 Growth in a Laplacian field

An interface separates two regions of a plane. Let us consider the case where the pressure is constant in one region (labelled 1, viscosity μ_1) and satisfies the Laplacian in the other one (labelled 2, viscosity $\mu_2 > \mu_1$)

$$\nabla^2 p = 0. \tag{3.1}$$

Interest is focused on situations in which the interface between the two fluids of distinct viscosities moves towards region 2 in a local gradient of p with a normal velocity

$$v_n \propto \mathbf{n} \cdot \nabla p, \tag{3.2}$$

with $\mathbf{n}$ the normal unit vector to the interface directed towards the fluid of higher viscosity. The displacement of the interface modifies the field p with an effect on the interface velocity. This process leads to the so-called Saffman-Taylor instability.

If one considers a situation where the two fluids are initially separated by a flat interface with a small perturbation of lengthscale L, it is easy to determine that the curves of constant values of p will be parallel lines, only distorted in front of the bump (Figure 3.2). Due to a property of Laplacian fields, this distortion will only affect these curves on a lengthscale of order L. The gradient of p is consequently locally larger in front of the protrusion. The same occurs to the velocity and the amplitude of the protusion will grow: the interface is unstable. One should however note that if the fluids were flowing in the opposite direction, the protusion would tend to disappear.

Ideally, the more pointed the protrusion the larger the gradient and the velocity. Several works consequently have suggested that the instability will then lead to the formation of cusp-like singularities in finite time [343, 344, 345]. However in real experiments, the interface is stabilised at small scales due to surface tension.

3.1.2 Linear stability analysis of the front between two fluids of different viscosity

Linear stability analysis is a common tool allowing to predict whether a flow is stable. As this analysis has to be performed with regard to perturbations of all spatial

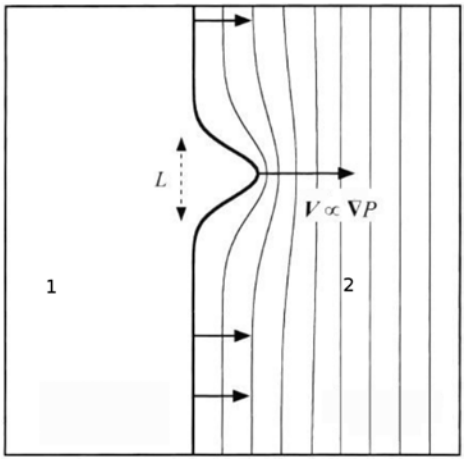

Figure 3.2: Sketch of the lines of constant values of the scalar field p in front of a local disturbance of a plane front (in the absence of surface tension). [115]

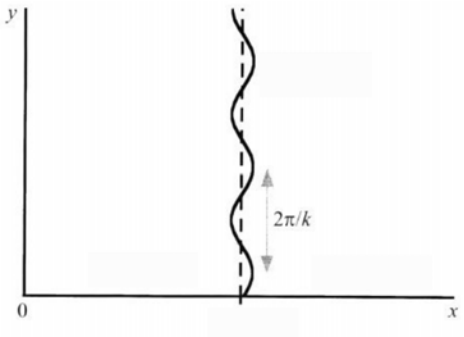

Figure 3.3: Definition of the axes for the stability analysis. [115]

periodicities, a straight interface with a periodic disturbance of arbitrary wave-vector **k** is considered [176].

3.1.2.1 The basic flow

A Hele-Shaw cell is modeled by an infinite plane in which the two fluids occupy two half-planes separated by a linear interface (dashed line on Figure 3.3). In the basic state the two fluids move along the x-axis with velocity

$$u_i^0 = U, \tag{3.3}$$

where $i = 1$ or 2 respectively for the two fluids.

By integrating Darcy's law, one can find the pressure distribution

$$p_i^0 = \frac{U}{K_i}(x - Ut), \tag{3.4}$$

where $p = 0$ on the interface located at $x = \zeta = Ut$ and $K_i = -b^2/(12\mu_i)$.

3.1.2.2 The disturbance of the interface

A sinusoidal disturbance of wave-vector $\mathbf{k}$ is imposed on the interface, in order to determine whether the amplitude of the disturbance will grow (unstable) or decrease in time (stable). A small disturbance amplitude $\epsilon \exp(\sigma t)$ is chosen. The front is stable if $\sigma \leqslant 0$ for all k. On the contrary, the flow will be unstable for all values of k such that $\sigma > 0$. At time t the interface is

$$\zeta = Ut + \epsilon e^{\omega t} \sin ky. \tag{3.5}$$

The velocity and pressure fields can be written as the addition of the basic values and the disturbance

$$p_i^T = p_i^0 + p_i \qquad \text{and} \qquad \mathbf{u}_i^T = \mathbf{u}_i^0 + \mathbf{u}_i. \tag{3.6}$$

Darcy's law and incompressibility equation (equation (3.1)) are valid for both undisturbed and total disturbed fields. They are thus still holding for the disturbance ($\mathbf{u}_i$ and p_i). Solutions of the form

$$p_i = p_i'(x, t) \sin ky, \tag{3.7}$$

i.e. having the same spatial periodicity, are looked for. The amplitude p_i' will either grow or decrease in time with the interface disturbance itself. Its dependence on x ensures that on moving away from the interface the disturbance of the pressure field tends to zero. Due to its Laplacian-dependence, the pressure field has to decrease exponentially with a length scale fixed by $\mathbf{k}$

$$p_1 = A_1 e^{\omega t + kx} \sin ky \qquad \text{and} \qquad p_2 = A_2 e^{\omega t - kx} \sin ky. \tag{3.8}$$

3.1.2.3 Continuity of the normal velocities at the interfaces

At the interface, the continuity of the normal component of the velocity can be approximated in the limit of small deformations by

$$u_{x_1} = u_{x_2} = \frac{\partial \zeta}{\partial t} - U, \tag{3.9}$$

resulting in

$$K_i \left(\frac{\partial p_i}{\partial x} \right)_{x=\zeta} = \epsilon \omega e^{\omega t} \sin ky. \tag{3.10}$$

It is thus possible to determine A_1 and A_2 by keeping the first-order terms and considering $\zeta = Ut$. One gets the following pressure fields

$$p_1 = \frac{\epsilon \omega}{K_1 k} e^{\omega t + k(x-Ut)} \sin ky \qquad \text{and} \qquad p_2 = -\frac{\epsilon \omega}{K_2 k} e^{\omega t - k(x-Ut)} \sin ky. \tag{3.11}$$

3.1.2.4 The pressure jump at the interface due to surface tension

Surface tension induces a pressure jump Δp given by Laplace's law. The curvature κ_2 in the z-direction can be considered to be of order $\kappa_2 \approx 2/b$ and constant along the interface, so that its dynamical effect can be neglected (section 1.2.6). Only κ_1 ($x-y$ plane) is taken into account. This bold assumption neglects the wetting films left on the solid surface when the viscous fluid is pushed out of the cell. These wetting films have a thickness which is a function of the normal velocity of the interface [313, 346]. Both experimental [347] and theoretical [348] results have shown this assumption is not always valid. Tanveer [349] addressed the complete three-dimensional system and showed within which limits the two-dimensional assumption is valid.

When neglecting the higher-order terms in the expression of the curvature, one can write in 2D

$$p_2^T(\zeta) - p_1^T(\zeta) = \sigma \frac{\partial^2 \zeta}{\partial y^2}, \tag{3.12}$$

with

$$p_2^T(\zeta) - p_1^T(\zeta) = p_2^0(\zeta) - p_1^0(\zeta) + p_2(\zeta) - p_1(\zeta). \tag{3.13}$$

The pressure distribution and the different pressure fields are considered. By taking $\zeta = Ut$ in the last two terms $p_2(\zeta) - p_1(\zeta)$ to retain only first-order terms one can

obtain

$$\omega = \left(\frac{K_1 - K_2}{K_1 + K_2}\right) Uk + \sigma \left(\frac{K_1 K_2}{K_1 + K_2}\right) k^3, \tag{3.14}$$

i.e.

$$\omega = \left(\frac{\mu_2 - \mu_1}{\mu_1 + \mu_2}\right) Uk - \sigma \frac{b^2}{12} \left(\frac{1}{\mu_1 + \mu_2}\right) k^3. \tag{3.15}$$

In the case where $\mu = \mu_2 \gg \mu_1$

$$\omega \approx Uk - \sigma \frac{b^2}{12\mu} k^3. \tag{3.16}$$

The disturbance with maximum growth rate ω has a wave-vector

$$k_c = \frac{2}{b}\sqrt{\mathrm{Ca}}, \tag{3.17}$$

with $\mathrm{Ca} = \mu U/\sigma$, which corresponds to the most unstable wavelength

$$l_c = \pi b\, \mathrm{Ca}^{-1/2}. \tag{3.18}$$

The interface is however unstable for all wave-vectors verifying $k < k_{\max} = \sqrt{3} k_c$.

3.2 The existence of stable curved fronts

The instability of the plane fronts does not preclude the possibility of existence of stable steady solutions (*e.g.* Saffman-Taylor finger and parabolic needle crystal).

3.2.1 Isotropic case

3.2.1.1 Linear channel

This configuration is characterised by its translational invariance along the cell. In this geometry, the nature of the pattern is controled by a parameter proportional to the square of the ratio of the small to the large scale (the width W of the channel)

$$B = \frac{\sigma}{12\mu U} \left(\frac{b}{W}\right)^2 = 8.45 \times 10^{-3} \left(\frac{l_c}{W}\right)^2. \tag{3.19}$$

For a wide range of values of B a lone finger is observed, moving steadily with a well-defined width and shape (see Figure 3.4). The ratio λ of the finger width to the

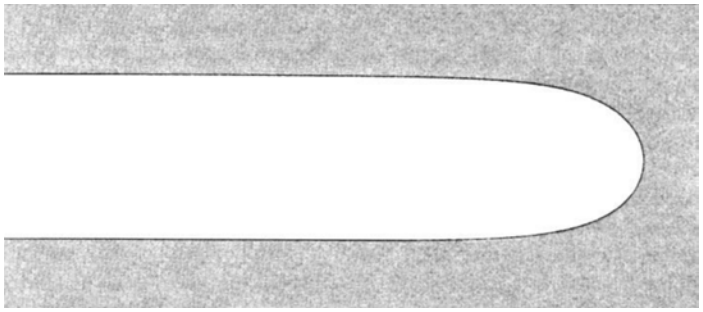

Figure 3.4: Saffman-Taylor finger of width $\lambda = 0.5$ obtained in a linear channel at $B \approx 2 \times 10^{-4}$. [115]

channel width tends towards $\lambda = 0.5$ with decreasing values of B. This finger is stable down to $B \approx 1.4 \times 10^{-4}$ (*i.e.* $W \approx 8\, l_c$). For lower values of B the finger becomes unstable.

By conformal mapping [114], it can be shown that in the absence of surface tension the shape of the interface in the Hele-Shaw cell $\mathbb{R} \times [-W/2, W/2]$ follows

$$x = \frac{W(1-\lambda)}{2\pi} \ln \frac{1}{2} \left[1 + \cos\left(\frac{2\pi y}{\lambda W} \right) \right] \tag{3.20}$$

where λ, their relative width, can take any value from 0 to 1 (Figure 3.5).

It however took some time to explain why a particular solution was selected. Such an explanation required to investigate the role of surface tension. The selection was first obtained in numerical investigations [177, 350, 351] and later understood in analytic works [352, 353, 354, 355]. Surface tension introduces higher-order terms in the integro-differential equation defining the interface, but cannot be treated as a perturbation. When considering the small terms due to surface tension in the limited expansion, a solvability condition is introduced by the required smoothness at the tip of the finger. For each value of B, there is only one discrete set of solutions of width λ_n satisfying this condition: all these solutions tend to have a width 0.5 for vanishing B. For very low values of B they vary as

$$\left(\lambda_n - \frac{1}{2} \right) = \frac{1}{8} a_n (16\pi^2 B)^{2/3} \tag{3.21}$$

with $a_n = 2(n + 4/7)^2$. This dependence can also be found numerically (Figure 3.6). Amongst the various branches, only the lower one is stable: the others are unstable

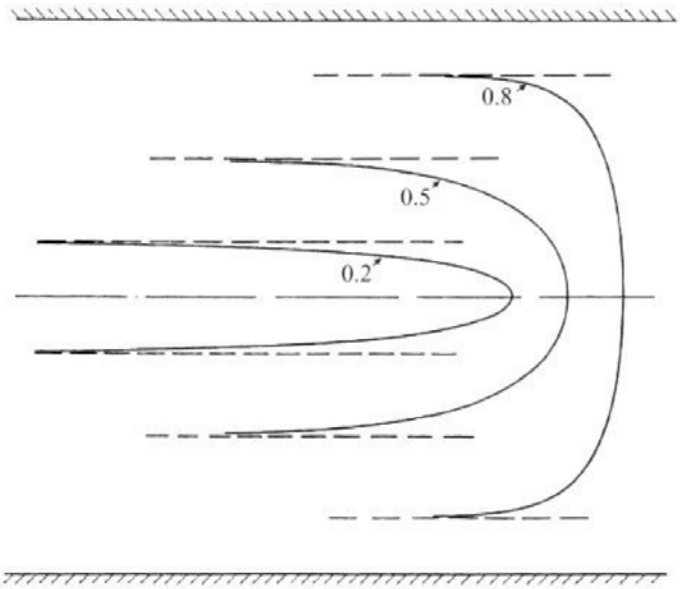

Figure 3.5: Three finger profiles of the continuous family of solutions given by equation (3.20). [114]

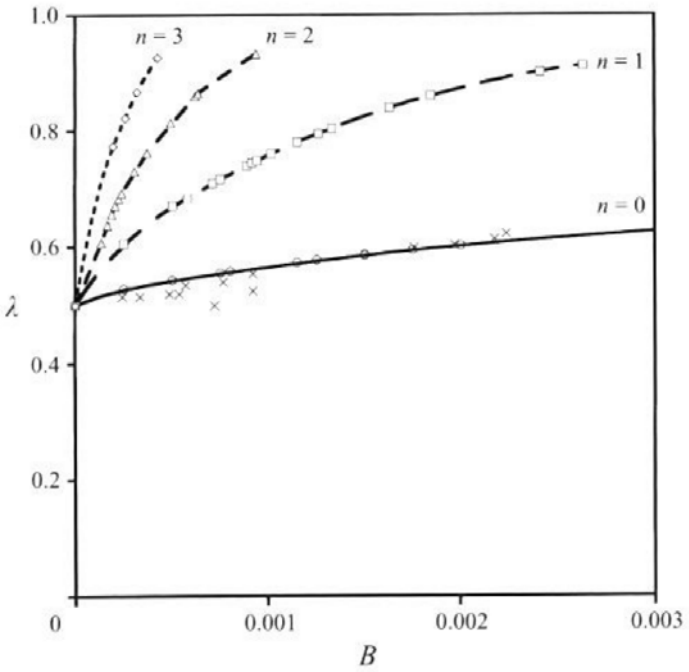

Figure 3.6: The B-dependence of the widths of the discrete set of solutions selected by surface tension. [115]

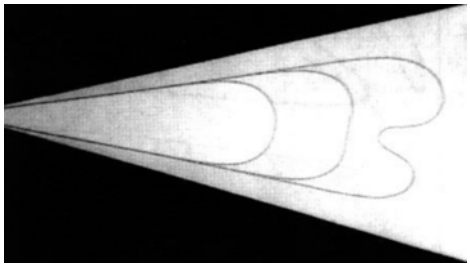

(a)

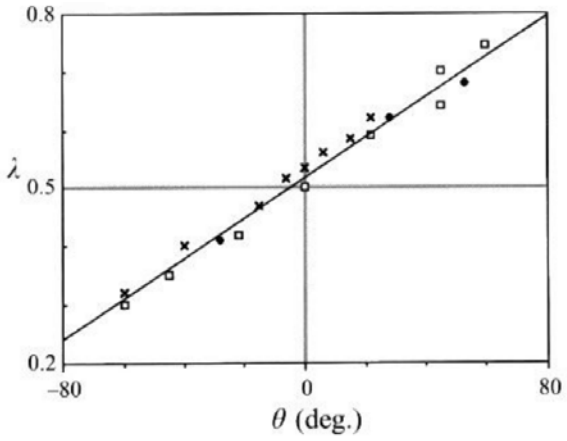

(b)

Figure 3.7: (a) Three superposed photographs of the evolution of a Saffman-Taylor finger of width $\lambda = 0.66$ obtained in a sector-shaped cell of angle $\theta_w = 30°$. (b) Width of the stable fingers as a function of the angle θ_w at $B \sim 10^{-3}$. [115]

through tip splitting [356, 357, 358].

One can finally note that an equivalent to surface tension can be introduced in DLA growth. It is then possible to recover the stable isotropic Saffman-Taylor finger in a linear channel [359, 360].

3.2.1.2 Sector-shaped cells

In a wedge-shaped cell the viscous finger moves between two lateral walls forming an angle θ_w. This angle is usually considered positive when the finger moves in the divergent direction. One can consider the parameter $B = 8.45 \times 10^{-3}(l_c/\theta_w r)^2$ where $r\theta_w$ is the curvilinear local width $W(r)$. A single finger occupies a finite fraction

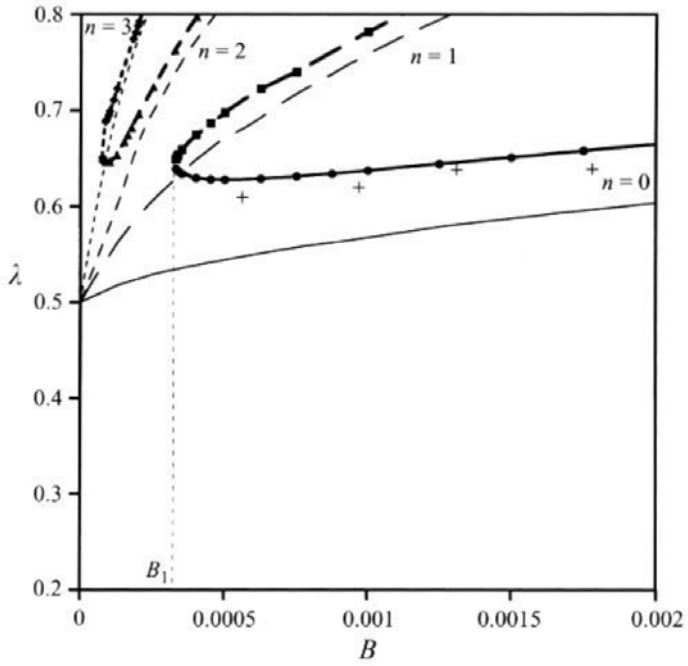

Figure 3.8: The B-dependence of the widths of the discrete set of solutions in a wedge of angle $\theta_w = 20°$ (thick lines). The thin lines show for comparison the discrete set in the linear cell. The crosses are experimental results. [115]

$\lambda_{\theta_w} > 0.5$ of the angular width for moderate values of B (Figure 3.7(a)). This fraction varies approximately as a linear function of the wedge angle (Figure 3.7(b)). When B is kept constant, *i.e.* U decreases as r^{-2}, the finger grows as a self-similar structure. In other cases, the finger becomes spontaneously unstable (Figure 3.7(a)).

Neglecting surface tension, a theoretical set of self-similar functions was first discovered for $\theta_w = 90°$ [332]. Then families of solutions parameterized by their width λ_{θ_w} were found for any value of θ_w [361]. The selection due to isotropic surface tension was then investigated both numerically [362, 363] and analytically [324]. Similar to the parallel channel geometry, for each value of B there is a discrete set of solutions (Figure 3.8). A comparison with the channel geometry highlights that the selected widths λ_{θ_w} are shifted to higher values. Moreover levels $n = 1$ and $n = 2$ coalesce at a value B_1 and thus form a loop: those levels consequently do not exist for $B < B_1$. Indeed experimental results show that at constant velocity the finger becomes unstable when reaching the limit value B_1.

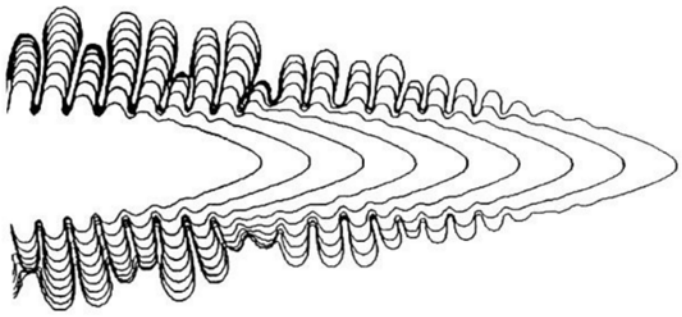

Figure 3.9: The growth of a parabolic dendritic monocrystal. [364]

3.2.1.3 Circular geometry

In the axisymmetric geometry the front destabilizes spontaneously after some time at the scale l_c and radially growing fingers are formed. These fingers look like those obtained in wedges [332]. Each finger grows as if enclosed in a cell with virtual walls formed by the bisectors of the region separating this finger from its neighbours.

3.2.2 Non-isotropic case

3.2.2.1 The dendrite

The structures formed during crystallisation of a solution or a melt are dendrites (Figure 3.9). Each dendrite is a monocrystal with parabolic tip growing in a well-defined direction (one of the main axes of the crystal lattice). The curved front becomes unstable at some distance from the tip and lateral branches grow along other main crystallographic directions.

3.2.2.2 The anomalous Saffman-Taylor finger

One can wonder whether it is possible to obtain viscous fingers looking like dendrites. It is indeed possible when preferential directions of growth are imposed on viscous fingering [226, 365, 366]. Actually, selection is a singular effect occurring at the tip, so a single disturbance localised there is sufficient to modify the growth [367, 368]. The effect of such a disturbance is as thus. In radial configuration, the fingers will grow faster than normal, have stable tips and exhibit dendritic-like side branches. In

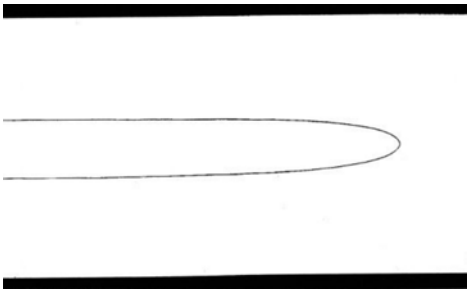

(a)

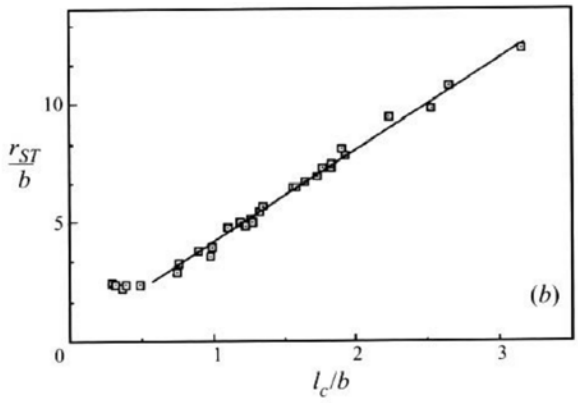

(b)

Figure 3.10: (a) A photograph of an anomalous finger of width $\lambda = 0.22$ obtained in a linear channel when one of the glass plates has a single groove etched along its axis. (b) A graph of the radius of curvature of the tip r_σ/b versus l_c/b [369]. The saturation occurs when $r_\sigma \approx 2.5b$ where the two-dimensionality breaks down. [115]

linear channels, the fingers are much narrower than usual (Figure 3.10(a))but their shapes are still very well fitted by the Saffman-Taylor analytical solutions of the same width λ (equation (3.20)).

Fingers grown in channels of different width have very different λ (even at same velocity) but a similar tip. From equation (3.20) the radius of curvature at the tip is

$$r_\sigma = \frac{\lambda^2 W}{\pi(1-\lambda)}. \tag{3.22}$$

r_σ is constant for anomalous fingers grown in various cells at the same velocity with the same disturbance. However, for varying velocities, it is proportional to the capillary

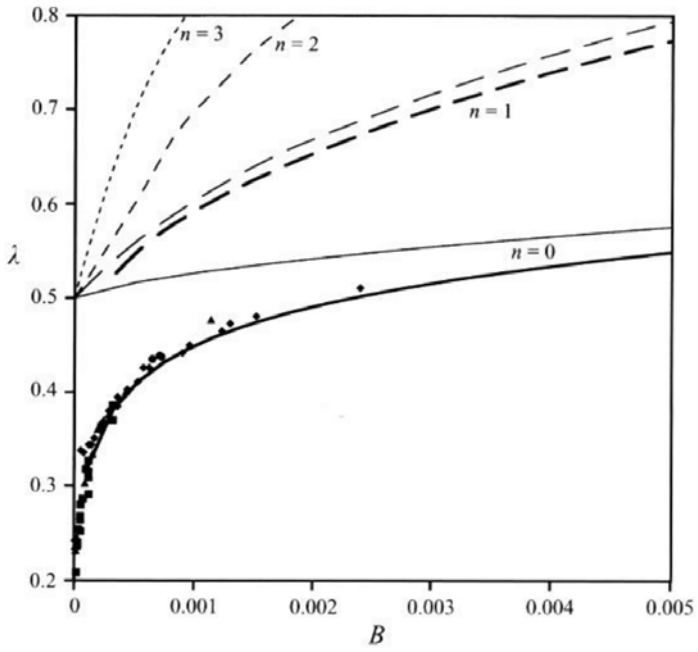

Figure 3.11: The B-dependence of the width of the discrete set of solutions in the presence of anisotropy (thick lines). Black symbols: measured witdh of fingers obtained with a given disturbance of the tip. The thin lines show the discrete set in the linear cell. [115]

length scale (Figure 3.10(b))

$$r_\sigma = \alpha l_c. \tag{3.23}$$

The coefficient α depends on the strength of the applied disturbance. As the radius of curvature varies for a dendrite as $r_d = 0.5\epsilon^{-7/5} l_c^{sc}$ with ϵ the anisotropy and l_c^{sc} the instability length scale [364, 370] anomalous fingers and dendrites obey the same rules. This was thoroughly investigated experimentally [369, 371, 372], numerically [373, 374] as well as theoretically [354, 375, 376].

In the presence of anisotropy parallel to the channel, the lower level of the discrete set tends towards $\lambda = 0$ instead of $\lambda = 0.5$ (Figure 3.11). It should be noted that for very fast growing fingers saturation is observed when the tip radius becomes of the order of the cell thickness ($r_\sigma \approx 2.5b$, Figure 3.10(b)). The two-dimensional-behaviour hypothesis is no longer valid.

3.3 Stability of the curved fronts

3.3.1 Isotropic case

Isotropic curved fronts have a scale of the same order as the channel width. When decreasing B the finger tip will become increasingly similar to a straight front, *i.e.* will tend to be unstable at the capillary length l_c corresponding to the local normal component of the velocity. Indeed in wedge geometry the finger is destabilized more and more easily through tip splitting for increasing angles [332] (when the local value of B at the tip reaches the value B_1). By contrast, in the linear channel the lower branch $n = 0$ (Figure 3.6) is linearly stable while the other branches are unstable [356, 357]. However experiments highlight an instability of the finger for B values smaller than 1.4×10^{-4} (Figure 3.12(a)). As B tends to zero the branches become more closely spaced; the natural noise is then enough to induce a subcritical transition to one of the neighbouring unstable states.

3.3.2 Anisotropic case

For non-isotropic fronts, whether dendrites or anomalous fingers, the tip is defined by the small scale. The tip radius of curvature remains in the same ratio to the capillary length scale for all values of B: for large anisotropy the tip is thus stable. On the contrary, lateral sides are always unstable in dendrites. In the case of anomalous fingers, as the scale of r_σ moves away from that of W, λ decreases and the finger shape becomes parabolic in an ever larger region behind the tip. A lateral instability then grows, identical in nature to that of crystalline dendrites (Figure 3.12(b)).

The specificity of the growth of such an instability (advected along a curved front) was first pointed out for flame fronts [377]. The growing wave is stretched by a kinematic effect resulting from the growing tangential velocity [378, 379]. Furthermore each region of the front is unstable. Indeed the normal velocity decreases continuously away from the tip along the curved front. Consequently the maximum amplification rate shifts continuously towards larger wavelengths (equation (3.18)) [380].

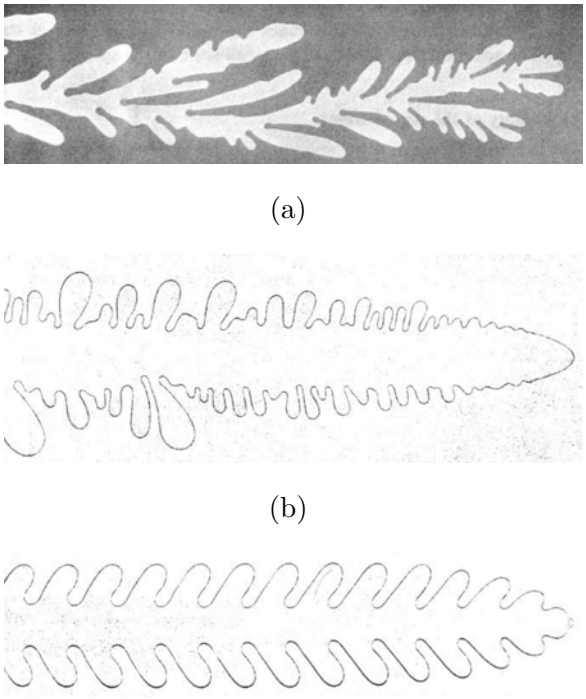

(a)

(b)

(c)

Figure 3.12: (a) A very unstable finger in a linear cell. (b) The natural instability of an anomalous Saffman-Taylor finger in a wide channel [369] to be compared with the dendrite (Figure 3.9) (c) An anomalous Saffman-Taylor finger subjected to a periodic forcing. [115]

The side branching is thus a convective instability [369, 381]: the medium behaves as a selective amplifier of the noise [364, 382]. However, if one replaces noise by a periodic forcing of larger amplitude, the instability becomes strictly periodic at the imposed frequency. It is consequently possible to generate a strictly periodic side branching by either modulating the input pressure (acts as a forcing frequency) or adding a small bubble at the finger tip (forms a small local oscillator, see Figure 3.12(c)).

3.4 Implementing Darcy flows in the Gerris Flow Solver

According to Chapter 2, the Euler equations for two-phase flow are written in the Gerris Flow solver as

$$\rho\left(\partial_t \mathbf{u} + \mathbf{u}\cdot\nabla\mathbf{u}\right) = -\nabla p + \rho\mathbf{f} \tag{3.24a}$$

$$\partial_t c + \nabla\cdot(c\mathbf{u}) = 0 \tag{3.24b}$$

$$\rho = \rho(c) = c\rho_1 + (1-c)\rho_2 \tag{3.24c}$$

The Gerris Flow Solver can simulate Darcy flow [83, 383]. Here we also describe how to obtain the time-dependent problem which was not considered in [83]. We cancel the advection term of equation (3.24a) and add a drag force $\mathbf{f} = -\beta\mathbf{u}$ ($\beta > 0$)

$$\partial_t \mathbf{u} = -\frac{1}{\rho}\nabla p - \beta\mathbf{u}. \tag{3.25}$$

We decompose the numerical solution into an exact and an error term

$$\mathbf{u}(t) = \mathbf{u}_0 + \mathbf{e}(t)$$

with $0 = -\nabla p - \rho\beta\mathbf{u}_0$ for the exact term. The error obeys $\partial_t\mathbf{e} = -\beta\mathbf{e}$ (consequence of equation (3.25)) for a steady exact solution and is $\mathbf{e} = -\mathbf{C}\exp(-\beta t)$. The error will be small after one timestep Δt if $\beta\Delta t \gg 1$. For a time-dependent exact solution $\mathbf{u}_0$, the same decomposition shows that the error scales as $\mathbf{u}_0/(\beta T_c)$ where T_c is the characteristic time of the exact solution and it thus requires that $\beta T_c \gg 1$. The latter condition is achieved by the choice of length and time units.

Thus the solver produces either a false-transient iteration towards the steady state or adiabatically follows the time-dependent solution of

$$\mathbf{u} = -\frac{1}{\beta\rho}\nabla p. \tag{3.26}$$

This equation can simulate Darcy flows if $\beta\rho = \mu/k$.

3.5 Saffman-Taylor fingering in a Hele-Shaw cell with central injection

We use the thickness b of the Hele-Shaw cell, the initial average radius R_0, the viscosity of the outer fluid μ_o, and the surface tension σ for non-dimensionalization. This defines the following velocity and pressure gauges:

$$U = \frac{\sigma b^2}{12\mu_o R_0^2} \text{ and } P = \frac{\sigma}{R_0} \tag{3.27}$$

From now on, all variables are dimensionless.

3.5.1 Equations governing the flow

Similar to references [322, 330], the present study addresses the development of Saffman-Taylor fingering in a Hele-Shaw cell with central injection in the presence of surface tension.

For this purpose, interest is focused on 2D square domains Ω of size L_d centred on $(0, 0)$

$$\Omega = [-L_d/2, L_d/2]^2.$$

The two components of the velocity are (u, v), *i.e.* $\mathbf{u} = u(x, y)\mathbf{e_x} + v(x, y)\mathbf{e_y}$. This domain is initially filled with a high-viscosity fluid ($\mu = 1$). A less viscous fluid ($\mu = M > 0$) is injected from the centre of the domain with a constant massflux $\nabla \cdot \mathbf{u} = C > 0$ inside a circle of radius $0.8 \ll L_d$. The side boundaries ($x = \pm L_d/2$ and $y = \pm L_d/2$) impose a quasi-circular "free" outflow condition for the fluids with Neumann boundary conditions for the velocity:

$$\partial_x u(\pm L_d/2, y) = 0 \tag{3.28a}$$

$$\partial_y v(x, \pm L_d/2) = 0 \tag{3.28b}$$

The fluids are considered incompressible ($\nabla \cdot \mathbf{u} = 0$) and move inside the domain ($(x, y) \in \mathring{\Omega}\backslash\Gamma$ with Γ the interface) according to Darcy's law [102, 108]:

$$\mathbf{u} = -\frac{1}{\mu}\nabla p \tag{3.28c}$$

Due to fluid incompressibility and equation (3.28c), the pressure field p obeys the Laplace equation [326]

$$\nabla^2 p = 0. \tag{3.29}$$

Boundary conditions are given at the interface which hold for the depth-averaged fields:

$$\begin{aligned} [\![\mathbf{n} \cdot \mathbf{u}]\!] &= 0 \\ [\![p]\!] &= A + \frac{\lambda_\sigma}{R} \end{aligned}$$

Here $[\![\ ]\!]$ denotes a jump, R is the principal radius of curvature of the projection, onto the plane, of the tip of the meniscus separating the two phases and λ_σ a characteristic lengthscale of the influence of surface tension, multiplied by some coefficient of order 1 [175].

The simulations address two-phase Darcy flows for fluids with viscosity ratios ranging from $M = \dfrac{\mu_2}{\mu_1} = 10^{-4}$ up to 10^{-2}. Using the pressure field p^* presented alongside equation (1.64) and adapted here as $p^* = p + Ac$, we only consider the planar contribution to the radius of curvature

$$[\![p^*]\!] = \frac{\lambda_\sigma}{R}. \tag{3.31}$$

In the following we rename p^* as p for simplicity.

The initial data is a slightly perturbed circular interface $r(\theta) = 1 + 1/10(\cos(3\theta) + \sin(2\theta))$ [384]. We only report on the early times $r_{\max}/L \ll 1$ to avoid finite size effects and mesh-induced anisotropy. We fix $\lambda_\sigma = 1/3$ so that the capillary lengthscale is somewhat smaller than the initial radius r and the grid size is $h = 1/60$. The results are presented in Figure 3.13.

3.5.2 Effects of mesh-induced noise and viscosity ratio

In related simulations (invasion from the side of a rectangular domain) it was found that if care is taken to ensure very low noise levels fingering disappears and plain, non-branching fingers advance linearly. Thus the simulations incorporate two different kind of noise: numerical or "mesh-induced" noise (resulting from the imperfect convergence

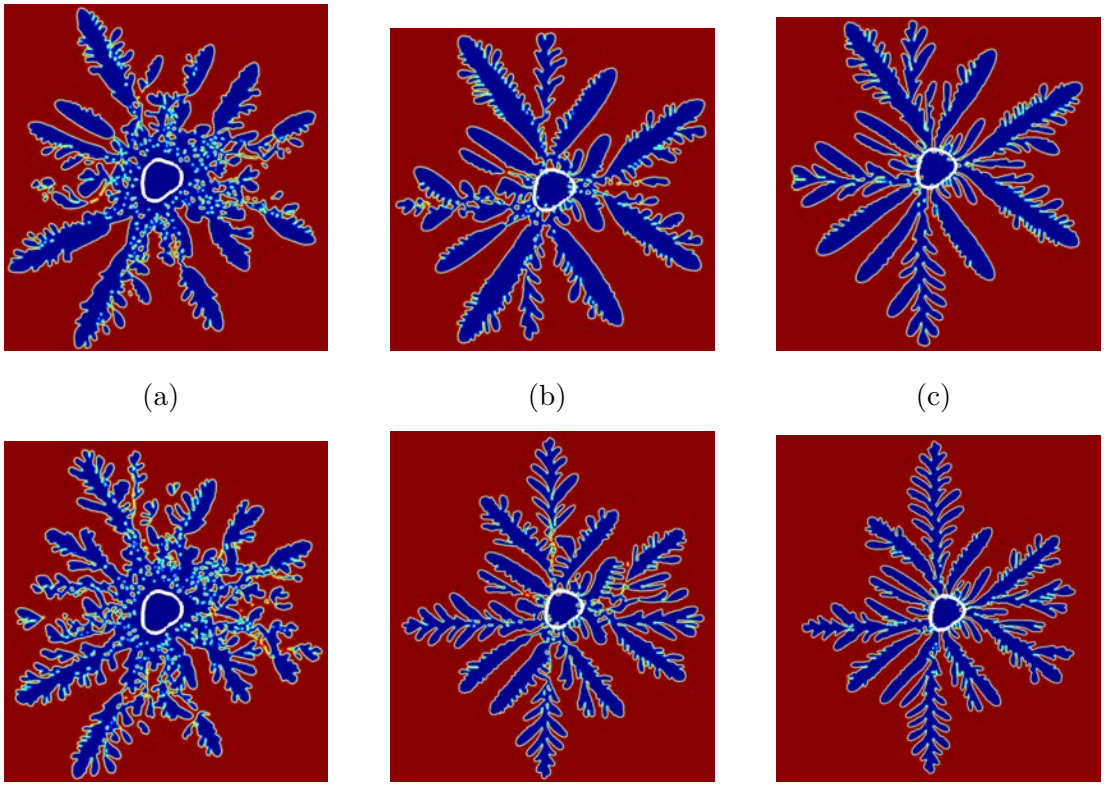

(a) (b) (c)

(d) (e) (f)

Figure 3.13: Development of Saffman-Taylor fingering for three different viscosity ratios: 10^{-2} (pictures (a) and (d)), 10^{-3} (pictures (b) and (e)), 10^{-4} (pictures (c) and (f)). The instability is generated by mesh-induced noise in the first row, while an isotropic noise is added to the simulations presented in the second row. In white, the initial position of the interface.

of the Poisson solver), and random perturbations of the local viscosity (viscosity added noise, constant in time).

The early-time instability amplifies the initial perturbation, then later-time fingers develop due to either mesh-induced noise (pictures 3.13(a) to 3.13(c)), or added noise (pictures 3.13(d) to 3.13(f), strong enough to cover the still-present mesh-induced noise). In this last case, the noise is also axis-dependent, due to the non-isotropic distribution of computational grid points. The viscosity added noise has standard deviation

$$\frac{\Delta(1/\mu)}{< 1/\mu >} = 5\%.$$

Viscosity ratio	10^{-2}	10^{-3}	10^{-4}
Mesh-induced noise	$1.79 \rightarrow 1.58$	$1.81 \rightarrow 1.60$	1.69
Added noise	$1.85 \rightarrow 1.56$	1.68	1.70

Table 3.1: Fractal dimensions of the clusters presented in Figure 3.13. When two different values are presented, the first one corresponds to the lower radii and the second one to the higher ones.

Strictly speaking, this added noise is equivalent to a permeability noise both in the case of porous media and Hele-Shaw cells ($\Delta(b^2)/ < b^2 >= 5\%$). It was added to try to account for the sensitivity of the fingering process to noise [385].

The error is due to several contributions: numerical uncertainty as stated above,mesh-size effects, finite-size effects (special care was taken to verify they are negligible: a specific flow was considered for several domain sizes L, resulting in convergence with an error lower than 2%), data range used to compute power-law fits, and quality of the fitting process for a specific data range.

At higher viscosity ratios, patches are seen to detach from the main bubble.

Moreover, some fingers tend to reconnect at later times, trapping some high viscosity droplets inside the less viscous main bubble (see pictures 3.13(a) and 3.13(d)). On the contrary, for lower viscosity ratio, the different early-time fingerings develop separately without uniting one with the other (no detaching droplets; pictures 3.13(c) and 3.13(f)). These two different cases result in different fractal-dimension regimes, presented in Table 3.1 (fitting uncertainty always lower than 2%): at higher viscosity ratio, the inner (lower radii) fractal dimension is higher than the outer (higher radii) one (around 1.8 *vs.* around 1.6); on the contrary at lower viscosity ratio, there exists only one fractal dimension for the whole bubble (around 1.7). It can be noted that the fractal dimensions obtained at low viscosity ratio are coherent with those presented in Figure 1.33.

It can also be noted that the transition from the two-fractal-dimension regime (high viscosity ratio, see above and Table 3.1) to the one-fractal-dimension one (low visosity ratio) occurs at higher viscosity ratio when the noise amplitude is higher.

Logically, the higher the noise amplitude, the more pronounced the resulting fingering (see Figure 3.13).

3.5.2.1 Comparison with experimental results

The detaching patches that were numerically highlighted above at higher viscosity ratios can also be seen experimentally (Figure 3.14). Such bubbles can also be observed in experiments of lateral injection in porous media (see Figure 3.15).

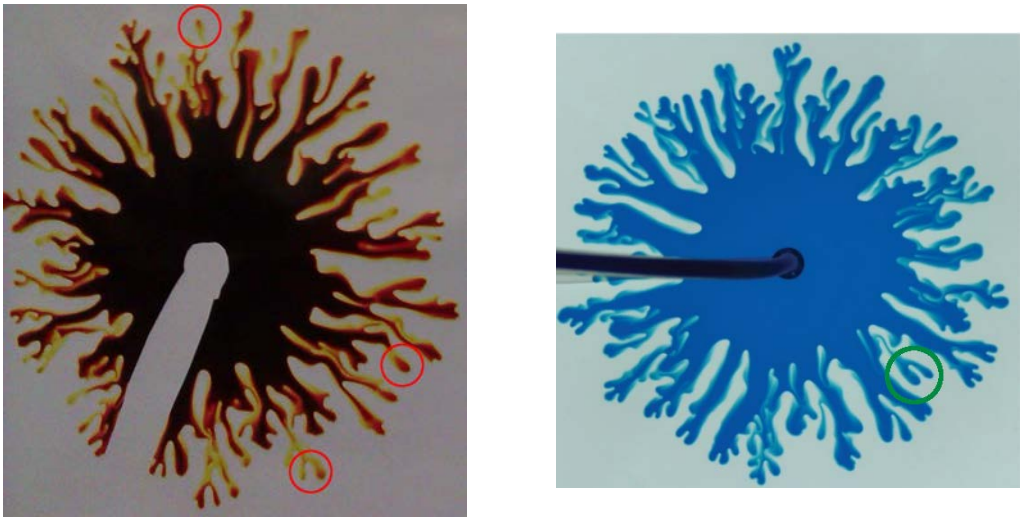

Figure 3.14: Detaching droplets in experimental miscible viscous fingering. [386, 387]

3.5.3 Zero-pressure approximation in the less viscous fluid

When numerically simulating Saffman-Taylor fingering [330, 389], it is common to consider a constant pressure field p_0 inside the less viscous fluid (usually considered equal to zero). This hypothesis is formally equivalent to the assumption of a zero-viscosity invading fluid, due to Darcy's law.

The presence of detaching droplets in pictures 3.13(a), 3.13(b) and 3.13(d) invalidates this hypothesis for fluids in the range $M = 10^{-2} - 10^{-3}$. Indeed, due to the maximum principle (a consequence of the open-mapping theorem), the maximum

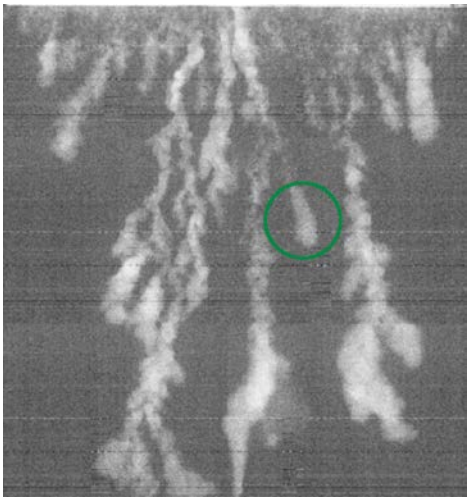

Figure 3.15: Detaching droplet in experimental viscous fingering in porous media. [388]

pressure of a Laplacian field such as p is only reached at the domain boundary, here the interface. The maximum is thus p_0 and is reached at the interface, with $p < p_0$ everywhere else. Thus the interface can only advance towards the more viscous fluid and never recede. This makes the pinch-off of invading fluid bubbles impossible. The presence of detaching droplets is thus a qualitative difference with infinite viscosity contrast models.

The results however do not oppose the zero-pressure approximation in the case of lower viscosity ratios (below 10^{-4}).

3.5.4 Interface length and area of the resulting cluster

In reference [330], Fast & Shelley explained that long time simulations of Saffman-Taylor fingering revealed an asymptotic scaling regime, where the interface length of the resulting bubble was related to the bubble area by a power-law relation: Area $\sim$ (Length)$^{\alpha}$ (in their case, $\alpha = 1.45$). The variation of this coefficient α is obviously disconnected from that of the fractal dimension D_F; indeed, as an example, one can consider a lone planar dendrite whose length and width vary as t and t^{γ} respectively (with $0 < \gamma < 1$), then $D_F = 2$ whatever the value of γ whereas $\alpha = 1 + \gamma$.

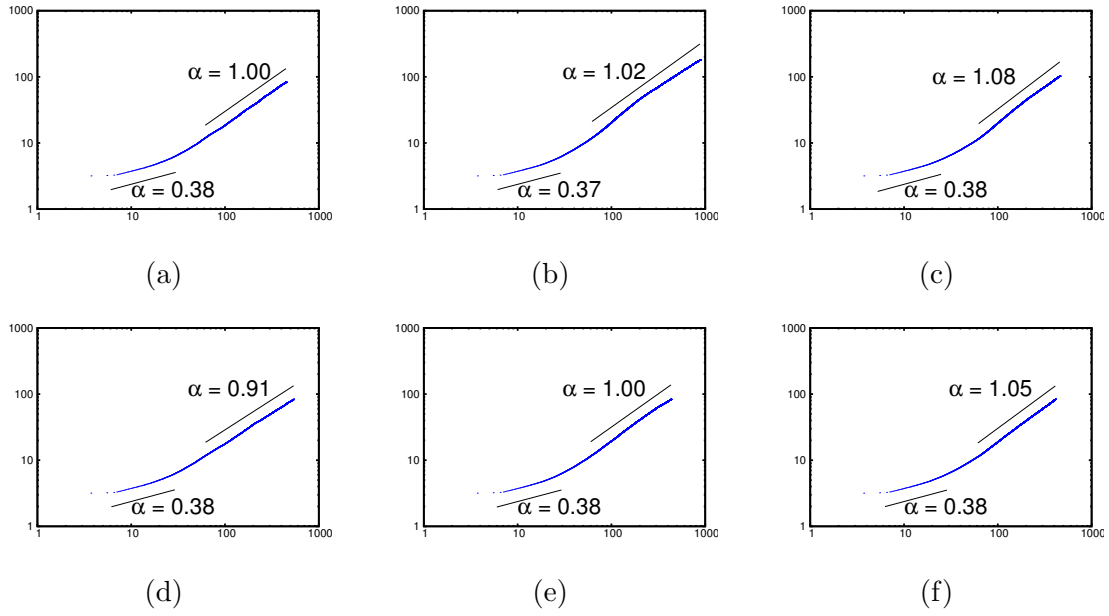

Figure 3.16: The dimensionless area A of the growing bubble *vs.* the dimensionless length L of the interface. The different viscosity ratios and noise origins are presented similarly to Figure 3.13.

Approximating fingers by their osculating parabolas [390], one gets $\gamma = 1/2$ and $\alpha = 3/2$. In the case of DLA clusters, $\alpha = 1$ whatever the fractal dimension.

Fast & Shelley also found that at shorter times, a second regime could be defined with another coefficient: $\alpha = 0.61$. This regime is characterised by numerous tip-splitting events that dramatically increase the number of fingers. On the contrary, at long times the growth rate of the arclength decreases and suggests fewer tip-splitting events occur in this region [322].

From now on, α_1 will be the short time coefficient and α_∞ the asymptotic one. According to Li *et al.* [322], though α_1 depends on the initial shape, at later times the scaling α_∞ is initial-data independent.

In the results presented in Figure 3.16, one can observe that the interface is indeed related to the bubble area by a power-law relation with two different regimes. However, the coefficients that we obtain are different: $\alpha_1 \approx 0.38$, and $\alpha_\infty \approx 1$, depending on the viscosity ratio and noise origin. The error, mostly due to mesh-size effects, on all values of both α_1 and α_∞ is of order 10%. However oscillations in the scaling

exponent are inherent to the self-similar character of the fingering [391] and could also account for part of the error.

It should also be noted that the coefficient α_∞ increases when the viscosity ratio decreases, although we have not enough numerical data to further comment on the significance of this increase. As the experiment presented in [330] was realised with the zero-pressure approximation, their value of α_∞ (1.45) is consistent with this remark and could be seen as a zero-viscosity limit.

Third scaling coefficient? Li *et al.* [322] distinguished three different parts in the area *vs.* interface length curve, corresponding to three different scalings. The first one was observed by Hou *et al.* [384] ($\alpha_1 = 0.61$) and the second was the one captured by Fast & Shelley[2] [330] ($\alpha_2 = 1.45$, see above). They identified a third regime where tip-splitting seemingly accelerates again ($\alpha_\infty = 1.39$, a new asymptotic coefficient).

We however think that, based on reference [391], α_2 should be considered as an oscillation of α_∞. Indeed, oscillations are inherent to lacunar fractals. Bessis *et al.* [392] proved their existence for certain fractal Julia sets (asymptotically, near the boundary of the support of the measure). Badii and Politi [393] found them in their analysis of the Zaslavsky attractor [394] using a method based on the nearest-neighbour distances. Smith *et al.* [391] observed them in many sets including Koch islands [395], the Hénon attractor [396], the Zaslavsky attractor [394] and Cantor dusts [395] in two and three dimensions. Apart from their intrinsic interest, the oscillations can produce fluctuations in the measurement of the dimension [397].

Consequently, as an oscillation of α_∞, α_2 should be overlooked and there exist only two scaling coefficients.

3.5.5 Accuracy of the asymptotic coefficient

Due to the high discrepancy of coefficient values between the previous results and those of reference [330], both Fast & Shelley's results and ours were compared to the experimental results presented by Praud & Swinney in reference [231]. This

[2]One should note that in this case α_2 is not the asymptotic scaling.



Figure 3.17: Time evolution of the fractal growth patterns for viscous fingering ($\Delta P =$ 1.25 atm). The colors indicate the ages of the patterns; the oldest (first created) region is blue and the youngest is red. From [231].

comparison was realised cautiously, for, while both the results presented above and Fast & Shelley's were obtained at constant massflux, Praud & Swinney's injection was realised at constant pressure. The experiments were also realised with the viscosity ratio $M \sim 5 \cdot 10^{-5}$, *i.e.* close to what we used for pictures 3.16(c) and 3.16(f). At $M \sim 5 \cdot 10^{-5}$ in the experiments or $M \sim 10^{-4}$ in the simulation very few or even no detached bubbles or trapped droplets are seen, making this case similar to the $M = 0$ one. A comparison with Fast & Shelley's results is thus consistent.

From Figure 3.17, it was possible to determine $\alpha_\infty = 1.14$, with the following fitting error: $\alpha_\infty \in [1.11, 1.23]$. The previous results ($\alpha_\infty \in [1.02, 1.08]$ with the uncertainty) are much closer than those of Fast & Shelley, whatever the noise that was used (mesh-induced or added).

3.5.6 Fractal dimension

In order to completely validate the model, the experiment presented in Figure 3.17 was simulated. The simulation was realised with a maximum number of authorised computational cells of 2^{13} in each direction with the same viscosity ratio as in Figure 3.17. As there was no blatant difference between the results of simulations obtained



Figure 3.18: Simulation of the experiment presented in [231] ($r_{\max}/\lambda_\sigma = 25$).

by applying a constant pressure (as in the experiment of Praud & Swinney) and those with a constant massflux, the results realised with a constant massflux, for which a length λ_σ was defined above, are presented in Figure 3.18.

Though Figures 3.17 and 3.18 look very much alike, it is obvious that these fingers begin to align themselves with the principal directions of the mesh: the x-axis, the y-axis and both bissectors of the axes.

The fractal dimension $D_F = 1.67$ of the resulting cluster was nonetheless determined, to be compared with $D_F = 1.69$ in Figure 3.17. For all we know, the fractal dimension of a Direct Numerical Simulation (DNS) of Saffman-Taylor fingering was never measured before.

3.5.7 Polar modelisation of viscous fingering

It is possible to define an orthogonal curvilinear coordinate system (r_x, r_y) distinct from the usual cartesian one (x, y), and its associated metric in the Gerris Flow Solver. It is however up to the user to specify transformations which guarantee the orthogonality of the coordinate system (for example using conformal mapping[3]). $\mathbf{u}_r =$

[3]A map $f : U \to V$ with $U, V \in \mathbb{R}^n$ is called conformal (or angle-preserving) at a point u_0 if it preserves oriented angles between curves through u_0 with respect to their orientation (*i.e.*, not just the magnitude of the angle). Conformal maps preserve both angles and the shapes of infinitesimally small figures, but not necessarily their size or curvature.

(u_r, v_r) will refer to the velocity vector in the (r_x, r_y) coordinate system. One should note that in the following $\mathbf{u}_r$ is not the velocity in polar coordinate!

In order to remove the alignment of the principal directions of the flow with the axes and bisectors, one can choose to use polar coordinates: $(r, \theta) \in [a, b] \times [-\pi, \pi[$ and $0 \leqslant a < b$.

Due to the singular point at $r = 0$, it is chosen to consider an annular domain Ω defined as

$$\Omega = \{(r, \theta) \in [0.8, L + 0.8] \times [-\pi, \pi]\}. \tag{3.32}$$

As by default Gerris only consider square domains of size 1 and centred on $(0, 0)$ when used in 2D, the domain

$$\left\{(r_x, r_y) \in \left[-\frac{1}{2}, \frac{1}{2}\right]\right\} \tag{3.33}$$

is considered. The metric is thus defined as

$$x = \left(0.8 + \frac{L}{2}(1 + 2r_x)\right)\cos(2\pi r_y), \tag{3.34a}$$

$$y = \left(0.8 + \frac{L}{2}(1 + 2r_x)\right)\sin(2\pi r_y). \tag{3.34b}$$

i.e. $r = 0.8 + \frac{L}{2}(1 + 2r_x)$ and $\theta = 2\pi r_y$.

The inverse metric is

$$r_x = \frac{1}{L}(\sqrt{x^2 + y^2} - 0.8) - \frac{1}{2}, \tag{3.35a}$$

$$r_y = \begin{cases} \dfrac{1}{2\pi}\arccos\left(\dfrac{x}{\sqrt{x^2 + y^2}}\right) & \text{if } y \geqslant 0, \\ -\dfrac{1}{2\pi}\arccos\left(\dfrac{x}{\sqrt{x^2 + y^2}}\right) & \text{if } y < 0. \end{cases} \tag{3.35b}$$

As the less viscous fluid is injected from the centre of the domain with a constant massflux $\nabla \cdot \mathbf{u} = 1$ inside a circle of radius 0.8, one can easily calculate the flux exiting from the disk of radius 0.8 from the divergence theorem: $\varphi = 0.64\pi$. The actual value of the velocity is unknown. This unknown boundary condition on $r_x = -1/2$ is approximated by a uniform Dirichlet boundary condition on the velocity

$$u_r = 0.64\pi, v_r = 0. \tag{3.36}$$

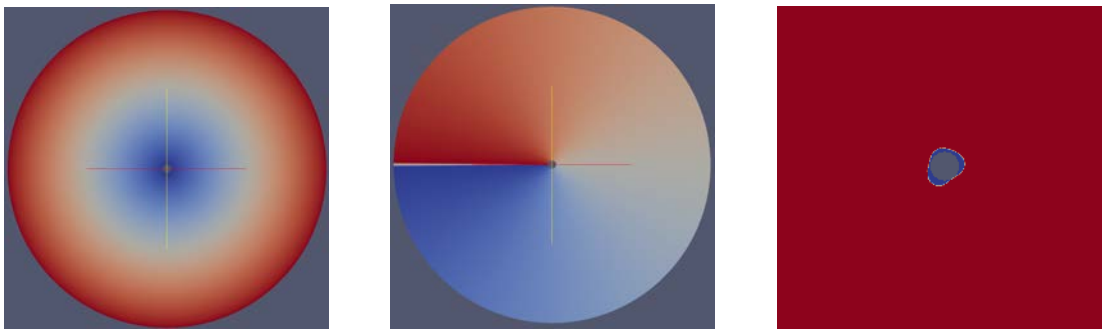

(a) (b) (c)

Figure 3.19: Polar metric for viscous fingering simulation. (a) Radius, (b) angle and (c) initial interface.

Note that this condition is coherent with the value of the flux presented above.

The initial interface is unchanged: $r(\theta) = 1+1/10(\cos(3\theta)+\sin(2\theta))$. The domain is presented at initial time in Figure 3.19.

To make sure the meshing remains fine enough to consider the precise development of viscous fingering at high radii, the mesh size h_r on the computational grid (r_x, r_y) has to vary as

$$h_r \propto \frac{1}{r} = \frac{1}{0.8 + \frac{L}{2}(1 + 2r_x)}. \tag{3.37}$$

in the radial direction. The mesh size will thus diminish with increasing r in the radial direction, but will remain as constant as possible in the tangential direction. Indeed, in this last direction, the mesh size varies as

$$h_\theta \sim r h_r \propto 1.$$

The module of Gerris which allows to use a different metric from the usual one is seldom used. Its implementation has consequently not been optimised for parallel many-core computation. It was thus only possible to simulate these injections on one core. The result of a 40-day simulation is presented in Figure 3.20. One should note the effect of the refinement level on the width of the interface. It is also obvious that the result of this computation does not depend on the principal axes of the domain.

It would indeed be possible to improve the Gerris module allowing to use a different metric from the usual one in order for it to be used for parallel computations.

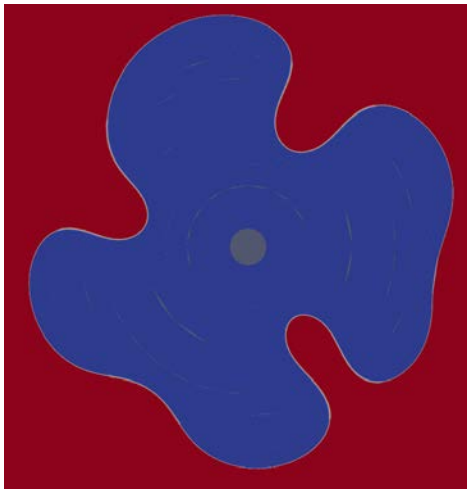

Figure 3.20: Polar simulation of central injection similar to the experiment of Praud and Swinney [231]: result after 40 days of computation on a single core.

3.6 Conclusion

As flows in Hele-Shaw cells obey the same laws as flows in porous media (Darcy's law), interest was focused on the injection of a lower-viscosity fluid inside a Hele-Shaw cell filled with a higher-viscosity one (Saffman-Taylor instability). The injection was realised from the centre of the cell.

Though Gerris normally solves the Navier-Stokes equation, it can be tricked into solving Darcy's law, by deactivating the advection term and adding a drag force.

The obtained clusters have a characteristic non-isotropic aspect. It is nonetheless interesting to notice that they obey the same scaling coefficients as isotropic injections.

The existence of two different fractal-dimension regimes in Saffman-Taylor fingering due to central injection was also observed: one at lower viscosity contrast with the coexistence of two different fractal dimensions in the resulting cluster, and one at higher viscosity contrast with only one dimension. In the case of low viscosity contrast, it can be noted that droplets tend to detach themselves from the main bubble (can be observed experimentally).

Finally, at late times, the area of the resulting pattern varies as the length of the interface to some power α_∞ , with different values for finite or infinite viscosity contrasts.

CHAPTER 4

Lateral injection in a quasi-2D geometry

In heavy oil reservoirs, waterflooding and polymer assisted waterflood are an alternative in cases where thermal methods are either impractical or uneconomic.

Experiments have been realised in quasi-2D square slabs of Bentheimer sandstone in order to study waterflooding and tertiary polymer injection in extra heavy oils [38].

Contents

4.1 Experiments of lateral injection in square slabs 192

4.1.1 Description of the experiments 192

4.1.2 Measuring system 192

4.1.3 Water and polymer injection 193

4.1.3.1 Injection of brine 193

4.1.3.2 Injection of polymer 194

4.1.4 Influence of waterflooding rate 196

4.2 Simulation of Darcy flows in rectangular slabs with lateral injection 198

4.2.1 Waterflood simulation 198

4.2.1.1 Square geometry 198
4.2.1.2 Reduced geometry 201
4.2.2 Injection of polymer after waterflooding 205
4.3 Conclusion 210

4.1 Experiments of lateral injection in square slabs

4.1.1 Description of the experiments

A quasi-2D square slab of size $30 \times 30 \times 2.5$ cm^3 of Bentheimer sanstone of porosity 25% was dried at 80°C. The measured pore volume was 564 cm^3 and the vaccum was saturated with 7 g.L^{-1} NaCl brine. This porous domain was then vertically drained with oil diluted with 18% of iododecane at rate 6 mL.h^{-1} till breakthrough. After breakthrough the invasion rate was increased up to 12 mL.h^{-1}. The porous domain was aged during 3 weeks at 50°C, with occasional injection in both directions (up to down and reverse).

The first experiment consisted of an injection of water from the bottom at ambiant temperature and rate 3 mL.h^{-1} [398]. The total injected volume was equal to 2.3 pore volumes (PV). In a second time, an industrial polymer (SNF Flopaam 3630S) diluted in NaCl/$NaHCO_3$ solution was injected at rate 3 mL.h^{-1}. A total of 1.3 pore volume of polymer solution was injected [38].

4.1.2 Measuring system

A narrow beam of electromagnetic radiation is emited either by an X-ray or a low energy Gamma-ray source and attenuated by the rock sample (Figure 4.1). The intensity of the attenuated beam is then measured by both a scintillation photon counting detector and an X-ray camera.

As the amount of attenuation depends on the composition of the porous medium and the fluids it is saturated with, this measurement provides an accurate assessment of the actual composition of the flow [399].

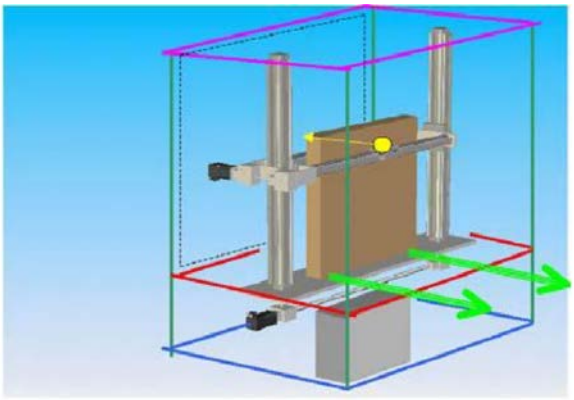

Figure 4.1: Schematic setup of the slab in the 2-D scanner. The same alignment was used for gammameasurements, X-ray, and X-ray camera. [38]

The image is finally filtered by convolution in order to reduce the influence of image artifacts [38, 400, 401].

4.1.3 Water and polymer injection

Two different cases were considered. In one case (experiment E2000), the viscosity of the initially filling oil was $\mu_{2000} = 2.0$ kg.m^{-1}.s^{-1} = 2000 cP. In the other case (experiment E7000), the viscosity was $\mu_{7000} = 7.0$ kg.m^{-1}.s^{-1} = 7000 cP.

4.1.3.1 Injection of brine

In both cases, by injecting brine inside the porous medium, it is possible to recover part of the oil. This recovery is however inferior to 30%, even when considering that the recovery is somewhat higher in case E2000 than in case E7000 (Figure 4.2 and Table 4.1).

At early times of the injection, many fingers develop with a rapid growth. Some prominent fingers will tend to propagate faster than others and consequently inhibit the growth of smaller fingers. At later times, the fingers will tend to coalesce and expand to a thick water channel, with a much less fractal aspect than that of early-time fingers (Figures 4.3 and 4.4).

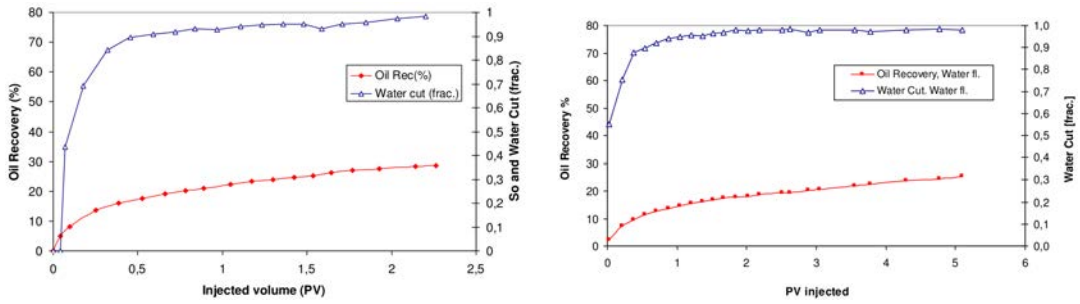

(a) (b)

Figure 4.2: Oil recovery and water cut during water injection: (a) E2000, (b) E7000. [38]

Injection	**E2000**		**E7000**	
	Injected PV	**Oil Recovery**	**Injected PV**	**Oil Recovery**
Waterflood	2.3	28.5%	5.1	26.4%
Polymer flood 1650ppm 3630S	1.5	66.8%	3.18	63.1%

Table 4.1: Oil recovery data. [38]

This coalescence of fingers occurs earlier and to a larger extent in case E2000 than in case E7000. The fingers are also less distinct in experiment E2000.

The waterflood is thus dominated by viscous fingering and later by channeling[1].

4.1.3.2 Injection of polymer

When polymer is injected as a second step, the oil recovery is doubled in both cases (Figure 4.5). The response to a change of invading fluid is fast, and the oil fractional flow increases quickly at those high oil viscosities. Nonetheless the test with the less viscous oil results in faster production and higher total oil recovery.

Figure 4.6 and 4.7 show polymer injection. A reference image is substracted to the actual image in order to highlight the saturation changes during polymer injection process. Blue parts indicate an increase in injected fluid saturation S_i, whereas

[1] expansion of a thick water channel in the middle of the domain

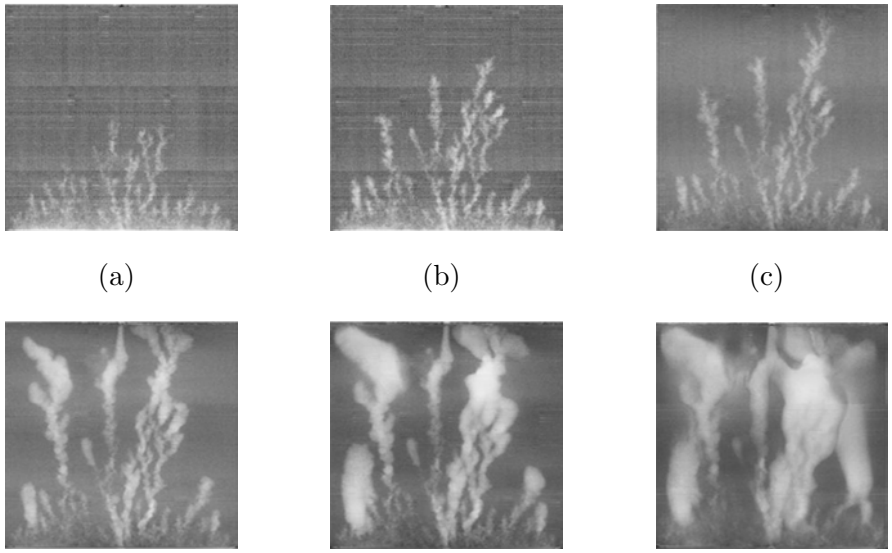

(a) (b) (c)

(d) (e) (f)

Figure 4.3: 2D imaging of waterflood in Bentheimer sandstone with 2.0 $kg.m^{-1}.s^{-1}$ crude oil. Water is injected from the bottom, white color is the injected water. (a) 0.01 PV, (b) 0.02 PV, (c) 0.04 PV, (d) 0.14 PV, (e) 0.53 PV, (f) 2.3 PV. [38]

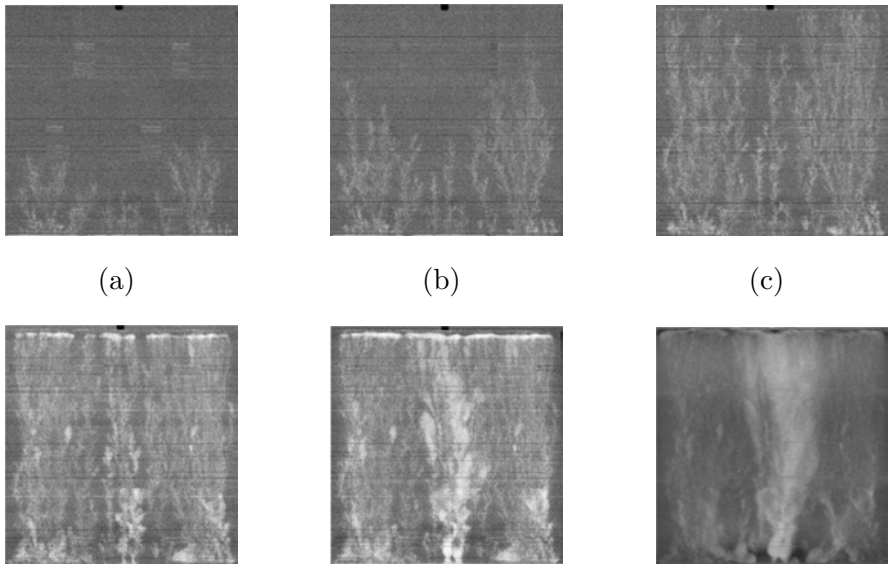

(a) (b) (c)

(d) (e) (f)

Figure 4.4: 2D imaging of waterflood in Bentheimer sandstone with 7.0 $kg.m^{-1}.s^{-1}$ crude oil. Water is injected from the bottom, white color is the injected water. (a) 0.01 PV, (b) 0.02 PV, (c) 0.04 PV, (d) 0.24 PV, (e) 0.72 PV, (f) 1.2 PV. [38]

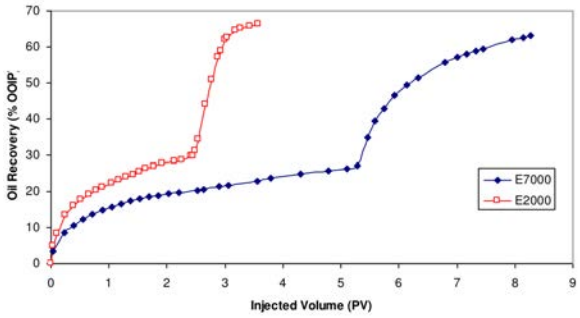

Figure 4.5: Oil recovery by water flood and polymer flood. [38]

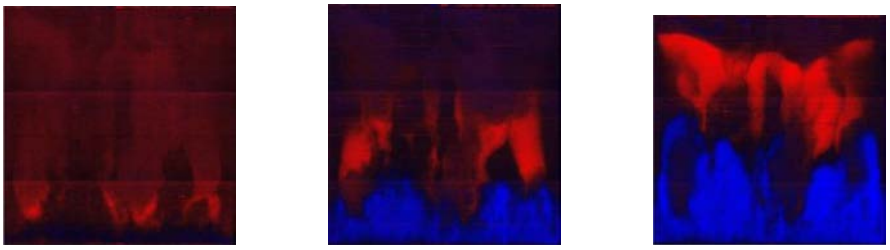

(a) (b) (c)

Figure 4.6: Polymer injection E2000, change in saturation. In blue: increase in S_w; in red: increase in S_o. (a) 0.02 PV, (b) 0.11 PV, (c) 0.25 PV. [38]

red color highlights an increase in oil saturation S_o. One can easily notice that the mobilised oil follows the water channels that were established during the waterflood.

4.1.4 Influence of waterflooding rate

It is possible to modify the relative significance of viscous and capillary forces by varying the water injection rate. Experimentally it is easy to show that oil production rates are higher and waterfloods more efficient at lower injection rate. This is indeed blatantly noticeable in Figure 4.8 (injection of water to recover an oil of viscosity 11.5 kg.m^{-1}.s^{-1}).

The decrease in water injection rate can also occur late in the life of a waterflood with comparable results. Two oils are shown in Figure 4.9: HO2 is the same as that used in Figure 4.8, while HO1 is a less viscous one (4.65 kg.m^{-1}.s^{-1}).

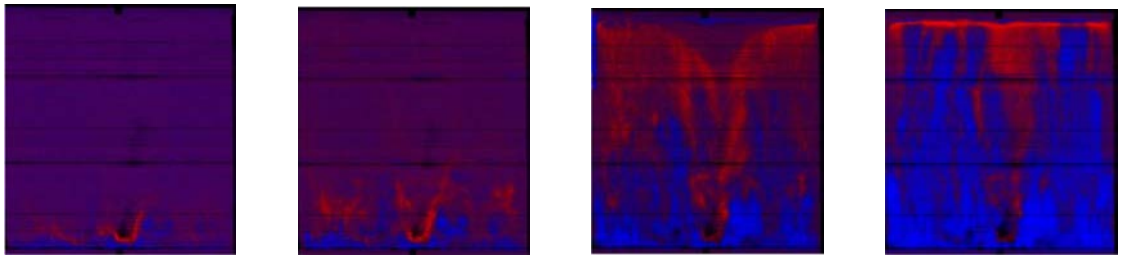

(a) (b) (c) (d)

Figure 4.7: Polymer injection E7000, change in saturation. In blue: increase in S_w; in red: increase in S_o. (a) 0.02 PV, (b) 0.04 PV, (c) 0.15 PV, (d) 0.49 PV. [38]

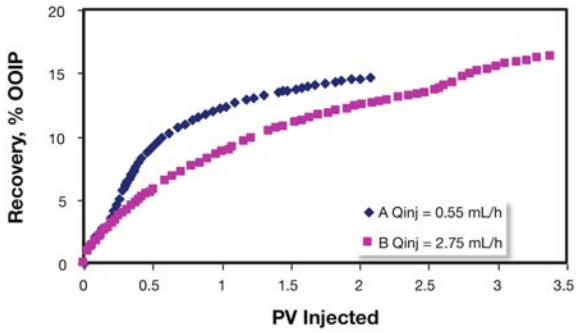

Figure 4.8: Oil recovery profile for waterflood at different injection rates. [402]

It should be noted that continuous water channels are already present at this time, and consequently do not oppose the increase of oil recovery. Indeed, while during high-rate waterflooding oil is recovered only close to the water channels, during low rate waterfloods the water moves away from the continuous fingers and accesses a much larger area of the porous medium [402].

Capillary forces thus appear to be largely responsible for oil production after waterflooding. Indeed, in the case of low rate water injection, water imbibes into the original oil region perpendicularly to the water channel [403]. Experiments were realised in a 2D etched glass micromodel, though at lower viscosity ratio ($M = 95.3$, see Figure 4.10).

Water film thickening, snap-off and oil-refilling are the main mechanisms leading to water imbibition, alongside emulsion [403].

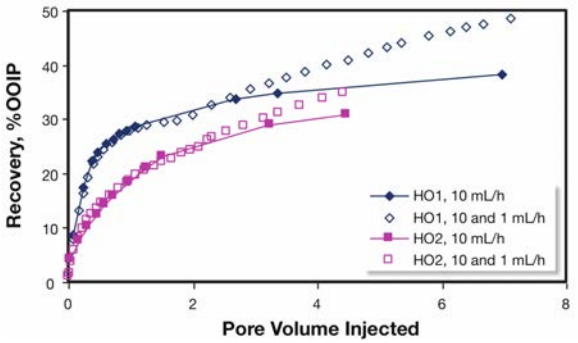

Figure 4.9: Effect of reducing injection rate for two heavy oils. [402]

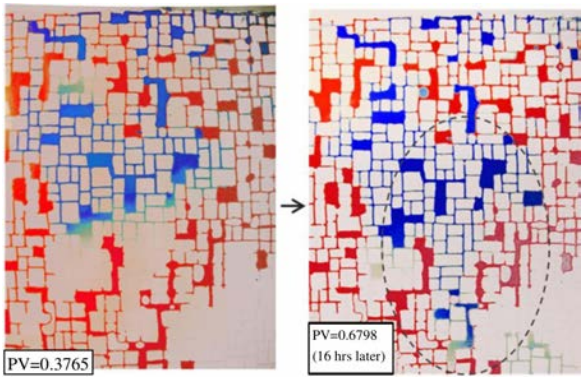

Figure 4.10: Direction of imbibition after breakthrough. The main flow goes from left to right. [403]

This imbibition could explain the thickening of the fingers and creation of water channels presented in section 4.1.3.1.

4.2 Simulation of Darcy flows in rectangular slabs with lateral injection

4.2.1 Waterflood simulation

4.2.1.1 Square geometry

The injection of water in an initially oil-filled square porous medium is considered in the following. For this purpose, similarly to chapter 3 attention is focused on 2D

Minimum size of a cell	**Case 1**	**Case 2**
	$h_1 = \frac{L}{2^{11}}$	$h_2 = \frac{L}{2^{12}}$

Table 4.2: Two different refinements.

square domains Ω of size[2] L centred on $(0,0)$

$$\Omega = [-L/2, L/2]^2.$$

The two components of the velocity are (u,v), *i.e.* $\mathbf{u} = u(x,y)\mathbf{e_x} + v(x,y)\mathbf{e_y}$. This domain is initially filled with a high-viscosity fluid (μ_o). A less viscous fluid (μ_w) such as $M = \dfrac{\mu_w}{\mu_o} = 10^{-3}$ is injected from one side of the domain with a constant massflux $\mathbf{u}(-L/2, y) = U_{\text{in}}\mathbf{e_x}$. The side boundaries $y = \pm L/2$ impose a slip condition, while the last side allows a "free" outflow condition for the fluids.

The fluids are considered incompressible ($\nabla \cdot \mathbf{u} = 0$) and move inside the domain ($(x,y) \in \overset{\circ}{\Omega}\backslash\Gamma$ with Γ the interface) according to Darcy's law [102, 108]:

$$\mathbf{u} = -\frac{k}{\mu}\nabla p. \tag{4.1}$$

As discussed in section 1.2.6, one can use only equation (4.1), with no reference to surface tension.

The simulation of waterflooding was realised during 120 hours of wall-clock CPU time on 64 cores[3] with only numerical or "mesh-induced" noise to initiate the fingering process. Two different refinements were used with adaptive mesh refinement, defining two different cases[4] (see Table 4.2). The results are presented in Figure 4.11.

As expected, the interface between both fluids is unstable and one can observe the creation of fingers with both refinements. It is also obvious that with time some fingers tend to dominate and inhibit the growth of smaller fingers.

It is also possible to ensure that the fingering process occurs earlier by adding random perturbations of the local viscosity (see chapter 3 and Figure 4.12).

[2] In this case, as the ultimate goal is to simulate the experiments realised at Bergen [38], $L = 30$ cm.

[3] The use of *Hypre* solver allows to use a much higher timestep than when using the default solver of Gerris and converges much faster. However, there is a bug in the linking process between Gerris and *Hypre* inducing a drastic decrease of solving performance when using more than 64 cores.

[4] In these simulations, it corresponds to $h_1 = 150\,\mu$m and $h_2 = 75\,\mu$m. h_2 is thus of the order of the pore size (though slightly higher).

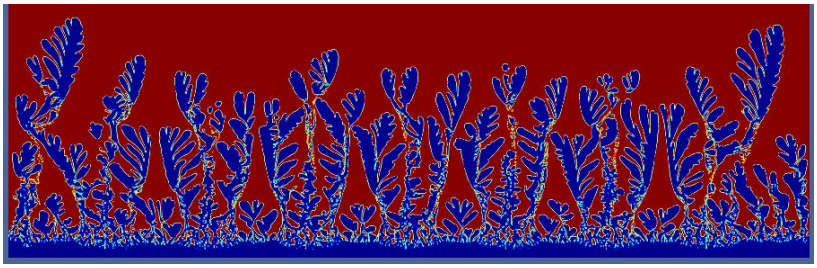

(a)

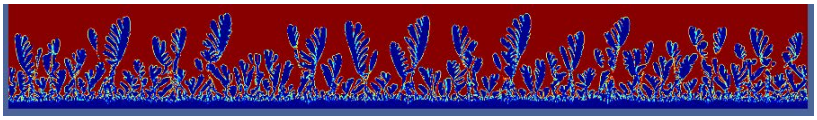

(b)

Figure 4.11: Waterflooding simulated during 120 hours of wall-clock CPU time with $M = 10^{-3}$ (injection from the bottom side): (a) case 1, (b) case 2.



(a)

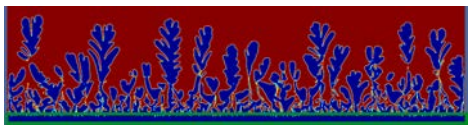

(b)

Figure 4.12: Effect of the noise on the initiation of the fingering process: the stable front (in green) is smaller when adding perturbations of the local viscosity (picture (b)) than without (picture (a)). The computational setup allows up to 2^{10} cells in the horizontal direction.

The fractal dimension of the fingering process was determined from the density-density correlation function $C(r) = \langle[\rho(r')][\rho(r'+r)]\rangle$ (see Appendix C). It appears that the measured fractal dimension (Figure 4.13) is slightly lower for finer refinement ($D_F = 1.69 \pm 0.01$) than for coarser one ($D_F = 1.73 \pm 0.01$). The use of a finer refinement indeed generates a smaller lengthscale (in the absence of surface tension) and thus ensures that the fingers will have a smaller characteristic size. A study of the exponent relating the area of the fingers and the length of the overall interface (chapter 3) was also realised (Figure 4.14), with the following results: in case 1, $(\alpha_1, \alpha_\infty) = (0.54 \pm 0.01, 0.80 \pm 0.004)$, while $(\alpha_1, \alpha_\infty) = (0.38 \pm 0.005, 0.76 \pm 0.01)$ in case 2.

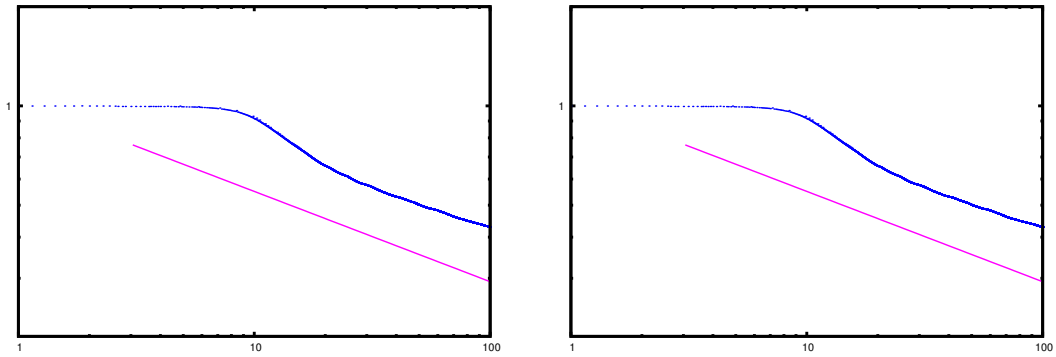

(a) (b)

Figure 4.13: Variation of the dimensionless covering area of the fingering process with respect to the dimensionless time (*i.e.* the actual area of the cluster, as the injection is realised at constant massflux: (a) case 1 ($\delta = -0.27$), (b) case 2 ($\delta = -0.31$). The slope δ of the curve is related to the fractal dimension as $D_F = 2 + \delta$.

4.2.1.2 Reduced geometry

The results presented above are indeed of interest. One can however regret that the result obtained after 120 hours of CPU time on 64 cores is not more developed: only the beginning of the fingering process is obtained. The simulation does not reach breakthrough time; the most advanced finger does not even reach the middle of the domain.

As the simulation authorises adaptive mesh refinement, one can expect that the required number of computational cells will tend to increase with the development of the fingers. Consequently, it will take (much) more CPU time for the tip of the fingering to go from abscissa $l_{\text{tip}} - L/2$ to abscissa $2l_{\text{tip}} - L/2$ than it took to reach abscissa $l_{\text{tip}} - L/2$ from the entrance.

In order to obtain less-demanding simulations and thus reach larger times, one faces two different possibilities to reduce the number of computational cells:

- either to reduce the size of the domain;
- or to consider coarser simulations.

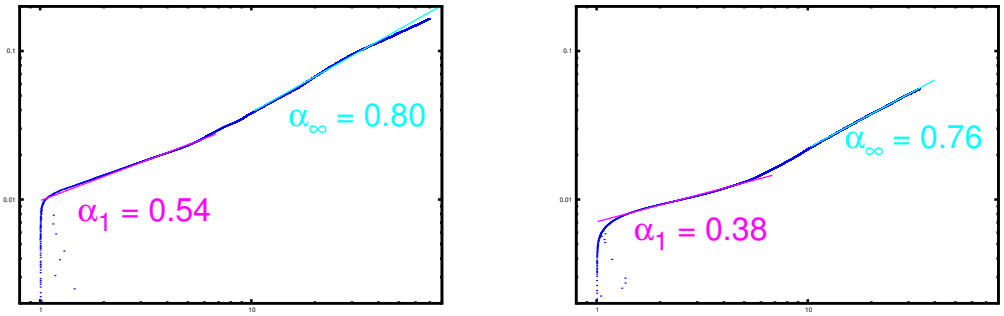

(a) (b)

Figure 4.14: Variation of the area of the fingering process with respect to the length of its interface: (a) case 1, (b) case 2.

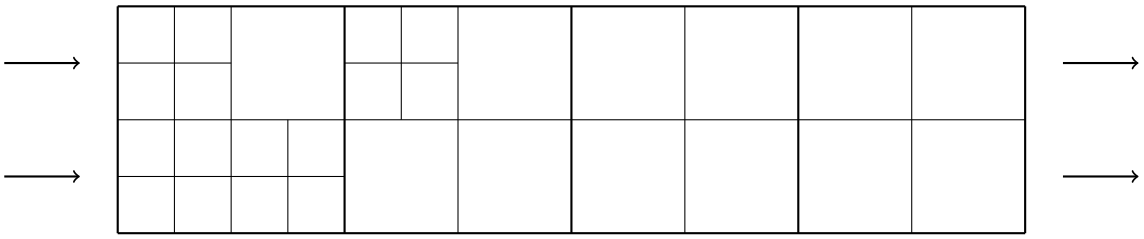

Figure 4.15: Injection in a domain constituted of four boxes of size $(L/4)^2$, linked one another in the x direction, with adaptive mesh refinement.

As the fingers obtained reference [38] are mostly aligned in a direction going from the entrance to the exit side, the considered domain is reduced to 2D rectangles Ω' of size $L \times L/4$ centred on $(0, 0)$

$$\Omega' = [-L/2, L/2] \times [-L/8, L/8].$$

The less viscous fluid is injected from the side $x = -L/2$ of the domain with a constant massflux $\mathbf{u}(-L/2, y) = U_{\text{in}}\mathbf{e_x}$. The side boundaries $y = \pm L/8$ impose a slip condition, while the remaining side allows a "free" outflow condition for the fluids.

In the Gerris Flow Solver, this is realised by considering four different boxes of size $(L/4)^2$, linked one another in the x direction (Figure 4.15). Each box can be subdivided in 2^{10} computational cells in each direction (one thus obtains a simulation with the same precision as case 2 presented above).



(a)



(b)

Figure 4.16: Waterflood in a rectangular domain with $M = 10^{-3}$ (injection from the left-hand side): (a) the tracer, (b) the velocity field (closer to black: low velocity; closer to white: higher velocity).

The result is presented in Figure 4.16. The fractal dimension of the resulting fingers is $D_F = 1.74 \pm 0.02$. One can observe the formation of relatively thick water channels, as in the Bergen experiments (see the velocity field in Figure 4.16(b)).

Those water channels are still present when simulating waterflooding till breakthrough. This can indeed be seen in Figure 4.17. One should however note that in order to reach breakthrough at a lower CPU time the maximum authorised refinement was reduced: each box (Figure 4.15) can be subdivided in 2^9 computational cells in each direction (one thus obtains a simulation with the same precision as case 1 presented above).

From the simulations presented in Figure 4.17, it is possible to obtain the variation of the area filled with injected fluid during the injection. This variation is presented in Figure 4.18. The dimensionless values are derived by dividing the area by that of the whole domain, and the time by that of breakthrough. One should realise that the dimensionless area is equal to the oil recovery. From this simulation, breakthrough should occur when 30% of the oil has been recovered. However, from the experiments

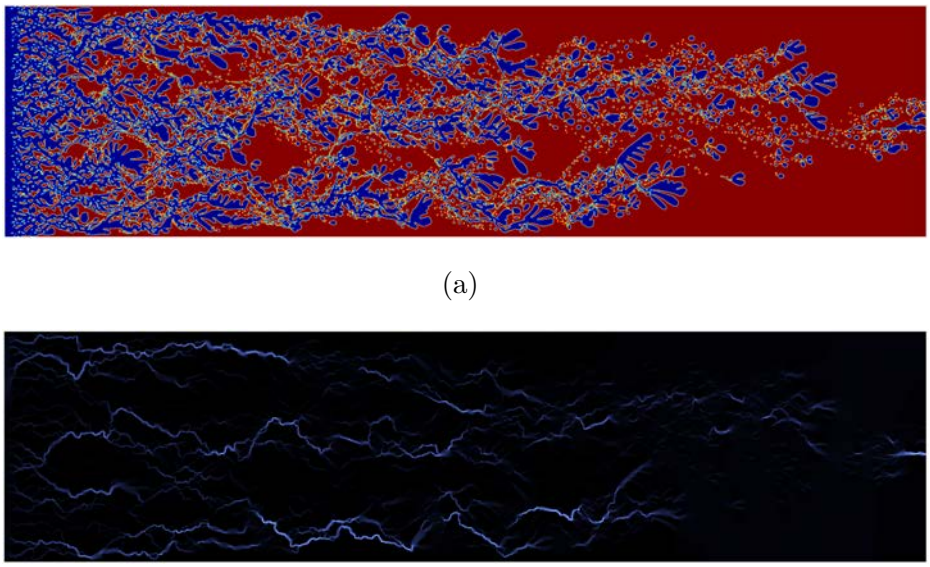

(a)

(b)

Figure 4.17: Waterflood in a rectangular domain till breakthrough with $M = 10^{-3}$ (injection from the left-hand side): (a) the tracer, (b) the velocity field (closer to black: low velocity; closer to white: higher velocity).

presented in section 4.1, breakthrough occurs when only 0.03 PV of water has been injected, *i.e.* the oil recovery at breakthrough is 3% [388]. This huge difference has two main causes. For some part it is a result of the 3D aspect of the fingering in the Bergen experiment which is neglected in these simulations. Indeed though the domain is quasi-2D the thickness of the porous medium slab is non-zero. Fingering thus also occurs in the third direction, reducing the necessary volume of injected fluid required to reach breakthrough... For another part, this overestimation is inherent to the numerical simulation of fractal clusters. Indeed, for a chosen mesh size h, the area of the resulting cluster varies as $A \propto h^d \left(\frac{L_f}{h}\right)^{D_F}$ where L_f is a characteristic lengthscale of the fingers, d is the embedding dimension and D_F the fractal dimension [341]. The computed area thus increases for increasing grid spacing[5] h. These simulations nonetheless reproduce the fact that oil production continues at a close rate to the pre-breakthrough one after breakthrough (Figure 4.18).

[5]In the case presented in Figure 4.17, the area is multiplied by more than 2 when multiplying the grid spacing by 10.

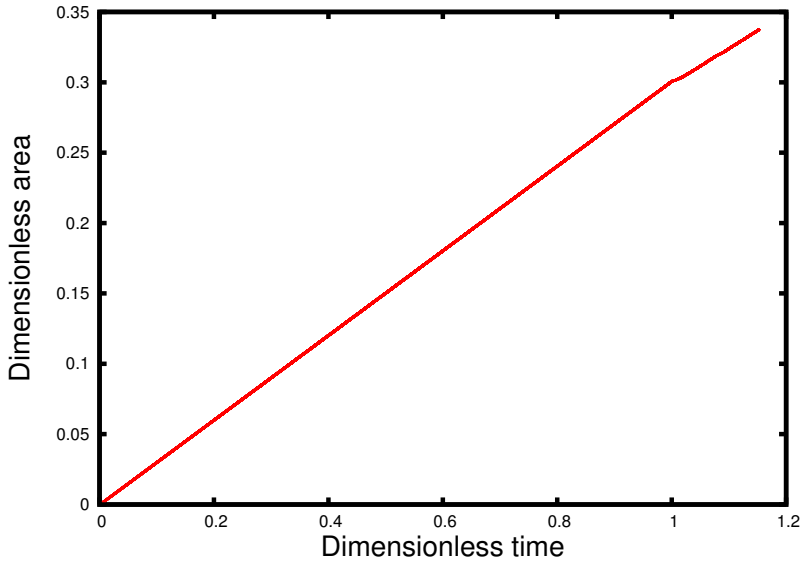

Figure 4.18: Dimensionless area filled with injected fluid as a function of dimensionless time ($t = 1$ at breakthrough).

The proportion of aqueous phase was also obtained at several abscissae for different dimensionless times. The results are presented in Figure 4.19 for a domain of length $L = 1$. These results are not consistent with those obtained in real quasi-2D experiments (much too high) for the same reasons as presented above (3D aspect of the experiments and variation of A with mesh size).

The proportion of aqueous phase at several abscissae for different times was compared for two different viscosity ratios: $M = 1/2500$ and $M = 1/7000$. The results, presented in Figure 4.20, are consistent with the trend of the experimental results (even if they are not consistent with the results themselves, see above): indeed, for higher viscosity contrast the tip of the fingering process moves more rapidly, ensuring breakthrough at shorter time. The expected recovery ratio is thus smaller for the case $M = 1/7000$, as was observed in the Bergen experiments.

4.2.2 Injection of polymer after waterflooding

The injection of polymer and brine is now considered in an initially oil-filled square porous medium in a two-step process. For this purpose, attention is focused on 2D

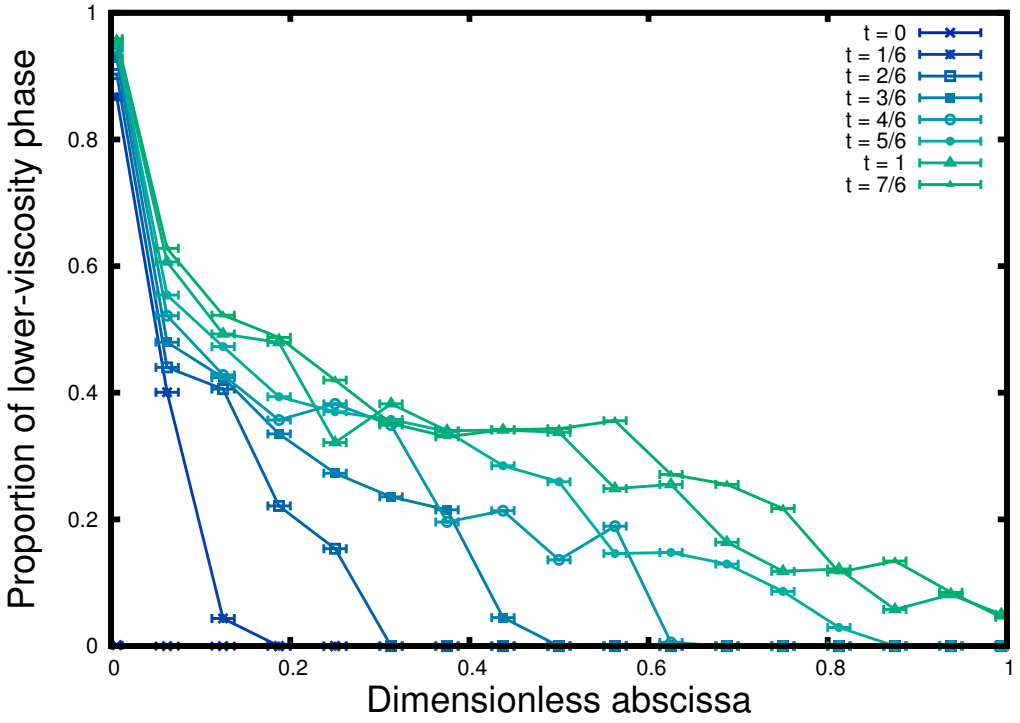

Figure 4.19: Proportion of aqueous phase as a function of dimensionless abscissa for several dimensionless times.

rectangular domains Ω' of size $L \times L/4$ centred on $(0, 0)$

$$\Omega' = [-L/2, L/2] \times [-L/8, L/8].$$

In a first step, the injection of brine is simulated in the domain similarly to what was presented previously. In their experiments, Skauge *et al.* [38] waited till long after breakthrough before beginning the injection of a polymer solution. In the following simulations, it was however decided to begin this injection before breakthrough, in order to reduce the required CPU time.

The injection of polymer is realised from the same side as the one that was used to inject brine. The different viscosity ratios are as follows

$$M_w = \frac{\mu_{\text{brine}}}{\mu_{\text{oil}}} = \frac{1}{2500}, \tag{4.2}$$

$$M_p = \frac{\mu_{\text{polymer}}}{\mu_{\text{oil}}} = \frac{1}{50}. \tag{4.3}$$

Three different cases are considered

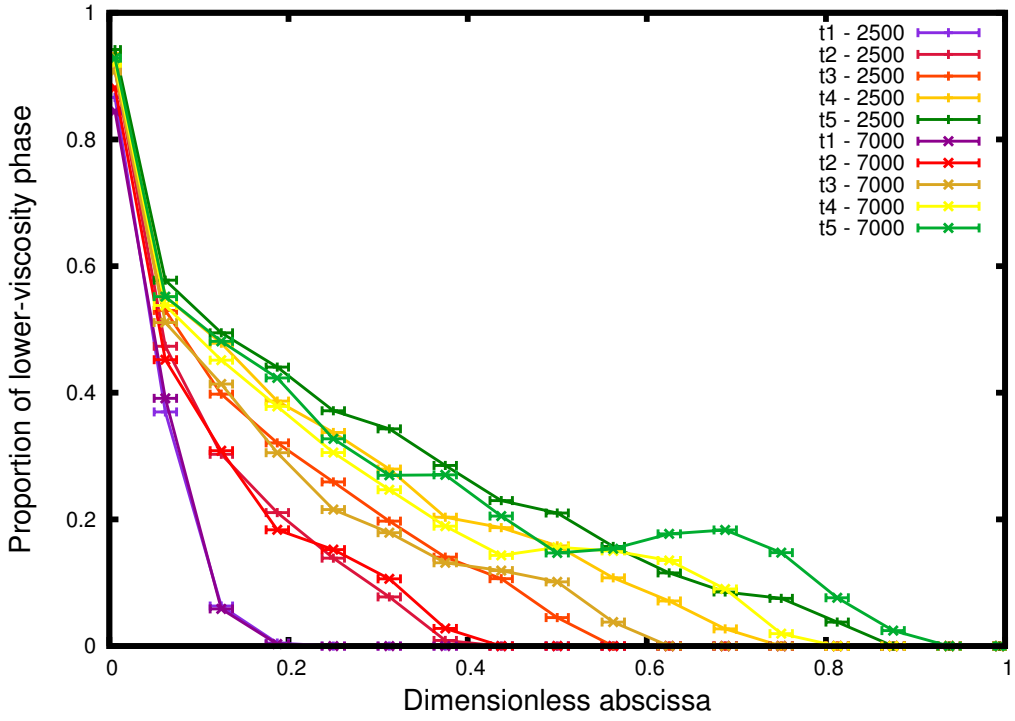

Figure 4.20: Proportion of aqueous phase as a function of abscissa for several times and different viscosity ratios ($M = 1/2500$ and $M = 1/7000$).

1. the polymer and the water are not miscible;

2. case 2: the polymer and the water are miscible but the low diffusion is only the result of the advection scheme;

3. case 3: the polymer and the water are miscible and diffuse one inside the other. In this case, it was checked that $\tau_{\text{Diffusion}} \sim \tau_{\text{Viscosity}} \gg \tau_{\text{CFL}}$.

There is no change in the injection rate (constant massflux $\mathbf{u}(-L/2, y) = U_{\text{in}}\mathbf{e_x}$) when switching from waterflooding to polymer injection occurs. The side boundaries $y = \pm L/2$ impose a slip condition, while the last side allows a "free" outflow condition for the fluids.

In all cases, the results reproduce that of the Bergen experiments. Indeed, the oil that remained after waterflooding is mobilised behind the fingering front by the invading polymer as can be seen in Figure 4.22. The result for waterflooding only is recalled in Figure 4.21 to allow comparison.



Figure 4.21: Waterflooding simulation. Inside the green rectangle, the oil is not mobilised by any polymer solution.



(a)



(b)

Figure 4.22: Injection of polymer as a second step in a rectangular domain (injection from the left-hand side) with diffusion of the polymer phase in the aqueous one: (a) in blue the phase containing both water and polymer, in red the organic one, (b) in red the polymer phase. Inside the green rectangle, the oil is mobilised by the polymer solution, compared to Figure 4.21 and thus the oil ratio decreases compared to waterflooding cases.

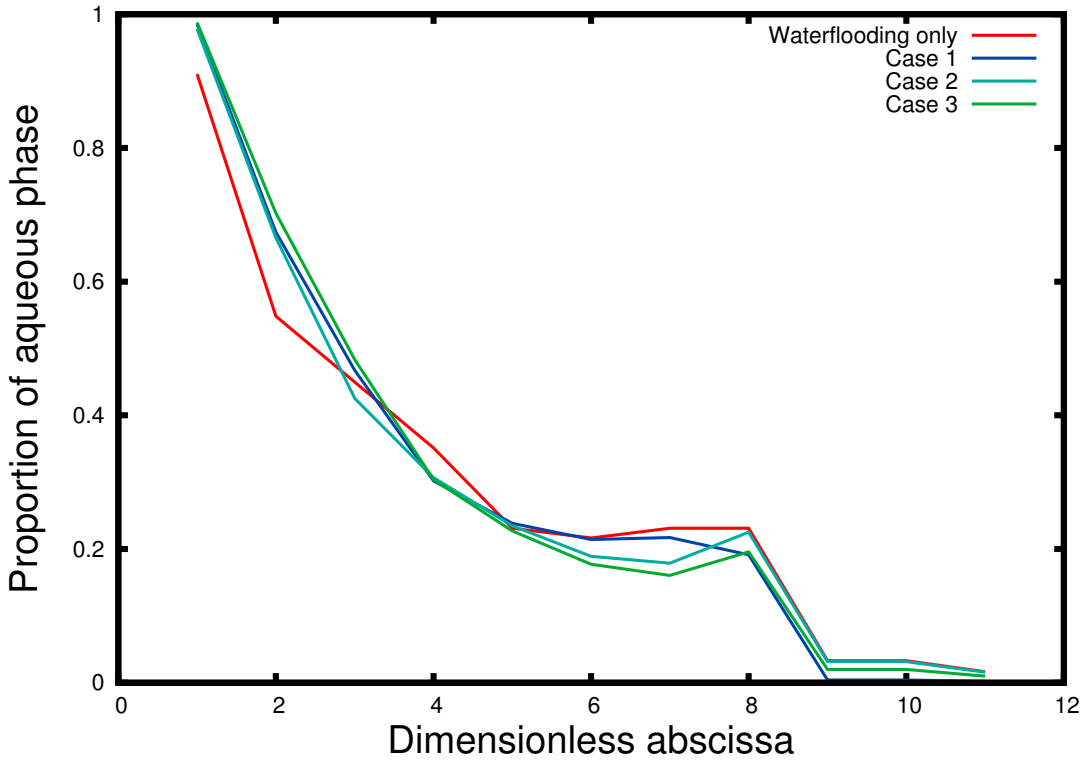

Figure 4.23: Proportion of aqueous phase for several abscissae at a fixed injected volume. The data are average values over thin slices of porous medium two specific abscissae.

The mobilisation of the receding fluid behind the fingering front is obvious when considering the proportion of aqueous phase at a fixed dimensionless time for several abscissae (Figure 4.23). Indeed, for low abscissae this proportion is increased by 10 to 20% for all cases 1, 2 and 3, compared to the simulation of the invasion of the porous medium by water only. On the contrary, the invasion by water alone better fills higher abscissae for a fixed dimensionless time (especially abscissae 4 and 7 in the figure).

Finally, the asymptotic coefficient α_∞ defined above is constant for the three cases ($\alpha_\infty \approx 0.63 \pm 0.02$, see Figure 4.24), but is significantly lower than when injecting water alone ($\alpha_\infty \sim 0.8$, see Figure 4.14). Consequently, when studying scaling properties of the two-step invasion of a porous medium by first a low-viscosity fluid and then an intermediate-viscosity one, one can choose any of the three modellings studied

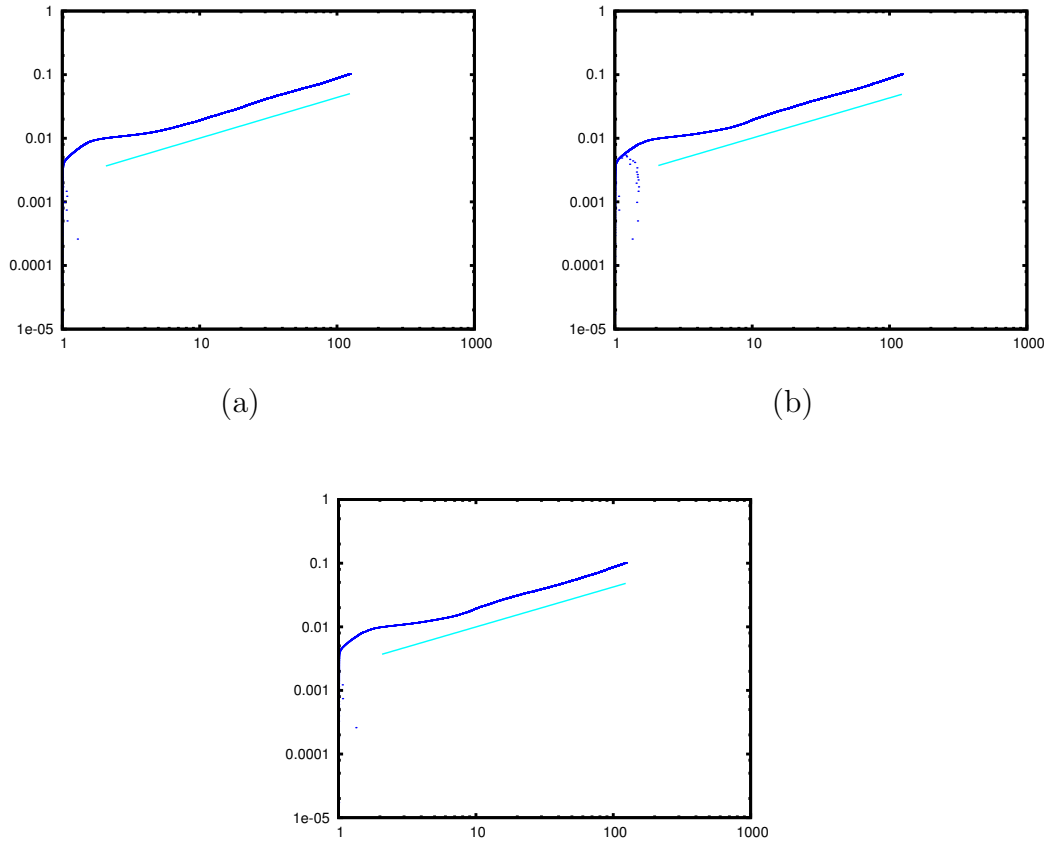

(a) (b)

(c)

Figure 4.24: Dimensionless area as a function of dimensionless length: (a) case 1 ($\alpha_\infty = 0.64 \pm 0.01$), (b) case 2 ($\alpha_\infty = 0.63 \pm 0.01$) and (c) case 3 ($\alpha_\infty = 0.63 \pm 0.01$).

above (for example the one presenting the best computational speed), with no lack of precision.

4.3 Conclusion

It was possible to replicate the Bergen experiments to some extent. Indeed, as observed in the experiments, breakthrough occurs at earlier times for higher viscosity contrast. However, breakthrough occurs much later in the simulations than in the experiments: this is due both to the fact that the 3D aspect of the fingering was neglected (fingering occurs also in the third direction) and to the variation of the area of a fractal cluster with its lower lengthscale (here the mesh size).

When injecting an intermediate-viscosity fluid in a second step, the high-viscosity one is mobilised even behind the fingering front, as was expected after close examination of the experiments. The asymptotic coefficient α_∞ was however constant for the three different cases. As a result, to study scaling properties of the two-step invasion of a porous medium by first water (*i.e.* a low-viscosity fluid) and then a solution of polymers (*i.e.* an intermediate-viscosity one), it is possible to choose any of the three different modellings (for example the fastest computing one) without any lack of precision.

Conclusion and perspectives

Conclusion

This work was focused on studying numerically and theoretically multiphase flow in porous media. To reach this goal, the Gerris Flow Solver was used to model and simulate such flows.

The solid phase was modelled in a new way by considering that the whole domain is filled with fluid. This fluid cannot move inside the solid phase. With such a modelling, the Gerris software efficiently simulates multiphase flows in porous media. Indeed, both strong and weak scalabilities up to 4096 cores are quite good even at reduced porosity and the computational speed is reasonably high. The results are also quite accurate, both in a simple Poiseuille flow test and in randomly generated porous media.

In theory, Gerris is optimised for High-Performance-Computer (HPC) simulation: it uses adaptive mesh refinement and is highly parallelised. Restart of simulations is of course possible. In practice, its use in HPC simulations is not necessarily that easy. The software has also two main drawbacks when dealing with flows in porous media: the absence of relative permeabilities as input when realising Darcy-scale simulations and some problems with the solver *Hypre* as presented in chapter 2.

Simulations of real rocks were realised in three dimensions on both clusters *babbage2* (*Institut d'Alembert* - UPMC) and *Rostand* (*CST Jean Féger* - TOTAL SA) with very promising results. Though it was not possible to attain realistic Reynolds and capillary numbers yet, we could simulate flows in domains of physical size up to $1.152^3\,\mathrm{mm}^3$ in reasonable CPU time.

As flows in Hele-Shaw cells obey the same laws as flows in porous media (Darcy's law), interest was focused on the injection of a lower-viscosity fluid inside a Hele-Shaw cell filled with a higher-viscosity one. Such an injection was studied in two cases: either the fluid was injected from the centre of a square cell or from the side of the domain (in order to replicate experiments of invasion of Bentheimer sandstone). Though the obtained clusters had a characteristic non-isotropic aspect, it was interesting to note that they obeyed the same scaling coefficients as isotropic injections. Indeed, the fractal dimensions in the simulations were quite close to the ones of experimental injections. The existence of two different fractal-dimension regimes in Saffman-Taylor fingering due to central injection was also observed: one at higher viscosity ratio with the coexistence of two different fractal dimensions in the resulting cluster, and one at lower viscosity ratio with only one dimension. What is more, at late times, the area of the resulting bubble varies as the length of the interface to some power α_∞, with different values for finite or infinite viscosity contrasts.

Concerning lateral injection simulation, it was possible to replicate the experiments recalled above to some extent. Indeed, as observed in the experiments, breakthrough occurs at earlier times for higher viscosity contrast. However, breakthrough occurs much later in the simulations than in the experiments: this is due both to the fact that the 3D aspect of the fingering was neglected (fingering occurs also in the third direction) and to the variation of the area of a fractal cluster with its lower lengthscale (here the mesh size). When injecting polymer in a second step, the oil is mobilised even behind the fingering front, as was expected after close examination of the experiments.

Perspectives

Future developments could be made in the code in order to reach bigger simulations. Indeed, though the CFL number cannot be improved for theoretical reasons, the computational speed would need increasing. This could be realised by several means.

The best way to increase substantially the computational speed would be to implement an implicit version of surface tension inside Gerris instead of the present explicit implementation. The computation would allow much higher timesteps for reasonable additional CPU time, and it would be much easier to reduce the capillary number without too much computational cost.

The computational speed could be increased also both by using better Poisson solvers (for example by understanding why *Hypre* does not currently perform well and correcting it) and by improving the compilation of the code on the different clusters.

The accuracy of the code could also be improved. An easy way to do so would be to implement an even better version of the solids where the velocity is completely removed inside the solid phase. Indeed, for now, some velocity can be generated between two timesteps... This improvement would also improve the computational speed as a side-effect. It would indeed no longer be necessary to use a computationally-demanding drag force to reduce this parasite velocity.

These improvements would allow to consider bigger simulations in domains of physical size of the order of 1 cm. These simulations could allow to measure the permeability of such domains. The results could then be used in Darcy-scale simulations in order to better understand what occurs inside the reservoir.

Finally, another improvement could be realised by implementing contact angle inside Gerris [404]. As of now, it is indeed only possible to consider either totally non-wetting rocks or totally-wetting ones with the modelling of the solid phase that was used in this study. On the contrary with the default modelling of the solids, only 90° contact angles are considered. Such an improvement would allow to consider a much broader range of rocks, including solid matrices with varying contact angles due to diverse mineral inclusions.

APPENDIX A

Invasion percolation

Contents

A.1 Basic process 217

A.2 Algorithm 218

A.3 Comparison with ordinary percolation 219

A.4 Fractal dimension 220

This appendix is mainly extracted from [405] with slight modifications.

A.1 Basic process

Invasion pecolation is a dynamic percolation process introduced by Wilkinson and Willemsen [192], motivated by the study of the flow of two immiscible fluids in porous media [406, 407]. Consider the case in which oil is displaced by water in a porous medium. When the water is injected very slowly then the process takes place at very low capillary numbers Ca. This implies that the capillary forces completely dominate the viscous forces, and therefore the dynamics of the process is determined on the

pore level. In the limit of vanishing capillary numbers one may neglect any pressure drops both in the invading and the receding fluids.

One often finds that water is the "wetting" fluid, *i.e.* the water will spontaneously invade the oil-filled porous medium unless the pressure in the water is kept below that of the receding fluid.

Wilkinson and Willemsen proposed to simulate this process in an idealised medium where the network of pores may be viewed as a regular lattice in which the sites and bonds of the lattice represent the pores and the throats respectively. Randomness of the medium is incorporated by assigning random numbers to the sites and bonds to represent the sizes of these pores and throats. Simulation of the process in a given realisation of the lattice thus consists of following the motion of the water-oil interface as it advances through the smallest available pore, marking the pores filled with the invading fluid.

This model also applies in the case where a non-wetting fluid displaces a wetting fluid. In this case the pressure in the invading fluid is above that of the receding fluid and the interface advances quickly through the large pores and gets stuck in the narrow throats connecting the pores.

During percolation, the invading fluid traps regions of the receding fluid. As the invader advances, it is possible for it to completely surround regions of the defending fluid from the exit side of the sample. This is one origin of the phenomenon of "residual oil". Since oil is incompressible, Wilkinson and Willemsen introduced the new rule that water cannot invade trapped regions of oil.

A.2 Algorithm

The algorithms describing invasion percolation are now simple to describe:

- Assign random numbers r in the range $[0, 1]$ to each site of an $L \times L$ lattice.
- Select sites of injection for the invading fluid and sites of extraction for the receding fluid.

- Identify the growth sites as the sites which belong to the receding fluid and are neighbours to the invading fluid.
- Advance the invading fluid to the growth site that has the lowest random number r.
- TRAPPING: growth sites in regions completely surrounded by the invading fluid are not active and are eliminated from the list of growth sites.
- End the invasion process when the invading fluid reaches an exit site.

This model advances the invading fluid to new sites one by one, always selecting the possible growth site with the lowest random number associated with it. This is an algorithm that lets the invading cluster grow in a manner subject to local properties. The rule that a trapped region cannnot be invaded introduces a nonlocal aspect into the model. The question whether or not a region is trapped cannot be answered locally, and involves a global search of the system.

A.3 Comparison with ordinary percolation

It is interesting to compare the invasion percolation process without trapping to the ordinary percolation process [408]. In the ordinary percolation process one may grow percolation clusters as follows. The sites on an $L \times L$ lattice are assigned random numbers r inthe range $[0, 1]$ and one places a seed on the lattice. Then for a given choice of the occupation probability p ($0 \leqslant p \leqslant 1$) the cluster grows by occupying all available sites with random numbers $r \leqslant p$. The growth of the percolation cluster stops when no more such numbers are found on the boundary of the cluster. Of course, most of the sites chosen will generate clusters of a finite size. Only if the seed site happens to lie on the incipient percolating cluster at p_c[1], or on the percolating

[1]The critical probability p_c of ordinary percolation process is defined as the largest value of p for which the percolation probability P_∞ (probability that a fluid injected at a site, chosen at random, will wet infinitely many pores) verifies $P_\infty = 0$. For a quadratic lattice, $p_c = 0.59275 \pm 0.00003$ [409]. For a triangular lattice, $p_c = 1/2$ [405].

cluster for $p > p_c$, will the percolation cluster grow to a size that spans the lattice. By contrast, in invasion percolation the cluster grows by always selecting the smallest random number, no matter how large. However, once a large number r_0 has been chosen, it is not necessarily true that subsequently every number $r \geqslant r_0$ will be chosen – smaller numbers will in general become available at the interface and will thus be chosen.

A.4 Fractal dimension

Naturally in the finite geometry, the invader will gradually fill the entire lattice if the invasion process is continued. Wilkinson and Willemsen found that the number of sites $M(L)$ in the central $L \times L$ portion of the lattice at breakthrough increases with the size of the lattice as follows

$$M(L) = AL^{D_{inv}}, \tag{A.1}$$

with $D_{inv} \approx 1.89$. An analogous equation can be found for ordinary percolation processes and the fractal dimension of invasion percolation without trapping, D_{inv} is found to equal the fractal dimension of the incipient percolation cluster at p_c. There is now considerable evidence that invasion percolation in fact is in the same universality class as ordinary percolation [410].

Trapping changes the invasion percolation quite drastically in two dimensions. The number of sites varies as

$$M(L) = AL^{D_{trap}}, \tag{A.2}$$

with $D_{trap} \approx 1.82$ [192]. Lenormand and Zarcone [193] investigated experimentally the invasion of air at a very slow rate into a 2D square-grid network filled with glycerol (see Figure A.1). They found that the number of ducts filled by the invading fluid counted inside boxes of side L followed equation (A.2) with $1.80 < D_{trap} < 1.83$ consistent with the numerical simulations.

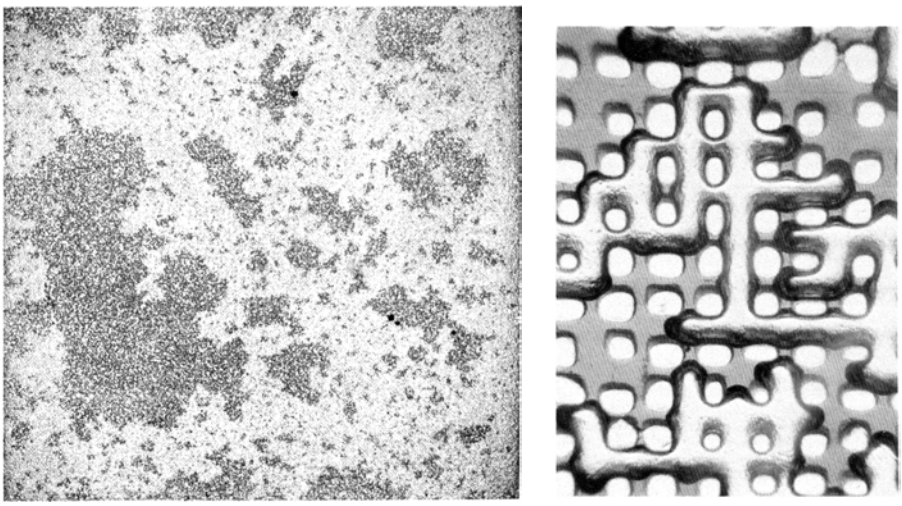

(a) (b)

Figure A.1: Experiments of drainage in a 2D network. (a) Displacement of the wetting fluid (black) by the non-wetting fluid (white) injected on the left-hand side of the network. On the right-hand side, a semipermeable membrane prevents the nonwetting fluid from flowing outside. (b) Close-up of the situation of the wetting fluid (black) and nonwetting fluid (white) in the ducts of the etched network. The distance between two nodes is about 0.8 mm. [193]

APPENDIX B

Diffusion-Limited Aggregation

Contents

B.1 The basic concept 223

B.2 Laplacian growth and Dielectric Breakdown Model . . . 226

B.3 Conformal mapping 229

B.3.1 Loewner evolution and the Hastings-Levitov scheme 229

This appendix is mainly extracted from [340] with slight modifications.

B.1 The basic concept

The original DLA algorithm [327, 194] was quite simple: on a lattice, declare that the point at the origin is the first member of the cluster. Then launch a random walker from a distant point and allow it to wander until it arrives at a neighbouring site to the origin, and attach it to the cluster, *i.e.* freeze its position. Then launch another walker from a new distant point and let it attach to one of the two previous points, and so on. The name, diffusion-limited aggregation, refers to the fact that random



(a) From a seed (b) From a line

Figure B.1: Diffusion-Limited Aggregation clusters in two dimension. (a) The red particles have attached most recently to the cluster and are concentrated at the tips of the growing branches. By contrast, relatively few particles penetrate deeply into the "fjords" [231]. (b) The lines represent the successive equipotentials of random walker probability densities for a two-dimensional DLA cluster growing from a single line. Clearly the random walker probability declines precipitously as one progresses down a fjord, leading to very small growth probabilities at the bottom compared with the growing tips of the cluster [418].

walkers, *i.e.* diffusing particles, control the growth. DLA is a simplified view of a common physical process: growth limited by diffusion.

It became evident that for large clusters the overall shape is dependent on the lattice type [411, 412], that is, DLA clusters are deformed by lattice anisotropy. This is an interesting subject [411, 413, 414, 415, 416] but most modern work is on DLA clusters without anisotropy, *i.e.* off-lattice clusters. The off-lattice algorithm is similar to the original one: instead of a random walk on a lattice, the particle is considered to have a radius a. For each step of the walk the particle moves its center from the current position to a random point on its perimeter. If it overlaps a particle of the current cluster, it is backed up until it just touches the cluster, and frozen at that point. Then another walker is launched. Most of the work on DLA has been realised in two dimensions, but dimensions up to 8 have been considered [417].

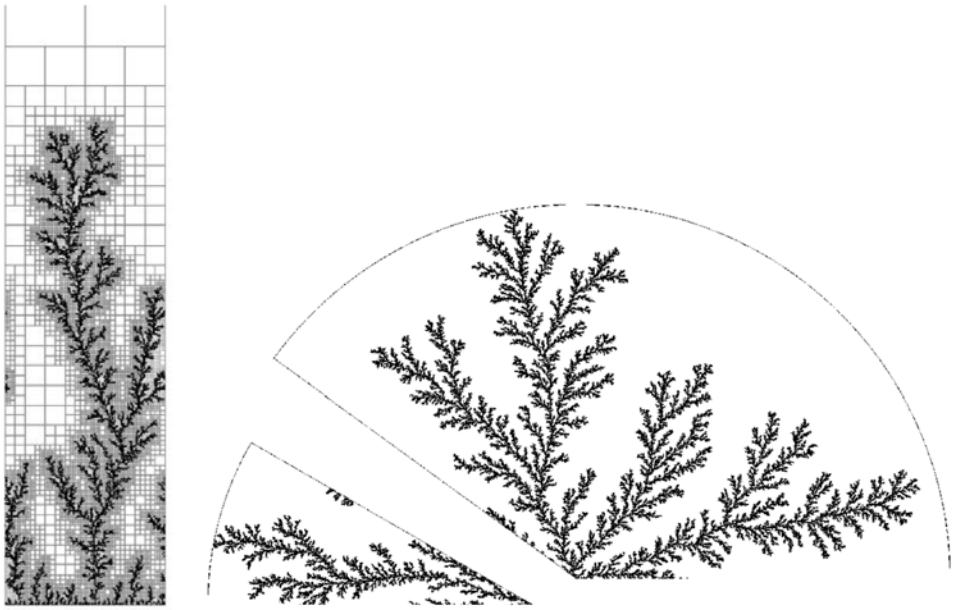

(a) (b)

Figure B.2: DLA grown in (a) a channel [340] and (b) wedges for $\alpha = 30°$ and $144°$ [425]. The DLA cluster is grown using quadtree adaptive mesh refinement in the channel case (see Chapter 2).

Patterns like Figure B.1(a) have been analysed for fractal properties. Careful measurements of both D_0 and D_2 (using the method mentioned in Appendix C of fitting $n(r)$ to r^{D_2}) give the same fractal dimension $D_F = 1.71$ [417, 419, 420]. There is some disagreement about the next digit. There have been suggestions that DLA is a mass multifractal [421] but most authors now agree that all of the D_q are the same for the mass distribution. For three dimensions $D_F \approx 2.5$ [416, 417] and for four dimensions $D_F \approx 3.4$ [417].

However, some authors [422, 423] have claimed that plane DLA is not a self-similar fractal at all, and that the fractal dimension will drift towards 2 as the number of particles increases. More recent works based on conformal maps [424] have cast doubt on this.

Plane DLA can be grown in restricted geometries (Figure B.2). The shape of such clusters is an interesting problem in pattern formation [333, 425, 426, 427]. It was long thought that DLA grown in a channel had a different fractal dimension than

in radial geometry [428, 429, 430]. However, more careful work has shown that the dimensions are the same in the two cases [420].

B.2 Laplacian growth and Dielectric Breakdown Model

Let us wonder how the cluster of Figure B.1(a) gets to be rough. If the cluster already has a rough shape, it is quite difficult for a random walker to penetrate a narrow channel (Figure B.1(b)). The channels do not fill in and the shape might be preserved. But the real question is to explain why a smooth line, *e.g.* a disk, does not continue to grow smoothly. in fact, it is easy to test that any initial condition is soon forgotten in the growth [194]. If the growth starts with a smooth shape it roughens immediately because of a growth instability intrinsic to diffusion-limited growth. This instability was discovered by Mullins and Sekerka [431] who used a statement of diffusion-limited growth in continuum terms: this is known as the Stefan problem [317, 432] and is the standard way to idealize crystallisation in the diffusion-limited case.

The Stefan problem goes as follows: suppose that we have a density $\phi(\mathbf{r}, t)$ of particles that diffuse until they reach the growing cluster where they deposit. Then we have

$$\frac{\partial \phi}{\partial t} = \nu \nabla^2 \phi, \tag{B.1}$$

$$\frac{\partial \phi}{\partial n} \propto u_n. \tag{B.2}$$

ϕ should thus obey the diffusion equation, with μ the diffusion constant. The normal growth velocity u_n of the interfacce is proportional to the flux onto the surface $\partial\phi/\partial n$. However the term $\partial\phi/\partial t$ is of order $\nu\partial\phi/\partial x$ where ν is a typical growth velocity. Now $|\nabla^2\phi| \approx (\nu/D)|\partial\phi/\partial n|$. In the DLA case, we launch one particle at a time so the velocity goes to zero. Hence equation (B.1) reduces to the Laplace equation

$$\nabla^2 \phi = 0. \tag{B.3}$$



Figure B.3: A DLA-like cluster obtained by diffusive growth from a copper sulfate solution in an electrodeposition cell. [433]

Since the cluster absorbs the particles, we should think of it as having $\phi = 0$ on the surface. We are to solve an electrostatics problem: the cluster is a grounded conductor with fixed electric flux far away. We grow by an amount proportional to the electric field at each point on the surface. This is called the quasi-static or Laplacian growth regime for deterministic growth. A linear stability analysis of these equations gives the Mullins-Sekerka instability [431]. The qualitative reason for the instability is that near the tips of the cluster the contours of ϕ are compressed so that the growth rate $\partial\phi/\partial n$ is large. Thus tips grow unstably. We expect DLA to have a growth instability.

However, we can turn the argument and use these observations to give a restatement of the DLA algorithm in continuum terms: we calculate the electric field on the surface of the aggregate, and interpret equation (B.2) as giving the distribution of growth probability p at a point on the surface. We add a particle with this probability distribution, recalculate the potential using equation (B.3) and continue. This is called Laplacian growth. Simulations of Laplacian growth yield the same sort of clusters as the original discrete algorithm.

DLA is thus closely related to one of the classical problems of mathematical physics, dendritic crystal growth in the quasistatic regime (Figure B.3). However it is not quite the same for several reasons: DLA is dominated by noise whereas the Stefan problem is deterministic. Also, the boundary conditions are different [432]: for a crystal, if we interpret u as $T - T_m$ where T is the temperature and T_m the melting temperature, we have $\phi = 0$ only on a flat surface. On a curved surface, we need

$\phi \propto \gamma\kappa$ with γ the surface stiffness and κ its curvature. The surface tension acts as a regularisation which prevents the Mullins-Sekerka instability from producing sharp cusps [343]. In DLA the regularisation is provided by the finite particle size. And, of course, crystals have anisotropy in the surface tension.

These considerations led Niemeyer, Pietronero and Weismann [228] to a clever generalisation of Laplacian growth. They were interested in dielectric breakdown with ϕ representing a real electrostatic potential. This is known to be a threshold process so that we expect that the breakdown probability is non-linear in $\partial\phi/\partial n$. To generalise they chose

$$p \propto \left(\frac{\partial\phi}{\partial n}\right)^{\eta}, \tag{B.4}$$

where $\eta \in \mathbb{R}^{+}$.

There are some interesting special cases for this model (Figure B.4). For $\eta = 0$ each growth site is equally likely to be used. This is the Eden model [434]. For $\eta = 1$ we have the Laplacian growth version of DLA, and for larger η, we get a higher probability to grow at the tips so that the aggregates are more spread out. There is a remarkable fact which was suggested numerically in [435] and confirmed more recently [436, 437]: for $\eta > 4$ the aggregate prefers growth at tips so much that it besomes essentially linear and non-fractal.



(a) (b) (c) (d)

Figure B.4: DBM patterns for 1000 particles on a triangular lattice. (a) $\eta = 0.5$, (b) $\eta = 1$ *i.e.* this is a small DLA cluster, (c) $\eta = 2$ and (d) $\eta = 3$. [340]

B.3 Conformal mapping

For pattern formation in two dimensions the use of analytic function theory and conformal mapping methods allows a new look at growth processes. The idea is to think of a pattern in the z plane as the image of a simple reference shape, *e.g.* the unit circle in the w plane, under a time-dependent analytic function $z = F_t(w)$. More precisely, the region outside of the pattern is considered as the image of the region outside of the reference shape. By the Riemann mapping theorem [438] the map exists and is unique if one sets a boundary condition such as $F(w) \to r_0 w$ as $|w| \to +\infty$. We will also use the inverse map $w = G(z) = F^{-1}(z)$.

For Laplacian growth processes this idea is particularly interesting since the growth rules depend on solving the Laplace equation outside the cluster. As the Laplace equation is conformally invariant, one can solve in the w plane and transform the solution: if $\nabla^2\phi(w) = 0$, $\phi = 0$ on the unit circle and ϕ is the real part of a complex potential Φ in the w plane, then Re $\Phi(G(z))$ solves the Laplace equation in the z plane with Re $\Phi = 0$ on the cluster boundary. Thus as $\Phi = \ln(w)$ in w-space, the solution outside the cluster is

$$\Phi(z) = \ln G(z). \tag{B.5}$$

Note that the constant r_0 is the radius of the disk that gives the same potential as the cluster far away [340].

The growth probability is uniform around the unit circle in the w plane. This means that equal intervals on the unit circle in w space map into equal regions of growth probability in the z plane. The map thus contains information about the growth probability

$$|\nabla\Phi| = |G'| = \frac{1}{|F'|}. \tag{B.6}$$

The problem remains to construct the maps G or F for a given cluster.

B.3.1 Loewner evolution and the Hastings-Levitov scheme

A useful approach to finding F is to impose a dynamics on the map which gives rise to the growth of the cluster. This is closely related to Loewner evolution where a

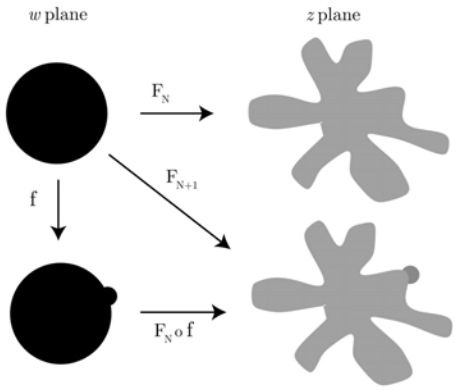

Figure B.5: The Hastings-Levitov scheme for fractal growth. At each stage, a bump of the proper size is added to the unit circle. The composition of the bump map f with the map at stage N gives the map at stage $N+1$. [340]

curve in the z plane is generated by a map that obeys an equation of motion

$$\frac{dG_t(z)}{dt} = \frac{2}{G_t(z) - \xi(t)}. \tag{B.7}$$

The map is to the upper half plane from the upper half plane minus the set of singularities $G = \xi$ [439]. If $\xi(t)$ is a stochastic process then many interesting statistical objects such as percolation clusters can be generated.

For DLA a similar approach was presented by Hastings and Levitov [415, 440]. In this case, the evolution is discrete, and is designed to represent the addition of particles to a cluster. The process is iterative: suppose we know the map F_N for N particles. Then we want to add a bump corresponding to a new particle. This is accomplished by adding a bump of area λ in the w-plane on the surface of unit circle at angle θ. There are various explicit functions that generate bumps [440]. Such functions depend on a parameter which gives the aspect ratio of the bump.

Let us call the resulting transformation $f_{\lambda,\theta}$. If we use F_N to transform the unit circle with a bump we get a cluster with an extra bump in the z-plane, *i.e.* we have added a particle to the cluster and $F_{N+1} = F_N \circ f$ (Figure B.5).

There are two matters that need to be dealt with. First, we need to pick θ. Since the probability to grow is uniform on the circle in the w-plane, we take θ to be a random variable uniformly distributed between 0 and 2π. Also we need the bump

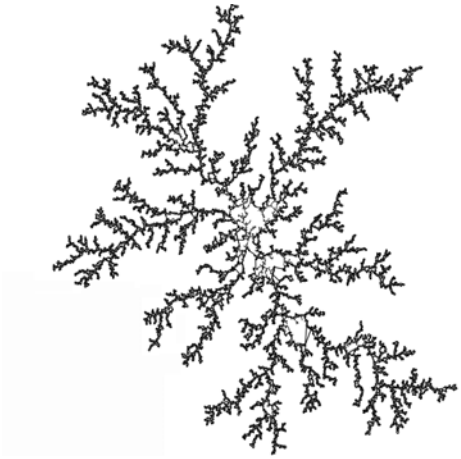

Figure B.6: A DLA cluster made by iterated conformal maps. [340]

in the z-space to have a fixed area, λ_0. That means that the bump in the w-space needs to be adjusted because conformal transformations stretch lengths by $|F'|$. A first guess for the area is

$$\lambda_{N+1} = \frac{\lambda_0}{|F'_N(e^{i\theta_{N+1}})|^2}. \tag{B.8}$$

However this is just a first guess. The stretching of lengths varies over the cluster and there can be some regions where the approximation of equation (B.8) is not adequate. In this case an iterative procedure is necessary to get the area right [415, 420]. The transformation itself is given by

$$F_N = f_{\lambda_1,\theta_1} \circ f_{\lambda_2,\theta_2} \circ \cdots \circ f_{\lambda_N,\theta_N}. \tag{B.9}$$

All of the information needed to specify the mapping is contained in the list λ_j, θ_j, $1 \leqslant j \leqslant N$ (Figure B.6).

If we choose θ uniformly in w-space, we have chosen points with the harmonic measure $|F'|^{-1}$ and we make DLA clusters. To simulate DBM clusters with $\eta \neq 1$ one must choose the angles non-uniformly [436].

When realised in wedge-like geometries, the fractal dimension depends significantly on the opening angle β of the sector (see Figure B.7). It however tends towards the usual DLA value for $\beta \to 2\pi$ [441].

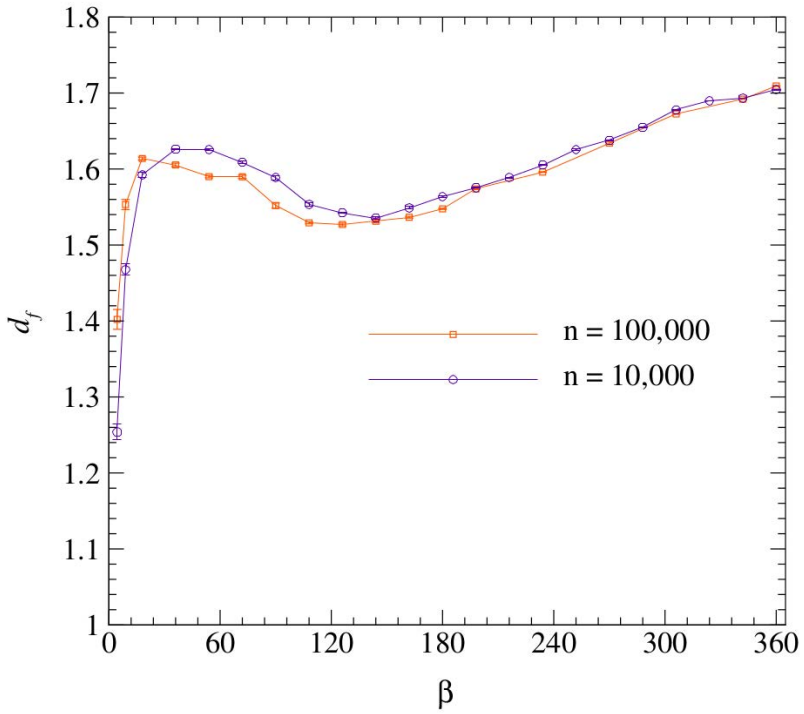

Figure B.7: The fractal dimension D_F of the patterns produced by using a restricted Hastings-Levitov algorithm with uniform measure as a function of the opening angle β in the w-plane. The averages were taken over 400 clusters of size $n = 10^4$ (circles) and 30 clusters of size $n = 10^5$ (squares). [441]

APPENDIX C

Fractals and multifractals

Contents

C.1 Definition 233

C.2 Fractal dimension 234

C.3 How to calculate the fractal dimension? 237

C.4 Fatou and Julia sets 237

C.1 Definition

In the 1970s, Benoît Mandelbrot [395, 442, 443] developed the idea of fractal geometry to unify a number of earlier studies of irregular shapes and natural processes [405]. Mandelbrot focused on a particular set of such objects and shapes, those that are self similar, *i.e.* where a part of the object is identical (either in shape, or for a set of shapes, in distribution) to a larger piece (Figure C.1). He dubbed these fractals and noted the surprising ubiquity of self-similar shapes in nature.

In 1982, he offered the following tentative definition of a fractal:

"A fractal is by definition a set for which the Hausdorff-Besicovitch dimension strictly exceeds the topological dimension."

This definition requires a definition of the terms set, Hausdorff-Besicovitch dimension (D_F) and topological dimension[1] D, which is always an integer. In fact, Mandelbrot [444] retracted this tentative definition and proposed instead the following one:

"A fractal is a shape made of parts similar to the whole in some way."

Following the seminal article by Mandelbrot [442], great interest has surrounded many fractal processes in fields as diverse as computer science [446], hydrology [447] or finance [448].

C.2 Fractal dimension

The kind of objects we deal with is highly irregular (see Figure C.1). We think of the object as being made up of a large number N of units and to be of overall linear dimension R. In growth processes the objects are formed by adding the units according to some dynamics. We will call the units "particles" and take their size to be a.

Such patterns need not be merely random, but can have well defined scaling properties in the regime $a \ll R$ (*e.g.* Koch snowflake).

In order to characterise the geometry of such complex objects, we first cover the points in question with a set of $n(l)$ boxes of fixed size, with $a \ll l \ll R$ (Figure C.2). Clearly, for a smooth curve, the product $ln(l)$ approaches a limit (the length of the

[1]The Lebesgue covering dimension or topological dimension of a topological space is one of several different ways of defining the dimension of the space in a topologically invariant way.

An open cover of a topological space X is a family of open sets whose union is X. The ply of a cover is the smallest number n (if it exists) such that each point of the space belongs to at most n sets in the cover. A refinement of a cover C is another cover, each of whose sets is a subset of a set in C; its ply may be smaller than, or possibly larger than, the ply of C. The covering dimension of a topological space X is defined to be the minimum value of n, such that every finite open cover C of X has a refinement with ply at most $n+1$. If no such minimal n exists, the space is said to be of infinite covering dimension.

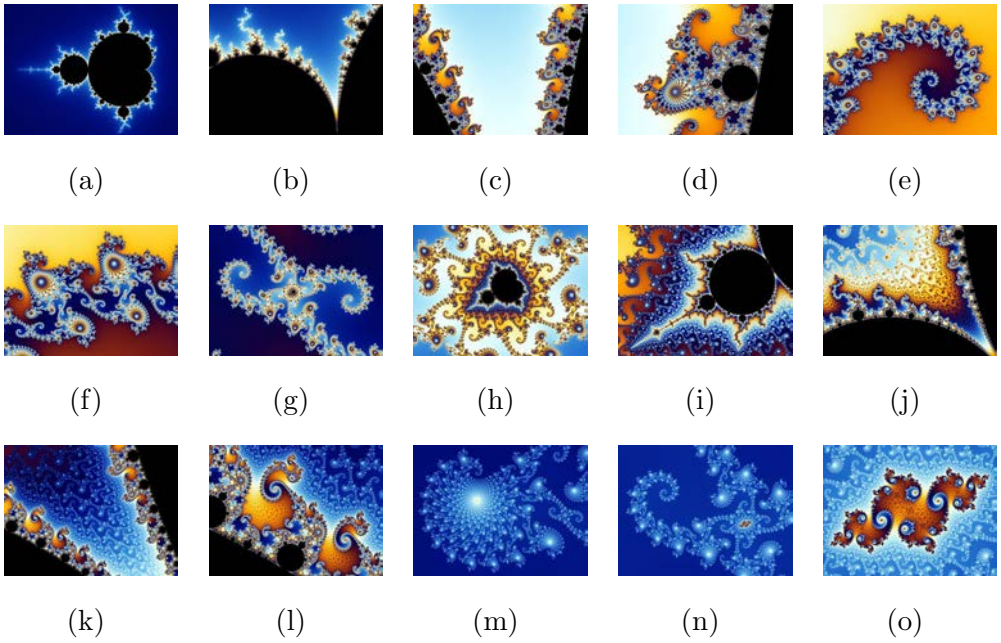

(a) (b) (c) (d) (e)

(f) (g) (h) (i) (j)

(k) (l) (m) (n) (o)

Figure C.1: Mandelbrot set. (a) - (o) Zoom on point $z = -0.743643887037151 + 0.13182590420533i$, revealing the self-similarity of the set. The magnification of picture (o) with respect to the initial image is $59,979,000,000$. [445]

curve) as $l \to 0$. This is a number of order R. For a planar region with smooth boundaries, $l^2 n(l)$ approaches the area, of order R^2. The objects of ordinary geometry geometry in d dimensions have measures given by the limit of $l^d n(l)$. For an object with many scales (a fractal), in general none of these relations hold. Rather, the product $l^{D_F} n(l)$ approaches a limit with D_F not necessarily an integer: D_F is called the (similarity) fractal dimension or Hausdorff-Besicovitch dimension [449, 450, 451]. Said another way, we define the fractal dimension by

$$n(l) \propto (R/l)^{D_F}. \tag{C.1}$$

For an infinite fractal there are no characteristic lengths. For a finite size object there is a characteristic length, the overall scale, R.

It is useful to generalise this definition in two ways. First we consider not only a geometric object, but also a measure, that is a non-negative function μ defined on the points of the object such that $\int d\mu = 1$. For the geometry, we take the measure

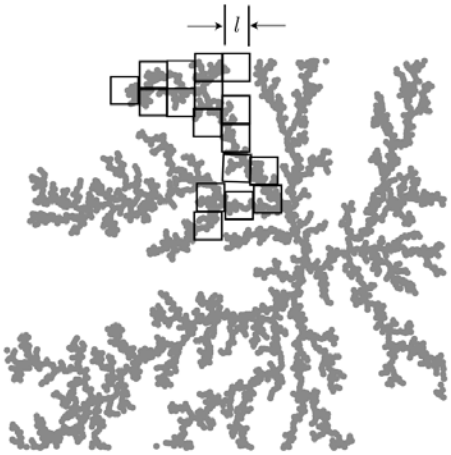

Figure C.2: A partial covering of a pattern with boxes. Smaller boxes reveal smaller scales of the pattern. For a pattern with many scales there is a non-trivial scaling between the box size l and the number of boxes. [340]

to be uniform on the points. However, for growing fractals we could also consider the growth probability at a point. Second, we define a sequence of generalised dimensions. If we are interested in geometry, we denote the mass of the object covered by box i by p_i. For an arbitrary measure, we define

$$p_i = \int d\mu, \tag{C.2}$$

where the integral is over the box labeled i. Then, following [452, 453] we define a partition function for the p_i

$$\chi(q) = \sum_{i=1}^{n} p_i^q, \tag{C.3}$$

where $q \in \mathbb{R}$. For an object with well-defined scaling properties we often find that χ scales with l in the following way as $l/R \to 0$

$$\begin{aligned} \chi(q) \propto (R/l)^{-\tau(q)} &\equiv (R/l)^{-(q-1)D_q}, \\ \tau(q) &= (q-1)D_q. \end{aligned} \tag{C.4}$$

Objects with this property are called fractals if all the D_q are the same. Otherwise they are multifractals [339].

Some of the D_q have special significance. The similarity dimension mentioned above is D_0 since in this case $\chi = n$. If we take the limit $q \to 1$ we have the

information dimension of dynamical systems theory

$$D_1 = \frac{d\tau}{dq}\Big|_{q=1} = \sum_i p_i \frac{\ln\, p_i}{\ln\, l}. \tag{C.5}$$

D_2 is called the correlation dimension since p_i^2 measures the probability that two points are close together, *i.e.* the number of pairs within distance l. This interpretation gives rise to a popular way to measure D_2. If we suppose that the structure is homogeneous, then the number of pairs of points can be found by focusing on any point, and drawing a d-dimensional disk of radius r around it. The number of other points in the disk will scale as r^{D_2}.

For a simple fractal all of the D_q are the same and we use the symbol D_F. If the generalised dimensions differ, then we have a multifractal. Multifractals were introduced by Mandelbrot [454] in the context of turbulence.

C.3 How to calculate the fractal dimension?

Special attention was devoted to ways to determine the Hausdorff-Besicovitch dimension D_F of fractal sets [455, 456, 457, 458]. It turns out to be very difficult to determine D_F by the box-counting method, especially when $D_F > 2$ [458]. Consequently, Grassberger and Procaccia [459] suggested to deduce the properties of clusters from the density-density correlation function $C(r) = \langle[\rho(r')][\rho(r'+r)]\rangle$.

Indeed, it seems the correlation function varies as $C(r) \sim r^{-\delta}$ for small values of r in both viscous fingering and DLA in circular geometry [341]. It is easy to demonstrate the exponent is closely related to the dimension of the considered fractal cluster ($D_F = D_2 = d - \delta$ with d the embedding dimension).

This method has another important advantage: it is much easier to use than the box-counting method when computing trajectories of a dynamical system.

C.4 Fatou and Julia sets

In the context of complex dynamics, a topic of mathematics, the Julia set and the Fatou set are two complementary sets defined from a function (Figure C.3). Informally,

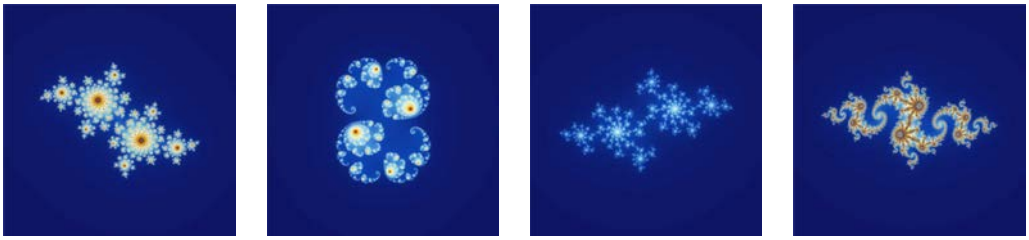

Figure C.3: Examples of Julia sets. [460]

the Fatou set of the function consists of values with the property that all nearby values behave similarly under repeated iteration of the function, and the Julia set consists of values such that an arbitrarily small perturbation can cause drastic changes in the sequence of iterated function values. Thus the behavior of the function on the Fatou set is "regular", while on the Julia set its behavior is "chaotic".

These sets are named after the French mathematicians Gaston Julia [461] and Pierre Fatou [462] whose work began the study of complex dynamics during the early 20th century.

Let $f(z)$ be a complex rational function from the plane into itself, that is, $f(z) = p(z)/q(z)$, where $p(z)$ and $q(z)$ are complex polynomials. Then there is a finite number of open sets $F_1, \cdots, F_r$, that are left invariant by $f(z)$ and are such that:

- the union of the F_i's is dense in the plane;
- $f(z)$ behaves in a regular and equal way on each of the sets F_i.

The last statement means that the termini of the sequences of iterations generated by the points of F_i are either precisely the same set, which is then a finite cycle, or they are finite cycles of circular or annular shaped sets that are lying concentrically. In the first case the cycle is attracting, in the second it is neutral.

These sets F_i are the Fatou domains of $f(z)$, and their union is the Fatou set $F(f)$ of $f(z)$. Each of the Fatou domains contains at least one critical point of $f(z)$, that is, a (finite) point z satisfying $f'(z) = 0$, or $z = \infty$, if the degree of the numerator $p(z)$ is at least two larger than the degree of the denominator $q(z)$, or if $f(z) = 1/g(z) + c$ for some c and a rational function $g(z)$ satisfying this condition.

The complement of $F(f)$ is the Julia set $J(f)$ of $f(z)$. $J(f)$ is a nowhere dense set (it is without interior points) and an uncountable set (of the same cardinality as the real numbers). Like $F(f)$, $J(f)$ is left invariant by $f(z)$, and on this set the iteration is repelling, meaning that $|f(z) - f(w)| > |z - w|$ for all w in a neighbourhood of z (within $J(f)$). This means that $f(z)$ behaves chaotically on the Julia set. Although there are points in the Julia set whose sequence of iterations is finite, there are only a countable number of such points (and they make up an infinitely small part of the Julia set). The sequences generated by points outside this set behave chaotically, a phenomenon called deterministic chaos.

There has been extensive research on the Fatou set and Julia set of iterated rational functions, known as rational maps. For example, it is known that the Fatou set of a rational map has either 0,1,2 or infinitely many components. Each component of the Fatou set of a rational map can be classified into one of four different classes.

APPENDIX D

Simple Line Interface Calculation method

This appendix is extracted from [463] with slight modifications.

The Simple Line Interface Calculation method (SLIC) [279] is a line technique that was proposed to maintain a well defined interface within a volume fraction framework. It was specifically developed to deal with multiphase flow. The fluid distribution in an interface-containing cell is computed by using the volume fraction distribution in the neighbouring cells. Several methods can be found in the literature.

In the original SLIC method the interface is approximated in each mesh cell by a line parallel to one of the coordinate axes. We consider different fluid configurations in that cell when dealing with the horizontal and vertical movements respectively. For the x-sweep, one uses only the volume fraction values on the left and right of a cell, while for the y-sweep one focuses on the values found above and underneath the cell. Only four different types of interface cells can be found with the original SLIC method [279]. They are:

1. each neighbour is filled with a different fluid (Figure D.1(a));

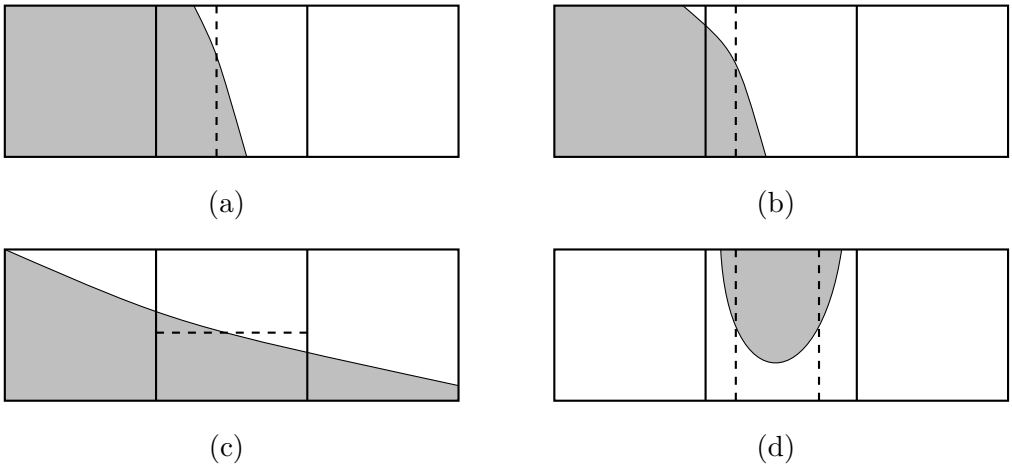

Figure D.1: Interface approximations for the centre cell with the SLIC method (dashed lines).

2. one of the neighbours is cut by the interface (Figure D.1(b));

3. both neighbours are cut by the interface (Figure D.1(c));

4. both neighbours are filled with the same fluid (Figure D.1(d)).

A similar set can be constructed for the y-sweep. Both sets form the building bocks with which the SLIC interface is reconstructed (Figure D.2(a)).

This method was first improved by Chorin [464] by using all the direct neighbouring cells to approximate the fluid distribution in an interface cell. A fifth type of building block was also introduced, namely a corner element. Similar to the original SLIC method, the direction of motion is taken into account and different fluid distributions in a cell are considered for the different sweeps (Figure D.2(b)).

The next refinement of the SLIC method consisted of using oblique lines to approximate the interface in a cell (Piecewise-Linear Interface Calculation) [465, 466]. Further improvement was obtained by constructing the line-segments on the cell faces [467] (Figure D.2(c)).

From the local velocities one can move the reconstructed fluid distributions in each cell in a Lagrangian manner, and then update the volume fraction value in each cell from the new fluid distribution.

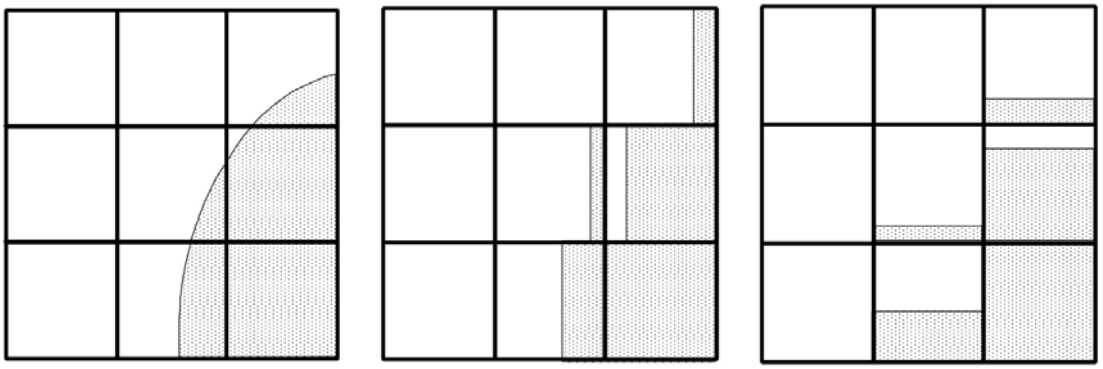

Original fluid distribution | Noh & Woodward (1976) x-sweep | Noh & Woodward (1976): y-sweep

(a)

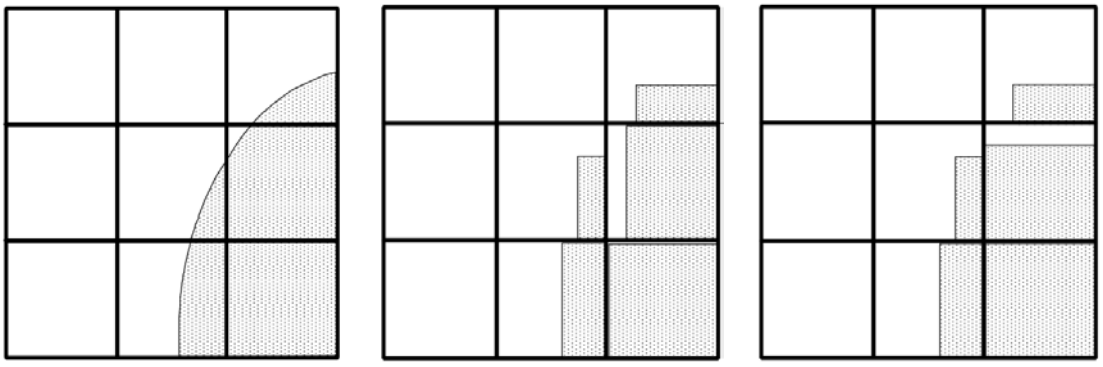

Original fluid distribution | Chorin (1980): x-sweep | Chorin (1980): y-sweep

(b)

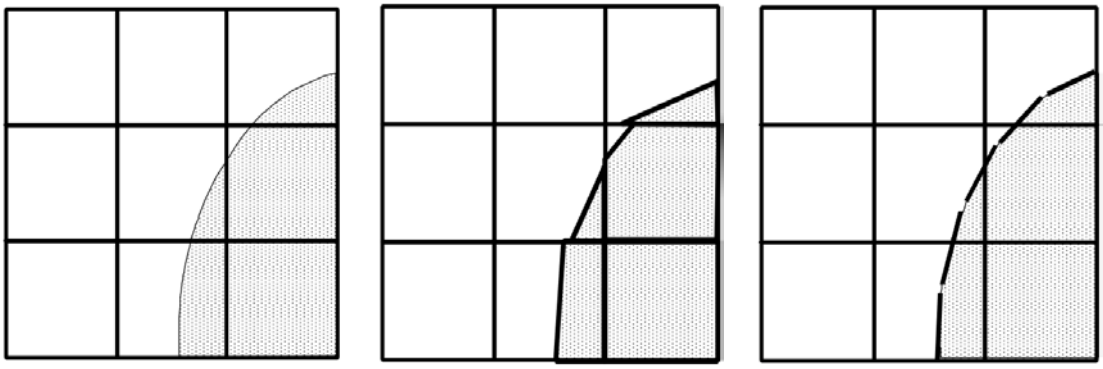

Original fluid distribution | Lötstedt (1982) & Youngs (1982) | Ashgriz & Poo (1990)

(c)

Figure D.2: Comparison of different line techniques for the prediction of the fluid distribution in a cell.

The rectangular shapes of the mesh cells are used (implicitly) by the reconstruction algorithm of the interface (in all the methods presented above). The complexity of the recontruction of the fluid distribution would increase substantially if one used arbitrary shaped cells in three dimensions.

APPENDIX E

Two-phase Poiseuille flow

We consider a two-phase horizontal Poiseuille flow. A volume force $\mathbf{f} = f\sin(\theta)\mathbf{e}_x - f\cos(\theta)\mathbf{e}_y, \theta \in [0, \frac{\pi}{2}]$ is applied to the fluid. The geometry of this flow is presented in Figure E.1.

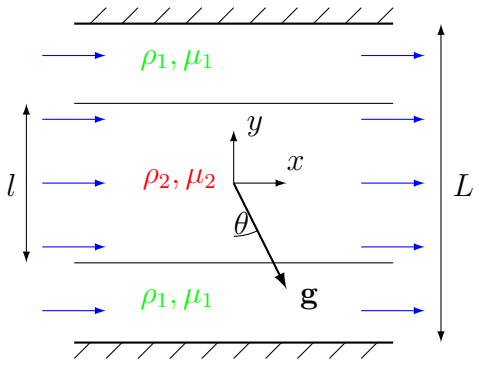

Figure E.1: Two-phase Poiseuille flow in a horizontal geometry.

We suppose that $\mathbf{u} = u(y)\mathbf{e}_x$. The external fluid ($|y| \geqslant l/2$) is referred to as Fluid 1 (ρ_1, μ_1) while the internal one ($|y| \leqslant l/2$) is Fluid 2 (ρ_2, μ_2). In the following, i can be either 1 or 2, depending on the ordinate of the considered point.

According to Navier-Stokes equation (equation (1.13)), the flow is governed by:

- y projection
$$0 = -\frac{\partial p}{\partial y} - \rho_i f \cos\theta, \tag{E.1}$$
- x projection
$$0 = -\frac{\partial p}{\partial x} + \rho_i f \sin\theta + \frac{\partial}{\partial y}\tau_{xy} \tag{E.2}$$
with $\tau_{xy} = 2\mu_i e_{xy} = \mu_i \left(\frac{\partial u}{\partial y} + \frac{\partial v}{\partial x}\right)$.

Thus, one has
$$0 = \frac{1}{\mu_i}\left(-\frac{\partial p}{\partial x} + \rho_i f \sin\theta\right) + \frac{\partial^2 u}{\partial y^2}. \tag{E.3}$$
If we name $A_i = -\frac{\partial p}{\partial x} + \rho_i f \sin\theta$ (A_i is a constant), we can obtain
$$u(y) = -\frac{1}{2}\frac{A_i}{\mu_i}y^2 + b_i y + c_i, (b_i, c_i) \in \mathbb{R}^2. \tag{E.4}$$

Note that (b_1, c_1) can have two different values depending on whether one considers the positive-ordinate domain filled with Fluid 1, or the negative-ordinate domain. These different values will be written as (b_1^+, c_1^+) and (b_1^-, c_1^-) respectively. In the following, we will only consider the half-domain $y \geqslant 0$ (the solution in the other half-domain will be derived by symmetry) and consequently we neglect the $^+$ notation for b_1 and c_1.

The boundary conditions on the free surface are as follows:
$$\mu_1 \left.\frac{\partial u}{\partial y}\right|_1 = \mu_2 \left.\frac{\partial u}{\partial y}\right|_2, \tag{E.5}$$
$$u_1 = u_2. \tag{E.6}$$

The boundary condition on the domain boundary ($y = L/2$) is
$$u = 0 \tag{E.7}$$

From boundary condition (E.5) one obtains
$$b_2\mu_2 - b_1\mu_1 = -(A_1 - A_2)\frac{l}{2}. \tag{E.8}$$

Boundary condition (E.6) gives

$$(b_1 - b_2)\frac{l}{2} + c_1 - c_2 = -\frac{1}{2}\frac{A_2}{\mu_2}\frac{l^2}{4} + \frac{1}{2}\frac{A_1}{\mu_1}\frac{l^2}{4}. \tag{E.9}$$

From boundary condition (E.7) one can derive

$$-\frac{1}{2}\frac{A_1}{\mu_1}\frac{L^2}{4} + b_1\frac{L}{2} + c_1 = 0 \tag{E.10}$$

The symmetry of the domain gives $b_2 = 0$ (but b_1 is not necessarily equal to zero, see above). Thus from equation (E.8)

$$b_1 = -\frac{A_2 - A_1}{\mu_1}\frac{l}{2}. \tag{E.11}$$

Equation (E.10) gives

$$c_1 = \frac{1}{2}\frac{A_1}{\mu_1}\frac{L^2}{4} + \frac{A_2 - A_1}{\mu_1}\frac{lL}{4}. \tag{E.12}$$

Finally, from equation (E.9) it is possible to write

$$c_2 = A_2\left(-\frac{l^2}{4\mu_1} + \frac{lL}{4\mu_1} + \frac{l^2}{8\mu_2}\right) + A_1\left(\frac{l^2}{4\mu_1} + \frac{L^2}{8\mu_1} - \frac{lL}{4\mu_1} - \frac{l^2}{8\mu_1}\right). \tag{E.13}$$

To conclude, in Fluid 1 ($y \geqslant 0$) the velocity is

$$\boxed{u(y) = -\frac{1}{2}\frac{A_1}{\mu_1}y^2 - \frac{A_2 - A_1}{\mu_1}\frac{l}{2}y + \frac{A_1}{\mu_1}\frac{L^2}{4} + \frac{A_2 - A_1}{\mu_1}\frac{lL}{4}.} \tag{E.14}$$

The velocity in Fluid 2 is

$$\boxed{u(y) = -\frac{1}{2}\frac{A_2}{\mu_2}y^2 + \frac{A_2}{\mu_2}\left[\left(-\frac{l^2}{4} + \frac{lL}{4}\right)\frac{\mu_2}{\mu_1} + \frac{1}{2}\frac{l^2}{4}\right] + \frac{A_1}{\mu_1}\left(\frac{1}{2}\frac{l^2}{4} - \frac{lL}{4} + \frac{1}{2}\frac{L^2}{4}\right).} \tag{E.15}$$

When $\theta = 0 \pmod{\pi}$, it is possible to write the velocity as

$$\boxed{\begin{array}{rcl} \forall y \in [-L,-l]\cup[l,L], u(y) & = & \left\{\begin{array}{l} \dfrac{\rho_1 g L^2}{8\mu_1}\left(1 - \left(\dfrac{2y}{L}\right)^2\right) \\ +2\dfrac{(\rho_2-\rho_1)glL}{8\mu_1}\left(1 - \left|\dfrac{2y}{L}\right|\right) \end{array}\right. \\ \\ \forall y \in [-l,l], u(y) & = & \left\{\begin{array}{l} \dfrac{\rho_2 g l^2}{8\mu_2}\left(1 - \left(\dfrac{2y}{l}\right)^2\right) + \\ \dfrac{\rho_1 g L^2}{8\mu_1}\left(1 - \left(\dfrac{l}{L}\right)^2\right) \\ +2\dfrac{(\rho_2-\rho_1)glL}{8\mu_1}\left(1 - \dfrac{l}{L}\right) \end{array}\right. \end{array}} \tag{E.16}$$

with $g = -\frac{dp}{dx}$ (p only depends on x in this case).

If $\mu_1 = \mu_2 = \mu$ and $\rho_1 = \rho_2 = \rho$, one obtains the single-phase Poiseuille-flow velocity

$$u(y) = \frac{\rho g L^2}{8\mu}\left(1 - \left(\frac{2y}{L}\right)^2\right). \tag{E.17}$$

List of Figures

1 Energy Consumption Fuel Shares 17
2 Oil supply profiles 18
3 Associated oil-gas reservoir 19
4 Tar sandstone of southern California 20
5 Naturally burning oil shale 22
6 Costs of production 24
7 Expected sequence of oil recovery methods in a typical oil field 25
8 Steam Assisted Gravity Drainage 26
9 A schematic of the immiscible displacement technique 26
10 Secondary oil recovery by waterflooding 28
11 Water displacing oil from a pore 29
12 Typical waterflood performance 30

1.1 Measured value as a function of resolution 36
1.2 Behaviour of time-independent non-Newtonian fluids 38
1.3 The two classes of time-dependent fluids 39
1.4 Diagram of the forces on molecules of a fluid 41
1.5 Saddle surface with normal planes in directions of principal curvatures . 41

1.6 Idealised examples of contact angle and spreading of a liquid on a flat, smooth solid 44
1.7 Capillary rise in a cylindrical tube of radius r 45
1.8 Anchoring of a drop on a strong edge 46
1.9 Structure of a porous material 47
1.10 Idealised types of dead-end pore volume 50
1.11 Relative permeability hysteresis for a mixed-wet sample from the Kingfish field 52
1.12 Oil/water relative permeabilities for Torpedo sandstone with varying wettability 53
1.13 Two-phase flow in a Hele-Shaw cell 54
1.14 Interface between air and glycerine in a Hele-Shaw cell 55
1.15 Bundle of tubes model 56
1.16 Transient Lattice Boltzmann simulation / Smoothed Particle Hydrodynamics simulation / Level-Set simulation 57
1.17 A network of pores connected by throats 58
1.18 Definition of tortuosity 59
1.19 Tortuosity calculation from an X-ray tomography reconstruction of a porous sandstone 60
1.20 Circulation of the fluids in the system and displacement of the meniscus at pore scale 71
1.21 Circulation of the fluids in the system and displacement of the meniscus at pore scale 73
1.22 Phase diagram in the case of drainage 74
1.23 Fingering pattern realised in a Hele-Shaw cell 77
1.24 Identification of two types of pores 78
1.25 Phase diagrams in the case of imbibition 79
1.26 Description of the patterns obtained by statistical models 80
1.27 The jamming phase diagram proposed by Liu and Nagel 82
1.28 Branching structure of close-packed grains obtained by injecting air in an initially circular granular-fluid system 83

1.29 Layer of compacted grains of width L ahead of the interface 83
1.30 Stick-slip bubbles 85
1.31 Experimental patterns of viscous fingering, capillary fingering and fracturing 86
1.32 Experimental patterns of viscous fingering, capillary fingering and fracturing 86
1.33 Fractal dimension and displacement pattern for rigid medium 88
1.34 Phase diagrams of fluid-fluid displacement patterns in the experiments 89
1.35 Phase diagram of drainage in granular media 90
1.36 Fractal dimension and displacement pattern for rigid medium 90
1.37 Tentative phase diagram of morphologies in the $\varphi^{-1} - q$ plane 92

2.1 Measured value as a function of resolution 96
2.2 Example of quadtree discretisation and corresponding tree representation 102
2.3 Optimised hierarchical adaptation used by Gerris 104
2.4 Interface cut by a mesh and its associated volume fraction field 106
2.5 Geometrical flux estimation 107
2.6 Geometrical flux estimation for quadtree discretisation 107
2.7 Examples of the grids used to calculate the curvature 109
2.8 Only two of the three interface heights are consistent for either the vertical or the horizontal stencils 110
2.9 Example of sixteen square cells (2D) with their attributed number . . . 111
2.10 Additional constraints on the quadtree discretisation due to solid boundaries 112
2.11 Cubic cell of a Face-Centred Cubic lattice 115
2.12 Face-Centred Cubic lattices at different levels 116
2.13 Velocity field after ten timesteps in cases 1 & 2 117
2.14 Weak scalability on cluster *babbage2* 118
2.15 Strong scalability on cluster *babbage2* 119
2.16 Weak scalability on cluster *Rostand* 120

2.17 Strong scalability on cluster *Rostand* 121
2.18 Velocity of the tip of the fingering *vs* Darcy velocity 123
2.19 Length of the longest finger *vs* characteristic lengthscale of the injection surface 124
2.20 Single-phase Poiseuille flow in a horizontal geometry 127
2.21 Convergence of the error norms as functions of the resolution in the case of single-phase horizontal Poiseuille flow 128
2.22 Single-phase Poiseuille flow in a slanted geometry 129
2.23 Convergence of the error norms as functions of the resolution in the case of single-phase slanted Poiseuille flow 130
2.24 Two-phase Poiseuille flow in a horizontal geometry 131
2.25 Convergence of the error norms as functions of the resolution in the case of two-phase horizontal Poiseuille flow 132
2.26 Comparison of Gerris Flow Solver results with analytical curve in horizontal geometry 133
2.27 Error between Gerris Flow Solver results and theoretical value for horizontal geometry 133
2.28 Two-phase Poiseuille flow in a slanted geometry 134
2.29 Convergence of the error norms as functions of the resolution in the case of two-phase slanted Poiseuille flow 135
2.30 Comparison of Gerris Flow Solver results with analytical curve in slanted geometry 136
2.31 Error between Gerris Flow Solver results and theoretical value for slanted geometry (1/2) 137
2.32 Error between Gerris Flow Solver results and theoretical value for slanted geometry (2/2) 137
2.33 Difference between theoretical and computed velocities. 138
2.34 Results from Cancelliere *et al.*, 1990 139
2.35 Examples of randomly generated porous media 140
2.36 Dimensionless permeability k/R^2 as a function of solid fraction 142
2.37 Dimensionless permeability k/R^2 as a function of maximum timestep . 144

2.38 Contact angles in Gerris flow solver . . . 146
2.39 Totally wetting contact angle . . . 147
2.40 A single pore of size $92.16^3\,\mu\text{m}^3$ . . . 148
2.41 Position of the interface during injection in a single pore . . . 149
2.42 The pore space is more filled in the water-wetting case . . . 149
2.43 The shape of the injected finger will be closer to that of the pore in the water-wetting case . . . 150
2.44 Position of the tip of the interface for different viscosity ratios . . . 151
2.45 Comparison of Z/np when using 8 or 64 cores . . . 152
2.46 Z/np for 64 cores . . . 153
2.47 Z/np on *Jade* and *Rostand vs. babbage2* . . . 154
2.48 Cfl study on *babbage2* . . . 155
2.49 Cfl study on *Rostand vs. babbage2* . . . 155
2.50 Cross section of the 400^3 geometry . . . 156
2.51 Time series of invasion of a real rock . . . 157
2.52 Dimensionless abscissa of the tip of the most-advanced finger . . . 157
2.53 Invasion of a real rock at dimensionless time $t = 2.25$ . . . 158

3.1 Time evolution of the fractal growth patterns for viscous fingering . . . 160
3.2 Sketch of the lines of constant values of the scalar field p in front of a local disturbance of a plane front . . . 164
3.3 Definition of the axes for the stability analysis . . . 164
3.4 Saffman-Taylor finger of width $\lambda = 0.5$ . . . 168
3.5 Three finger profiles . . . 169
3.6 The B-dependence of the widths of the discrete set of solutions selected by surface tensions . . . 169
3.7 Fingers in wedge geometry . . . 170
3.8 The B-dependence of the widths of the discrete set of solutions in a wedge of angle $\theta_w = 20°$ . . . 171
3.9 The growth of a parabolic dendritic monocrystal . . . 172
3.10 Anomalous fingers in non-isotropic situations . . . 173

3.11 The B-dependence of the width of the discrete set of solutions in the presence of anisotropy . . . 174
3.12 Unstable fingers in channel situation . . . 176
3.13 Development of Saffman-Taylor fingering for three different viscosity ratios . . . 180
3.14 Detaching droplets in experimental miscible viscous fingering . . . 182
3.15 Detaching droplet in experimental viscous fingering in porous media . . 183
3.16 The dimensionless area A of the growing bubble *vs.* the dimensionless length L of the interface . . . 184
3.17 Time evolution of the fractal growth patterns for viscous fingering . . . 186
3.18 Simulation of the experiment presented in [231] ($r_{\max}/\lambda_\sigma = 25$). . . . 187
3.19 Polar metric for viscous fingering simulation . . . 189
3.20 Polar simulation of central injection . . . 190

4.1 Schematic setup of the slab in the 2-D scanner . . . 193
4.2 Oil recovery and water cut during water injection . . . 194
4.3 2D imaging of waterflood with 2.0 kg.m^{-1}.s^{-1} crude oil . . . 195
4.4 2D imaging of waterflood with 7.0 kg.m^{-1}.s^{-1} crude oil . . . 195
4.5 Oil recovery by water flood and polymer flood . . . 196
4.6 Polymer injection E2000, change in saturation . . . 196
4.7 Polymer injection E7000, change in saturation . . . 197
4.8 Oil recovery profile at different injection rates . . . 197
4.9 Effect of reducing injection rate for two heavy oils . . . 198
4.10 Direction of imbibition after water breakthrough . . . 198
4.11 Waterflooding simulated during 120 hours . . . 200
4.12 Effect of the noise on the initiation of the fingering process . . . 200
4.13 Variation of the dimensionless covering area of the fingering process with respect to the dimensionless time . . . 201
4.14 Variation of the area of the fingering process with respect to the length of its interface . . . 202
4.15 Injection in a domain constituted of four boxes . . . 202

4.16 Waterflood in a rectangular domain 203
4.17 Waterflood in a rectangular domain till breakthrough 204
4.18 Area *vs.* time 205
4.19 Proportion of aqueous phase 206
4.20 Proportion of aqueous phase for two viscosity ratios 207
4.21 Waterflooding simulation 208
4.22 Injection of polymer as a second step 208
4.23 Proportion of aqueous phase for several abscissae at a fixed dimensionless time 209
4.24 Dimensionless area as a function of dimensionless length: (a) case 1 ($\alpha_\infty = 0.64 \pm 0.01$), (b) case 2 ($\alpha_\infty = 0.63 \pm 0.01$) and (c) case 3 ($\alpha_\infty = 0.63 \pm 0.01$). 210

A.1 Experiments of drainage in a 2D network 221

B.1 Diffusion-Limited Aggregation clusters in two dimension 224
B.2 DLA grown in a channel and a wedge 225
B.3 A DLA-like cluster obtained by diffusive growth from a copper sulfate solution in an electrodeposition cell 227
B.4 DBM patterns for 1000 particles on a triangular lattice 228
B.5 The Hastings-Levitov scheme for fractal growth 230
B.6 A DLA cluster made by iterated conformal maps 231
B.7 A DLA cluster made by iterated conformal maps 232

C.1 Mandelbrot set 235
C.2 A partial covering of a pattern with boxes 236
C.3 Examples of Julia sets 238

D.1 Interface approximations for the centre cell with the SLIC method . . . 242
D.2 Comparison of different line techniques for the prediction of the fluid distribution in a cell 243

E.1 Two-phase Poiseuille flow in a horizontal geometry 245

List of Tables

1 Heavy oil classification 21

1.1 Table summarising the different shapes at network scale 81

2.1 CPU time required to compute ten timesteps 120
2.2 CPU time required to compute ten timesteps 122
2.3 CPU time to breakthrough in oil-wetting case 150

3.1 Fractal dimensions of the clusters presented in Figure 3.13 181

4.1 Oil recovery data 194
4.2 Two different refinements 199

Bibliography

[1] Institute for Energy Research. World Energy Intel, 2012. [Online; accessed 14-May-2014].

[2] Energy Information Administration. Annual Energy Outlook 2013, 2012. [Online; accessed 14-May-2014].

[3] Energy Information Administration. Annual Energy Outlook 2013, 2012. [Online; accessed 14-May-2014].

[4] International Energy Agency, 2002.

[5] Mehdi Chraïbi. *Modélisation de l'expansion de gaz dissous dans les huiles lourdes en milieu poreux*. PhD thesis, Paris 6, 2008.

[6] James W. Amyx, Daniel M. Bass, and Robert L. Whiting. *Petroleum reservoir engineering: physical properties*, volume 1. McGraw-Hill College, 1960.

[7] International Energy Agency, 2013. [Online; accessed 15-May-2014].

[8] Wikipedia. Oil sands — Wikipedia, The Free Encyclopedia, 2014. [Online; accessed 15-May-2014].

[9] Emil D. Attanasi and Richard F. Meyer. *Survey of energy resources*, chapter Natural Bitumen and Extra-Heavy Oil, pages 123–140. World Energy Council., 22nd edition, 2010.

[10] Alberta's Oil Sands: Opportunity, Balance. Technical report, Government of Alberta, March 2008.

[11] Bitumen and heavy crudes: the energy security problem solved? *Oil and Energy Trends*, 31(6):3–6, 2006.

[12] An Mai, Jonathan Luke Bryan, N. Goodarzi, and Apostolos Kantzas. Insights Into Non-Thermal Recovery of Heavy Oil. In *World Heavy Oil Conference (WHOC), Calgary, Alberta*, 2006.

[13] MB Dusseault et al. Comparing Venezuelan and Canadian heavy oil and tar sands. In *Canadian International Petroleum Conference, Calgary, Alberta, Canada*, pages 2001–061, 2001.

[14] Survey of Energy Resources 2007: Natural Bitumen - Definitions. Technical report, World Energy Council, 2007.

[15] Mihkel Koel. Estonian oil shale. *Oil Shale Extra*, 1999.

[16] Richard Moody. Oil & Gas Shales, Definitions & Distribution In Time & Space. *The History of On-Shore Hydrocarbon Use in the UK. Geological Society of London*, page 1, 2007.

[17] Wikipedia. Oil shale — Wikipedia, The Free Encyclopedia, 2014. [Online; accessed 16-May-2014].

[18] John S. Huang and Ramesh Varadaraj. Colloid and interface science in the oil industry. *Current Opinion in Colloid & Interface Science*, 1(4):535 – 539, 1996.

[19] E. Tzimas, A Georgakaki., C. Garcia Cortes, and S. D. Peteves. Enhanced oil recovery using carbon dioxide in the european energy system. *Report EUR*, 21895, 2005.

[20] Riley B. Needham and Peter H. Doe. Polymer flooding review. *Journal of Petroleum Technology*, 39(12):1–503, 1987.

[21] Wolfgang Littmann. *Polymer flooding*. Elsevier Science Publishers, 1988.

[22] A. G. Putz, B. Bazin, and B. M. Pedron. Commercial Polymer Injection in the Courtenay Field, 1994 Update. Paper SPE 28601 presented at the SPE Annual Technical Conference and Exhibition, New Orleans, Louisiana, 25–28 September, 1994.

[23] Mun-Hong Hui and Martin J. Blunt. Effects of Wettability on Three-Phase Flow in Porous Media. *The Journal of Physical Chemistry B*, 104(16):3833–3845, 2000.

[24] Huanzhong Dong, Shufen Fang, Dongmei Wang, Jiaying Wang, Zhen Lin Liu, and Weihong Hou. Review of practical experience & management by polymer flooding at Daqing. In *SPE Symposium on Improved Oil Recovery*. Society of Petroleum Engineers, 2008.

[25] S. Thomas. Enhanced Oil Recovery - An Overview. *Oil & Gas Science and Technology-Revue de l'IFP*, 63(1):9–19, 2008.

[26] W. D. Owens and V. E. Suter. Steam Stimulation–Newest Form of Secondary Petroleum Recovery. *Oil and Gas J.*, pages 82–87, 1965.

[27] S. M. Farouq Ali and R. F. Meldau. Current steamflood technology. *J. Petrol. Technol.*, 31:1332–1342, 1979.

[28] D. D. Stokes and T. M. Doscher. Shell makes a success of steam flood at Yorba Linda. *Oil Gas J.*, 72(35), 1974.

[29] R. M. Butler. A new approach to the modelling of steam-assisted gravity drainage. *Journal of Canadian Petroleum Technology*, 24(03), 1985.

[30] V. Shako and D. Rudenko. Temperature Variation Across The Wellbore in SAGD Producer. In *Canadian International Petroleum Conference*. Petroleum Society of Canada, 2007.

[31] Chu Cheih. A Study of Fireflood Field Projects. *Journal of Petroleum Technology*, 29(02):111–120, 1977.

[32] Chu Cheih. State-of-the-Art Review of Fireflood Field Projects. *Journal of Petroleum Technology*, 34(01):19–36, 1982.

[33] L. W. Holm. Carbon dioxide solvent flooding for increased oil recovery. Jan 1959.

[34] J. L. Sánchez, A. Astudillo, F. Rodríguez, J. Morales, and A. Rodríguez. Nitrogen Injection in the Cantarell Complex: Results After Four Years of Operation. In *Proceedings of SPE Latin American and Caribbean Petroleum Engineering Conference, Rio de Janeiro, Brazil*, pages 20–23, 2005.

[35] Sara Thomas and S. M. Farouq Ali. Field Experience with Chemical Oil Recovery Methods. In *Proceedings of the 21st Australian Chemical Engineering Conference (Chemeca 93)*, page 45. Institution of Engineers, Australia, Sept 1993.

[36] Sara Thomas and S. M. Farouq Ali. Status and assessment of chemical oil recovery methods. *Energy sources*, 21(1-2):177–189, 1999.

[37] Harry L. Chang. Polymer Flooding Technology Yesterday Today and Tomorrow. *Journal of Petroleum Technology*, 30(08):1–113, 1978.

[38] Arne Skauge, Per Arne Ormehaug, Tiril Gurholt, Bartek Vik, Igor Bondino, and Gerald Hamon. 2-D Visualisation of Unstable Waterflood and Polymer Flood for Displacement of Heavy Oil. In *SPE Improved Oil Recovery Symposium*. Society of Petroleum Engineers, 2012.

[39] P. Somasundaran and H. S. Hanna. Adsorption of sulfonates on reservoir rocks. *Society of Petroleum Engineers Journal*, 19(04):221–232, 1979.

[40] P. H. Krumrine and J. S. Falcone Jr. Surfactant Polymer and Alkali Interactions in Chemical Flooding Processes. In *SPE Oilfield and Geothermal Chemistry Symposium*. Society of Petroleum Engineers, 1983.

[41] C. E. Johnson Jr. Status of caustic and emulsion methods. *Journal of Petroleum Technology*, 28(01):85–92, 1976.

[42] E. H. Mayer, R. L. Berg, J. D. Carmichael, and R. M. Weinbrandt. Alkaline injection for enhanced oil recovery - A status report. *Journal of Petroleum Technology*, 35(01):209–221, 1983.

[43] W. B. Gogarty and W. C. Tosch. Miscible-type waterflooding: oil recovery with micellar solutions. *Journal of Petroleum Technology*, 20(12):1–407, 1968.

[44] S. M. Farouq Ali and S. Thomas. Tertiary oil recovery of two Alberta oils by micellar flooding. In *Proceedings of the 37th Annual Technical Meeting of the Petroleum Society of CIM*, pages 8–11, 1986.

[45] Gao Shutang, Li Huabin, Yang Zhenyu, MJ Pitts, Harry Surkalo, and Wyatt Kon. Alkaline/Surfactant/Polymer Pilot Performance of the West Central Saertu Daqing Oil Field. *SPE Reservoir Engineering*, 11(03):181–188, 1996.

[46] Wyatt Kon, Malcolm J Pitts, Harry Surkalo, et al. Mature waterfloods renew oil production by alkaline-surfactant-polymer flooding. In *SPE Eastern Regional Meeting*. Society of Petroleum Engineers, 2002.

[47] Norman R. Morrow, Hau T. Lim, and Jill S. Ward. Effect of crude-oil-induced wettability changes on oil recovery. *SPE Formation Evaluation*, 1(01):89–103, 1986.

[48] A. B. Dixit, S. R. McDougall, K. S. Sorbie, and J. S. Buckley. Pore-Scale Modeling of Wettability Effects and Their Influence on Oil Recovery. Technical report, SPE Reservoir Evaluation and Engineering, 1999.

[49] Paul D. Torrey. Modern Practice in Water-flooding of Oil Sands in the Bradford and Allegany Fields. *Transactions of the AIME*, 86(01):259–276, 1930.

[50] T. F. Lawry. Flowing vs. Pumping Operations In Water Flooding. *Drilling and Production Practice*, 1943.

[51] Marc Schneider. *Wettability Patterning in Microfluidic Systems and Applications in the Petroleum Industry*. PhD thesis, Université Pierre et Marie Curie-Paris VI, 2011.

[52] William G. Anderson. Wettability literature survey part 5: the effects of wettability on relative permeability. *Journal of Petroleum Technology*, 39(11):1453–1468, 1987.

[53] S. H. Raza, L. E. Treiber, and D. L. Archer. Wettability of reservoir rocks and its evaluation. *Producers Monthly*, 32(4), 1968.

[54] K. K. Mohanty, H. T. Davis, and L. E. Scriven. Physics of oil entrapment in water-wet rock. *SPE Reservoir Engineering*, 2(01):113–128, 1987.

[55] A. C. Payatakes. Dynamics of oil ganglia during immiscible displacement in water-wet porous media. *Annual Review of Fluid Mechanics*, 14(1):365–393, 1982.

[56] William G. Anderson. Wettability literature survey-part 4: Effects of wettability on capillary pressure. *Journal of Petroleum Technology*, 39(10):1–283, 1987.

[57] William G. Anderson. Wettability literature survey-part 6: the effects of wettability on waterflooding. *Journal of Petroleum Technology*, 39(12):1–605, 1987.

[58] Digante Bhusan Das and S. M. Hassanizadeh. *Upscaling Multiphase Flow in Porous Media: From Pore to Core and Beyond*. Springer, 2005.

[59] Muhammad Sahimi. Flow phenomena in rocks: from continuum models to fractals, percolation, cellular automata, and simulated annealing. *Rev. Mod. Phys.*, 65:1393–1534, Oct 1993.

[60] M. Ferer, Shelley L. Anna, Paul Tortora, J. R. Kadambi, M. Oliver, Grant S. Bromhal, and Duane H. Smith. Two-Phase Flow in Porous Media: Predicting Its Dependence on Capillary Number and Viscosity Ratio. *Transport in Porous Media*, 86(1):243–259, 2011.

[61] Can Ulas Hatiboglu and Tayfun Babadagli. Experimental and visual analysis of co- and counter-current spontaneous imbibition for different viscosity ratios, interfacial tensions, and wettabilities. *Journal of Petroleum Science and Engineering*, 70(3–4):214 – 228, 2010.

[62] A. Bazylak, V. Berejnov, B. Markicevic, D. Sinton, and N. Djilali. Numerical and microfluidic pore networks: Towards designs for directed water transport in GDLs. *Electrochimica Acta*, 53(26):7630 – 7637, 2008.

[63] S. Litster, D. Sinton, and N. Djilali. Ex situ visualization of liquid water transport in PEM fuel cell gas diffusion layers. *Journal of Power Sources*, 154(1):95 – 105, 2006.

[64] Viatcheslav Berejnov, Ned Djilali, and David Sinton. Lab-on-chip methodologies for the study of transport in porous media: energy applications. *Lab on a Chip*, 8(5):689–693, 2008.

[65] M. Reiner. The Deborah Number. *Physics Today*, 17:62, 1964.

[66] $\Pi\lambda\acute{\alpha}\tau\ \omega\nu.\ K\rho\alpha\tau\upsilon\lambda o\sigma.$ 401,d & 402,a.

[67] The Bible, Book of Judges. 5,5.

[68] André Rougé. *Introduction à la physique subatomique*. Éditions École Polytechnique, 2005.

[69] Philip W. Anderson. More is different. *Science*, 177(4047):393–396, 1972.

[70] L. D. Landau and E. M. Lifshitz. *Statistical Physics*. 1958.

[71] Laurent Jacquin. La représentation du fluide. Transparents d'amphi du cours MEC432 à l'École Polytechnique, 2013.

[72] Patrick Huerre. *Mécanique des fluides - Tome 1*. École Polytechnique, 1998. Cours à l'École Polytechnique.

[73] Pijush K. Kundu and Ira M. Cohen. *Fluid Mechanics*. Elsevier Academic Press, Fourth edition, 2008.

[74] Wikipedia. Non-Newtonian fluid — Wikipedia, The Free Encyclopedia, 2014. [Online; accessed 7-February-2014].

[75] Taha Sochi. Non-Newtonian flow in porous media . *Polymer*, 51(22):5007 – 5023, 2010.

[76] Joseph Boussinesq. Sur un mode simple d'écoulement des nappes d'eau d'infiltration à lit horizontal, avec rebord vertical tout autour lorsqu'une partie de ce rebord est enlevée depuis la surface jusqu'au fond. *CR Acad Sci*, 137:5–11, 1903.

[77] E. A. Spiegel and G. Veronis. On the Boussinesq approximation for a compressible fluid. *The Astrophysical Journal*, 131:442, 1960.

[78] Tim T. Schowalter. Mechanics of secondary hydrocarbon migration and entrapment. *AAPG bulletin*, 63(5):723–760, 1979.

[79] Antonin Marchand, Joost H. Weijs, Jacco H. Snoeijer, and Bruno Andreotti. Why is surface tension a force parallel to the interface? *American Journal of Physics*, 79(10):999–1008, 2011.

[80] C. Jho, D. Nealon, S. Shogbola, and A. D. King Jr. Effect of pressure on the surface tension of water: Adsorption of hydrocarbon gases and carbon dioxide on water at temperatures between 0 and 50°C. *Journal of Colloid and Interface Science*, 65(1):141 – 154, 1978.

[81] Wikipedia. Surface tension — Wikipedia, The Free Encyclopedia, 2014. [Online; accessed 10-February-2014].

[82] Wikipedia. Principal curvature — Wikipedia, The Free Encyclopedia, 2013. [Online; accessed 10-February-2014].

[83] Shahriar Afkhami and Yuriko Renardy. A volume-of-fluid formulation for the study of co-flowing fluids governed by the Hele-Shaw equations. *Physics of Fluids (1994-present)*, 25(8):1–19, 2013.

[84] Pierre-Gilles de Gennes. Wetting: statics and dynamics. *Reviews of modern physics*, 57(3):827, 1985.

[85] Daniel Bonn, Jens Eggers, Joseph Indekeu, Jacques Meunier, and Etienne Rolley. Wetting and spreading. *Reviews of modern physics*, 81(2):739, 2009.

[86] Thomas Young. An essay on the cohesion of fluids. *Philosophical Transactions of the Royal Society of London*, 95:65–87, 1805.

[87] Ivan Lunati. Young's law and the effects of interfacial energy on the pressure at the solid-fluid interface. *Physics of Fluids (1994-present)*, 19(11), 2007.

[88] Pierre-Gilles de Gennes, Françoise Brochard-Wyart, David Quéré, Marc Fermigier, and Christophe Clanet. *Gouttes, bulles, perles et ondes*. Belin Paris, 2002.

[89] R. H. Brooks and A. T. Corey. Hydraulic properties of porous media. 1964.

[90] Wikipédia. Mouillage (physique) — Wikipédia, l'encyclopédie libre, 2013. [Online; accessed 24-February-2014].

[91] G. E. P. Elliott and A. C. Riddiford. Dynamic contact angles: I. The effect of impressed motion. *Journal of Colloid and Interface Science*, 23(3):389–398, 1967.

[92] Jacob Bear, Dan Zaslavsky, and Shraga Irmay. Physical principles of water percolation and seepage. 1968.

[93] Jacob Bear. *Dynamics of fluids in porous media*. New York: Dover Publications, 1972.

[94] Wael Abdallah, Jill S Buckley, Andrew Carnegie, John Edwards, Bernd Herold, Edmund Fordham, Arne Graue, Tarek Habashy, Nikita Seleznev, Claude Signer, Hassan Hussain, Bernard Montaron, and Murtaza Ziauddin. Fundamentals of wettability. *Technology*, 38:1125–1144, 1986.

[95] K. H. Coats and B. D. Smith. Dead-end pore volume and dispersion in porous media. *Society of petroleum engineers journal*, 4(01):73–84, 1964.

[96] Alfred Delville. Structure and properties of confined liquids: a molecular model of the clay-water interface. *The Journal of Physical Chemistry*, 97(38):9703–9712, 1993.

[97] Philip F. Low. Physical chemistry of clay-water interaction. *Advances in agronomy*, 13:269–327, 1961.

[98] Henry Darcy. *Les fontaines publiques de la ville de Dijon. Exposition et application des principes à suivre et des formules à employer dans les questions de distribution d'eau : ouvrage terminé par un appendice relatif aux fournitures d'eau de plusieurs villes au filtrage des eaux et à la fabrication des tuyaux de fonte, de plomb, de tole et de bitume*. Victor Dalmont, 1856.

[99] T. J. Marshall. A relation between permeability and size distribution of pores. *Journal of Soil Science*, 9(1):1–8, 1958.

[100] Ignacio Garcia-Bengochea, Adolph G. Altschaeffl, and Charles William Lovell. Pore distribution and permeability of silty clays. *Journal of the Geotechnical Engineering Division*, 105(7):839–856, 1979.

[101] Stephen Whitaker. Advances in theory of fluid motion in porous media. *Industrial & engineering chemistry*, 61(12):14–28, 1969.

[102] Stephen Whitaker. Flow in porous media I: A theoretical derivation of Darcy's law. *Transport in Porous Media*, 1:3–25, 1986.

[103] Jian Liu. *Etude expérimentale de la perméabilité relative des matériaux cimentaires et simulation numérique du transfert d'eau dans le béton*. PhD thesis, Ecole Centrale de Lille, 2011.

[104] E. M. Braun and R. F. Holland. Relative Permeability Hysteresis: Laboratory Measurements and a Conceptual Model. *SPE Reservoir Engineering*, 10(03):222–228, 1995.

[105] Arthur T. Corey. The interrelation between gas and oil relative permeabilities. *Producers monthly*, 19(1):38–41, 1954.

[106] S. E. Buckley and M. C. Leverett. Mechanism of fluid displacement in sands. *Transactions of the AIME*, 146(1):107–116, 1942.

[107] W. W. Owens and D. L. Archer. The effect of rock wettability on oil-water relative permeability relationships. *Journal of Petroleum Technology*, 23(07):873–878, 1971.

[108] Stephen Whitaker. Flow in porous media II: The governing equations for immiscible, two-phase flow. *Transport in Porous Media*, 1:105–125, 1986.

[109] H. S. Hele-Shaw. Flow of water. *Nature*, 58:520, 1898.

[110] C.-W. Park and G. M. Homsy. The instability of long fingers in Hele–Shaw flows. *Physics of Fluids*, 28(6):1583–1585, 1985.

[111] H. H. Rachford Jr. Instability in water flooding oil from water-wet porous media containing connate water. *Society of Petroleum Engineers Journal*, 4(02):133–148, 1964.

[112] T. K. Perkins and O. C. Johnston. A study of immiscible fingering in linear models. *Society of Petroleum Engineers Journal*, 9(01):39–46, 1969.

[113] R. A. Wooding and Hubert J. Morel-Seytoux. Multiphase fluid flow through porous media. *Annual review of fluid mechanics*, 8(1):233–274, 1976.

[114] P. G. Saffman and Geoffrey I. Taylor. The penetration of a fluid into a porous medium or Hele-Shaw cell containing a more viscous fluid. *Proceedings of the Royal Society of London*, 245(1242):312–329, 1958.

[115] Stephen H. Davis, Yves Couder, T. J. Pedley, Patrick. Huerre, Javier Jiménez, P. F. Linden, Henry Keith Moffatt, M. G. Worster, Herbert E. Huppert, Chris Garrett, and Michael E. McIntyre. *Perspectives in fluid dynamics: a collective introduction to current research*. Cambridge University Press, 2000.

[116] Aurélien Duboin. *Écoulements de fluides complexes en présence d'interfaces dans des systèmes microfluidiques*. PhD thesis, Université Pierre et Marie Curie-Paris VI, 2013.

[117] M. R. Todd and W. J. Longstaff. The development, testing, and application of a numerical simulator for predicting miscible flood performance. *Journal of Petroleum Technology*, 24(07):874–882, 1972.

[118] M. Th. Van Genuchten. A closed-form equation for predicting the hydraulic conductivity of unsaturated soils. *Soil science society of America journal*, 44(5):892–898, 1980.

[119] Amir Riaz and Hamdi A. Tchelepi. Linear stability analysis of immiscible two-phase flow in porous media with capillary dispersion and density variation. *Physics of Fluids (1994-present)*, 16(12):4727–4737, 2004.

[120] Amir Riaz and Hamdi A. Tchelepi. Numerical simulation of immiscible two-phase flow in porous media. *Physics of Fluids (1994-present)*, 18(1), 2006.

[121] Amir Riaz and Hamdi Tchelepi. Stability of two-phase vertical flow in homogeneous porous media. *Physics of Fluids (1994-present)*, 19(7), 2007.

[122] S. Assouline, S. W. Tyler, J. S. Selker, I. Lunati, C. W. Higgins, and M. B. Parlange. Evaporation from a shallow water table: Diurnal dynamics of water and heat at the surface of drying sand. *Water Resources Research*, 49(7):4022–4034, 2013.

[123] Francesco Ciocca, Ivan Lunati, and Marc B. Parlange. Effects of the water retention curve on evaporation from arid soils. *Geophysical Research Letters*, 41(9):3110–3116, 2014.

[124] L. J. Klinkenberg. The permeability of porous media to liquids and gases. *Drilling and production practice*, 1941.

[125] William G. Gray and Kevin O'Neill. On the general equations for flow in porous media and their reduction to Darcy's Law. *Water Resources Research*, 12(2):148–154, 1976.

[126] Helge K. Dahle, Michael A. Celia, and S. Majid Hassanizadeh. Bundle-of-tubes model for calculating dynamic effects in the capillary-pressure-saturation relationship. *Transport in Porous media*, 58(1-2):5–22, 2005.

[127] Kunio Watanabe and Markus Flury. Capillary bundle model of hydraulic conductivity for frozen soil. *Water Resources Research*, 44(12):n/a–n/a, 2008.

[128] Markus Hilpert and Cass T. Miller. Pore-morphology-based simulation of drainage in totally wetting porous media. *Advances in Water Resources*, 24(3–4):243 – 255, 2001. Pore Scale Modeling.

[129] I. I. Bogdanov, F. Guerton, J. Kpahou, and A. M. Kamp. Direct pore-scale modeling of two-phase flow through natural media. In *Proceedings of the 2011 COMSOL Conference in Stuttgart; http://www. comsol. com/paper/download/83497/bogdanov_paper. pdf*, 2011.

[130] D. Koroteev, O. Dinariev, N. Evseev, D. Klemin, A. Nadeev, S. Safonov, O. Gurpinar, S. Berg, C. van Kruijsdijk, R. Armstrong, M. T. Myers, L. Hathon, and H. de Jong. Direct Hydrodynamic Simulation of Multiphase Flow in Porous Rock. *SCA2013-014*, 2013.

[131] Daniel H. Rothman and Stéphane Zaleski. *Lattice-Gas Cellular Automata: Simple Models of Complex Hydrodynamics*. Cambridge University Press, 1997.

[132] Tatyana Sergeevnq Torskaya, Guodong Jin, and Carlos Torres-Verdin. Pore-Level Analysis of the Relationship Between Porosity Irreducible Water Saturation and Permeability of Clastic Rocks. In *SPE Annual Technical Conference and Exhibition*. Society of Petroleum Engineers, 2007.

[133] Thomas Ramstad, Pål-Eric Øren, and Stig Bakke. Simulation of two-phase flow in reservoir rocks using a lattice Boltzmann method. *SPE Journal*, 2010.

[134] B. Ahrenholz, J. Niessner, R. Helmig, and M. Krafczyk. Pore-scale determination of parameters for macroscale modeling of evaporation processes in porous media. *Water Resources Research*, 47(7), 2011.

[135] Uditha C. Bandara, Alexandre M. Tartakovsky, and Bruce J. Palmer. Pore-scale study of capillary trapping mechanism during CO_2 injection in geological formations. *International Journal of Greenhouse Gas Control*, 5(6):1566 – 1577, 2011.

[136] Saeed Ovaysi and Mohammad Piri. Direct pore-level modeling of incompressible fluid flow in porous media. *Journal of Computational Physics*, 229(19):7456 – 7476, 2010.

[137] Saeed Ovaysi and Mohammad Piri. Multi-GPU acceleration of direct pore-scale modeling of fluid flow in natural porous media. *Computer Physics Communications*, 183(9):1890 – 1898, 2012.

[138] Saeed Ovaysi and Mohammad Piri. Pore-space alteration induced by brine acidification in subsurface geologic formations. *Water Resources Research*, 50(1):440–452, 2014.

[139] Maša Prodanović and Steven L. Bryant. A level set method for determining critical curvatures for drainage and imbibition. *Journal of Colloid and Interface Science*, 304(2):442 – 458, 2006.

[140] H. N. Man and X. D. Jing. Pore Network Modelling of Electrical Resistivity and Capillary Pressure Characteristics. *Transport in Porous Media*, 41(3):263–285, 2000.

[141] Martin J. Blunt. Flow in porous media — pore-network models and multiphase flow. *Current Opinion in Colloid & Interface Science*, 6(3):197 – 207, 2001.

[142] H. N. Man and X. D. Jing. Network modelling of strong and intermediate wettability on electrical resistivity and capillary pressure. *Advances in Water Resources*, 24(3–4):345 – 363, 2001. Pore Scale Modeling.

[143] Marc Prat. Recent advances in pore-scale models for drying of porous media. *Chemical Engineering Journal*, 86(1–2):153 – 164, 2002.

[144] H. F. Nordhaug, M. Celia, and H. K. Dahle. A pore network model for calculation of interfacial velocities. *Advances in Water Resources*, 26(10):1061 – 1074, 2003.

[145] S. Bekri, C. Laroche, and O. Vizika. Pore network models to calculate transport and electrical properties of single or dual-porosity rocks. In *International symposium of the society of core analysts, Toronto*, 2005.

[146] Per H. Valvatne, Mohammad Piri, Xavier Lopez, and Martin J. Blunt. Predictive pore-scale modeling of single and multiphase flow. In D.B. Das and S.M. Hassanizadeh, editors, *Upscaling Multiphase Flow in Porous Media*, pages 23–41. Springer Netherlands, 2005.

[147] Marc. Prat. On the influence of pore shape, contact angle and film flows on drying of capillary porous media. *International Journal of Heat and Mass Transfer*, 50(7–8):1455 – 1468, 2007.

[148] Taha Sochi and Martin J. Blunt. Pore-scale network modeling of Ellis and Herschel–Bulkley fluids. *Journal of Petroleum Science and Engineering*, 60(2):105 – 124, 2008.

[149] S. Veran-Tissoires, M. Marcoux, and Marc Prat. Discrete Salt Crystallization at the Surface of a Porous Medium. *Phys. Rev. Lett.*, 108:054502, Feb 2012.

[150] Pål-Eric Øren, Stig Bakke, and Ole Jakob Arntzen. Extending predictive capabilities to network models. *SPE Journal-Richardson-*, 3:324–336, 1998.

[151] Pål-Eric Øren and Stig Bakke. Process based reconstruction of sandstones and prediction of transport properties. *Transport in Porous Media*, 46(2-3):311–343, 2002.

[152] Mohammad Piri and Martin J. Blunt. Three-dimensional mixed-wet random pore-scale network modeling of two- and three-phase flow in porous media. i. model description. *Phys. Rev. E*, 71:026301, Feb 2005.

[153] Martin J. Blunt, Matthew D. Jackson, Mohammad Piri, and Per H. Valvatne. Detailed physics, predictive capabilities and macroscopic consequences for pore-network models of multiphase flow. *Advances in Water Resources*, 25(8–12):1069 – 1089, 2002.

[154] Xavier Lopez, Per H. Valvatne, and Martin J. Blunt. Predictive network modeling of single-phase non-Newtonian flow in porous media . *Journal of Colloid and Interface Science*, 264(1):256 – 265, 2003.

[155] Christian L. Perrin, Philippe M. J. Tardy, Ken S. Sorbie, and John C. Crawshaw. Experimental and modeling study of Newtonian and non-Newtonian fluid flow in pore network micromodels . *Journal of Colloid and Interface Science*, 295(2):542 – 550, 2006.

[156] Pierre M. Adler. *Porous media: geometry and transports*. Butterworth-Heinemann, 1992.

[157] M. Ben Clennell. Tortuosity: a guide through the maze. *Geological Society, London, Special Publications*, 122(1):299–344, 1997.

[158] Charles N. Satterfield. *Mass Transfer in Heterogeneous Catalysis*. Cambridge: MIT Press, 1970.

[159] Cedric J. Gommes, Anton-Jan Bons, Silvia Blacher, John H. Dunsmuir, and Andy H. Tsou. Practical methods for measuring the tortuosity of porous materials from binary or gray-tone tomographic reconstructions. *AIChE Journal*, 55(8):2000–2012, 2009.

[160] Y. L. Golin, V. E. Karyarin, B. S. Pospelov, and V. I. Sevedkin. Pore tortuosity estimates in porous media. *Soviet Electrochemistry*, 28:87–91, 1992.

[161] Pil H. Lee and John J. Kozak. Calculation of the tortuosity factor in single-phase transport through a structured medium. *The Journal of Chemical Physics*, 86(8):4617–4627, 1987.

[162] Josef Kozeny. Ueber kapillare leitung des wassers im boden. *Sitzungsber. Akad. Wiss. Wien*, 136:271–301, 1927.

[163] J. van Brakel. Pore space models for transport phenomena in porous media review and evaluation with special emphasis on capillary liquid transport. *Powder Technology*, 11(3):205 – 236, 1975.

[164] John Happel and Howard Brenner. *Low Reynolds number hydrodynamics: with special applications to particulate media*. Prentice-Hall, NY, 1973.

[165] Owen M. Phillips. *Flow and reactions in permeable rocks*. Cambridge University Press, 1991.

[166] P. C. Carman. Flow of gases through porous media. *Buttherworths, London*, 1956.

[167] P. C. Carman. Fluid flow through granular beds. *Transactions-Institution of Chemical Engineeres*, 15:150–166, 1937.

[168] Norman Epstein. On tortuosity and the tortuosity factor in flow and diffusion through porous media. *Chemical Engineering Science*, 44(3):777–779, 1989.

[169] Francis A. L. Dullien. *Porous media: fluid transport and pore structure*. Academic press, San Diego, 1992.

[170] Antonio Cancelliere, Celeste Chang, Enrico Foti, Daniel H. Rothman, and Sauro Succi. The permeability of a random medium: Comparison of simulation with theory. *Physics of Fluids A: Fluid Dynamics (1989-1993)*, 2(12):2085–2088, 1990.

[171] K. Witt and J. Brauns. Permeability-Anisotropy Due to Particle Shape. *Journal of Geotechnical Engineering*, 109(9):1181–1187, 1983.

[172] Olivier Coussy. Mechanics of porous continua. *John Wiley*, 1995.

[173] Jon Arch and Alex Maltman. Anisotropic permeability and tortuosity in deformed wet sediments. *Journal of Geophysical Research: Solid Earth*, 95(B6):9035–9045, 1990.

[174] J. Scott Shepard. Using a fractal model to compute the hydraulic conductivity function. *Soil Science Society of America Journal*, 57(2):300–306, 1993.

[175] C.-W. Park and G. M. Homsy. Two-phase displacement in Hele Shaw cells: theory. *Journal of Fluid Mechanics*, 139:291–308, 1 1984.

[176] R. L. Chuoke, P. van Meurs, and C. van der Poel. The instability of slow, immiscible, viscous liquid-liquid displacements in permeable media. *Trans. AIME*, 216:188, 1959.

[177] J. W. McLean and P. G. Saffman. The effect of surface tension on the shape of fingers in a Hele Shaw cell. *Journal of Fluid Mechanics*, 102:455–469, 1981.

[178] P. G. Saffman. Fingering in porous media. *Macroscopic Properties of Disordered Media*, pages 208–215, 1982.

[179] J. U. Brackbill, D. B. Kothe, and C. Zemach. A continuum method for modeling surface tension. *Journal of Computational Physics*, 100(2):335 – 354, 1992.

[180] Jean-Léonard-Marie Poiseuille. *Recherches expérimentales sur le mouvement des liquides dans les tubes de très-petits diamètres.* Imprimerie Royale, 1844.

[181] Roland Lenormand. Liquids in porous media. *Journal of Physics: Condensed Matter*, 2(S):SA79, 1990.

[182] Roland Lenormand, Cesar Zarcone, and A. Sarr. Mechanisms of the displacement of one fluid by another in a network of capillary ducts. *Journal of Fluid Mechanics*, 135:337–353, 1983.

[183] Roland Lenormand, Eric Touboul, and Cesar Zarcone. Numerical models and experiments on immiscible displacements in porous media. *Journal of Fluid Mechanics*, 189:165–187, 1988.

[184] Roland Lenormand and Cesar Zarcone. Role of roughness and edges during imbibition in square capillaries. *SPE J*, 13264, 1984.

[185] Li Yu (Y. Li) and Norman Claude Wardlaw. The influence of wettability and critical pore-throat size ratio on snap—off. *Journal of Colloid and Interface Science*, 109(2):461 – 472, 1986.

[186] Ekwere J. Peters and Donald L. Flock. The onset of instability during two-phase immiscible displacement in porous media. *Society of Petroleum Engineers Journal*, 21(02):249–258, 1981.

[187] S. Hill. Channeling in packed columns. *Chemical Engineering Science*, 1(6):247 – 253, 1952.

[188] D. N. Dietz. A Theoretical Approach to the Problem of Encroaching and By-Passing Edge Water. In *Proc. Akad. van Wetenschappen*, volume 56-B, pages 83–92, 1953.

[189] C. Van der Poel and J. W. Killian. Attic Oil. In *Fall Meeting of the Society of Petroleum Engineers of AIME*. Society of Petroleum Engineers, 1957.

[190] W. F. Engelberts and L. J. Klinkenberg. Laboratory Experiments on the Displacement of Oil by Water from Packs of Granular Material. In *3rd World Petroleum Congress*. World Petroleum Congress, 1951.

[191] Roland Lenormand. Pattern growth and fluid displacements through porous media. *Physica A: Statistical Mechanics and its Applications*, 140(1):114–123, 1986.

[192] David Wilkinson and Jorge F. Willemsen. Invasion percolation: a new form of percolation theory. *Journal of Physics A: Mathematical and General*, 16(14):3365, 1983.

[193] Roland Lenormand and Cesar Zarcone. Invasion percolation in an etched network: Measurement of a fractal dimension. *Physical review letters*, 54:2226–2229, 1985.

[194] Thomas A. Witten and Leonard M. Sander. Diffusion-limited aggregation. *Phys. Rev. B*, 27:5686–5697, May 1983.

[195] Knut Jørgen Måløy, Jens Feder, and Torstein Jøssang. Viscous Fingering Fractals in Porous Media. *Phys. Rev. Lett.*, 55:2688–2691, Dec 1985.

[196] Lincoln Paterson. Diffusion-Limited Aggregation and Two-Fluid Displacements in Porous Media. *Phys. Rev. Lett.*, 52:1621–1624, Apr 1984.

[197] Paul Meakin and J. M. Deutch. The formation of surfaces by diffusion limited annihilation. *The Journal of Chemical Physics*, 85(4):2320–2325, 1986.

[198] Eran Sharon, Mitchell G. Moore, William D. McCormick, and Harry L. Swinney. Coarsening of Fractal Viscous Fingering Patterns. *Phys. Rev. Lett.*, 91:205504, Nov 2003.

[199] L. M. Sander, P. Ramanlal, and E. Ben-Jacob. Diffusion-limited aggregation as a deterministic growth process. *Phys. Rev. A*, 32:3160–3163, Nov 1985.

[200] Leonard M. Sander. Fractal growth processes. *Nature*, 322:789–793, 1986.

[201] Felipe Barra, Benny Davidovitch, Anders Levermann, and Itamar Procaccia. Laplacian Growth and Diffusion Limited Aggregation: Different Universality Classes. *Phys. Rev. Lett.*, 87:134501, Sep 2001.

[202] R. C. Ball and E. Somfai. Theory of Diffusion Controlled Growth. *Phys. Rev. Lett.*, 89:135503, Sep 2002.

[203] J. Mathiesen, I. Procaccia, H. L. Swinney, and M. Thrasher. The universality class of diffusion-limited aggregation and viscous fingering. *EPL (Europhysics Letters)*, 76(2):257, 2006.

[204] Norman C. Wardlaw and Li Yu. Fluid topology, pore size and aspect ratio during imbibition. *Transport in Porous Media*, 3(1):17–34, 1988.

[205] Andrea J. Liu and Sidney R. Nagel. Nonlinear dynamics: Jamming is not just cool any more. *Nature*, 396(6706):21–22, 1998.

[206] V. Trappe, V. Prasad, Luca Cipelletti, P. N. Segre, and D. A. Weitz. Jamming phase diagram for attractive particles. *Nature*, 411(6839):772–775, 2001.

[207] M. van Hecke. Jamming of soft particles: geometry, mechanics, scaling and isostaticity. *Journal of Physics: Condensed Matter*, 22(3):033101, 2010.

[208] C. H. Liu, Sydney R. Nagel, D. A. Schecter, S. N. Coppersmith, Satya Majumdar, Onuttom Narayan, and T. A. Witten. Force fluctuations in bead packs. *Science*, 269:513–515, 1995.

[209] Trushant S. Majmudar and Robert P. Behringer. Contact force measurements and stress-induced anisotropy in granular materials. *Nature*, 435(7045):1079–1082, 2005.

[210] A. Tordesillas. Force chain buckling, unjamming transitions and shear banding in dense granular assemblies. *Philosophical Magazine*, 87(32):4987–5016, 2007.

[211] Paul Meakin. Models for Material Failure and Deformation. *Science*, 252(5003):226–234, 1991.

[212] Xiang Cheng, Lei Xu, Aaron Patterson, Heinrich M. Jaeger, and Sidney R. Nagel. Towards the zero-surface-tension limit in granular fingering instability. *Nature Physics*, 4(3):234–237, 2008.

[213] B. Sandnes, H. A. Knudsen, K. J. Måløy, and E. G. Flekkøy. Labyrinth patterns in confined granular-fluid systems. *Phys. Rev. Lett.*, 99:038001, Jul 2007.

[214] B. Sandnes, E. G. Flekkøy, H. A. Knudsen, K. J. Måløy, and H. See. Patterns and flow in frictional fluid dynamics. *Nature communications*, 2:288, 2011.

[215] Xiang-Zhao Kong, Wolfgang Kinzelbach, and Fritz Stauffer. Morphodynamics during air injection into water-saturated movable spherical granulates. *Chemical Engineering Science*, 65(16):4652 – 4660, 2010.

[216] Germán Varas, Valérie Vidal, and Jean-Christophe Géminard. Morphology of air invasion in an immersed granular layer. *Phys. Rev. E*, 83:061302, Jun 2011.

[217] C. Chevalier, A. Lindner, M. Leroux, and E. Clément. Morphodynamics during air injection into a confined granular suspension. *Journal of Non-Newtonian Fluid Mechanics*, 158(1–3):63 – 72, 2009. Visco-plastic fluids: From theory to application.

[218] Bernard P. Boudreau, Chris Algar, Bruce D. Johnson, Ian Croudace, Allen Reed, Yoko Furukawa, Kelley M. Dorgan, Peter A. Jumars, Abraham S. Grader, and Bruce S. Gardiner. Bubble growth and rise in soft sediments. *Geology*, 33(6):517–520, 2005.

[219] Lei Xu, Simon Davies, Andrew B. Schofield, and David A. Weitz. Dynamics of Drying in 3D Porous Media. *Phys. Rev. Lett.*, 101:094502, Aug 2008.

[220] Hosung Shin and J. Carlos Santamarina. Fluid-driven fractures in uncemented sediments: Underlying particle-level processes. *Earth and Planetary Science Letters*, 299(1–2):180 – 189, 2010.

[221] Jeong-Hoon Choi, Yongkoo Seol, Ray Boswell, and Ruben Juanes. X-ray computed-tomography imaging of gas migration in water-saturated sediments: From capillary invasion to conduit opening. *Geophysical Research Letters*, 38(17), 2011.

[222] Yoshihiro Yamazaki and Tsuyoshi Mizuguchi. Front Aggregation and Labyrinthine Pattern in the Drying Process of Two-Dimensional Wet Granular Systems. *Journal of the Physical Society of Japan*, 69(8):2387–2390, 2000.

[223] Yoshihiro Yamazaki, Shin-ya Komura, and Ken Suganuma. Percolation in Aggregation of Granular Particles Formed by Sweeping Front Dynamics. *Journal of the Physical Society of Japan*, 75(4):043001, 2006.

[224] Ran Holtzman and Ruben Juanes. Crossover from fingering to fracturing in deformable disordered media. *Phys. Rev. E*, 82:046305, Oct 2010.

[225] Ran Holtzman, Michael L. Szulczewski, and Ruben Juanes. Capillary Fracturing in Granular Media. *Phys. Rev. Lett.*, 108:264504, Jun 2012.

[226] Jing-Den Chen and David Wilkinson. Pore-Scale Viscous Fingering in Porous Media. *Phys. Rev. Lett.*, 55:1892–1895, Oct 1985.

[227] Vidar Frette, Jens Feder, Torstein Jøssang, Paul Meakin, and Knut Jørgen Måløy. Fast, immiscible fluid-fluid displacement in three-dimensional porous media at finite viscosity contrast. *Phys. Rev. E*, 50:2881–2890, Oct 1994.

[228] L. Niemeyer, L. Pietronero, and H. J. Wiesmann. Fractal dimension of dielectric breakdown. *Physical Review Letters*, 52(12):1033–1036, 1984.

[229] Martin Blunt and Peter King. Macroscopic parameters from simulations of pore scale flow. *Phys. Rev. A*, 42:4780–4787, Oct 1990.

[230] Grunde Løvoll, Yves Méheust, Renaud Toussaint, Jean Schmittbuhl, and Knut Jørgen Måløy. Growth activity during fingering in a porous hele-shaw cell. *Phys. Rev. E*, 70:026301, Aug 2004.

[231] Olivier Praud and Harry L. Swinney. Fractal dimension and unscreened angles measured for radial viscous fingering. *Phys. Rev. E*, 72:011406, Jul 2005.

[232] Julio F. Fernández, Rafael Rangel, and Juan Rivero. Crossover length from invasion percolation to diffusion-limited aggregation in porous media. *Phys. Rev. Lett.*, 67:2958–2961, Nov 1991.

[233] M. Ferer, Chuang Ji, Grant S. Bromhal, Joshua Cook, Goodarz Ahmadi, and Duane H. Smith. Crossover from capillary fingering to viscous fingering for immiscible unstable flow:Experiment and modeling. *Phys. Rev. E*, 70:016303, Jul 2004.

[234] Yves Méheust, Grunde Løvoll, Knut Jørgen Måløy, and Jean Schmittbuhl. Interface scaling in a two-dimensional porous medium under combined viscous, gravity, and capillary effects. *Phys. Rev. E*, 66:051603, Nov 2002.

[235] Grétar Tryggvason, Ruben Scardovelli, and Stéphane Zaleski. *Direct numerical simulations of gas-liquid multiphase flows*. Cambridge University Press, 2011.

[236] Bart J. Daly. A technique for including surface tension effects in hydrodynamic calculations. *Journal of Computational Physics*, 4(1):97 – 117, 1969.

[237] Hideaki Miyata. Finite-difference simulation of breaking waves. *Journal of Computational Physics*, 65(1):179 – 214, 1986.

[238] W. Shyy, H. S. Udaykumar, M. M. Rao, and R. W. Smith. Computational fluid dynamics with moving boundaries. *Taylor & Francis, London*, 1996.

[239] J. Glimm, M. J. Graham, J. Grove, X. L. Li, T. M. Smith, D. Tan, F. Tangerman, and Q. Zhang. Front tracking in two and three dimensions. *Computers & Mathematics with Applications*, 35(7):1 – 11, 1998. Advanced Computing on Intel Architectures.

[240] Stanley Osher and James A. Sethian. Fronts propagating with curvature-dependent speed: Algorithms based on Hamilton-Jacobi formulations. *Journal of Computational Physics*, 79(1):12 – 49, 1988.

[241] Stanley Osher and Ronald P. Fedkiw. Level Set Methods: An Overview and Some Recent Results. *Journal of Computational Physics*, 169(2):463 – 502, 2001.

[242] J. A. Sethian and Peter Smereka. Level set methods for fluid interfaces. *Annual Review of Fluid Mechanics*, 35(1):341–372, 2003.

[243] Benoit Granier, Alain Lerat, and Zi-Niu Wu. An implicit centered scheme for steady and unsteady incompressible one and two-phase flows. *Computers & Fluids*, 26(4):373 – 393, 1997.

[244] Constantine Pozrikidis. *Boundary integral and singularity methods for linearized viscous flow*. Cambridge University Press, 1992.

[245] Constantine Pozrikidis. Interfacial Dynamics for Stokes Flow. *Journal of Computational Physics*, 169(2):250 – 301, 2001.

[246] Thomas Y. Hou, John S. Lowengrub, and Michael J. Shelley. Boundary Integral Methods for Multicomponent Fluids and Multiphase Materials. *Journal of Computational Physics*, 169(2):302 – 362, 2001.

[247] Ali Q. Raeini, Martin J. Blunt, and Branko Bijeljic. Modelling two-phase flow in porous media at the pore scale using the volume-of-fluid method. *Journal of Computational Physics*, 231(17):5653 – 5668, 2012.

[248] Ali Qaseminejad Raeini. *Modelling multiphase flow through micro-CT images of the pore space*. PhD thesis, Imperial College London, 2013.

[249] Torsten Clemens, Kostas Tsikouris, Markus Buchgraber, Louis M. Castanier, and Anthony Kovscek. Pore-Scale Evaluation of Polymers Displacing Viscous Oil–Computational-Fluid-Dynamics Simulation of Micromodel Experiments. *SPE Reservoir Evaluation & Engineering*, 16(02):144–154, 2013.

[250] P. Rauschenberger, A. Criscione, K. Eisenschmidt, D. Kintea, S. Jakirlić, Ž. Tuković, I.V. Roisman, B. Weigand, and C. Tropea. Comparative assessment of Volume-of-Fluid and Level-Set methods by relevance to dendritic ice growth in supercooled water. *Computers & Fluids*, 79(0):44 – 52, 2013.

[251] Pavel Tomin and Ivan Lunati. Hybrid Multiscale Finite Volume method for two-phase flow in porous media. *Journal of Computational Physics*, 250(0):293 – 307, 2013.

[252] Ali Q. Raeini, Branko Bijeljic, and Martin J. Blunt. Numerical Modelling of Sub-pore Scale Events in Two-Phase Flow Through Porous Media. *Transport in Porous Media*, 101(2):191–213, 2014.

[253] Stéphane Popinet. Gerris: a tree-based adaptive solver for the incompressible Euler equations in complex geometries. *Journal of Computational Physics*, 190(2):572 – 600, 2003.

[254] Stéphane Popinet. An accurate adaptive solver for surface-tension-driven interfacial flows. *Journal of Computational Physics*, 228(16):5838 – 5866, 2009.

[255] Hermann von Helmholtz. Über Integrale der hydrodynamischen Gleichungen, welcher der Wirbelbewegungen entsprechen (On integrals of the hydrodynamic equations which correspond to vortex motions). *Journal für die reine und angewandte Mathematik*, 55:25–55, 1858.

[256] Alexandre Joel Chorin. Numerical solution of the Navier-Stokes equations. *Mathematics of computation*, 22(104):745–762, 1968.

[257] Pierre-Yves Lagrée, Lydie Staron, and Stéphane Popinet. The granular column collapse as a continuum: validity of a two-dimensional Navier–Stokes model with a μ (I)-rheology. *Journal of Fluid Mechanics*, 686:378–408, 2011.

[258] John B. Bell, Phillip Colella, and Harland M. Glaz. A second-order projection method for the incompressible navier-stokes equations. *Journal of Computational Physics*, 85(2):257 – 283, 1989.

[259] R. Courant, K. Friedrichs, and H. Lewy. Über die partiellen differenzengleichungen der mathematischen physik. *Mathematische Annalen*, 100(1):32–74, 1928.

[260] J. Crank and P. Nicolson. A practical method for numerical evaluation of solutions of partial differential equations of the heat-conduction type. *Mathematical Proceedings of the Cambridge Philosophical Society*, 43:50–67, 1 1947.

[261] Daniel Fuster, Anne Bagué, Thomas Boeck, Luis Le Moyne, Anthony Leboissetier, Stéphane Popinet, Pascal Ray, Ruben Scardovelli, and Stéphane Zaleski. Simulation of primary atomization with an octree adaptive mesh refinement and {VOF} method. *International Journal of Multiphase Flow*, 35(6):550 – 565, 2009.

[262] Anne Bagué, Daniel Fuster, Stéphane Popinet, Ruben Scardovelli, and Stéphane Zaleski. Instability growth rate of two-phase mixing layers from a linear eigenvalue problem and an initial-value problem. *Physics of Fluids (1994-present)*, 22(9):–, 2010.

[263] Stéphane Popinet. Creeping Couette flow of Generalised Newtonian fluids, 2005.

[264] Christophe Josserand, Pierre-Yves Lagrée, Daniel Lhuillier, Stéphane Popinet, Pascal Ray, and Lydie Staron. The spreading of a granular column from a Bingham point of view. *Powders and Grains*, pages 631–634, 2009.

[265] Hanan Samet. Applications of Spatial Data Structures. 1989.

[266] A. Almgren, J. Bell, and W. Szymczak. A Numerical Method for the Incompressible Navier-Stokes Equations Based on an Approximate Projection. *SIAM Journal on Scientific Computing*, 17(2):358–369, 1996.

[267] A. Almgren, J. Bell, P. Colella, and T. Marthaler. A Cartesian Grid Projection Method for the Incompressible Euler Equations in Complex Geometries. *SIAM Journal on Scientific Computing*, 18(5):1289–1309, 1997.

[268] Ann S. Almgren, John B. Bell, Phillip Colella, Louis H. Howell, and Michael L. Welcome. A Conservative Adaptive Projection Method for the Variable Density Incompressible Navier–Stokes Equations. *Journal of Computational Physics*, 142(1):1 – 46, 1998.

[269] A. Almgren, J. Bell, and W. Crutchfield. Approximate Projection Methods: Part I. Inviscid Analysis. *SIAM Journal on Scientific Computing*, 22(4):1139–1159, 2000.

[270] Elbridge Gerry Puckett, Ann S. Almgren, John B. Bell, Daniel L. Marcus, and William J. Rider. A High-Order Projection Method for Tracking Fluid Interfaces in Variable Density Incompressible Flows. *Journal of Computational Physics*, 130(2):269 – 282, 1997.

[271] Jie Li. Calcul d'interface affine par morceaux. *Comptes rendus de l'Académie des sciences. Série II, Mécanique, physique, chimie, astronomie*, 320(8):391–396, 1995.

[272] Ruben Scardovelli and Stéphane Zaleski. Direct numerical simulation of free-surface and interfacial flow. *Annual Review of Fluid Mechanics*, 31(1):567–603, 1999.

[273] Hai Huang, Paul Meakin, and Moubin Liu. Computer simulation of two-phase immiscible fluid motion in unsaturated complex fractures using a volume of fluid method. *Water Resources Research*, 41(12), 2005.

[274] Gbémého Gilou Agbaglah. *Dynamique et instabilité des nappes liquides*. PhD thesis, Paris 6, 2011.

[275] Denis Gueyffier, Jie Li, Ali Nadim, Ruben Scardovelli, and Stéphane Zaleski. Volume-of-fluid interface tracking with smoothed surface stress methods for three-dimensional flows. *Journal of Computational Physics*, 152(2):423 – 456, 1999.

[276] Ruben Scardovelli and Stéphane Zaleski. Analytical Relations Connecting Linear Interfaces and Volume Fractions in Rectangular Grids. *Journal of Computational Physics*, 164(1):228 – 237, 2000.

[277] E. Aulisa, S. Manservisi, R. Scardovelli, and S. Zaleski. Interface reconstruction with least-squares fit and split advection in three-dimensional Cartesian geometry. *Journal of Computational Physics*, 225(2):2301 – 2319, 2007.

[278] R. DeBar. Fundamentals of the KRAKEN code. *Tech. rep., UCID-17366, California Univ., Livermore (USA), Lawrence Livermore Lab.*, 1974.

[279] William F. Noh and Paul Woodward. SLIC (simple line interface calculation). In *Proceedings of the Fifth International Conference on Numerical Methods in Fluid Dynamics June 28–July 2, 1976 Twente University, Enschede*, pages 330–340. Springer, 1976.

[280] Ruben Scardovelli and Stéphane Zaleski. Interface reconstruction with least-square fit and split Eulerian–Lagrangian advection. *International Journal for Numerical Methods in Fluids*, 41(3):251–274, 2003.

[281] William J. Rider and Douglas B. Kothe. Reconstructing Volume Tracking. *Journal of Computational Physics*, 141(2):112 – 152, 1998.

[282] Bruno Lafaurie, Carlo Nardone, Ruben Scardovelli, Stéphane Zaleski, and Gianluigi Zanetti. Modelling merging and fragmentation in multiphase flows with {SURFER}. *Journal of Computational Physics*, 113(1):134 – 147, 1994.

[283] Stéphane Popinet and Stéphane Zaleski. A front-tracking algorithm for accurate representation of surface tension. *International Journal for Numerical Methods in Fluids*, 30(6):775–793, 1999.

[284] D. J. E. Harvie, M. R. Davidson, and M. Rudman. An analysis of parasitic current generation in Volume of Fluid simulations. *Applied Mathematical Modelling*, 30(10):1056 – 1066, 2006. Special issue of the 12th Biennial Computational Techniques and Applications Conference and Workshops (CTAC-2004) held at The University of Melbourne, Australia, from 27th September to 1st October 2004.

[285] Yuriko Renardy and Michael Renardy. PROST: A Parabolic Reconstruction of Surface Tension for the Volume-of-Fluid Method. *Journal of Computational Physics*, 183(2):400 – 421, 2002.

[286] Marianne M. Francois, Sharen J. Cummins, Edward D. Dendy, Douglas B. Kothe, James M. Sicilian, and Matthew W. Williams. A balanced-force algorithm for continuous and sharp interfacial surface tension models within a volume tracking framework. *Journal of Computational Physics*, 213(1):141 – 173, 2006.

[287] Sharen J. Cummins, Marianne M. Francois, and Douglas B. Kothe. Estimating curvature from volume fractions. *Computers & Structures*, 83(6–7):425 – 434,

2005. Frontier of Multi-Phase Flow Analysis and Fluid-Structure Frontier of Multi-Phase Flow Analysis and Fluid-Structure.

[288] Marcus S. Day, Phillip Colella, Michael J. Lijewski, Charles A. Rendleman, and Daniel L. Marcus. Embedded boundary algorithms for solving the poisson equation on complex domains. Technical Report LBNL-41811, Lawrence Berkeley National Laboratory, May 1998.

[289] Philippe Angot, Charles-Henri Bruneau, and Pierre Fabrie. A penalization method to take into account obstacles in incompressible viscous flows. *Numerische Mathematik*, 81(4):497–520, 1999.

[290] Qianlong Liu and Oleg V. Vasilyev. A Brinkman penalization method for compressible flows in complex geometries. *Journal of Computational Physics*, 227(2):946–966, 2007.

[291] André B. Bondi. Characteristics of Scalability and Their Impact on Performance. In *Proceedings of the 2Nd International Workshop on Software and Performance*, WOSP '00, pages 195–203, New York, NY, USA, 2000. ACM.

[292] Pietro Asinari, Taku Ohwada, Eliodoro Chiavazzo, and Antonio F. Di Rienzo. Link-wise artificial compressibility method. *Journal of Computational Physics*, 231(15):5109 – 5143, 2012.

[293] W. von Ohnesorge. Die Bildung von Tropfen an Düsen und die Auflösung flüssiger Strahlen. *Z. Angew. Math. Mech*, 16(4):355–358, 1936.

[294] W. von Ohnesorge. *Anwendung eines kinematographischen Hochfrequenzapparates mit mechanischer Regelung der Belichtung zur Aufnahme der Tropfenbildung und des Zerfalls flüssiger Strahlen.* Konrad Triltsch, Würzburg, 1937.

[295] P. van Meurs and C. van der Poel. A Theoretical Description of Water-Drive Processes Involving Viscous Fingering. *Trans. AIME*, 213:103–112, January 1958.

[296] David Wilkinson. Percolation model of immiscible displacement in the presence of buoyancy forces. *Phys. Rev. A*, 30:520–531, Jul 1984.

[297] David Wilkinson. Percolation effects in immiscible displacement. *Phys. Rev. A*, 34:1380–1391, Aug 1986.

[298] Paul Meakin, Jens Feder, Vidar Frette, and Torstein Jøssang. Invasion percolation in a destabilizing gradient. *Phys. Rev. A*, 46:3357–3368, Sep 1992.

[299] Ioannis N. Tsimpanogiannis and Yannis C. Yortsos. The critical gas saturation in a porous medium in the presence of gravity. *Journal of Colloid and Interface Science*, 270(2):388 – 395, 2004.

[300] Nicos S. Martys, S. Torquato, and D. P. Bentz. Universal scaling of fluid permeability for sphere packings. *Phys. Rev. E*, 50:403–408, Jul 1994.

[301] Harold L. Weissberg and Stephen Prager. Viscous Flow through Porous Media. III. Upper Bounds on the Permeability for a Simple Random Geometry. *Physics of Fluids (1958-1988)*, 13(12):2958–2965, 1970.

[302] James G. Berryman and Graeme W. Milton. Normalization constraint for variational bounds on fluid permeability. *The Journal of Chemical Physics*, 83(2):754–760, 1985.

[303] H. C. Brinkman. A calculation of the viscous force exerted by a flowing fluid on a dense swarm of particles. *Appl. Sci. Res. A*, 1:27–34, 1947.

[304] G. N. Hounsfield. A Method of and Apparatus for Examination of a Body by Radiation Such as X or Gamma Radiation. *British Patent No. 1.283.915, London*, 1972.

[305] S. Akin and A. R. Kovscek. Computed tomography in petroleum engineering research. *Geological Society, London, Special Publications*, 215(1):23–38, 2003.

[306] Wikipedia. Xeroradiography — Wikipedia, The Free Encyclopedia, 2014. [Online; accessed 4-April-2014].

[307] G. E. Sedgwick and E. Miles-Dixon. Application Of X-Ray Imaging Techniques To Oil Sands Experiments. *Journal of Canadian Petroleum Technology*, 27(02), 1988.

[308] Pierre Bouguer. *Essai d'optique sur la gradation de la lumière*. 1729.

[309] Johann Heinrich Lambert. Photometria sive de mensura et gradibus luminis colorum et umbrae. 1760.

[310] August Beer. Bestimmung der Absorption des rothen Lichts in farbigen Flüssigkeiten. *Annalen der Physik*, 162(5):78–88, 1852.

[311] Harold J. Vinegar and Scott L. Wellington. Tomographic imaging of three-phase flow experiments. *Review of Scientific Instruments*, 58(1):96–107, 1987.

[312] O. Klein and Y. Nishina. Über die Streuung von Strahlung durch freie Elektronen nach der neuen relativistischen Quantendynamik von Dirac. *Zeitschrift für Physik*, 52(11-12):853–868, 1929.

[313] F. P. Bretherton. The motion of long bubbles in tubes. *Journal of Fluid Mechanics*, 10(02):166–188, 1961.

[314] Pascale Aussillous and David Quéré. Quick deposition of a fluid on the wall of a tube. *Physics of Fluids (1994-present)*, 12(10):2367–2371, 2000.

[315] J. S. Langer. Dendrites, Viscous Fingers, and the Theory of Pattern Formation. *Science*, 243(4895):1150–1156, 1989.

[316] Eshel Ben-Jacob and Peter Garik. The formation of patterns in non-equilibrium growth. *Nature*, 343:523–530, 1990.

[317] J. S. Langer. Instabilities and pattern formation in crystal growth. *Rev. Mod. Phys.*, 52:1–28, Jan 1980.

[318] C.-W. Park, S. Gorell, and G. M. Homsy. Two-phase displacement in Hele-Shaw cells: experiments on viscously driven instabilities. *Journal of Fluid Mechanics*, 141:275–287, 1984.

[319] J. V. Maher. Development of Viscous Fingering Patterns. *Phys. Rev. Lett.*, 54:1498–1501, Apr 1985.

[320] Eshel Ben-Jacob, G. Deutscher, Peter Garik, Nigel D. Goldenfeld, and Y. Lareah. Formation of a Dense Branching Morphology in Interfacial Growth. *Phys. Rev. Lett.*, 57:1903–1906, Oct 1986.

[321] H. Z. Cummins, L. Fourtune, and M. Rabaud. Successive bifurcations in directional viscous fingering. *Phys. Rev. E*, 47:1727–1738, Mar 1993.

[322] Shuwang Li, John S. Lowengrub, and Perry H. Leo. A rescaling scheme with application to the long-time simulation of viscous fingering in a Hele–Shaw cell. *Journal of Computational Physics*, 225(1):554 – 567, 2007.

[323] E. A. Brener, D. A. Kessler, H. Levine, and W.-J. Rappei. Selection of the Viscous Finger in the 90° Geometry. *EPL (Europhysics Letters)*, 13(2):161, 1990.

[324] R. Combescot and M. Ben Amar. Selection of Saffman-Taylor fingers in the sector geometry. *Phys. Rev. Lett.*, 67:453–456, July 1991.

[325] Shuwang Li, John S. Lowengrub, Perry H. Leo, and Vittorio Cristini. Nonlinear theory of self-similar crystal growth and melting. *Journal of Crystal Growth*, 267(3–4):703 – 713, 2004.

[326] Chao Tang. Diffusion-limited aggregation and the Saffman-Taylor problem. *Phys. Rev. A*, 31:1977–1979, March 1985.

[327] Thomas A. Witten and Leonard M. Sander. Diffusion-Limited Aggregation, a Kinetic Critical Phenomenon. *Phys. Rev. Lett.*, 47:1400–1403, Nov 1981.

[328] J. Bataille. Stabilité d'un écoulement radial non miscible. In *Revue de l'Institut Français du Pétrole et Annales des Combustibles Liquides*, volume 23, page 1349, 1968.

[329] Lincoln Paterson. Radial fingering in a Hele Shaw cell. *Journal of Fluid Mechanics*, 113:513–529, 12 1981.

[330] Petri Fast and Michael J. Shelley. Moore's law and the Saffman–Taylor instability. *Journal of Computational Physics*, 212(1):1 – 5, 2006.

[331] Shuwang Li, John S. Lowengrub, Jake Fontana, and Peter Palffy-Muhoray. Control of Viscous Fingering Patterns in a Radial Hele-Shaw Cell. *Phys. Rev. Lett.*, 102:174501, Apr 2009.

[332] H. Thomé, M. Rabaud, V. Hakim, and Y. Couder. The Saffman–Taylor instability: From the linear to the circular geometry. *Physics of Fluids A: Fluid Dynamics*, 1:224, 1989.

[333] A. Arneodo, J. Elezgaray, M. Tabard, and F. Tallet. Statistical analysis of off-lattice diffusion-limited aggregates in channel and sector geometries. *Phys. Rev. E*, 53:6200–6223, Jun 1996.

[334] David Bensimon, Leo P. Kadanoff, Shoudan Liang, Boris I. Shraiman, and Chao Tang. Viscous flows in two dimensions. *Rev. Mod. Phys.*, 58:977–999, October 1986.

[335] David Bensimon. Stability of viscous fingering. *Phys. Rev. A*, 33:1302–1308, February 1986.

[336] Saleh Tanveer. Surprises in viscous fingering. *Journal of Fluid Mechanics*, 409:273–308, 2000.

[337] P. van Meurs. The Use of Transparent Three-Dimensional Models for Studying the Mechanism of Flow Processes in Oil Reservoirs. *Trans. AIME*, 210:295–301, 1957.

[338] G. M. Homsy. Viscous fingering in porous media. *Annual Review of Fluid Mechanics*, 19:271–311, 1987.

[339] Thomas C. Halsey. Diffusion-limited aggregation: A model for pattern formation. *Physics Today*, 2000.

[340] Leonard M. Sander. Fractal Growth Processes. In Robert A. Meyers, editor, *Mathematics of Complexity and Dynamical Systems*, pages 429–445. Springer New York, 2011.

[341] Massimo Conti, Baruch Meerson, and Pavel V. Sasorov. Breakdown of Scale Invariance in the Phase Ordering of Fractal Clusters. *Phys. Rev. Lett.*, 80:4693–4696, May 1998.

[342] Benny Davidovitch, Anders Levermann, and Itamar Procaccia. Convergent calculation of the asymptotic dimension of diffusion limited aggregates: Scaling and renormalization of small clusters. *Phys. Rev. E*, 62:R5919–R5922, November 2000.

[343] B. Shraiman and D. Bensimon. Singularities in nonlocal interface dynamics. *Phys. Rev. A*, 30:2840–2842, Nov 1984.

[344] S. D. Howison. Fingering in Hele-Shaw cells. *J. Fluid Mech*, 167:43–53, 1986.

[345] David Bensimon and Pierre Pelcé. Tip-splitting solutions to a Stefan problem. *Phys. Rev. A*, 33:4477–4478, Jun 1986.

[346] L. Landau and B. Levich. Dragging of a liquid by a moving plate. *Acta Physicochimica URSS*, 17:42–54, 1942.

[347] P. Tabeling, G. Zocchi, and A. Libchaber. An experimental study of the Saffman-Taylor instability. *Journal of Fluid Mechanics*, 177:67–82, 1987.

[348] D. A. Reinelt. The effect of thin film variations and transverse curvature on the shape of fingers in a Hele–Shaw cell. *Physics of Fluids (1958-1988)*, 30(9):2617–2623, 1987.

[349] Saleh Tanveer. Analytic theory for the selection of Saffman-Taylor fingers in the presence of thin film effects. *Proceedings of the Royal Society of London. A. Mathematical and Physical Sciences*, 428(1875):511–545, 1990.

[350] L. W. Schwartz and A. J. DeGregoria. Simulation of Hele-Shaw fingering with finite-capillary-number effects included. *Phys. Rev. A*, 35:276–279, Jan 1987.

[351] Jean-Marc Vanden-Broeck. Fingers in a Hele–Shaw Cell with surface tension. *Physics of Fluids (1958-1988)*, 26(8):2033–2034, 1983.

[352] Roland Combescot, Thierry Dombre, Vincent Hakim, Yves Pomeau, and Alain Pumir. Shape selection of saffman-taylor fingers. *Phys. Rev. Lett.*, 56:2036–2039, May 1986.

[353] Roland Combescot, Vincent Hakim, Thierry Dombre, Yves Pomeau, and Alain Pumir. Analytic theory of the Saffman-Taylor fingers. *Phys. Rev. A*, 37:1270–1283, Feb 1988.

[354] D. C. Hong and J. S. Langer. Analytic Theory of the Selection Mechanism in the Saffman-Taylor Problem. *Phys. Rev. Lett.*, 56:2032–2035, May 1986.

[355] Boris I. Shraiman. Velocity Selection and the Saffman-Taylor Problem. *Phys. Rev. Lett.*, 56:2028–2031, May 1986.

[356] David Bensimon, Pierre Pelcé, and Boris I. Shraiman. Dynamics of curved fronts and pattern selection. *Journal de Physique*, 48(12):2081–2087, 1987.

[357] S. Tanveer. Analytic theory for the linear stability of the Saffman–Taylor finger. *Physics of Fluids (1958-1988)*, 30(8):2318–2329, 1987.

[358] David A. Kessler, Joel Koplik, and Herbert Levine. Pattern selection in fingered growth phenomena. *Advances in Physics*, 37(3):255–339, 1988.

[359] Leo P. Kadanoff. Simulating hydrodynamics: A pedestrian model. *Journal of Statistical Physics*, 39(3-4):267–283, 1985.

[360] Shoudan Liang. Random-walk simulations of flow in Hele-Shaw cells. *Phys. Rev. A*, 33:2663–2674, Apr 1986.

[361] Martine Ben Amar. Exact self-similar shapes in viscous fingering. *Phys. Rev. A*, 43:5724–5727, May 1991.

[362] Martine Ben Amar, Vincent Hakim, Maurice Mashaal, and Yves Couder. Self-dilating viscous fingers in wedge-shaped Hele-Shaw cells. *Physics of Fluids A: Fluid Dynamics (1989-1993)*, 3(9):2039–2042, 1991.

[363] Martine Ben Amar. Viscous fingering in a wedge. *Phys. Rev. A*, 44:3673–3685, Sep 1991.

[364] A. Dougherty and J. P. Gollub. Steady-state dendritic growth of NH_4Br from solution. *Phys. Rev. A*, 38:3043–3053, Sep 1988.

[365] Eshel Ben-Jacob, R. Godbey, Nigel Goldenfeld, H. Levine, T. Mueller, and Leonard M. Sander. Experimental demonstration of the role of anisotropy in interfacial pattern formation. *Physical review letters*, 55(12):1315–1318, 1985.

[366] Agnes Buka, János Kertész, and Tamás Vicsek. Transitions of viscous fingering patterns in nematic liquid crystals. *Nature*, 323(6087):424–425, 1986.

[367] Y. Couder, O. Cardoso, D. Dupuy, P. Tavernier, and W. Thom. Dendritic Growth in the Saffman-Taylor Experiment. *EPL (Europhysics Letters)*, 2(6):437, 1986.

[368] Y. Couder, N. Gérard, and M. Rabaud. Narrow fingers in the Saffman-Taylor instability. *Phys. Rev. A*, 34:5175–5178, Dec 1986.

[369] M. Rabaud, Yves Couder, and N. Gerard. Dynamics and stability of anomalous Saffman-Taylor fingers. *Phys. Rev. A*, 37:935–947, Feb 1988.

[370] J. Maurer, B. Perrin, and P. Tabeling. Three-Dimensional Structure of NH_4Br Dendrites Growing within a Gel. *EPL (Europhysics Letters)*, 14(6):575, 1991.

[371] Anne R. Kopf-Sill and G. M. Homsy. Narrow fingers in a Hele–Shaw cell. *Physics of Fluids (1958-1988)*, 30(9):2607–2609, 1987.

[372] Giovanni Zocchi, Bruce E. Shaw, Albert Libchaber, and Leo P. Kadanoff. Finger narrowing under local perturbations in the Saffman-Taylor problem. *Phys. Rev. A*, 36:1894–1900, Aug 1987.

[373] Alan T. Dorsey and Olivier Martin. Saffman-Taylor fingers with anisotropic surface tension. *Phys. Rev. A*, 35:3989–3992, May 1987.

[374] Subir K. Sarkar and David Jasnow. Viscous fingering in an anisotropic Hele-Shaw cell. *Phys. Rev. A*, 39:5299–5307, May 1989.

[375] D. C. Hong and J. S. Langer. Pattern selection and tip perturbations in the Saffman-Taylor problem. *Phys. Rev. A*, 36:2325–2332, Sep 1987.

[376] R. Combescot and T. Dombre. Selection in the anomalous Saffman-Taylor fingers induced by a bubble. *Phys. Rev. A*, 39:3525–3535, Apr 1989.

[377] A. B. Zel'Dovich, A. G. Istratov, N. I. Kidin, and V. B. Librovich. Flame propagation in tubes: hydrodynamics and stability. *Combustion Science and Technology*, 24(1-2):1–13, 1980.

[378] Pierre Pelcé and P. Clavin. The Stability of Curved Fronts. *EPL (Europhysics Letters)*, 3(8):907, 1987.

[379] D. A. Kessler and H. Levine. Determining the Wavelength of Dendritic Sidebranches. *EPL (Europhysics Letters)*, 4(2):215, 1987.

[380] Caroli, B., Caroli, C., and Roulet, B. On the linear stability of needle crystals : evolution of a Zel'dovich localized front deformation. *J. Phys. France*, 48(9):1423–1437, 1987.

[381] X. W. Qian and H. Z. Cummins. Dendritic sidebranching initiation by a localized heat pulse. *Phys. Rev. Lett.*, 64:3038–3041, Jun 1990.

[382] Ph. Bouissou, A. Chiffaudel, B. Perrin, and P. Tabeling. Dendritic Side-Branching Forced by an External Flow. *EPL (Europhysics Letters)*, 13(1):89, 1990.

[383] Geordie D. McBain. Simple example of groundwater flow following Darcy's law. Test case on the Gerris website.

[384] Thomas Y. Hou, John S. Lowengrub, and Michael J. Shelley. Removing the stiffness from interfacial flows with surface tension. *Journal of Computational Physics*, 114(2):312 – 338, 1994.

[385] H. Thomé, R. Combescot, and Y. Couder. Controlling singularities in the complex plane: Experiments in real space. *Phys. Rev. A*, 41:5739–5742, May 1990.

[386] Jane Chui, Pietro de Anna, and Ruben Juanes. The Impact of Miscible Viscous Fingering on Fluid Mixing. Poster presented at the 2013 Annual Meeting of the APS Division of Fluid Dynamics, Pittsburgh, PA, USA, November 2013.

[387] Jane Chui, Michael Szulczewski, Birendra Jha, and Ruben Juanes. Interface Evolution during Miscible Viscous Fingering, 2013.

[388] Gérald Hamon. Point d'avancement sur le troisième essai de balayage d'huile extra lourde par l'eau et eau polymérisée au 15/06/2010. June 2010.

[389] Petri Fast and Michael J. Shelley. A moving overset grid method for interface dynamics applied to non-Newtonian Hele–Shaw flow. *Journal of Computational Physics*, 195(1):117 – 142, 2004.

[390] G. P. Ivantsov. Temperature around a spheroidal, cylindrical and acicular crystal growing in a supercooled melt. In *Dokl. Akad. Nauk*, volume 58, pages 567–569, 1947.

[391] L. A. Smith, J.-D. Fournier, and E. A. Spiegel. Lacunarity and intermittency in fluid turbulence. *Physics Letters A*, 114(8–9):465 – 468, 1986.

[392] D. Bessis, J. S. Geronimo, and P. Moussa. Complex spectral dimensionality on fractal structures. *J. Physique Lett.*, 44(24):977–982, 1983.

[393] R. Badii and A. Politi. Intrinsic oscillations in measuring the fractal dimension. *Physics Letters A*, 104(6–7):303 – 305, 1984.

[394] G. M. Zaslavsky. The simplest case of a strange attractor. *Physics Letters A*, 69(3):145 – 147, 1978.

[395] Benoît B. Mandelbrot. The Fractal Geometry of Nature. 1982.

[396] M. Hénon. A two-dimensional mapping with a strange attractor. *Communications in Mathematical Physics*, 50(1):69–77, 1976.

[397] J. Guckenheimer. Dimension estimates for attractors. *Contemp. Math.*, 28:357–367, 1984.

[398] I. Bondino, R. Nguyen, G. Hamon, P. A. Ormehaug, A. Skauge, and S. Jouenne. Tertiary polymer flooding in extra-heavy oil: an investigation using 1D and 2D experiments, core scale simulation and pore-scale network models. In *Review Proceedings for the 25th International Symposium of the Society of Core Analysis, Austin, Texas, USA*, 2011.

[399] Arne Skauge, K. Sorbie, Per Arne Ormehaug, and T. Skauge. Experimental and Numerical Modeling Studies of Viscous Unstable Displacement. In *15th European Symposium on Improved Oil Recovery*, 2009.

[400] John G. Proakis and Dimitris G. Manolakis. Digital Signal Processing: Principles, Algorithms and Applications, 1996.

[401] Rafael C. Gonzales and Richard E. Woods. Digital image processing.

[402] An Mai and Apostolos Kantzas. Mechanisms of heavy oil recovery by low rate waterflooding. *Journal of Canadian Petroleum Technology*, 49(3):44–50, 2010.

[403] Songyi Mei, Jonathan Luke Bryan, and Apostolos Kantzas. Experimental Study of the Mechanisms in Heavy Oil Waterflooding Using Etched Glass Micromodel. In *SPE Heavy Oil Conference Canada*. Society of Petroleum Engineers, 2012.

[404] Pierre Horgue, Marc Prat, and Michel Quintard. A penalization technique applied to the "Volume-Of-Fluid" method: Wettability condition on immersed boundaries. *Computers & Fluids*, 100(0):255 – 266, 2014.

[405] Jens Feder. Fractals, 1988.

[406] Pierre-Gilles de Gennes and E. Guyon. Lois générales pour l'injection d'un fluide dans un milieu poreux aléatoire. *J. Mec*, 17(3):403–432, 1978.

[407] Richard Chandler, Joel Koplik, Kenneth Lerman, and Jorge F. Willemsen. Capillary displacement and percolation in porous media. *Journal of Fluid Mechanics*, 119:249–267, 1982.

[408] S. R. Broadbent and J. M. Hammersley. Percolation processes. In *Mathematical Proceedings of the Cambridge Philosophical Society*, volume 53, pages 629–641. Cambridge Univ Press, 1957.

[409] Robert M. Ziff. Test of scaling exponents for percolation-cluster perimeters. *Phys. Rev. Lett.*, 56:545–548, Feb 1986.

[410] M. M. Dias and D. Wilkinson. Percolation with trapping. *Journal of Physics A: Mathematical and General*, 19(15):3131, 1986.

[411] R. C. Ball and R. M. Brady. Large scale lattice effect in diffusion-limited aggregation. *Journal of Physics A: Mathematical and General*, 18(13):L809, 1985.

[412] Robin C. Ball, Robert M. Brady, Giuseppe Rossi, and Bernard R. Thompson. Anisotropy and cluster growth by diffusion-limited aggregation. *Phys. Rev. Lett.*, 55:1406–1409, Sep 1985.

[413] Paul Meakin, Robin C. Ball, P. Ramanlal, and L. M. Sander. Structure of large two-dimensional square-lattice diffusion-limited aggregates: Approach to asymptotic behavior. *Phys. Rev. A*, 35:5233–5239, Jun 1987.

[414] Jean-Pierre Eckmann, Paul Meakin, Itamar Procaccia, and Reuven Zeitak. Asymptotic shape of diffusion-limited aggregates with anisotropy. *Phys. Rev. Lett.*, 65:52–55, Jul 1990.

[415] M. G. Stepanov and L. S. Levitov. Laplacian growth with separately controlled noise and anisotropy. *Phys. Rev. E*, 63:061102, May 2001.

[416] Nicholas R. Goold, Ellák Somfai, and Robin C. Ball. Anisotropic diffusion limited aggregation in three dimensions: Universality and nonuniversality. *Phys. Rev. E*, 72:031403, Sep 2005.

[417] Susan Tolman and Paul Meakin. Off-lattice and hypercubic-lattice models for diffusion-limited aggregation in dimensionalities 2¡i¿–¡/i¿8. *Phys. Rev. A*, 40:428–437, Jul 1989.

[418] Benoît B. Mandelbrot and Carl J. G. Evertsz. The potential distribution around fractal clusters. *Nature*, 348(6297):143–145, November 1990.

[419] Peter Ossadnik. Multiscaling analysis of large-scale off-lattice {DLA}. *Physica A: Statistical Mechanics and its Applications*, 176(3):454 – 462, 1991.

[420] Ellák Somfai, Robin C. Ball, Jason P. DeVita, and Leonard M. Sander. Diffusion-limited aggregation in channel geometry. *Phys. Rev. E*, 68, 2003.

[421] T. Vicsek, F. Family, and P. Meakin. Multifractal Geometry of Diffusion-Limited Aggregates. *EPL (Europhysics Letters)*, 12(3):217, 1990.

[422] B. B. Mandelbrot, H. Kaufman, A. Vespignani, I. Yekutieli, and C.-H. Lam. Deviations from Self-Similarity in Plane DLA and the "Infinite Drift" Scenario. *EPL (Europhysics Letters)*, 29(8):599, 1995.

[423] B. B. Mandelbrot, A. Vespignani, and H. Kaufman. Crosscut Analysis of Large Radial DLA: Departures from Self-Similarity and Lacunarity Effects. *EPL (Europhysics Letters)*, 32(3):199, 1995.

[424] E. Somfai, L. M. Sander, and R. C. Ball. Scaling and crossovers in diffusion limited aggregation. *Phys. Rev. Lett.*, 83:5523–5526, Dec 1999.

[425] D. A. Kessler, Z. Olami, J. Oz, I. Procaccia, E. Somfai, and L. M. Sander. Diffusion-limited aggregation and viscous fingering in a wedge: Evidence for a critical angle. *Phys. Rev. E*, 57:6913–6916, Jun 1998.

[426] Yuhai Tu and Herbert Levine. Mean-field theory of the morphology transition in stochastic diffusion-limited growth. *Phys. Rev. E*, 52:5134–5141, Nov 1995.

[427] Leonard M. Sander and Ellák Somfai. Random walks, diffusion limited aggregation in a wedge, and average conformal maps. *Chaos: An Interdisciplinary Journal of Nonlinear Science*, 15(2):–, 2005.

[428] Paul Meakin and Fereydoon Family. Diverging length scales in diffusion-limited aggregation. *Phys. Rev. A*, 34:2558–2560, Sep 1986.

[429] F. Argoul, A. Arneodo, G. Grasseau, and Harry L. Swinney. Self-similarity of diffusion-limited aggregates and electrodeposition clusters. *Phys. Rev. Lett.*, 61:2558–2561, Nov 1988.

[430] Boaz Kol and Amnon Aharony. Diffusion-limited aggregation as a markovian process: Site-sticking conditions. *Phys. Rev. E*, 63:046117, Mar 2001.

[431] W. W. Mullins and R. F. Sekerka. Morphological Stability of a Particle Growing by Diffusion or Heat Flow. *Journal of Applied Physics*, 34(2):323–329, Feb 1963.

[432] Pierre Pelcé. *New visions on form and growth: fingered growth, dendrites, and flames*. Oxford University Press, 2004.

[433] Wikipedia. Diffusion-limited aggregation — Wikipedia, The Free Encyclopedia, 2013. [Online; accessed 27-February-2014].

[434] Murray Eden. A two-dimensional growth model. In *Neyman J. (ed) Proceedings of the 4th Berkeley symposium on mathematics, statistics, and probability. University of California Press, Berkeley*, 1961.

[435] A. Sánchez, F. Guinea, L. M. Sander, V. Hakim, and E. Louis. Growth and forms of Laplacian aggregates. *Phys. Rev. E*, 48:1296–1304, Aug 1993.

[436] M. B. Hastings. Fractal to nonfractal phase transition in the dielectric breakdown model. *Phys. Rev. Lett.*, 87:175502, 2001.

[437] M. B. Hastings. Growth exponents with 3.99 walkers. *Phys. Rev. E*, 64:046104, 2001.

[438] Bernhard Riemann. *Grundlagen für eine allgemeine Theorie der Functionen einer veränderlichen complexen Grösse*. PhD thesis, Georg-August-Universität Göttingen, 1851.

[439] Ilya A. Gruzberg and Leo P. Kadanoff. The Loewner Equation: Maps and Shapes. *Journal of Statistical Physics*, 114(5-6):1183–1198, 2004.

[440] M. B. Hastings and L. S. Levitov. Laplacian growth as one-dimensional turbulence. *Physica D: Nonlinear Phenomena*, 116(1–2):244 – 252, 1998.

[441] F. Mohammadi, A. A. Saberi, and S. Rouhani. Fractal structure of Hastings–Levitov patterns restricted in a sector geometry. *Journal of Physics A: Mathematical and Theoretical*, 43(37):375208, 2010.

[442] Benoît B. Mandelbrot. How long is the coast of Britain. *Science*, 156(3775):636–638, 1967.

[443] Benoît B. Mandelbrot. *Les Objets Fractals*. Flammarion, 1975.

[444] Benoît B. Mandelbrot. Self-affine fractal sets. In Amsterdam L. Pietronero & E. Tosatti, North-Holland, editor, *Fractals in physics*, pages 3–28, 1986.

[445] Wikipédia. Ensemble de Mandelbrot — Wikipédia, l'encyclopédie libre, 2014. [Online; accessed 26-February-2014].

[446] Azriel Rosenfeld. Picture Processing by Computer. *ACM Comput. Surv.*, 1(3):147–176, September 1969.

[447] G. Blöschl and M. Sivapalan. Scale issues in hydrological modelling: A review. *Hydrological Processes*, 9(3-4):251–290, 1995.

[448] Benoit B. Mandelbrot. *Fractals and scaling in finance: Discontinuity and concentration*. Springer Verlag, 1997.

[449] Felix Hausdorff. Dimension und äußeres Maß. *Mathematische Annalen*, 79(1-2):157–179, 1918.

[450] A. S. Besicovitch. On linear sets of points of fractional dimension. *Mathematische Annalen*, 101(1):161–193, 1929.

[451] A. S. Besicovitch and H. D. Ursell. Sets of Fractional Dimensions (V): on Dimensional Numbers of Some Continuous Curves. *Journal of the London Mathematical Society*, s1-12(1):18–25, 1937.

[452] H. G. E. Hentschel and Itamar Procaccia. The infinite number of generalized dimensions of fractals and strange attractors. *Physica D: Nonlinear Phenomena*, 8(3):435 – 444, 1983.

[453] Thomas C. Halsey, Mogens H. Jensen, Leo P. Kadanoff, Itamar Procaccia, and Boris I. Shraiman. Fractal measures and their singularities: The characterization of strange sets. *Phys. Rev. A*, 33:1141–1151, Feb 1986.

[454] Benoît B. Mandelbrot. Intermittent turbulence in self-similar cascades: divergence of high moments and dimension of the carrier. *Journal of Fluid Mechanics*, 62(02):331–358, 1974.

[455] David A. Russell, James D. Hanson, and Edward Ott. Dimension of strange attractors. *Phys. Rev. Lett.*, 45(14), 1980.

[456] Harold Froehling, J. P. Crutchfield, Doyne Farmer, N. H. Packard, and Rob Shaw. On determining the dimension of chaotic flows. *Physica D: Nonlinear Phenomena*, 3(3):605 – 617, 1981.

[457] Peter Grassberger. On the Hausdorff dimension of fractal attractors. *Journal of Statistical Physics*, 26(1):173–179, 1981.

[458] H. S. Greenside, A. Wolf, J. Swift, and T. Pignataro. Impracticality of a box-counting algorithm for calculating the dimensionality of strange attractors. *Phys. Rev. A*, 25:3453–3456, June 1982.

[459] Peter Grassberger and Itamar Procaccia. Measuring the strangeness of strange attractors. *Physica D*, 9:189–208, 1983.

[460] Wikipedia. Julia set — Wikipedia, The Free Encyclopedia, 2013. [Online; accessed 26-March-2014].

[461] Gaston Julia. Mémoire sur l'itération des fonctions rationnelles. *Journal de mathématiques pures et appliquées*, pages 47–246, 1918.

[462] Pierre Fatou. Sur les substitutions rationnelles. *Comptes Rendus de l'Académie des Sciences de Paris*, 164:806–808, 1917.

[463] Onno Ubbink. *Numerical prediction of two fluid systems with sharp interfaces.* PhD thesis, University of London UK, 1997.

[464] Alexandre Joel Chorin. Flame advection and propagation algorithms. *Journal of Computational Physics*, 35(1):1 – 11, 1980.

[465] D. L. Youngs. Time-dependent multi-material flow with large fluid distortion. *Numerical methods for fluid dynamics*, 24:273–285, 1982.

[466] Per Lötstedt. A front tracking method applied to Burgers' equation and two-phase porous flow. *Journal of Computational Physics*, 47(2):211 – 228, 1982.

[467] N. Ashgriz and J. Y. Poo. FLAIR: Flux line-segment model for advection and interface reconstruction. *Journal of Computational Physics*, 93(2):449 – 468, 1991.

Extended summary in French - Résumé détaillé

L'étude détaillée des écoulements multiphasiques en milieu poreux revêt une importance cruciale pour de multiples applications industrielles et écologiques [58]. En effet, comme, à l'heure actuelle, 90 % de l'énergie consommée de par le monde est d'origine fossile [1, 2, 3], la demande mondiale de pétrole augmente en permanence. Pour répondre à cette demande, le pétrole est extrait selon un processus en deux voire trois temps :

- lors de la récupération primaire, entre 5 % et 15 % du pétrole initialement piégé dans le réservoir est produit par déplétion des hydrocarbures ;
- dans un second temps, il est possible d'extraire entre 15 % et 30 % du pétrole par injection forcée de saumure [18, 19] ;
- un ensemble de techniques connues sous le nom générique de récupération assistée de pétrole est alors mis en œuvre pour extraire un surplus compris entre 5 % et 15 % [19, 23, 25].

Comme les processus de déplacement dans les milieux poreux naturels jouent un rôle crucial dans la mise en œuvre de ces techniques, il est capital d'identifier et d'étudier les processus d'écoulements multiphasiques aussi bien à l'échelle microscopique que macroscopique.

Ces travaux s'inscrivent dans le cadre du projet R&D d'étude des « Huiles Lourdes » de TOTAL SA. Le but de ce projet est de comprendre et modéliser l'invasion de milieux poreux saturés en huiles lourdes par de l'eau et des polymères.

Cette étude s'intéresse donc à l'une des techniques de récupération assistée de pétrole consistant à injecter une solution de polymères [37] afin de réduire le contraste de viscosité entre le fluide injecté et celui déplacé et/ou augmenter le nombre capillaire. Bien que la mouillabilité des roches soit d'une importance capitale dans la récupération d'huile (la vitesse d'extraction et le taux d'huile récupérée sont en général beaucoup plus importants dans le cas d'une imprégnation que d'un drainage), cette étude ne s'intéresse pas à ces considérations [53, 57].

Le but ultime du projet de recherche est d'augmenter le ratio d'huile récupérée lors de l'extraction, à des coûts réduits, grâce à une meilleure compréhension des différentes lois physiques régissant les écoulements dans le réservoir.

Éléments de théorie des fluides et des milieux poreux

On définit un fluide comme un milieu continu ne pouvant pas rester au repos sous un chargement de cisaillement. Cela correspond à peu près à considérer les matériaux à faible nombre de Déborah [65]

$$\mathrm{Deb} = \frac{\tau_r}{\tau_o}$$

où τ_r est le temps caractéristique de relaxation du matériau et τ_o le temps caractéristique d'observation. On distingue d'autre part au sein des fluides les gaz (forte compressibilité) des liquides (faible compressibilité). Pour des raisons évidentes de taille du problème, on ne considère pas le mouvement de chaque molécule composant le fluide, mais plutôt des valeurs moyennes appliquées à un continuum [72].

Parmi les différentes propriétés des fluides, on définit la viscosité μ comme une mesure de la résistance au cisaillement dudit fluide lorsque ce fluide est en mouvement. On considérera dans la présente étude uniquement des fluides newtoniens, c'est-à-dire pour lesquels μ est une constante [74]. Comme les vitesses attendues sont faibles, les fluides sont considérés comme incompressibles [73, 76, 77].

Les fluides obéissent par conséquent aux équations suivantes :

- conservation de la masse

$$\nabla \cdot \mathbf{u} = 0 \ ;$$

- conservation de la quantité de mouvement (équations de Navier-Stokes)

$$\rho \frac{\mathrm{D}\mathbf{u}}{\mathrm{D}t} = -\nabla p + \rho \mathbf{g} + \mu \nabla^2 \mathbf{u}.$$

D'autre part, lorsque deux fluides immiscibles sont en contact, l'interface entre ces deux fluides est soumise à une tension de surface résultant des forces d'attraction intermoléculaires [79]. Cette tension de surface est à l'origine d'un saut de pression à la traversée de l'interface lorsque celle-ci est courbée, tel que

$$p_i - p_o = \frac{\sigma}{R},$$

où p_i (côté concave) et p_o sont les pressions de part et d'autre de l'interface, et R le rayon de courbure moyen de l'interface. Ce saut de pression est dénommé pression capillaire ou pression de Laplace [88].

La tension de surface est intégrée dans les équations de Navier-Stokes par le biais d'un traceur $c(\mathbf{x}, t)$ valant 0 dans l'un des fluides et 1 dans l'autre fluide :

$$\rho \frac{\mathrm{D}\mathbf{u}}{\mathrm{D}t} = -\nabla p + \rho \mathbf{g} + \mu \nabla^2 \mathbf{u} + \frac{2\sigma}{R(\mathbf{x}, t)} \nabla c.$$

Cette méthode peut aisément être étendue à plus de deux fluides par le biais de plusieurs traceurs.

Il est possible d'adimensionner les équations de Navier-Stokes. On fait alors apparaître deux nombres sans dimension :

- le nombre de Reynolds $\mathrm{Re} \equiv \frac{\rho l U}{\mu}$ présentant le rapport entre inertie et forces visqueuses,

- le nombre capillaire $\mathrm{Ca} \equiv \frac{\mu U}{\sigma}$ présentant le rapport entre forces visqueuses et tension de surface.

Enfin, on définit la mouillabilité comme la capacité d'un fluide à garder contact avec une surface solide en présence d'un deuxième fluide précisé [51]. La mouillabilité

est mesurée par l'angle de contact θ, qui représente l'angle de jonction entre l'interface fluide/fluide et la surface solide. Celui-ci vérifie l'équation de Young [86]

$$\sigma_{SG} - \sigma_{SL} - \sigma_{LG} \cos\theta = 0$$

avec σ_{SG}, σ_{SL} et σ_{LG} les tensions inter-faciales entre solide/gaz, solide/liquide et liquide/gaz respectivement.

Un milieu poreux vérifie trois propriétés différentes [92, 93] :

1. c'est une portion de l'espace occupée par une matière hétérogène, dont au moins l'une des phases n'est pas solide. On peut distinguer une matrice solide et un espace poreux fluide ;
2. la phase solide est distribuée dans l'intégralité du milieu poreux ;
3. au moins une partie des pores est interconnectée.

Le milieu poreux peut être considéré de deux manières différentes. Soit chacune des phases le composant est considérée séparément (étude à l'échelle des pores), soit on considère les déplacements fluides moyennés sur des volumes de taille supérieure au pores mais petits devant l'échelle du milieu complet (échelle de Darcy).

Un milieu poreux est défini par sa porosité définie comme le rapport entre le volume du vide (V_{pores}) et le volume total (V_{total})

$$\phi \equiv \frac{V_{\text{pores}}}{V_{\text{total}}} = \frac{V_{\text{pores}}}{V_{\text{pores}} + V_{\text{matrice}}}$$

où V_{matrice} est le volume de la phase solide comprise dans V_{total}.

L'écoulement monophasique dans un milieu poreux est décrit pour un fluide newtonien de viscosité μ par l'équation de Darcy [98, 101, 102]

$$\mathbf{u} = -\frac{k}{\mu}\nabla p$$

où $\mathbf{u}$ est la vitesse de Darcy de l'écoulement dans le milieu poreux. k est la perméabilité du milieu poreux. Ce paramètre décrit la capacité du matériau poreux à laisser passer un fluide sans modifier sa structure interne.

Dans le cas d'un écoulement multiphasique, il est possible d'écrire une équation de Darcy pour chaque phase en introduisant des perméabilités effectives $k_{r,i}$ ainsi que plusieurs champs de pression pour les n fluides [103, 108]

$$\mathbf{u}_i = \frac{kk_{r,i}}{\mu_i}\nabla p_i, i \in [\![1, n]\!].$$

La capacité d'un fluide à se déplacer dans un milieu poreux est ainsi décrite par le paramètre de mobilité

$$\text{Mob} \equiv \frac{kk_r}{\mu}.$$

On définit le rapport de mobilité comme le rapport de la mobilité du fluide déplacé divisée par celle du fluide invasif. En négligeant les perméabilités relatives (ce qui sera considéré par la suite), ce rapport est réduit au rapport de viscosités

$$M = \frac{\mu_{\text{invasif}}}{\mu_{\text{déplacé}}}$$

Comme les équations gouvernant les écoulements sont identiques [73, 83], il est possible d'étudier les écoulements en milieu poreux dans des cellules de Hele-Shaw [109]. La perméabilité du milieu est alors $b^2/12$ avec b l'épaisseur de la couche fluide dans la cellule.

Quatre types de méthodes sont utilisés couramment pour étudier les écoulements en milieu poreux :

- une approche continue dans laquelle le milieu poreux est caractérisé par des paramètres macroscopiques (par exemple, sa perméabilité). La loi de Darcy est un de ces modèles [124, 125].

- le modèle dit à faisceau de capillaires (*capillary bundle model*) où le volume atteignable par l'écoulement est assimilé à un ensemble de capillaires [126, 127].

- une approche visant à décrire le milieu poreux à l'échelle des pores par des méthodes numériques et résoudre les équations à cette échelle [128, 129, 130]. On peut citer les méthodes *Lattice-Boltzmann* [131, 134], *Smoothed Particle Hydrodynamics* [135], *Modified Moving Particle Semi-implicit* [136, 137, 138] et *Level-Set* [139].

- la modélisation dite *Pore-scale Network Modelling* dans laquelle le milieu poreux est approximé par une réseau de capillaires reliant des pores ayant des géométries idéalisées [140, 141, 142, 144, 145, 148].

Dans une cellule de Hele-Shaw, il est assez aisé de prendre en compte l'effet de la tension de surface entre les différents fluides mis en jeu. Il suffit pour cela de réécrire l'équation de Darcy [83]

$$\mathbf{u} = \frac{b^2}{12\mu}(-\nabla p + \sigma\kappa\nabla c).$$

Dans le cas d'un milieu poreux considéré avec une modélisation de Darcy, l'influence de la tension de surface peut être intégrée dans le champ de pression. Il n'est par conséquent pas nécessaire d'ajouter de terme à l'équation de Darcy, contrairement au cas ci-dessus [83].

Roland Lenormand a étudié les écoulements diphasiques newtoniens dans des réseaux contenant des phases aqueuse et organique [181]. Deux types de déplacement différents ont été analysés :

- drainage, c'est-à-dire l'injection d'un fluide non mouillant dans un milieu poreux saturé en fluide mouillant ;

- imprégnation, soit l'injection d'un fluide mouillant dans un milieu poreux saturé en fluide non mouillant.

Les travaux de Lenormand *et al.* [182] ont montré qu'au cours du déplacement d'un fluide par un autre dans un réseau de capillaires, les deux fluides sont présents simultanément dans les canaux.

Dans le cas d'un drainage, le ménisque entre les deux fluides ne peut se déplacer qu'en mode piston (partie gauche de la Figure 1.20(a)). En revanche, en cas d'imprégnation, plusieurs cas sont possibles. Le ménisque peut toujours se déplacer en mode piston (Figure 1.20(b)). Le fluide mouillant peut également arriver à une intersection par trois canaux adjacents et remplir le dernier canal (mode I_1, Figure 1.20(d)). En mode I_2, le fluide mouillant arrive à une intersection par deux canaux adjacents et remplit les deux canaux restants (Figure 1.20(e)). Enfin, le ménisque peut également

se déplacer en mode *snap-off* (Figure 1.20(c)). À chacun de ces modes est associée une pression seuil dépendant de la géométrie du réseau de capillaire.

Les travaux de Roland Lenormand ont permis d'établir un diagramme de phases dans le cas du drainage (Figure 1.22) [181]. Trois différents domaines sont identifiés dans le plan (rapport de viscosités M, nombre capillaire Ca) : une zone dominée par la digitation visqueuse ($M < 1$ et Ca élevé) similaire au modèle de *Diffusion-Limited Aggregation* (DLA, voir Annexe B), une zone de déplacement visqueux stable similaire à l'*anti-DLA* ($M > 1$ et Ca élevé), et une zone dominée par la digitation capillaire (Ca faible).

Dans le cas d'une imprégnation, deux cas extrêmes peuvent être considérés. Dans le cas d'un rapport d'aspect important (taille des pores grande par rapport aux canaux), l'invasion du réseau s'effectue en remplissant les canaux et en emprisonnant du fluide non mouillant dans les pores. En revanche dans le cas de petits pores, le réseau est envahi en remplissant les pores. Dans chacun de ces cas, on observe trois domaines distincts dans le diagramme de phases correspondant (Figure 1.25) [181, 184] : une zone correspondant aux nombres capillaires élevés ($\log_{10} \mathrm{Ca} > -4$) où l'écoulement est dominé par la viscosité (cette zone peut être subdivisée en deux sous-domaines stable et instable comme dans le cas du drainage), un domaine capillaire continu ($-6 \leqslant \log_{10} \mathrm{Ca} \leqslant -4$) associé à des écoulements par films de coin, et un domaine capillaire discontinu ($\log_{10} \mathrm{Ca} \leqslant -7$) associé à des écoulements du fluide mouillant le long de la rugosité des parois.

Dans les milieux déformables tels les milieux granulaires, l'écoulement d'un fluide peut déplacer les particules solides et ainsi affecter la géométrie des pores, qui va ensuite altérer les caractéristiques de l'écoulement. En raison de cette interaction entre fluide et particules, une grande variété de motifs peut être observée, parmi lesquels les fissures de dessiccation [211], les digitations granulaires [212], les structures labyrinthiques [213], les bulles communément dénommées *stick-slip bubbles* [214], les canaux ouverts [215, 216] et les fractures [214, 217, 218, 219, 220, 221].

Afin de résumer les conditions d'apparition des différents motifs de déplacement, Sandnes *et al.* [214] ont combiné leurs découvertes avec les résultats de divers auteurs [217, 224, 230] pour tracer une proposition de diagramme de phases dans l'espace

$\varphi^{-1} - q$ où φ est la fraction volumique initiale des grains[1] et q est la vitesse d'injection du fluide (Figure 1.37).

Gerris, un code de simulation numérique directe (*Direct Numerical Simulation*)

La mécanique des fluides numérique consiste à étudier le mouvement d'un fluide, ou ses effets, en résolvant numériquement les équations de l'écoulement. Dans cette étude, les simulations sont réalisées à l'aide du solveur d'écoulements multiphasiques Gerris. Ce logiciel libre a été développé par Stéphane Popinet [253, 254]. Bien qu'écrit en langage C, Gerris utilise un langage orienté objet.

Une discrétisation décalée en temps de la fraction volumique de fluide, de la masse volumique et de la pression à l'aide d'un pas de temps Δt permet d'obtenir une discrétisation du second ordre en temps des équations de Navier-Stokes qui donne pour l'étape n

$$\begin{aligned}
\rho_{n+\frac{1}{2}}\left[\frac{\mathbf{u}_{n+1}-\mathbf{u}_n}{\Delta t}+\mathbf{u}_{n+\frac{1}{2}}\cdot\nabla\mathbf{u}_{n+\frac{1}{2}}\right] &= -\nabla p_{n+\frac{1}{2}}+\nabla\cdot\left[\mu_{n+\frac{1}{2}}(\mathbf{e}_n+\mathbf{e}_{n+1})\right] \\
&\quad +(\sigma\kappa\delta_s\mathbf{n})_{n+\frac{1}{2}}+\mathbf{f}_{\text{ext}}, \\
\nabla\cdot\mathbf{u}_n &= 0,
\end{aligned}$$

où $\mathbf{e}$ est le tenseur des déformations linéarisé.

À l'aide d'une décomposition de la vitesse de Hodge [255] et en estimant le terme d'advection $\mathbf{u}_{n+\frac{1}{2}}\cdot\nabla\mathbf{u}_{n+\frac{1}{2}}$ à l'aide du schéma de Godunov du second ordre décalé de Bell-Colella-Glaz [258], on obtient les équations scalaires découplées suivantes

$$\begin{aligned}
\frac{\rho_{n+\frac{1}{2}}}{\Delta t}\mathbf{u}_\star-\frac{1}{2}\nabla\cdot\left(\mu_{n+\frac{1}{2}}\nabla\mathbf{u}_\star\right) &= \nabla\cdot\left(\mu_{n+\frac{1}{2}}\mathbf{e}_n\right)+\rho_{n+\frac{1}{2}}\left(\frac{\mathbf{u}_n}{\Delta t}-\mathbf{u}_{n+\frac{1}{2}}\cdot\nabla\mathbf{u}_{n+\frac{1}{2}}\right)+\mathbf{f}_{\text{ext}} \\
&\quad +(\sigma\kappa\delta_s\mathbf{n})_{n+\frac{1}{2}}+\frac{1}{2}(\nabla\mathbf{u}_n)^T\nabla\mu_{n+\frac{1}{2}}, \\
\mathbf{u}_{n+1} &= \mathbf{u}_\star-\frac{\Delta t}{\rho_{n+\frac{1}{2}}}\nabla p_{n+\frac{1}{2}}, \\
\nabla\cdot\mathbf{u}_{n+1} &= 0.
\end{aligned}$$

[1] normalisée de telle manière que $\varphi = 1$ pour des empilements compacts de grains

Le domaine de calcul est discrétisé à l'aide de carrés (des cubes en trois dimensions) de volumes finis organisés hiérarchiquement suivant une structure de type arbre, appelée *quadtree* (ou *octree* en 3D). Toutes les variables (composantes de la quantité de mouvement, pression et traceurs passifs) sont localisées au centre de chaque volume de discrétisation carré (cube en 3D). Une méthode de projection [266, 267, 268, 269] est utilisée pour la discrétisation spatiale de l'équation de pression corrigée (voir ci-dessus) et la divergence associée dans l'équation de Poisson.

La divergence du champ de vitesse auxiliaire est calculée sur chaque volume de contrôle comme une approximation de volume fini

$$\nabla \cdot \mathbf{u}_\star = \frac{1}{h} \sum_f \mathbf{u}_\star^f \cdot \mathbf{n}^f,$$

où $\mathbf{n}^f$ représente le vecteur unitaire normal à la face et h l'échelle de longueur de la cellule.

Le champ de vitesse au centre de la cellule au temps $n+1$ est obtenu en appliquant la correction de pression au centre de la cellule

$$\mathbf{u}_{n+1}^c = \mathbf{u}_\star^c - \left| \frac{\Delta t}{\rho^f_{n+\frac{1}{2}}} \nabla^f p_{n+\frac{1}{2}} \right|^c,$$

où $\rho^f_{n+\frac{1}{2}}$ est obtenu par moyenne des valeurs au centre de la cellule $\rho^c_{n+\frac{1}{2}}$, ∇^f est l'opérateur gradient par rapport au centre d'une face d'une cellule et l'opérateur $|\cdot|^c$ représente la moyenne sur toutes les faces délimitant la cellule. Le champ de vitesse obtenu $\mathbf{u}_{n+1}^c$ est approximativement sans divergence.

Une des particularités de Gerris est son raffinement adaptatif du maillage. Plusieurs critères de raffinement peuvent être utilisés simultanément.

Pour les écoulements diphasiques, l'approximation d'une interface infiniment mince est utilisée, et l'on définit une fonction de Heaviside

$$c(\mathbf{x}, t) = \begin{cases} 1 \text{ si } \mathbf{x} \text{ est dans le fluide 1,} \\ 0 \text{ si } \mathbf{x} \text{ est dans le fluide 2.} \end{cases}$$

On définit également la fraction volumique c_γ d'une cellule carrée γ de volume V

$$c_\gamma = \frac{1}{V} \int_V c(\mathbf{x}, t)\, d\mathbf{x}.$$

L'équation d'advection pour la densité peut alors être remplacée par

$$\partial_t c_\gamma + \nabla \cdot (c_\gamma \mathbf{u}) = 0.$$

Cette équation est ensuite résolue à l'aide d'un schéma géométrique affine par morceaux VOF (*Volume of Fluid*) [235, 271, 272, 273] généralisé pour la géométrie *quadtree/octree* utilisée.

Afin d'obtenir une estimation précise du terme de tension de surface $(\sigma\kappa\delta_s\mathbf{n})_{n+\frac{1}{2}}$, une approche de Force de Surface Continue (CSF) [179] est mise en œuvre

$$\begin{aligned} \sigma\kappa\delta_S\mathbf{n} &\approx \sigma\kappa\nabla^h\tilde{c}, \\ \kappa &\approx \nabla^h \cdot \tilde{n} \end{aligned}$$

où $\tilde{n} \equiv \frac{\nabla^h\tilde{c}}{|\nabla^h\tilde{c}|}$, ∇^h est un opérateur de différences finies et $\tilde{c}$ le champ de fraction volumique filtrée spatialement.

Afin que l'estimation de la courbure soit robuste et simple à implémenter, son calcul se fait par le biais d'une fonction de hauteur [287]. Si l'interface varie comme $y = f(x)$, la courbure peut ainsi être calculée de la manière suivante

$$\kappa = \frac{f''}{(1 + (f')^2)^{3/2}}.$$

à l'aide d'approximations de différences finies.

Comme Gerris utilise des carrés en 2D (cubes en 3D), il est possible de l'utiliser en parallèle, en définissant des cellules racines à un niveau non nul (Figure 2.9).

Afin de prendre en compte les frontières solides au cours de la discrétisation spatiale, les cellules traversées par une telle frontière sont considérées comme des cellules mixtes, et donc gérées de la même manière que celles contenant une interface entre deux fluides. La frontière solide est ainsi définie par une approche de type VOF. Une condition de glissement est ensuite imposée à la frontière

$$\mathbf{u} \cdot \mathbf{n} = 0,$$

où $\mathbf{n}$ est le vecteur unitaire dirigé vers l'extérieur situé au niveau de la frontière solide $\partial\Omega_s$. D'autre part, les cellules intégralement situées dans la phase solide sont retirées du calcul.

Malheureusement, lorsque l'échelle caractéristique des écoulements fluides et/ou des solides est inférieure à la taille du maillage, l'efficacité du solveur multigrille est bridée [288].

Afin de contourner ce problème, cette étude a majoritairement utilisé une autre modélisation des éléments solides. Dans cette méthode, dite des « solides virtuels », le domaine solide $\Omega_s = \overline{\Omega}_s$ n'est pas retiré du calcul. Par conséquent, le code considère que l'intégralité du domaine $\Omega = \overline{\Omega}$ est remplie de fluide. Afin de modéliser le comportement d'une matrice solide, on impose une condition de vitesse nulle dans la phase solide

$$\forall \mathbf{x} \in \Omega_s, \mathbf{u}(\mathbf{x}) = 0.$$

Cette condition est imposée à chaque pas de temps. Les propriétés (densité, viscosité) du fluide doivent également être constantes au sein de tout sous-ensemble connexe par arc du domaine solide. Afin d'éviter la génération au sein de la matrice solide d'une vitesse numérique non physique entre deux pas de temps due au gradient de pression, une force de traînée strictement numérique est ajoutée dans la phase solide aux équations de Navier-Stokes

$$\mathbf{f}_{\text{drag}} = -M\mathbf{u}.$$

Afin de valider l'utilisation de Gerris dans le cadre de simulations d'écoulements multiphasiques en milieu poreux, plusieurs tests ont été effectués.

Des tests de scalabilité à faible porosité ont été réalisés. On rappelle qu'il existe deux notions de scalabilité :

- la scalabilité forte, définie comme la façon avec laquelle le temps pour atteindre une solution varie lorsqu'on fait varier le nombre de processeurs dans un problème total de taille fixe ;

- la scalabilité faible, définie comme la façon avec laquelle le temps pour atteindre une solution varie lorsqu'on fait varier le nombre de processeurs dans un problème de taille par processeur fixe.

Pour effectuer ces études de scalabilité, on définit le nombre de mise à jour de cellules par seconde et par cœur

$$Z_{/np} \equiv \frac{Z}{N_p} = \frac{N_x \times N_y \times N_z \times N_{dt}}{T_{CPU/np} \times N_p},$$

où N_x (respectivement N_y, N_z) est le nombre de cellules dans la direction x (respectivement y, z), N_{dt} le nombre de pas de temps considéré, $T_{CPU/np}$ le temps d'horloge CPU[2] requis pour calculer ces pas de temps et N_p le nombre de cœurs utilisé.

Les tests sont réalisés dans une structure poreuse idéale dont la matrice poreuse est un réseau cubique à faces centrées de sphères (la porosité obtenue est $\phi = 26$ %). Deux clusters distincts sont utilisés :

- le cluster *babbage2* situé à l'Institut Jean le Rond d'Alembert (UPMC-Paris VI) pour des tests allant de 1 à 64 cœurs ;
- le cluster *Rostand* situé au Centre Scientifique et Technique Jean-Féger (TOTAL SA) pour des tests allant de 1 à 4096 cœurs.

Deux solveurs différents sont comparés : le solveur par défaut de Gerris et le solveur parallèle *High Performance Preconditioners* (*Hypre*).

Les très mauvais résultats obtenus avec *Hypre* conduisent à ne pas l'utiliser pour la suite de cette étude. En revanche, les résultats obtenus avec le solveur par défaut de Gerris sont prometteurs. Ils permettent en outre de déterminer que la vitesse de calcul de Gerris est plus importante en utilisant la méthode des « solides virtuels » pour modéliser les solides qu'avec la modélisation par défaut des solides. Avec cette modélisation, les scalabilités aussi bien forte que faible sont proches de la perfection ($Z_{/np}$ quasi constant en changeant le nombre de cœurs).

Avec le cluster *babbage2*, la vitesse de calcul de Gerris est de l'ordre de 20.000 mises à jour de cellules par seconde et par cœur (Figures 2.14 et 2.15). Avec le cluster *Rostand*, cette vitesse varie de 20.000 à 50.000 mises à jour de cellules par seconde et par cœur en fonction des cas (Figures 2.16 et 2.17).

La connaissance de la vitesse de calcul d'un code permet d'estimer le temps d'horloge CPU nécessaire pour simuler une invasion dans un milieu poreux 3D jusqu'à

[2] *Central Processing Unit*

la percée, à l'aide de la formule suivante

$$T_{CPU/np} = N_{P/L}^4 \, n_{ce/p}^4 \, (\chi Z_{/np} \times n_p)^{-1}$$

où

$$\begin{cases} N_{P/L} &= \text{nombre de « pores » dans chaque direction} \\ n_{ce/p} &= \text{nombre de cellules par pore} \\ \chi &= \text{nombre CFL} \\ Z_{/np} &= \text{vitesse de calcul par cœur} \\ n_p &= \text{nombre de cœurs} \end{cases}$$

Pour rappel, le nombre CFL[3] est défini par $\text{CFL} = \frac{U\Delta t}{h}$ avec U une vitesse caractéristique, Δt le pas de temps et h la taille caractéristique du maillage.

D'autre part, dans le cadre de la simulation de l'invasion d'un milieu poreux 3D, le nombre CFL varie comme

$$\chi \propto \text{Ca}^{\gamma} \, \text{La}^{1/2} \, n_{ce/p}^{-1/2} / \phi$$

où

$$\begin{cases} \text{Ca} = \mu V_D / \sigma &= \text{nombre capillaire calculé à partir de la vitesse de Darcy} \\ \text{La} = \frac{\sigma \rho l}{\mu^2} &= \text{nombre de Laplace} \\ \phi &= \text{porosité} \\ n_{ce/p} &= \text{nombre de cellules par pore} \\ \gamma = 1 - \frac{\nu}{\nu+1}(3 - D_F) &= \text{exposant dû à la structure fractale des digitations} \\ D_F &= \text{dimension fractale} \\ \nu &= \text{exposant de la longueur de corrélation} \end{cases}$$

En 3D, $\nu/(\nu+1) \approx 0,5$ [299]. Ainsi, pour $D_F \approx 2,5$, $\gamma \approx 3/4$.

De cette équation, on peut déduire que :

- le nombre CFL diminue avec le nombre capillaire. Ceci a tendance à augmenter de manière conséquente les temps de calcul en milieu poreux, lesquels sont réalisés à très faible nombre capillaire (de l'ordre de $10^{-8} - 10^{-6}$).

[3] Courant-Friedrichs-Lewy

- le nombre CFL varie avec le nombre de Laplace, ce qui peut s'avérer dangereux en raison de la grande variété des viscosités possibles.

L'influence de ces inconvénients pourrait être fortement minorée en implémentant une gestion totalement implicite de la tension de surface dans Gerris.

Divers tests ont également été réalisés afin de s'assurer de la précision des résultats fournis par Gerris. A ces fins, les normes L_1, L_2 et L_∞ usuelles ont été étendues aux solutions ξ définies sur un domaine de taille N^3 par

- $L_\infty(\xi) = \max\limits_{c \in Cellules} L_\infty(\xi(c))$,
- $L_1(\xi) = \frac{1}{N^3} \sum\limits_{c \in Cellules} L_1(\xi(c))$,
- $L_2(\xi) = \left(\frac{1}{N^3} \sum\limits_{c \in Cellules} (L_2(\xi(c)))^2 \right)^{1/2}$.

La simulation d'écoulements de Poiseuille [180] a été effectuée dans les cas mono- et diphasique. Deux géométries distinctes ont été considérées : dans un cas, l'écoulement de Poiseuille est aligné avec l'une des directions principales du maillage (dans les faits avec la direction x) ; dans l'autre, la direction de l'écoulement est en biais par rapport aux directions principales du maillage.

Dans le cas d'un écoulement monophasique dans la direction x, la convergence de l'erreur entre champs de vitesse théorique et simulé est quasi-quadratique lorsqu'on fait varier la résolution, quelle que soit la norme utilisée. En revanche, dans le cadre d'un écoulement monophasique en biais, cette convergence atteint un plancher de l'ordre de 10^{-4}, quelle que soit la modélisation choisie pour la phase solide.

Dans le cas d'un écoulement diphasique (cas $\mu_1/\mu_2 = 2$ avec le fluide le plus visqueux au centre) dans la direction x, la convergence de l'erreur entre champs de vitesse théorique et simulé est moins rapide que linéaire lorsqu'on fait varier la résolution, quelle que soit la norme utilisée. D'autre part, les résultats obtenus par Gerris sous-estiment la valeur du champ de vitesse. Comme cette sous-estimation est inférieure à 2 % (l'erreur est maximale au centre du domaine), les résultats obtenus sont satisfaisants.

Enfin, dans le cadre d'un écoulement diphasique en biais, la convergence de l'erreur entre champs de vitesse théorique et simulé atteint un plancher de l'ordre de 10^{-4}, quelle que soit la modélisation choisie pour la phase solide. Dans le cas de la modélisation standard de la phase solide, les résultats obtenus par Gerris sous-estiment la valeur du champ de vitesse. Quand on néglige les effets de bord, l'erreur, maximale au centre du domaine, est inférieure à 6 %. En revanche, dans le cas d'une modélisation de la phase solide par la méthode des « solides virtuels », les résultats obtenus par Gerris sur-estiment la valeur du champ de vitesse d'environ 10 % (en négligeant les effets de bord).

D'autres tests ont été réalisés afin de mesurer la perméabilité numérique d'un milieu poreux [170] généré à l'aide de sphères réparties aléatoirement sur un réseau cubique à faces centrées. Les résultats sont comparés à divers modèles : une limite supérieure proposée par Weissberg et Prager [301] ; l'estimation de Brinkman, valable à forte porosité [303] ; la courbe semi-empirique de Kozeny-Carman [162, 166, 167].

À forte porosité, les résultats obtenus concordent parfaitement avec l'estimation proposée par Brinkman. À porosité moyenne ($20\% \leqslant \phi \leqslant 70\%$), les perméabilités calculées sont légèrement plus élevées que les valeurs obtenues à partir de la courbe semi-empirique de Kozeny-Carman (tout en étant néanmoins du même ordre de grandeur, soit deux à trois fois plus importantes). Comme aucun accord strict n'est en théorie requis avec la courbe de Kozeny-Carman (certains milieux poreux sont en accord, contrairement à d'autres) [170], les perméabilités obtenues sont acceptables. Les valeurs obtenues ont cependant tendance à se rapprocher de la courbe de Kozeny-Carman pour des perméabilités faibles. Par conséquent, les perméabilités mesurées paraissent satisfaisantes pour une large gamme de porosités.

Suite à la validation de Gerris par les différents tests présentés, des simulations ont été effectuées d'invasion de milieux poreux réels obtenus par micro-tomographie.

Des simulations dans un pore unique ($M = \frac{\mu_{\text{eau}}}{\mu_{\text{huile}}} = 1/2500$, $\text{Ca}_{\text{huile}} \sim 10$, $\text{Ca}_{\text{eau}} \sim 4 \times 10^{-3}$, $\text{Re}_{\text{huile}} \sim 8 \times 10^{-5}$, $\text{Re}_{\text{eau}} \sim 2.5$) d'invasions à débit massique constant ont mis en évidence une augmentation du temps nécessaire pour atteindre la percée dans le cas mouillant à l'eau ($\theta = 0°$) par rapport au cas mouillant à l'huile ($\theta = 180°$). Dans le cas mouillant à l'eau, le fluide invasif occupe en effet une plus grande part du

pore considéré, ce qui résulte en une vitesse plus faible de l'avancée de l'extrémité de la digitation.

D'autre part, en faisant varier le rapport de viscosités, on observe que, même si le temps physique de la percée varie peu, le temps CPU nécessaire pour atteindre cette percée augmente quand on augmente le contraste de viscosités.

Enfin, des simulations ($M = \frac{\mu_{\text{eau}}}{\mu_{\text{huile}}} = 1/10$, $\text{Ca}_{\text{eau}} \sim 3 \cdot 10^{-2}$ et $\text{Re}_{\text{eau}} \sim 100$) ont été réalisées dans des géométries plus complexes, d'une taille de 256^3 voxels, soit $737,28^3\,\mu\text{m}^3$. La valeur du nombre CFL est alors très satisfaisante, puisqu'elle reste très proche de la valeur théorique maximale des méthodes VOF, soit $0,5$.

D'autres simulations sont réalisées dans une géométrie encore plus grande (400^3 voxels, soit $1,152^3\,\text{mm}^3$) avec les caractéristiques suivantes : $M = \frac{\mu_{\text{eau}}}{\mu_{\text{huile}}} = 1/10$ et $\text{Re}_{\text{eau}} \sim 250$. La percée est obtenue au bout d'un jour de temps CPU dans le cas $\text{Ca}_{\text{eau}} \sim 3 \cdot 10^{-3}$ lorsque la simulation est réalisée avec 400 cœurs. Le processus de digitation induit par la géométrie est patent (Figure 2.51). De plus, en faisant varier le nombre capillaire depuis $3 \cdot 10^{-2}$ jusqu'à $3 \cdot 10^{-5}$, on observe que la vitesse de la digitation la plus avancée décroît de manière substantielle avec le nombre capillaire. Les digitations observées sont également plus épaisses pour de plus faibles nombres capillaires. L'effet de la tension de surface étant plus importante dans ces cas, celle-ci va avoir tendance à réduire la courbure des digitations. Ainsi, le fluide invasif remplit de manière plus complète les pores, créant des films de Bretherton le long des parois des pores [313, 314].

Digitation visqueuse en 2D

On considère une cellule de Hele-Shaw, assimilée à un plan. Une interface sépare ce plan en deux régions. On s'intéresse au cas où l'interface se déplace en direction du fluide le plus visqueux (noté 2 pour une viscosité égale à μ_2 ; la viscosité de l'autre fluide, noté 1, est μ_1) avec une vitesse normale

$$v_n \propto \mathbf{n} \cdot \nabla p,$$

où $\mathbf{n}$ est le vecteur normal unitaire dirigé vers le fluide 2. On considère que la pression est constante dans le fluide 1 et vérifie

$$\nabla^2 p = 0$$

dans le fluide 2.

Une telle situation est instable : toute irrégularité de l'interface va avoir tendance à se développer indéfiniment. Il est aisé de montrer que la déstabilisation de l'interface aura un taux de croissance maximal pour le vecteur d'onde

$$k_c = \frac{2}{b}\sqrt{\mathrm{Ca}},$$

où b est l'épaisseur de la cellule de Hele-Shaw, ce qui correspond à une longueur d'onde d'instabilité maximale

$$l_c = \pi b\, \mathrm{Ca}^{-1/2}.$$

L'interface est cependant instable pour tout vecteur d'onde tel que $k < k_{\max} = \sqrt{3}k_c$.

Cette instabilité de l'interface n'empêche cependant pas l'existence de solutions stables. Dans le cas d'une cellule de Hele-Shaw linéaire de largeur W, le motif obtenu est contrôlé par le paramètre

$$B = \frac{\sigma}{12\mu U}\left(\frac{b}{W}\right)^2 = 8.45 \times 10^{-3}\left(\frac{l_c}{W}\right)^2.$$

Une unique digitation est observée pour une grande gamme de valeurs de B. Le rapport λ entre la largeur de la digitation et celle de la cellule tend vers $\lambda = 0,5$ quand B diminue. Cette digitation unique est stable jusqu'à une valeur $B \approx 1,4 \times 10^{-4}$ (soit $W \approx 8\, l_c$). En dessous de cette valeur, le motif est instable.

On rappelle également que, en l'absence de tension de surface, la forme de l'interface vérifie

$$x = \frac{W(1-\lambda)}{2\pi} \ln \frac{1}{2}\left[1 + \cos\left(\frac{2\pi y}{\lambda W}\right)\right],$$

où $\lambda \in [0\,,\,1]$ (Figure 3.5).

Dans le cadre d'une cellule de Hele-Shaw angulaire d'angle θ_w (positif si l'écoulement se fait dans la direction divergente), on peut considérer le paramètre $B = 8,45 \times 10^{-3}(l_c/\theta_w r)^2$ où $r\theta_w$ est l'épaisseur curviligne locale $W(r)$. Une unique digitation occupe une fraction finie $\lambda_{\theta_w} > 0.5$ de l'épaisseur angulaire pour des valeurs modérées de

B. Cette fraction varie approximativement de manière linéaire par rapport à l'angle du domaine. Pour B constant, soit U variant comme r^{-2}, la digitation croît selon une structure autosimilaire. Dans les autres cas, la digitation devient spontanément instable.

Il est possible de simuler des écoulements de Darcy avec Gerris. Pour cela, il est nécessaire de supprimer le terme d'advection dans les équations de Navier-Stokes, et considérer une force de traînée $\mathbf{f} = -\beta\mathbf{u}$

$$\partial_t \mathbf{u} = -\frac{1}{\rho}\nabla p - \beta\mathbf{u}.$$

On décompose alors la solution numérique en un terme exact et une erreur

$$\mathbf{u}(t) = \mathbf{u}_0 + \mathbf{e}(t)$$

avec $0 = -\nabla p - \beta\rho\mathbf{u}_0$ pour le terme exact. L'erreur est solution de $\partial_t \mathbf{e} = -\beta\mathbf{e}$ pour une solution exacte stable, soit $\mathbf{e} = -\mathbf{C}\exp(-\beta t)$. L'erreur est ainsi petite après un pas de temps Δt si $\beta\Delta t \gg 1$. Pour une solution exacte dépendant du temps $\mathbf{u}_0$, la même décomposition permet de montrer que l'erreur varie comme $\mathbf{u}_0/(\beta T_c)$ où T_c est le temps caractéristique de la solution exacte et requiert donc $\beta T_c \gg 1$. On obtient cette condition par le choix des unités de temps et de longueur.

Le solveur permet donc soit d'obtenir une itération faussement variable vers la solution d'équilibre, soit de suivre de manière adiabatique une solution dépendant du temps de

$$\mathbf{u} = -\frac{1}{\beta\rho}\nabla p.$$

On s'intéresse au développement des digitations de Saffman-Taylor dans une cellule de Hele-Shaw avec injection centrale en présence de tension de surface [322, 330]. On considère ainsi des domaines 2D carrés de taille adimensionnée L_d centrés en $(0, 0)$

$$\Omega = [-L_d/2, L_d/2]^2.$$

Les deux composantes de la vitesse sont (u, v). Le domaine est initialement rempli avec un fluide de forte viscosité ($\mu = 1$). Un fluide moins visqueux ($\mu = M > 0$) est injecté au centre du domaine avec un débit massique constant. Les limites du domaine sont soumis à une condition quasi-circulaire de sortie libre du fluide.

Les fluides sont considérés incompressibles et se déplacent suivant la loi de Darcy [102, 108]. Le champ de pression obéit ainsi à une équation de Laplace [326].

Les simulations s'intéressent à des écoulements diphasiques pour des rapports de viscosités allant de $M = \frac{\mu_2}{\mu_1} = 10^{-4}$ à 10^{-2}. Comme présenté ci-dessus, il est possible de ne considérer que la contribution dans le plan du rayon de courbure

$$[\![p]\!] = \frac{\lambda_\sigma}{R}. \tag{E.18}$$

où $[\![\ ]\!]$ dénote un saut, R est le rayon de courbure principal de la projection dans le plan de l'extrémité du ménisque séparant les deux phases et λ_σ une longueur caractéristique de l'influence de la tension de surface.

On part d'une interface circulaire légèrement perturbée $r(\theta) = 1 + 1/10(\cos(3\theta) + \sin(2\theta))$ [384]. Ne sont considérés que les temps courts. On impose d'autre part $\lambda_\sigma = 1/3$ et la taille du maillage est $h = 1/60$.

À faible contraste de viscosité, des bulles secondaires se détachent de la bulle principale. Certains digitations ont également tendance à se reconnecter au bout d'un certain temps, emprisonnant ainsi des gouttes à forte viscosité à l'intérieur de la bulle à faible viscosité. Au contraire, à fort contraste de viscosité, les différentes digitations se développent de manière indépendante, sans réunion ultérieure. À ces deux cas sont associés deux régimes de dimension fractale distincts. La transition s'effectue à un plus faible contraste de viscosité lorsque l'amplitude du bruit générant l'instabilité est plus important.

Fast & Shelley ont d'autre part expliqué [330] que, à temps long, la longueur de l'interface d'une simulation de digitations de Saffman-Taylor est reliée à l'aire de la bulle correspondante par une loi de puissance Aire $\sim$ (Longueur)$^\alpha$ (dans leur cas, $\alpha = 1,45$). On peut noter que la variation de ce coefficient α est déconnectée de celle de la dimension fractale. Un second régime peut être défini aux temps courts avec un autre coefficient ($\alpha = 0,61$ dans le cas de Fast & Shelley). Par la suite, α_1 sera le coefficient aux temps courts, et α_∞ le coefficient asymptotique.

Dans les simulations exposées ci-dessus, les coefficients obtenus sont distincts de ceux trouvés par Fast & Shelley : on trouve $\alpha_1 \in [0.37, 0.38]$, et $\alpha_\infty \in [0.91, 1.08]$, avec des variations en fonction du rapport de viscosités et de l'origine du bruit générant la

déstabilisation de l'interface. Il semblerait également que le coefficient α_∞ augmente avec le contraste de viscosités, même si l'amplitude du changement observé est trop faible pour pouvoir être péremptoire.

Les valeurs obtenues numériquement ont été comparées avec une mesure expérimentale. À partir des résultats d'une expérience réalisée par Praud & Swinney [231] pour laquelle $M \sim 5 \cdot 10^{-5}$, il a été possible de déterminer $\alpha_\infty = 1,14$. Enfin, une simulation de cette expérience a été réalisée à l'aide de Gerris, permettant d'obtenir un motif de digitations de dimension fractale $D_F = 1,67$, soit très proche de celle calculée à partir des résultats de Praud & Swinney ($D_F = 1,69$).

Des simulations en coordonnées polaires ont également été réalisées. Cependant, cette fonctionnalité de Gerris étant très rarement utilisée, l'implémentation du parallélisme est pour l'heure déficiente dans ce module. Seules des simulations sur un cœur ont ainsi pu être réalisées.

Injection latérale dans une géométrie quasi-2D

Dans les réservoirs, l'injection d'eau et/ou de solutions de polymères est une alternative pour récupérer les huiles lourdes lorsque les méthodes thermiques sont soit impraticables, soit non rentables. Des expériences d'invasion d'eau et/ou de solutions de polymères ont ainsi été réalisées dans des échantillons carrés quasi-bidimensionnels de grès de Bentheimer [38].

Ces expériences ont été effectuées avec deux huiles de viscosités distinctes : $\mu_{2000} = 2,0$ kg.m^{-1}.s^{-1} = 2000 cP (expérience E2000) et $\mu_{7000} = 7,0$ kg.m^{-1}.s^{-1} = 7000 cP (expérience E7000).

Lors d'un balayage avec de la saumure, le taux de récupération est inférieur à 30 %. Ce taux est cependant légèrement plus élevé dans le cas E2000 que dans le cas E7000. Aux temps courts, un grand nombre de digitations est généré. Certaines d'entre elles vont se propager plus rapidement que d'autres et ainsi inhiber le développement des digitations plus petites. Aux temps longs, ces digitations vont avoir tendance à s'unir pour former d'épais canaux aqueux, dont l'aspect fractal est beaucoup moins marqué.

La coalescence des digitations est cependant plus précoce et plus marquée dans le cas E2000 que dans le cas E7000. Le balayage avec de la saumure est ainsi dominé d'abord pas la digitation visqueuse, puis par la formation de canaux aqueux.

L'injection dans un second temps d'une solution de polymères entraîne un doublement du taux de récupération dans les deux cas. Néanmoins, comme précédemment, dans le cas de l'expérience réalisée avec l'huile la moins visqueuse, la production d'huile est plus rapide et résulte en un taux de récupération plus important. L'huile mobilisée au cours de ce deuxième balayage suit les canaux aqueux établis précédemment lors du balayage de saumure.

Enfin, dans le cas d'un balayage d'eau, la vitesse de production (par rapport à la quantité d'eau injectée) est plus important pour des vitesses d'injection plus faibles. Alors que lors des balayages à forte vitesse d'injection l'huile est récupérée uniquement près des canaux aqueux cités précédemment, la phase aqueuse s'en éloigne lors des balayages à faible vitesse et visite une aire beaucoup plus importante du milieu poreux [402]. Cela est probablement dû à un processus d'imprégnation (le nombre capillaire est alors plus faible) [403].

Afin de mieux comprendre les processus en action dans les expériences présentées ci-dessus, des simulations d'écoulements darcéens dans des milieux rectangulaires avec injection latérale ont été réalisées ($M = \frac{\mu_{\text{eau}}}{\mu_{\text{huile}}} = 10^{-3}$). Comme attendu, l'interface est instable et des digitations se développent. De plus, les digitations les plus avancées inhibent le développement des digitations plus petites.

D'autre part, d'après les simulations, la percée devrait advenir lorsque 30 % de l'huile a été récupérée. Les expériences cependant permettent de déterminer que le taux de récupération à la percée est 3 % [388]. Cette surestimation flagrante a deux origines principales. D'une part, les simulations effectuées négligent l'aspect tridimensionnel des écoulements, alors qu'un processus de digitations est également en cours dans la troisième dimension. D'autre part, en raison du caractère fractal des digitations observées, l'aire simulée dépend de la taille caractéristique minimale (ici la taille du maillage h) selon une loi de puissance Aire $\propto h^{d-D_F}$: comme la taille du maillage est plus importante que la taille des pores, on surestime donc l'aire réelle.

En faisant varier le rapport de viscosité, on se rend compte que la pointe de la digitation la plus rapide a une vitesse plus importante dans le cas d'un plus grand contraste de viscosités, entraînant une percée plus précoce (comme observé dans les expériences).

Enfin, dans le cadre de la simulation d'injection de polymères dans un second temps, on observe bien une mobilisation de l'huile située derrière le front des digitations.

Abstract

Understanding multiphase flow in porous media is of tremendous importance for many industrial and environmental applications at various spatial and temporal scales. The present study consequently focuses on modelling multiphase flows by the Volume-of-Fluid method in porous media and shows simulations of Saffman-Taylor fingering motivated by the analysis of waterflooding experiments of extra-heavy oils in quasi-2D square slab geometries of Bentheimer sandstone. The Gerris code which allows efficient parallel computations with octree mesh refinement is used. It is tested for accuracy and computational speed using several levels of refinement and comparing to reference simulations in the literature. Simulations of real rocks are realised in three dimensions with very promising results. Though it is not yet possible to attain realistic capillary numbers, it is possible to simulate flows in domains of physical size up to 1 mm^3 in reasonable CPU time. 2D simulations of viscous fingering with both central and lateral injection are also presented in this study, based on Darcy's law. The fractal aspect of this fingering is studied by considering both its fractal dimension and the variation of the area of the resulting pattern with respect to its arclength. Finally, polymer flooding following waterflooding in a two-step process is simulated with Darcy modelling.

Keywords: porous medium, Volume-of-Fluid, Enhanced Oil Recovery, viscous fingering, multiphase flow, fractal patterns

Résumé

La compréhension des écoulements multiphasiques en milieu poreux revêt une importance capitale dans de nombreuses applications industrielles et environnementales, à des échelles spatiales et temporelles variées. Par conséquent, la présente étude propose une modélisation des écoulements multiphasiques en milieu poreux par le biais de la méthode Volume de Fluide, et présente des simulations de digitations de Saffman-Taylor, motivées par l'analyse d'expériences de balayage dans des blocs de grès de Bentheimer quasi bidimensionnels initialement saturés en huile extra-lourde par de l'eau. Le code Gerris, permettant des calculs parallèles efficaces à l'aide d'un maillage de type octree, est utilisé. Des tests de précision et de rapidité de calcul sont réalisés à l'aide de divers niveaux de raffinement, ainsi qu'une comparaison avec des simulations de référence dans la littérature. Des simulations 3D dans des milieux réels numérisés sont réalisés avec des résultats encourageants. Même s'il n'est pas encore possible d'atteindre des nombres capillaires réalistes, des écoulements dans des domaines cubiques de 1 mm de côté sont simulés, avec un temps de calcul raisonnable. Des simulations 2D de digitations visqueuses avec injection centrale ou latérale sont également présentées, basées sur la loi de Darcy. L'aspect fractal des digitations est étudié aussi bien à l'aide de la dimension fractale que de la variation de l'aire des motifs obtenus par rapport à leur périmètre. Enfin, des balayages à l'aide de polymères suivant des balayages à l'eau dans un processus en deux temps sont simulés à partir d'une modélisation darcéenne.

Mots-clés: milieu poreux, Volume de Fluide, récupération assistée du pétrole, digitation visqueuse, écoulement multiphasique, motifs fractals